学位論文

A Study of Low Frequency Vibration Isolation System for Large Scale Gravitational Wave Detectors
（大型重力波検出器のための低周波防振装置に関する研究）

平成27年12月博士（理学）申請

東京大学大学院理学系研究科
物理学専攻
関口 貴令

Abstract

Gravitational waves are distortions of spacetime which propagate through space at the speed of light. Several large-scale interferometers have been constructed around the world for the direct detection of them. The first generation detectors (TAMA, GEO, LIGO and Virgo) have performed scientific observation since 1999. They had detection probabilities of gravitational waves from binary neutron star coalescences only a few percent per year at best, and have not achieved the gravitational wave detection. Currently the second generation detectors (advanced LIGO, advanced Virgo and KAGRA) with improved sensitivities are being upgraded or constructed. They are designed to have detection probabilities of gravitational waves from binary neutron star coalescences multiple times per year, and are expected to achieve the first gravitational wave detection through years of observation. The second generation detectors also feature in expanding the detection band to lower frequency down to ~ 10 Hz, which allows detection of gravitational waves from a greater variety of astronomical sources, such as intermediate mass black hole (IMBH) binaries and spinning pulsars with long rotation periods.

To expand the detection band toward lower frequencies, it is required to suppress the seismic noise: vibration noise introduced by continuous and random ground motion. For the seismic noise reduction, the Japanese second generation detector KAGRA introduces SAS (Seismic Attenuation System) to the core optics of the interferometer. The SAS provides passive seismic attenuation starting from sufficiently low frequencies ($\lesssim 0.1$ Hz) and is expected to suppress the seismic noise well below other fundamental noise levels in the detection band of gravitational waves (> 10 Hz). On the other hand, the SAS introduce large fluctuation outside the detection band (< 1 Hz) through mechanical resonances and thermal drift of the mechanical filters. Such low frequency fluctuation disturbs the lock acquisition and stable operation of the interferometer and therefore is required to be suppressed by active control systems.

The study in this thesis mainly develops active control system of the SAS for the beam splitter and signal recycling mirrors in the KAGRA interferometer (so-called the type-B SAS). Specific requirements on the active control system are set for three different operation phases of the interferometer (the calm-down phase, the lock-acquisition phase and the observation phase). In the calm-down phase, the system is largely excited due to disturbances such as earthquakes and thus the $1/e$ decay time of mechanical resonances has to be suppressed less than 1 minute for quick recovery from excitation states. After

the system calms down, the detector gets into the lock-acquisition phase, in which the interferometer is being locked and the RMS (Root Mean Square) velocities of the optics are required to be suppressed (< 0.5 μm/sec) for attaining smooth lock-acquisition of the interferometer. After the lock of the interferometer is acquired (in the observation phase), long-term drift of the longitudinal displacements and angles have to be suppressed lower than 0.4 μm or 1 μrad) to keep the interferometer lock. At the same time, the control noise couplings in the detection band (> 10 Hz) should be suppressed below the required displacement noise level of the type-B SAS.

To meet these requirements, different types of control loops are designed for respective operation phases of the interferometer, and the stability and performance of the active controls are experimentally tested with the type-B SAS prototype constructed at TAMA300 in National Atronomical Observatory of Japan. Digital control system is introduced to attain complicated servos for the Multiple Input Multiple Output (MIMO) controls. The control loops for respective phases are adopted to the prototype active control system and performance is checked with vibration sensors. As there is only one prototype SAS, an interferometer with multiple suspended optics is not able to be constructed and instead photo-reflective sensors to monitor the longitudinal displacement of the mirror (with respect to the ground) are introduced.

The tests with the prototype SAS demonstrate that the designed active control system basically meets the requirements for smooth lock acquisition and continuous operation of the interferometer. The mechanical resonances which can affect the interferometer operation are efficiently damped and the decay time is suppressed to less than 1 min. The mirror RMS velocity and angles converted from the measured RMS values in conformity with the seismic vibration level of the KAGRA site meet the requirements for the interferometer lock acquisition. The drift of the mirror position and angles are measured by five days continuous operation of the active controls, and they are proved to be smaller than the required level to keep the interferometer lock. An automaton is introduecd in the long-term control test for switching the control loops for three different operation phases, and the five days continuous and stable operation demonstrates the soundness of the automaton state control. One problem found in the prototype test is the sensor noise couplings from the alignment control loops. The measured noise couplings are 1-2 orders of magnitude larger than the expected values in the simulation, and they are expected to degrade the detector sensitivities in the 10-20 Hz band. It is suspected that the larger noise couplings observed in the prototype test are caused by imperfection of the actuator diagonalization and thus can be improved by optimizing the diagonalization scheme.

Although the reduction of control noise couplings remains an issues, the type-B SAS with the designed active control system allows long-term observation of gravitational waves with the detection frequency limit as low as 20 Hz. It allows the detection of gravitational waves from spinning pulsars with rotation period less than 0.1 sec and binary IMBH coalesences with mass less than $\sim 10^3 M_\odot$ with reasonable detection probability in years of observation.

Table of Contents

Introduction

Chapter 1

This chapter describes the theoretical background on gravitational wave detection and the motivation for detecting low frequency gravitational waves. Section 1.1 gives a theoretical explanation on gravitational waves and section 1.2 introduces possible astrophysical sources of them. Section 1.3 explains the detection schemes using interferometers and possible upgrades for improving the detection sensitivities. Section 1.4 introduce gravitational wave detector projects with large-scale terrestrial interferometers, which have been constructed or are currently proposed around the world. The section also explains the contribution of seismic noise to the detector sensitivities. Section 1.5 describes the motivation for expanding the sensitivities of large-scale interferometric detectors toward a low frequency region.

1.1 Gravitational waves in general relativity

1.1.1 Formulation of gravitational waves

Existence of gravitational waves was predicted by A. Einstein in 1916 in his theory of general relativity [1]. The theory of general relativity describes gravity as consequence of the curvature of spacetime caused by the presence of mass, whereas it had been assumed to be a force between any two objects with mass in Newton's theory. The curvature of spacetime is expressed mathematically by the metric tensor $g_{\mu\nu}$, which gives the spacetime interval ds between two neighboring points via the following equation:

$$ds^2 = g_{\mu\nu} dx^\mu dx^\nu. \tag{1.1}$$

The symbol with a Greek index dx^μ ($\mu = 0, 1, 2, 3$) describes differential spacetime coordinates between two neighboring points. A flat spacetime without any gravity is described with the Minkowsky metric tensor noted as $\eta_{\mu\nu}$. The relationship between the spacetime and the mass or energy distribution is represented by Einstein field equations:

$$G_{\mu\nu} = \frac{8\pi G}{c^4} T_{\mu\nu}. \tag{1.2}$$

Here $G_{\mu\nu}$ is called the Einstein tensor and is a function of the metric tensor $g_{\mu\nu}$. $T_{\mu\nu}$ is called the stress-energy tensor, describing the energy density distribution in the field. G and c are the gravitational constant and the speed of light in vacuum, respectively.

The basic concept of gravitational waves is derived by a weak-field approximation of the above-mentioned formulization. In the weak-field limit, the metric tensor of the spacetime can be described as a small perturbation of the Minkovskii tensor:

$$g_{\mu\nu} = \eta_{\mu\nu} + h_{\mu\nu}, \quad \text{where} \quad |h_{\mu\nu}| \ll 1. \tag{1.3}$$

Assuming a vacuum condition with $T_{\mu\nu} = 0$, a linear approximation of the field equations and an adept coordinate transform results into the following wave equations for the spacetime perturbation [2]:

$$\left(\nabla^2 - \frac{1}{c^2}\frac{d^2}{dt^2}\right) h_{\mu\nu} = 0. \tag{1.4}$$

These equations indicates that small distortions of spacetime can propagate at the speed of light c in a field with no energy distribution. These distortions are called gravitational waves.

1.1.2 Measurable effect of gravitational waves

When one chooses a spatial coordinate system such that a gravitational wave travels in the z direction, the plane wave solution of the equations (1.4) can be written as [2]

$$h_{\mu\nu}(z,t) = \begin{pmatrix} 0 & 0 & 0 & 0 \\ 0 & -a_+ & a_\times & 0 \\ 0 & a_\times & a_+ & 0 \\ 0 & 0 & 0 & 0 \end{pmatrix} \exp\left[i\omega\left(t - \frac{z}{c}\right)\right]. \tag{1.5}$$

Here ω is the wave angular frequency, and a_+ and $a_\times$ represent the amplitudes of two independent wave polarizations. Measurable effects of the gravitational wave can be described in terms of test particles placed at spatially separated locations in the xy plane. When a particle is placed at the origin of the coordinate system and another is placed at $x^i = (L\cos\theta, L\sin\theta, 0)$, the proper distance between the two particles L' is altered by the gravitational wave and can be expressed as

$$L' \equiv \int \sqrt{ds^2} \approx L\left(1 + \frac{1}{2}a_+ e^{i\omega t}\cos 2\theta + \frac{1}{2}a_\times e^{i\omega t}\sin 2\theta\right). \tag{1.6}$$

Figure 1.1 shows an illustration of the tidal effects of the two polarization of the gravitational wave on circularly arranged particles. A passing gravitational wave stretches spacetime in one direction while compressing it by an equal amount in the perpendicular direction. The two polarizations of the gravitational wave are identical but 45 deg apart.

They are conveniently called the plus (+) mode and the cross (×) mode of the gravitational wave. The length shift is proportional to the original distance between the particles

$$\frac{\Delta L}{L} = \frac{1}{2}h, \tag{1.7}$$

where h is the spacetime distortion in the direction of measurement. Therefore the further the measurement targets are separated, the larger measurable effect the observer obtains. This becomes a big motivation to construct detectors as large as possible for gravitational wave observatories.

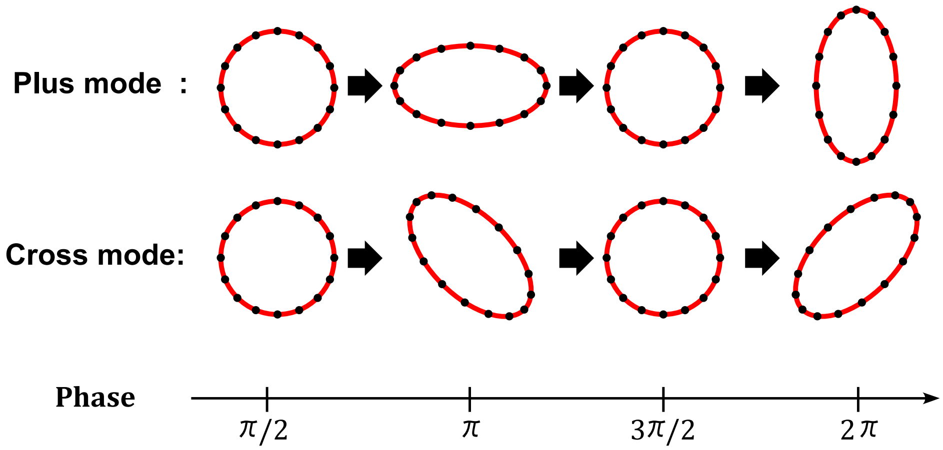

Figure 1.1: An illustration of the tidal effect of gravitational waves.

1.1.3 Gravitational wave emission

Gravitational waves can be emitted when objects with mass move around in spacetime. However, the conservation of energy and linear momentum forbid monopole and dipole radiation of gravitational waves and thus systems having spherical or axial symmetry cannot emit gravitational waves. Quadruple radiation is the lowest-possible order emission of gravitational waves. In the quadruple approximation, the amplitude of gravitational waves is calculated as [2]

$$h_{ij} = \frac{2G}{c^4 r}\ddot{Q}_{ij}. \tag{1.8}$$

Here Q_{ij} is the quadrupole moment of the mass distribution and r is the distance between the gravitational wave source and the observer. The amplitude of the gravitational wave expected from the formula (1.8) is extremely small. For example, two 100 kg masses connected with a 2-m beam, rotating at 100 cycles per second will emit 200 Hz gravitational wave of amplitude only $h \sim 10^{-43}$ at a distance of 1500 km [3]. It is extremely difficult to detect such a tiny distortion of spacetime. Detectable gravitational waves come from only violent astronomical events, involving large acceleration of massive and compact objects.

1.2 Astrophysical gravitational wave sources

This section briefly describes several types of possible astrophysical gravitational wave sources, and their predicted strengths and frequencies. More extensive studies of gravitational wave sources can be found in reference [4].

1.2.1 Compact binary star coalescence

A binary system formed by two compact stars such as black holes, neutron stars or white dwarfs is an extensively studied gravitational wave source. The waveforms of the inspiral gravitational waves are well-predicted and therefore it is considered to provide promising gravitational wave signals.

As the orbit of binary stars progresses in time, the orbital period and radius decrease due to energy loss by gravitational wave emission. Accordingly the amplitude and frequency of the emitted gravitational wave increase with time, which creates distinctive gravitational waveforms known as chirp signals [2]. The amplitude and frequency revolution of a chirp signal are approximately

$$\begin{aligned} f_{\mathrm{GW}}(\tau) &\approx& 135\ [\mathrm{Hz}] \left(\frac{M_{\mathrm{c}}}{1.2M_{\odot}}\right)^{5/8} \left(\frac{1\ \mathrm{sec}}{\tau}\right)^{-3/8}, \qquad (1.9) \\ h(\tau) &\approx& 2.1 \times 10^{-23} \left(\frac{M_{\mathrm{c}}}{1.2M_{\odot}}\right)^{5/3} \left(\frac{\tau}{1\ \mathrm{sec}}\right)^{-1/4} \left(\frac{r}{200\ \mathrm{Mpc}}\right)^{-1}. \qquad (1.10) \end{aligned}$$

Here τ is the time to coalescence of the binary stars, r is the distance between the source and observer and M_{c} is the chirp mass defined in terms of the masses of the two stars as $M_{\mathrm{c}} = (m_1 m_2)^{3/5}(m_1 + m_2)^{-1/5}$.

When the orbital radius falls below the Innermost Stable Circular Orbit (ISCO), stable circular orbits are no longer allowed and the binary stars eventually plunge toward each other and merge. A binary system of two neutron stars for example is expected to reach a frequency of about 800 Hz by the time the radius reaches the ISCO. Computation of merging neutron stars or black holes is quite challenging in terms of computation costs and thus numerous efforts have been made to calculate these dynamics and associated gravitational radiation waveform with supercomputers [5]. The merger of the binary stars results in a highly deformed single black hole which sheds its deformity by emitting gravitational waves referred to as ring-down signals.

1.2.2 Spin of compact stars

A spinning compact star such as a radio pulsar becomes a possible gravitational wave source when it has an asymmetry around its rotation axis. It is expected to provide a long continuous wave at a single frequency. Detection of monochromatic gravitational waves has an advantage that signal-to-noise ratio can be improved by integrating the signals over a long period of time. The gravitational wave amplitude from an axisymmetric spinning object is [2]

$$h \approx 1.1 \times 10^{-25} \left(\frac{\epsilon}{10^{-6}}\right) \left(\frac{I}{10^{38}\ \mathrm{kg\ m^2}}\right) \left(\frac{10\ \mathrm{kpc}}{r}\right) \left(\frac{f_{\mathrm{GW}}}{1\ \mathrm{kHz}}\right)^2 . \tag{1.11}$$

Here f_{GW} represents the frequency of the gravitational wave and is twice the spin frequency. I is the moment of inertia about the spin axis and ϵ is the equatorial ellipticity.

1.2.3 Supernovae

A supernova caused by gravitational collapse of a heavy-star core is expected to emit gravitational waves in a large amplitude since it accelerates an enormous amount of mass dramatically in a short term. Although prediction of the exact waveforms from supernovae is challenging, recent progress in the field of numerical relativity provides estimates of the magnitude of the emitted gravitational waves [6]. A rough estimate of the gravitational wave amplitude from a supernova occurring in a nearby galaxy is of the order of 10^{-21}-10^{-22} in spacetime strain. The explosion models suggest that the frequency of the emitted gravitational waves are spread widely around 1 kHz. Therefore a supernova in a nearby galaxy can be a reasonable target for terrestrial interferometric gravitational wave detectors, whose target frequency is 10-10^4 Hz.

1.2.4 Stochastic background

A stochastic background of gravitational waves can come from numerous unresolved astrophysical sources such as white dwarf binaries, as well as cosmological origins such as inflation, phase transition in the early universe and cosmic strings [7]. The magnitude and the frequency of the gravitational waves with cosmological origins vary from theory to theory.

Detection of a stochastic background generally involves cross-correlation between observations by several detectors. Analyses of the stochastic background have been performed using terrestrial interferometric gravitational wave detectors and the measurements provide restrictions and upper limits to several theories on cosmological gravitational wave sources [8].

1.3 Interferometric gravitational wave detection

The first attempt to detect gravitational waves was performed in the 1960's by J. Weber [9]. He invented the so-called resonant bar detector, which measures resonant vibrations of massive metal bars excited by passing gravitational waves. Following Weber's pioneering work, various resonant bar detectors with improved sensitivities were constructed around the world and coincident observations with a number of detectors were performed [10].

However, significant signals from passing gravitational waves were not found by resonant bar detectors.

Gravitational wave detectors developed nowadays are mainly based on laser interferometric techniques. This section briefly describes the detection schemes and possible improvement of detector sensitivities.

1.3.1 Basic detection scheme

The basic configuration of an interferometric gravitational wave detector is a Michelson interferometer composed of suspended mirrors. Its optical configuration is shown in Figure 1.2. An incoming beam from a coherent light source is split by the beam splitter into two orthogonal paths. The two beams are reflected by the end mirrors and recombined at the beam splitter. They interfere with each other, and a fraction of beam goes to the photo detector and the rest goes back to the light source. The beam intensity at the photo detector depends on the phase difference accumulated in the two optical paths and is calculated as

$$P_{\mathrm{PD}} = 2P_0(r_{\mathrm{BS}}t_{\mathrm{BS}})^2(1-\cos\delta\phi). \tag{1.12}$$

Here P_0 is the beam intensity injected from the light source and $\delta\phi$ is the phase difference between the two optical paths. t_{BS} and r_{BS} denote respectively the amplitude reflectivity and transmissivity of the beam splitter. The beam intensity on the photo detector is converted to photo current and then to forms convenient to the observers.

Suppose that a gravitational wave comes from the z direction with + polarization and amplitude of $h(t)$. The tidal effect of the gravitational wave changes the optical lengths of

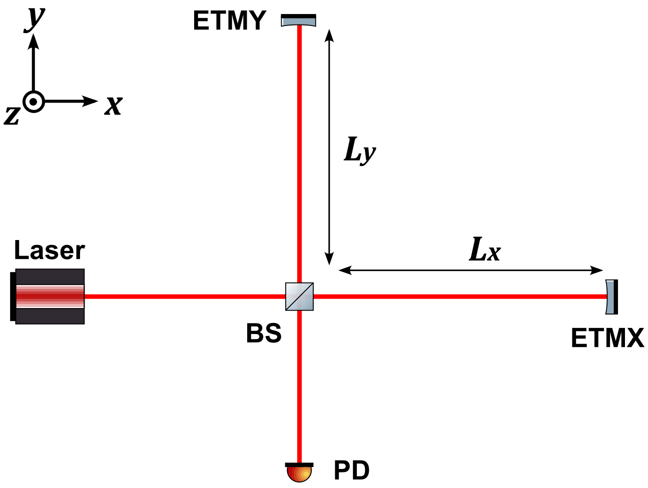

Figure 1.2: Optical configuration of a Michelson interferometer (BS: beam splitter, PD: photo detector, ETMX(Y): end test masses).

the two orthogonal arms and results in a differential phase shift. The phase difference of the two optical paths caused by the gravitational wave is calculated as [11]

$$\delta\phi_{\mathrm{GW}}(t) = \frac{2\pi c}{\lambda}\int_{t-2L/c}^{t} h(t')dt', \tag{1.13}$$

where λ is the wavelength of the laser beam and L is the length of the arms ($L_x \approx L_y \approx L$). The frequency response of the Michelson interferometer to gravitational waves is derived from the Fourier transform of this equation as

$$H_{\mathrm{MI}}(\omega) \equiv \frac{\tilde{\phi}_{\mathrm{GW}}(\omega)}{\tilde{h}(\omega)} = \frac{4\pi L}{\lambda}\exp(-i\omega L/c)\frac{\sin(\omega L/c)}{\omega L/c}. \tag{1.14}$$

Figure 1.3 shows the amplitude plots of H_{MI} as a function of frequency with various arm lengths. When the arm length is much shorter than the wavelength of the gravitational wave ($L \ll \lambda_{\mathrm{GW}}$), the frequency response can be approximated as $H_{\mathrm{MI}} \sim 4\pi L/\lambda$. It indicates that a detector with longer arms is more sensitive to gravitational waves. However, when the arm length gets longer than the wavelength of the gravitational wave ($L \gtrsim \lambda_{\mathrm{GW}}$), cancellation of the gravitational wave signals occurs. $|H_{\mathrm{MI}}|$ is maximized at

$$L = \frac{\pi c}{2\omega} = \frac{\lambda_{\mathrm{GW}}}{4}. \tag{1.15}$$

For a gravitational wave of 100 Hz, the optimum arm length is about 750 km. It is unrealistic to construct such a large interferometer on the Earth and thus some techniques to expand effective arm lengths are demanded to improve the sensitivities.

1.3.2 Delay-line and Fabry-Perot cavity

One way of expanding the effective optical path lengths is to introduce delay-lines to the interferometer arms, in which the light is multiply reflected at different points on the mirror surface. Another way is to introduce Fabry-Perot cavities, in which the light is reflected multiple times as in the delay-lines but the optical paths are aligned. A Michelson interferometer with folded arms is called a delay-line Michelson interferometer, while the detector is called a Fabry-Perot Michelson interferometer when Fabry-Perot cavities are used. The optical configurations of the two types are shown in figure 1.4.

A delay-line expands the effective arm length by a factor of $N/2$ when the beam is reflected on the mirror surfaces $N-1$ times. The expression for the frequency response of a delay-line-Michelson interferometer to gravitational waves is simply obtained by replacing L of $H_{\mathrm{MI}}(\omega)$ in formula (1.6) by $NL/2$:

$$H_{\mathrm{DLMI}}(\omega) = \frac{2\pi NL}{\lambda}\exp(-i\omega NL/2c)\frac{\sin(\omega NL/2c)}{\omega NL/2c}. \tag{1.16}$$

On the other hand, a Fabry-Perot cavity extends the effective arm length by multiple interference of the incident beam. A Fabry-Perot cavity is composed of two mirrors and one of them is partially reflective. The light introduced into the cavity is reflected back and forth many times between the mirrors. A fraction of the stored light inside the cavity is leaked out and goes back to the incident direction. The frequency response of a Fabry-Perot-Michelson interferometer to gravitational waves $H_{\mathrm{FPMI}}(\omega)$ is written as

$$H_{\mathrm{FPMI}}(\omega) = \frac{4\pi\alpha_{\mathrm{cav}}L}{\lambda}\frac{\exp(-i\omega L/c)}{1-r_{\mathrm{F}}r_{\mathrm{E}}\exp(-2i\omega L/c)}\frac{\sin(\omega L/c)}{\omega L/c}, \tag{1.17}$$

when the two Fabry-Perot cavities are in resonance [11]. α_{cav} is calculated as

$$\alpha_{\mathrm{cav}} = \frac{t_{\mathrm{F}}^2 r_{\mathrm{E}}}{1-r_{\mathrm{F}}r_{\mathrm{E}}}, \tag{1.18}$$

where r_{F} and $r_{\mathrm{E}} \sim 1$ are the amplitude reflectivity of the front and end mirrors, and t_{F} is the transmissivity of the front mirror. L is the length of the Fabry-Perot cavity. The average bounce number in a Fabry-Perot cavity is written as

$$N_{\mathrm{FP}} = \frac{2\sqrt{r_{\mathrm{F}}r_{\mathrm{E}}}}{1-r_{\mathrm{F}}r_{\mathrm{E}}} = \frac{2\mathcal{F}}{\pi}. \tag{1.19}$$

$\mathcal{F}$ is called the finesse, which represents the sharpness of the resonance of the Fabry-Perot cavity.

Figure 1.5 shows a comparison of frequency responses of different types of interferometers. The arm lengths are set 3 km in all the cases and the frequency responses of the delay-line Michelson and Fabry-Perot Michelson interferometers are optimized for a

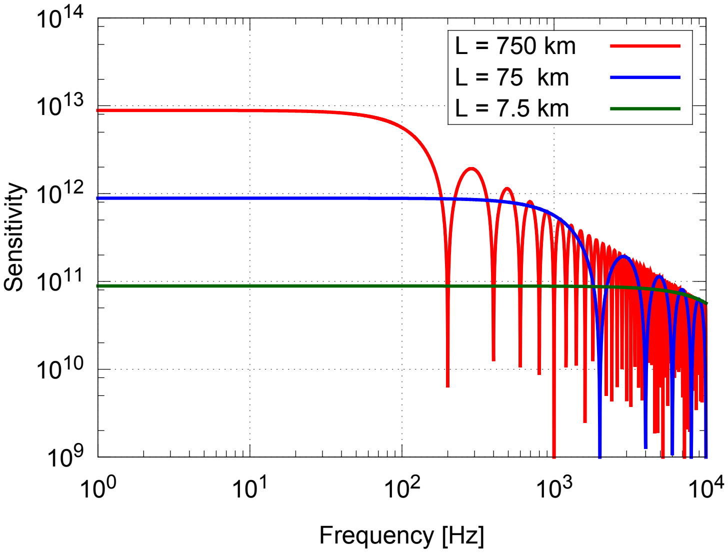

Figure 1.3: Frequency response of the Michelson interferometer to gravitational waves with various arm lengths.

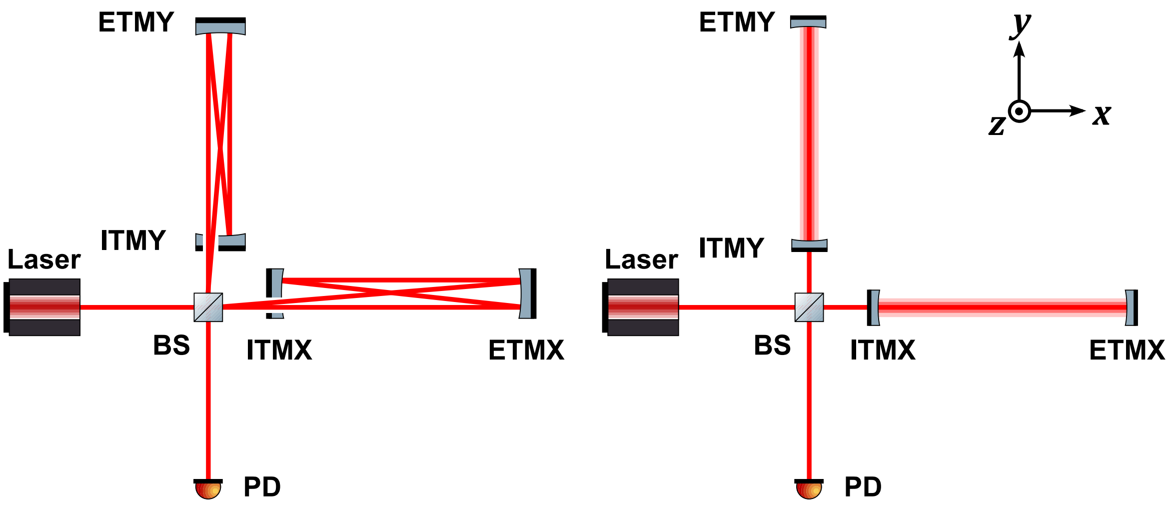

Figure 1.4: Optical configurations of a delay-line Michelson interferometer (left) and a Fabry-Perot Michelson interferometer (right). ITMX and ITMY (input test masses) are introduced to achieve multiple reflections.

gravitational wave with a frequency of 100 Hz. The Fabry-Perot Michelson interferometer shows a smoother frequency response than that of the delay-line Michelson interferometer, which becomes a big advantage in detecting wide-band gravitational waves. In addition to the differences in the frequency response, implementation of delay-lines with a large number of reflections has several practical problems, in terms of extreme mirror size and thermal noise issues. Therefore large-scale interferometric gravitational wave detectors developed nowadays adopt Fabry-Perot cavities, or delay-lines with only a small number of reflections.

1.3.3 Recycling cavities

Besides the devices for arm lengths expansion, recent interferometric gravitational wave detectors employ so-called recycling cavities to further improve the sensitivity and optimize the observational bandwidth. The scheme introduces additional partial-reflection mirrors immediately before and/or after the Michelson interferometer to create optical cavities with interference. The mirrors placed before and after the Michelson part is called the power recycling mirror and the signal recycling mirror respectively. Figure 1.6 shows the optical configuration of a Michelson interferometer with the two recycling mirrors introduced (a so-called dual-recycling interferometer). A brief introduction to the recycling schemes is given here. Detailed studies of the detection scheme and resulting sensitivities can be found in references [12, 13].

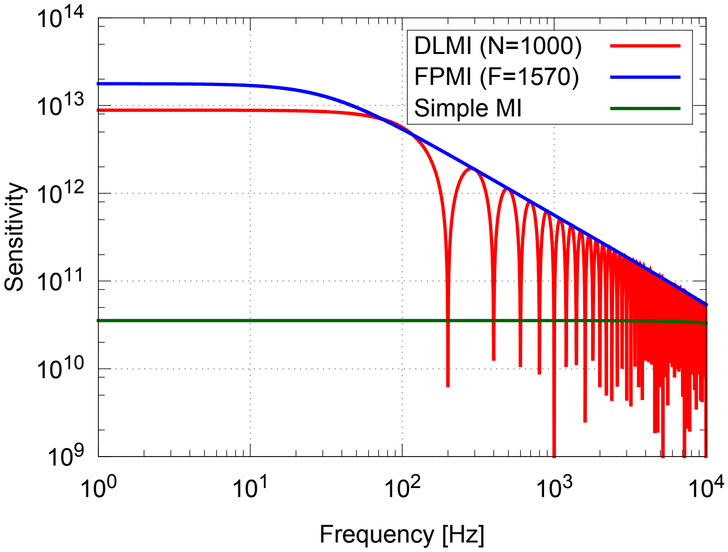

Figure 1.5: The frequency response of the delay-line Michelson, Fabry-Perot Michelson and simple Michelson interferometer with 3 km arm length. The frequency responses of the delay-line-Michelson and Fabry-Perot-Michelson interferometers are optimized for a gravitational wave of 100 Hz.

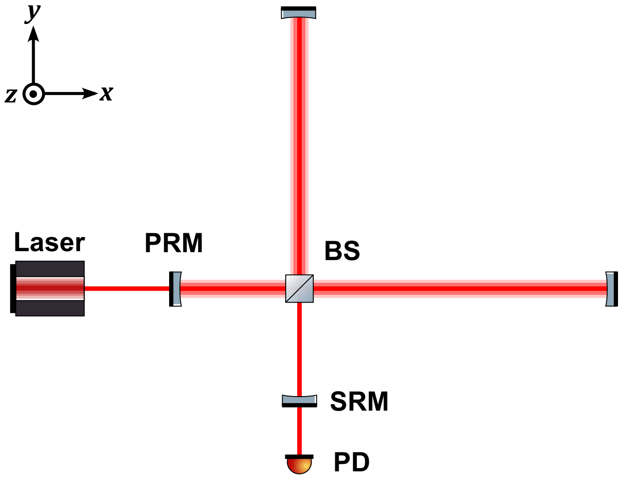

Figure 1.6: Optical configuration of a dual-recycling Michelson interferometer. PRM (power recycling mirror) and SRM (signal recycling mirror) are added to the simple Michelson interferometer.

Power Recycling

The power recycling mirror reflects the light coming back from the Michelson interferometer and recycles the laser power which would be otherwise discarded [14]. The primary intention of the power recycling is to increase the amount of laser power illuminating the beam splitter and to reduce the shot noise (see the next subsection) at the detection port where gravitational wave signals are monitored. The power recycling scheme has been adopted in the first-generation large-scale terrestrial interfeormeters.

Signal Recycling

The signal recycling mirror reflects the signal fields induced by gravitational waves and leads them back to the interferometer. It increases or decreases the effective finesse for gravitational wave signals, depending on the interference condition of the optical cavity created by the signal recycling mirror. The increase of effective finesse results in higher sensitivities to gravitational waves at low frequencies, while leading to a narrower observation bandwidth [15]. The decrease of effective finesse results in the opposite effects and this variation of the scheme is called resonant sideband extraction [16].

1.3.4 Noises in interferometers

There are various kinds of noise sources which disturb gravitational wave detection with interferometric detectors. The phase shifts of the optical paths in the interferometers are induced not only by spacetime distortions but also by vibrations of the optics excited by environmental noises and fluctuations of refractive indices in the optical paths. The readouts of the photo detectors can be contaminated by noises in electronics and beam amplitude fluctuations inherent in the light source. This section briefly explains noise sources which fundamentally or possibly degrade the detection performance of gravitational waves.

Seismic noise

The sensitivity of a ground-based detector at low frequencies is mainly limited by vibrations of the optics induced by seismic motions. This is called seismic noise. Seismic noise can be reduced by isolating the optics from the seismic vibration with vibration isolation systems composed of springs and pendulum stages. General background on seismic vibrations and vibration isolation systems is given in the next chapter.

Newtonian noise

Although the mechanical influence of seismic vibrations can be mitigated by suspending the optics through suitable number of attenuation stages, the direct coupling between the moving ground and the optics through Newtonian gravitational attraction cannot be shielded. This noise, called the Newtonian noise or gravity gradient noise, is the ultimate limitation on gravitational wave detection on the Earth. It can be reduced by moving the interferometer underground, where the optics are less under the effects of the gravity gradient field of surrounding rocks. The Newtonian noise can also be calculated and subtracted if motion of the ground surrounding the optics is measured, typically using a large number of sensors. More detailed studies on Newtonian noise are found in reference [17].

Thermal noise

The mirrors and their suspension systems are in thermal baths and receive energy from their surroundings. Random energy flow to and from the thermal baths causes fluctuations of the surface axial positions and shapes of the mirrors, which induce fluctuations of the optical paths in the interferometer. This noise is called thermal noise. Thermal noise induced in mirror substrates is sometimes called mirror thermal noise, while the noise caused in the suspension systems is called suspension thermal noise.

The level of thermal noise is related to the mechanical loss of the system and the noise spectrum can be estimated using the fluctuation-dissipation theorem [18]. In order to mitigate the impact from the thermal noise, one needs to use high quality material for the mirrors and the suspension components. Since fused silica has a high mechanical Q factor ($\sim 10^7$) at room temperature [19] and good optical properties, it is used for the mirror substrates in many interferometric gravitational wave detectors, and also for their suspension fibers in some advanced detectors [20]. Thermal noise can be also reduced by lowering the temperature. Since fused silica has a low quality factor at low temperature, it becomes unusable in cryogenic systems. On the other hand, sapphire and silicon have high quality factors ($\sim 10^8$) and large thermal conductivity at cryogenic temperatures around 20 K [21, 22], and are good candidates as the mirror substrates for cryogenic detectors.

Shot noise

Shot noise is a fundamental disturbance of optical power sensing associated with the quantum nature of light. A photo-detector counts the number of photons in a certain measurement time and produces photo-current proportional to the incident power. In the process, the counted number of photons, i.e., the electrons produced and contributing to the photo-current, has a Poisson distribution, which results in fluctuations of the measured rate. The noise induced by this fluctuation is called shot noise.

The noise in length sensing due to the probability distribution is proportional to the square-root of the incident power on the mirrors $\sqrt{P_{\mathrm{in}}}$. On the other hand, the signal amplitude of the gravitational wave is proportional to P_{in}, and therefore the signal to noise ratio is proportional to $1/\sqrt{P_{\mathrm{in}}}$. Consequently, the shot noise can be reduced by increasing the power of the laser. This motivates one to increase laser power and introduce the power recycling scheme.

Radiation pressure noise

When a photon is reflected by a mirror, a back-action force is exerted onto it. Owing to the quantum nature of light, the number of the photons hitting the mirror fluctuates, and thus the back-action force fluctuates, resulting in displacement noise of the mirror. The noise caused by this fluctuation is called the radiation pressure noise.

The fluctuating force level is proportional to the square root of the laser power $\sqrt{P_{\text{in}}}$. Since the photocurrent shot noise is proportional to $1/\sqrt{P_{\text{in}}}$, there is a trade-off between the shot noise and the radiation pressure noise. There is a limit on the sensitivity of an interferometer called the standard quantum limit (SQL), which corresponds to the quantum mechanical limit of the measurement from the Heisenberg uncertainty principle. Currently various methods to beat this limit are proposed [23].

Laser noise

As a laser interferometric gravitational wave detector measures the length between the mirrors using the wavelength of the laser as a reference, the noise in the laser degrades its sensitivity. The frequency fluctuation of the laser is in principle cancelled at the interference, if the two arms of the interferometer are identical. However, it is not completely cancelled in a real system because of a small asymmetry of the two arms. Therefore the frequency noise has to be suppressed with active controls in the interferometer.

The intensity fluctuation of the laser also introduces a noise in the output signal of the interferometer. The effect of the intensity fluctuation is minimized when the interferometer is operated at a dark fringe, i.e., under the condition that no light is injected to the photo detector in the absence of gravitational wave signals. However, in practice, there remains some light intensity due to residual motions of the mirrors. The fluctuation of the intensity contaminates the output of the detector and the residual motion around the fringe couples with the intensity noise of the laser. Therefore the intensity of the laser has to be stabilized and the control gain has to be large enough to suppress the residual mirror motions.

Residual gas noise

The random motions of molecules cause fluctuation of the refraction index in the optical paths of an interferometer. This causes the fluctuation of the effective arm lengths and the noise is called the residual gas noise. Terrestrial interferometric gravitational wave detectors nowadays are operated in an ultrahigh vacuum condition (10^{-6}-10^{-7} Pa) to mitigate the impact from the residual gas noise. Therefore the optics and suspension systems are designed to have small outgassing rates and the choice of materials for in-vacuum components are restricted.

Control noise

During the operation of an interferometer, the optical components of the interferometer are controlled to keep the Fabry-Perot arms and recycling cavities in resonance and the detection port at a dark fringe. Several auxiliary beam monitoring signals are used for these feedback loops. Detection and digitization noise of these auxiliary detectors, as well as the noise of the electric circuits for the control may reduce the sensitivity of the interferometer. Although this is not a fundamental noise, careful consideration and design are required to minimize the noise.

The noise in the active controls of the suspension systems can also contaminate the detector sensitivity. The noises in local sensors and actuators introduce vibration to the suspension system components through active controls and cause fluctuation of mirror displacements. The motivation and strategies of the active suspension controls will be discussed in chapter 5.

Scattered light noise

Although the reflection surfaces and substrates of the mirrors are carefully designed and manufactured, part of the laser beam injected to the mirrors scatters in various directions due to imperfection or inhomogeneity. Light scattered from the mirrors interacts with the surfaces of surrounding mechanical components, which are highly vibrating with seismic motions, and then is recombined to the main laser beam resulting in additional phase noise of the interferometer. Therefore in interferometric gravitational wave detectors, scattered light has to be retained as much as possible by placing black-coated optical baffles in appropriate positions to avoid scattered light noise.

1.4 Large-scale terrestrial laser interferometers

A number of large-scale laser interferometers have been constructed around the world with the aim of capturing the first gravitational wave signals and opening a new era of astronomy with gravitational waves. Coincident observations with several detectors are required in order to improve detection reliability and locate source positions in the sky. This section describes world-wide networks of gravitational wave observatories with large-scale interferometers which have been constructed or are proposed.

1.4.1 Overview of detector projects

Large-scale terrestrial interferometers operated or planned are summarized in table 1.1. The first generation detectors (TAMA [24], GEO [25], LIGO [26], Virgo [27]) have performed scientific observations since 1999. The first generation detectors had detection probabilities of gravitational wave events about a few percent per year. Although they did not detect gravitational waves, they demonstrated the effectiveness of the working principle and set upper limits to several gravitational wave sources [28].

Based on the experience gathered with the first generation detectors, second generation detectors have been designed, with thousands of times higher probability of gravitational wave detection. Several first generation detectors were upgraded (enhanced LIGO,

Generation	Project	Baseline	Observation	Place
1st	TAMA	300 m	1999∼	Mitaka, Japan
	GEO	600 m	2000∼	Hannover, Germany
	LIGO	4 km/2 km	2001∼	Livingston/Hanford, USA
	Virgo	3 km	2002∼	Pisa, Italy
2nd	Adv. LIGO	4 km	2016∼	Livingston/Hanford, USA
	Adv. Virgo	3 km	2016∼	Pisa, Italy
	KAGRA	3 km	2018∼	Kamioka Japan
3rd	ET	10 km	2025∼	under discussion

Table 1.1: Large-scale terrestrial interferometric gravitational wave detector projects.

Virgo+) with the sensitivities improved by introducing higher power lasers and advanced techniques such as monolithic suspensions [27]. They have been further upgraded to the second generation detectors (Advanced LIGO, Advanced Virgo) and are scheduled to start scientific observation in 2016. A Japanese second generation detector KAGRA [29] was funded in 2010 and is being constructed to follow up the observations. In addition to the same improvements as the other advanced interferometers, it features the use of cryogenic mirrors and underground environment, which are unique characteristics among the first and second generation detectors. KAGRA is scheduled to start scientific observation in 2018.

To go beyond the sensitivities of these detectors, there is a plan to construct a third generation detector, ET (Einstein Telescope) [30], which has been designed by European research institutes. It aims to reach a sensitivity about a factor of 10 better than the second generation detectors. The detector is planned to be constructed underground in order to mitigate Newtonian noise and expand the detection band toward lower frequencies.

1.4.2 Optical configuration

The first generation detectors mainly employed power-recycled Fabry-Perot Michelson interferometers. To improve the sensitivity and optimize the detection bandwidth, they are being upgraded to dual-recycled Fabry-Perot Michelson interferometers in the second generation detectors. Figure 1.7 shows a typical optical configuration of the second generation interferometers.

A seed laser beam from a Nd:YAG non-planar ring oscillator (NPRO), which has very low intensity noise, is passed through fiber/solid-state amplifiers, increasing the power up to the level of ∼200 W. The laser is then sent to a prestabilization system, where the phase of the laser is stabilized using rigid cavities, and phase/amplitude modulation is applied for interferometer sensing and controls. The input mode cleaner, denoted MC, filters the spatial modes and polarization of the laser beam with a triangular optical cavity consisting of suspended mirrors. It also provides a frequency reference for the laser at high frequencies.

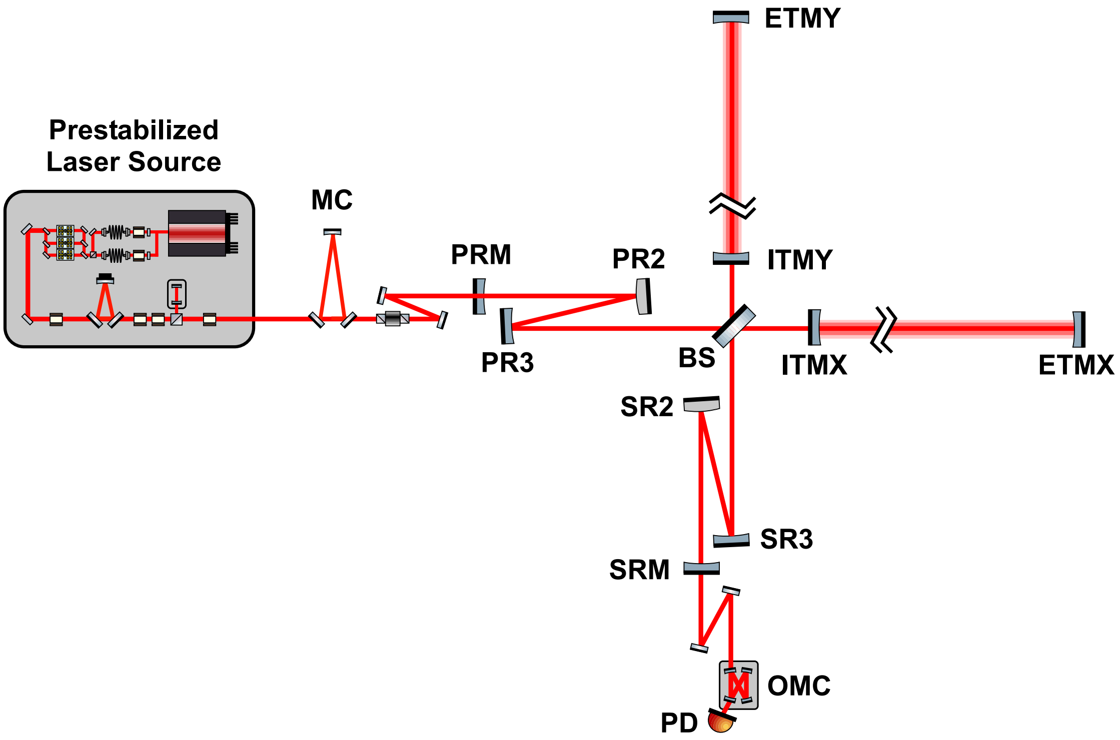

Figure 1.7: Optical configuration of the second generation gravitational wave detector (in the case of KAGRA). MC and OMC denote the input mode cleaner and the output mode cleaner, respectively.

The main part of the interferometer part is a dual-recycled Fabry-Perot interferometer with km-scale arm lengths. The beam between recycling mirrors and the beam splitter is folded into a Z-shape to improve the spatial mode stability of the recycling cavities. Downstream of the signal recycling mirror, there is an output mode cleaner (OMC) used to remove unwanted higher-order spatial modes from the output beam. The optical design and reasoning behind the design choices in the KAGRA interferometer are described in more detail in reference [31].

1.4.3 Detector sensitivities

Figure 1.8 shows the estimated noise curves of the 1st-3rd generation gravitational wave detectors in strain sensitivities. The LIGO detector reached its design sensitivity in 2007 and achieved a noise level of $3\times10^{-23}[1/\sqrt{\mathrm{Hz}}]$ at 100 Hz. The detector is sensitive enough to capture the gravitational wave signals from binary neutron stars of 1.4 solar masses at a distance of 15 Mpc, with a signal-to-noise ratio of 8 (averaged over sky directions and source orientations). This distance is one of the standard measures of a gravitational wave detector's sensitivity and is called the (binary neutron star) inspiral range. The noise curve

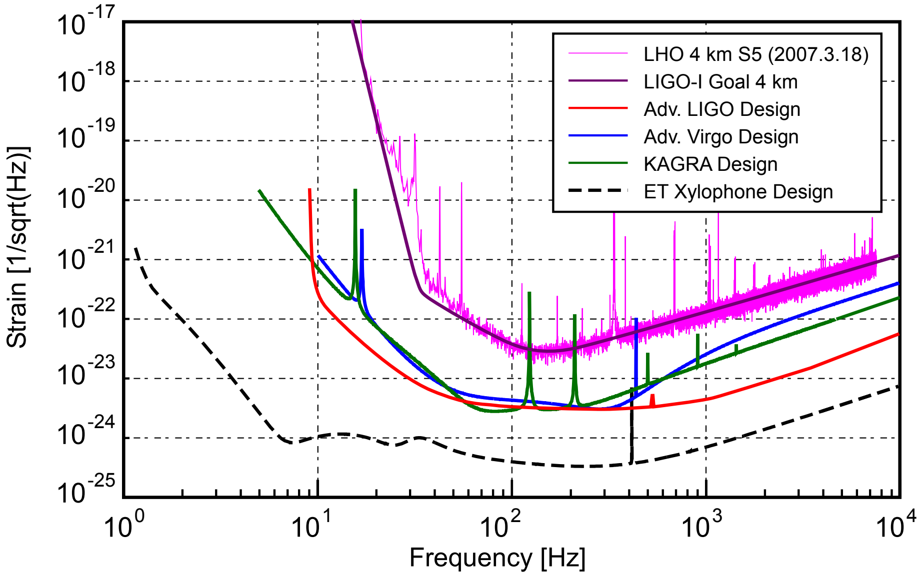

Figure 1.8: Predicted noise spectra of 1st-3rd generation gravitational wave detectors in spacetime strain equivalent. The measured noise spectrum of the LIGO Hanford 4 km interferometer in the 5th science run is also shown for comparison.

has a steep cutoff around 40 Hz, which limits the detection band on the low frequency side and is mainly caused by seismic disturbances.

The second generation detectors are designed to lower the noise level at high frequencies by about one order of magnitude. This results in pushing inspiral ranges as far as 200 Mpc, which is required for detecting the gravitational wave signals from binary neutron star coalescences multiple times per year. For instance, the event rate of binary neutron star coalescence is estimated as $5.4^{+13.7}_{-4.3}$ events/yr with 95% confidence interval for the KAGRA detector [29]. Therefore, years of observation with second generation detectors provide a high probability of capturing gravitational wave signals from binary neutron stars. The second generation detectors also aim to expand the gravitational wave detection band as low as 10 Hz. Although the sensitivity at low frequencies (< 40 Hz) does not affect the detectability of binary neutron stars, it affects the determination of astronomical parameters and detection of gravitational waves from other sources. Details are given in the next section.

Contributions of various noises to the detector sensitivities are shown in figure 1.9 for KAGRA and Advanced LIGO. The sensitivities of the second generation detectors are limited by quantum noise (the combination of shot noise and radiation pressure noise) and thermal noise in the detection frequency band. The sensitivities at low frequencies are limited by seismic noise which forms steep "walls" in the noise curves below 10 Hz.

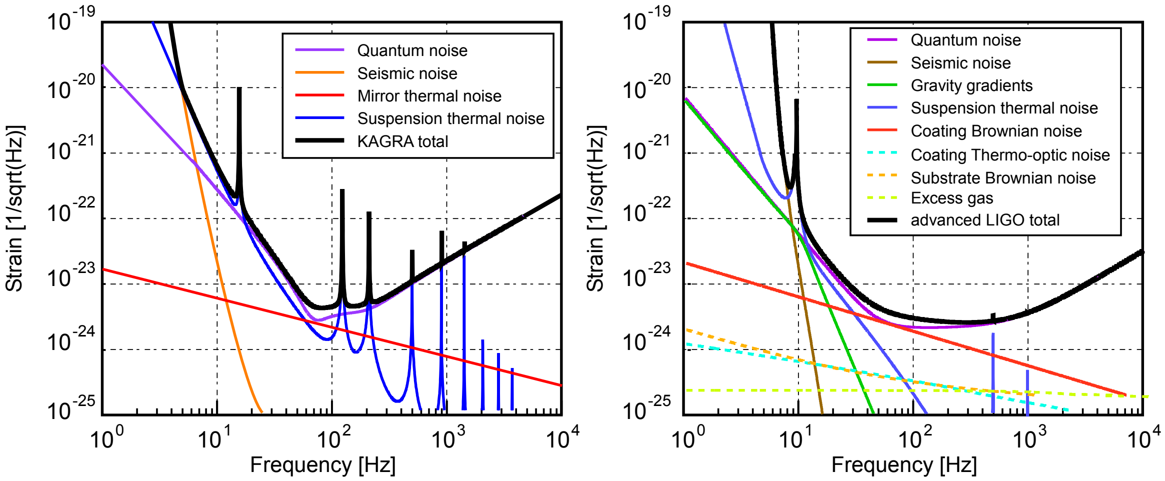

Figure 1.9: Noise budgets of KAGRA (*left*) and Advanced LIGO (*right*) [32, 33].

1.5 Motivation of improving low frequency sensitivity

As seen in the previous section, the sensitivities of terrestrial gravitational wave detectors at low frequencies are limited by seismic noise, and thus the performance of vibration isolation systems affects the detectability and measurability of low frequency gravitational waves. In order to detect the signals from low-frequency gravitational wave sources such as (intermediate mass) black hole binaries and pulsars with long rotation periods with a reasonable detection probability or observation time, it is required to expand the detection band as low frequency as 10 Hz. This section explains target gravitational wave sources and obtainable science goals in the detection of low-frequency gravitational waves.

1.5.1 Binary black holes

Although the existence of intermediate-mass black holes (IMBHs), with mass ranging between 10^2-$10^4 M_\odot$, has not been confirmed by optical observations, they are of high interest for astrophysics, and predicted gravitational waves from IMBH binary systems have been intensively studied. Figure 1.10 shows typical gravitational wave spectra from binary black hole merger events in comparison with the sensitivities of second generation detectors [34]. The cutoff frequency of the gravitational wave signal decreases as the mass of the black holes increases. The second generation detectors are expected to detect the gravitational waves from IMBH binaries with total mass less than a few thousand solar masses.

The event rate from the binary IMBH merger can be estimated as [35]

$$R = \int_{M_{\rm min}}^{M_{\rm max}} \frac{4\pi}{3} D(M)^3 \nu(M) n_{\rm gc} f(M) dM. \tag{1.20}$$

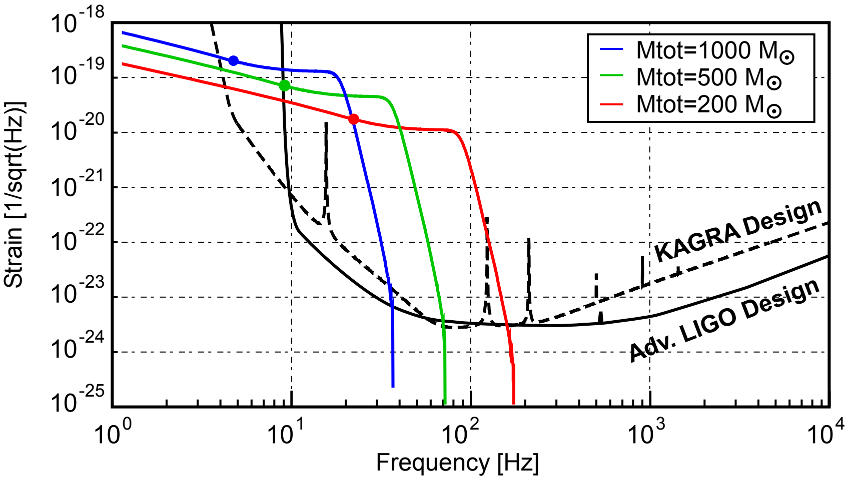

Figure 1.10: Expected gravitational wave amplitude spectra from binary black holes with various total masses [34] compared with the detector sensitivities. The sources are optimally oriented and placed 100 Mpc from the detectors. The binary system assumes equal-mass and non-spinning configuration. The solid circles on the curves represent the ISCO frequencies, which indicate the upper frequency limits of the inspiral phase.

Here $D(M)$ is the horizon distance as a function of black hole mass calculated from the detector sensitivity. The horizon distance calculated from the Advanced LIGO design sensitivity is 4 Gpc for $100M_\odot$ and 0.2 Gpc for $2000M_\odot$ with a S/N of 8 [34]. n_{gc} is the number density of global clusters, $\nu(M)$ is the rate at which compact objects merge with black holes of mass M, and $f(M)$ is the mass distribution of the black holes in clusters. The event rate of binary black hole mergers is estimated to be ~ 1 event per year for the Advanced LIGO detectors [34]. As the design sensitivity of KAGRA is about two times worse than that of Advanced LIGO in the 10-50 Hz band, which contributes to the detectability of binary IMBH merger events, the event rate in the KAGRA detector is expected to be several events per decade. Note that the event rate has a large uncertainty due to scarce knowledge of the formation rate of IMBH binary systems and varies by about an order of magnitude depending on the model.

The detection band of gravitational wave detectors on the low frequency side directly affects the detection rate of binary IMBH coalescence, since the lower frequency limit of the detector sensitivity determines the upper limit of the total mass of detectable binary systems. The detectable upper mass limit M_{max} is inversely proportional to the corner frequency of the sensitivity curve f_{min}, and the detection rate R of the merger event is approximately proportional to the maximum mass according to reference [35]. Thence one can derive the relation between the event rate and the frequency limit as $R \propto (f_{\mathrm{min}})^{-1}$. It means a reduction of the corner frequency enhances the detection rate by approximately the same factor.

1.5.2 Pulsars

Pulsars known from radio astronomy may emit gravitational waves at low frequencies. Figure 1.11 shows the maximum permitted gravitational wave amplitude of the known spinning pulsars, calculated under the assumption that the observed spin-down rate is fully dominated by the gravitational wave emission [36]. The KAGRA sensitivity with 1 year integration is also shown for comparison. The Vela pulsar, which rotates at 11.19 Hz and is expected to emit 22.39 Hz gravitational waves, is one of the candidates which can possibly emit gravitational waves with a detectable amplitude. Other pulsars in the frequency band between 10-40 Hz may also eimt detectable gravitational waves, and therefore it is essential to preserve the sensitivity in this region for gravitational wave searches for pulsars.

Note that a number of known pulsars with rotation frequencies higher than 10 Hz have been investigated by coincident searches in first generation gravitational wave detectors, which set upper limits on the emitted gravitational wave amplitude [37]. Having better sensitivities at low frequencies would provide better upper limits on the gravitational wave amplitude of such pulsars and/or possibility of detecting them.

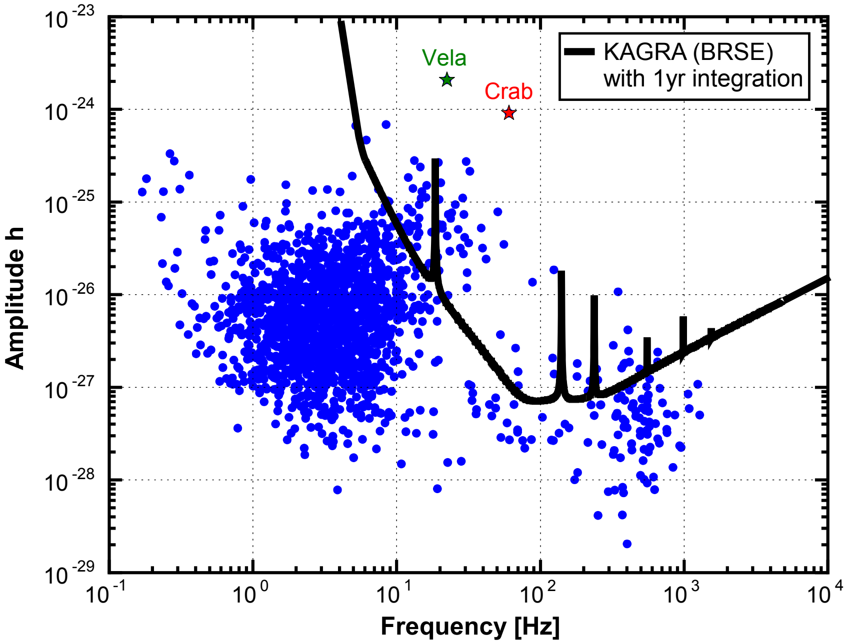

Figure 1.11: The maximum gravitational wave amplitude of the known spinning pulsars [36], overlaid with the KAGRA sensitivity with 1 year integration.

1.5.3 Binary neutron stars

Detectability of gravitational waves from a binary neutron star coalescence is not strongly affected by the detector sensitiviy around 10-40 Hz, since the system emits a large amplitude of gravitational waves just before the coalescence, with frequency components of 100-1000 Hz. Figure 1.12 shows the variation of signal-to-noise ratio for binary neutron star coalescences in the KAGRA detector, as a function of low-frequency limits of the analysis [38]. The SNR is degraded by only 3% even if the detector sensitivity below 50 Hz is lost.

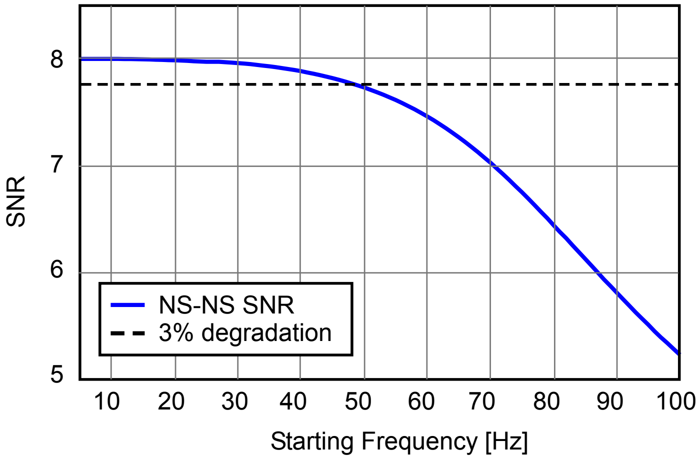

Figure 1.12: Signal to noise ratio of gravitational waves from $1.4M_{\odot}$-$1.4M_{\odot}$ binary neutron star merger, as a function of starting frequencies of the analysis in the KAGRA detector.

On the other hand, the low frequency sensitivity can affect the efficiency in estimating astrophysical parameters of the binary system from the observed gravitational wave signals. A study on parameter estimation algorithm shows that computation of the parameters of non-spinning binary neutron star inspirals can be sped up by a factor ∼150 when the low frequency limit of the sensitivity decreases from 40 Hz to 10 Hz [39].

1.5.4 Supernovae

Detection of burst gravitational waves will not be affected by the detector sensitivity at 10-40 Hz, but the extraction of physics may be affected once the gravitational wave signals are obtained. Several explosion models of supernovae, such as magnetohydrodynamic (MHD) explosion [40] and neutrino-driven convection with Standing Accretion Shock Instability (SASI) [41], provide gravitational waves with low frequency components (below 100 Hz). Figure 1.13 shows gravitational wave spectra in explosion models with SASI [41]. The spectrum shape below 50 Hz is affected by the initial condition of the explosion models. Hence improved sensitivity at low frequencies can contribute in determining astronomical parameters and distinguishing explosion mechanisms of supernovae.

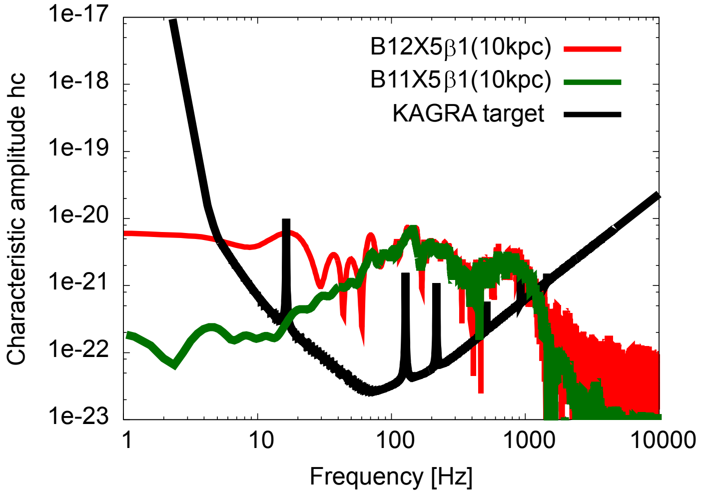

Figure 1.13: Gravitational wave spectra for representative explosion models of supernovae with SASI [41], compared with the KAGRA design sensitivity. The two models have different initial condition of magnetic field ($B = 10^{11}$ and 10^{12} G). The supernova is assumed to be located at the distance of 10 kpc.

1.6 Research target and thesis outline

The previous section explains expected low-frequency gravitational wave sources and possible physics derived from observations with second generation detectors, whose sensitivities are limited by fundamental noises (suspension thermal noise and quantum noise) in the frequency band above 10 Hz. The goal of this research is to design vibration isolation systems which preserve the design sensitivity in the detection band (> 10 Hz) by attenuating the seismic noise and allow the long-term observation of gravitational waves with expected sources and physics explained in section 1.5. To achieve this goal, the vibration isolation systems are required to have long-term stability and to suppress not only the seismic noise but also other technical noises such as control noise above 10 Hz. This research mainly focuses on the vibration isolation system for KAGRA, and studies their vibration isolation performance and active devices required for their stable operation.

The outline of the thesis is as follows. Chapter 2 explains the working principles of vibration isolation system and concerns for operating them in gravitational wave detectors. It also introduces various vibration isolation systems implemented for gravitational wave detector projects. Chapter 3 focuses on the low-frequency vibration isolation system called SAS (Seismic Attenuation System), which is adopted in KAGRA for the seismic noise reduction. Chapter 4 explains basic requirements and conceptual design of the KAGRA-SAS. The expected vibration isolation performance to meet the in-band noise requirement is also checked in this chapter. Chapter 5 describes the active control system, which is required for stable operation of the interferometer and thus for the long-term observation of gravitational waves. It specifies the requirements on the active control system for the KAGRA-SAS and describes possible noise couplings from the control system. Chapter 6 describes the experiments on the mechanical components of the KAGRA-SAS and the active control system. The performance of integrated system was tested with the prototype SAS constructed in National Astronomical Observatory of Japan (NAOJ), and the experimental setups and results on the integrated system are described in chapters 7 and 8, respectively. Chapter 9 summarizes the experimental results and draws conclusions.

Vibration isolation

Chapter 2

Seismic vibration is one of the fundamental and inevitable noise sources in terrestrial gravitational wave detectors. Seismic noise limits the detector sensitivities at low frequencies and restricts the detection band. This chapter addresses characteristics of seismic vibration and mechanisms that reduce its contribution to the detector sensitivity. Integrated vibration isolation systems for gravitational wave detectors are then introduced in the last section of this chapter (section 2.5).

2.1 Seismic motion

The continuous and random motion of the ground is induced by natural phenomena like oceanic and atmospheric activities, as well as by human activities. The amplitude of the seismic motion varies by a few orders of magnitude from site to site and from time to time, depending on the surrounding environment such as weather, industrial activities, and traffic condition in nearby cities.

J. Peterson set out to characterize seismic background noise by cataloguing data from a worldwide network of seismometer stations [42]. He derived the New High/Low Noise Model (NHNM/NLNM) from the upper and lower bounds of measured power spectral densities, which provide standard measures for comparison of stationary seismic spectra. Figure 2.1 shows the data and the upper/lower bounds set from Peterson's study.

The power spectrum densities increase rapidly at low frequencies below 1 mHz, where the Earth is subjected to tidal deformation due to gravitational attraction from the sun and the moon. This seismic motion at the very low frequencies moves the test masses in the gravitational wave detectors coherently and thus does not affect the interferometer operation or the detectability of gravitational waves. The remarkable peak observed around the periods of 2-10 s is known as the microseismic peak. It is caused by oceanic wave activities and therefore the peak is observed strongly along the coast and weakly in the middle of continents [43]. In large-scale gravitational wave detectors, the seismic motion around those frequencies is not coherent between the test mass locations, and thus can cause differential displacements between them. Therefore it is mandatory to suppress the

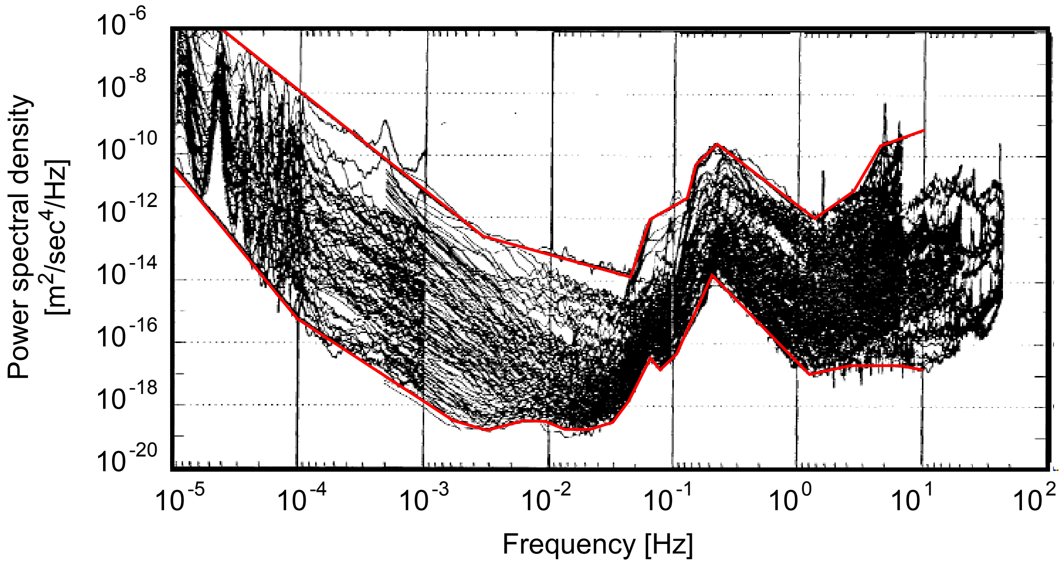

Figure 2.1: An overlay of seismic vibration spectra in Peterson's study together with the New High and Low Noise Model [42].

impact from microseismisms for stable operation of the interferometers.

Seismic motions at frequencies above 1 Hz are studied in the field of gravitational wave detection, since they can contaminate the detector sensitivities through its mechanical transmission to the optical components. Figure 2.2 shows typical power spectrum densities of the seismic vibration measured at the sites of gravitational wave detectors. Seismic vibration amplitudes are usually of the same order of magnitude in all three directions, and the displacement amplitude spactra of high frequency components (> 1 Hz) are typically written in the form of

$$\tilde{x}_{\mathrm{seism}}(f) = A \times \left(\frac{f}{1\ [\mathrm{Hz}]}\right)^{-2} \quad [\mathrm{m}/\sqrt{\mathrm{Hz}}]. \tag{2.1}$$

The amplitude factor A varies from site to site and is typically in the range 10^{-6}-10^{-9}.

The amplitude of the seismic motion in the KAGRA site (inside the Kamioka mine) is smaller than that in other places by 2-3 orders of magnitude. It is known that the seismic vibration decreases significantly in the underground environment, since the surrounding rocks isolate the vibration from atmospheric and human activities on the surface [45]. This becomes a big motivation to build gravitational wave detectors underground regardless of practical difficulties such as construction costs and safety issues. The natural isolation from being underground is especially effective at frequencies above 1 Hz, where the vibration originates from activities on the ground surface. On the other hand, the microseism at 0.1-1 Hz is not attenuated much since the vibration propagates through the continents.

The typical amplitude of the seismic motion is around 10^{-12}-10^{-10} m/$\sqrt{\mathrm{Hz}}$ at 100 Hz. On the other hand, the expected amplitude of the arm length variation due to a

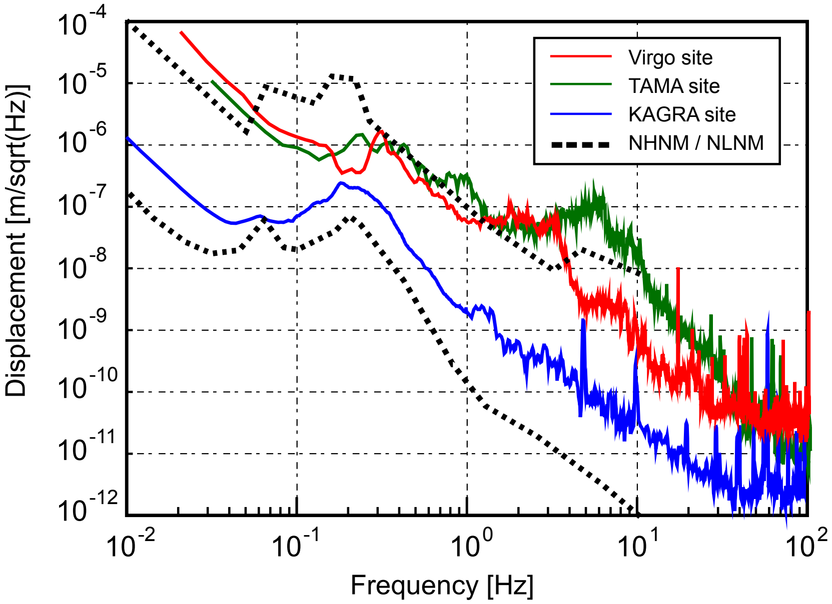

Figure 2.2: Typical power spectrum density of seismic vibration displacements at several sites of gravitational wave detectors [44].

gravitational wave is typically in the order of 10^{-20} m at that frequency. This means that an attenuation factor of 10^8-10^{10} is required for detection of gravitational waves.

2.2 Passive mechanical filter

2.2.1 Dynamics of the harmonic oscillator

Isolation from seismic motion can be realized by the use of mechanical filters with elastic components, such as springs and suspension wires. As the simplest example, consider a one-dimensional harmonic oscillator shown in figure 2.3. The oscillator consists of a spring with a spring constant k and a suspended payload with mass M. The displacements of the suspension point and the payload are denoted as x_0 and x respectively. The equation of motion of this system is written as

$$M\ddot{x} = -k(x - x_0). \tag{2.2}$$

This equation can be solved in the frequency domain by taking the Fourier transform as

$$H(\omega) \equiv \frac{\tilde{x}(\omega)}{\tilde{x}_0(\omega)} = \frac{1}{1 - (\omega/\omega_0)^2}, \tag{2.3}$$

where $\omega_0 = 2\pi f_0 = (k/M)^{1/2}$ is the resonant angular frequency of the system. $H(\omega)$ is called the transfer function from the displacement of the suspension point to the payload

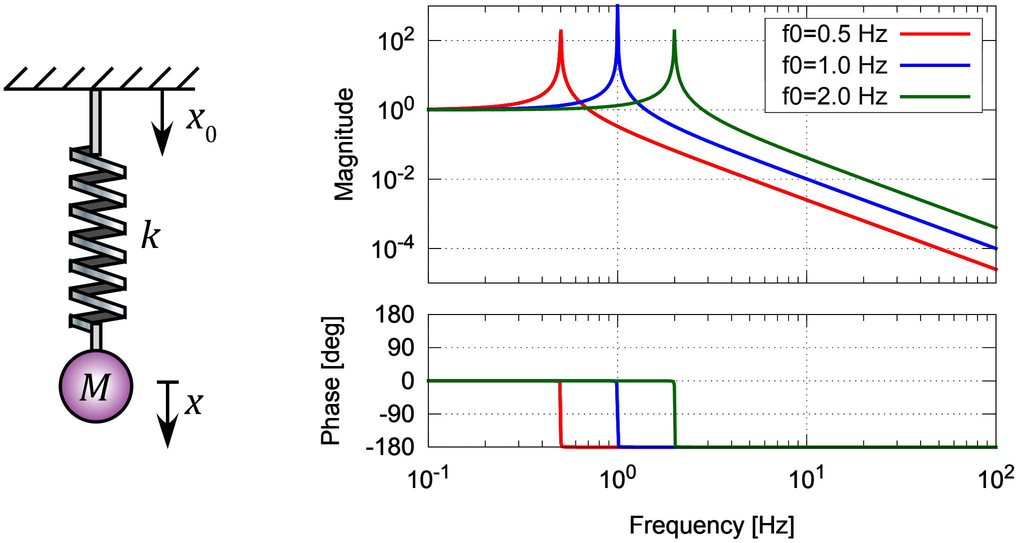

Figure 2.3: A spring-mass system as a mechanical filter (*left*) and its transfer function ($\tilde{x}/\tilde{x}_0$) with various resonant frequencies (*right*).

displacement. The amplitude and phase of $H(\omega)$ are plotted as a function of frequency in figure 2.3 with various resonant frequencies.

At low frequencies ($f \ll f_0$) the transfer function is close to one, which means that the motion of the payload follows that of the suspension point. Around the resonant frequency, the amplitude of the transfer function increases and, in absence of dissipation, goes to infinity at the resonant frequency. In the high frequency region ($f \gg f_0$) the amplitude of the transfer function rolls off proportional to f^{-2}, resulting in isolation of the suspended mass from the vibration of the suspension point. The vibration isolation ratio is approximately $(f/f_0)^{-2}$ at any given frequency above the resonance, which indicates that the suspended mass is isolated more by a mechanical filter with lower resonant frequency.

In an actual system, the transfer function does not diverge at the resonance due to the existence of dissipation. There are several dissipation mechanisms such as residual gas damping and thermoelastic damping. The dissipation caused by anelasticity in the elastic components is often called the structural damping and is expressed by adding an imaginary part to the spring constant as $k \to k(1+i\phi)$, in the frequency domain. Here ϕ is called the loss angle and is defined as the phase angle by which the displacement response x would lag behind a sinusoidal driving force applied to the payload. Typically $\phi \ll 1$ and the loss angle is related to the oscillator's quality factor as $Q = 1/\phi$. A number of measurements show that the intrinsic loss angles of elastic materials are independent from the frequency [46]. The resulting transfer function (2.3) has a peak amplitude of $1/\phi$ at the resonant frequency.

2.2.2 Multi-stage suspension

In an interferometric gravitational wave detector, every test mass is suspended as a pendulum so that it behaves almost as a free particle in the sensitive plane of the interferometer. Such a suspension also works as a mechanical isolator from the ground vibration. The resonant frequency of the pendulum is around 1 Hz with a reasonable length (a few tens of cm), therefore the vibration isolation ratio is about 10^{-4} at 100 Hz. Since the required attenuation is around 10^{-10}-10^{-8}, seismic attenuation by a simple pendulum is not sufficient for the detection of gravitational waves.

The required seismic attenuation is obtained by cascading mechanical filters, whose resonant frequencies are sufficiently lower than the frequency region of interest ($\gtrsim$ 10 Hz in second generation detectors). In an N-stage chain of mechanical filters, the ground motion transmits to the suspended mass with an attenuation factor proportional to f^{-2N}, at a frequency higher than the resonant frequencies of the chain. Figure 2.4 shows the attenuation performance of a multi-stage pendulum with various stage numbers. By employing sufficient numbers of isolation stages, strong attenuation of the seismic noise can be achieved in the high frequency region.

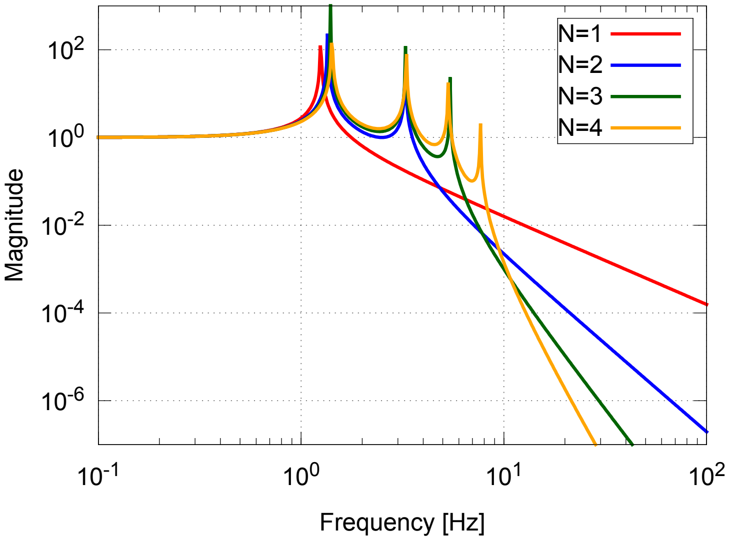

Figure 2.4: The amplitudes of the transfer functions of an N-stage multi-pendulum with $N = 1 \sim 4$, from the suspension point displacement to the bottom mass displacement. The total length of the pendulum is set to be 1 m in all cases.

2.2.3 Couplings from vertical and rotational motions

Since the horizontal ground motion transmits directly to the horizontal motions of the mirrors and contributes to the changes in the optical path lengths of the interferometer, isolation from the horizontal ground vibration is the most critical issue in gravitational wave detectors. However, isolation from the vertical ground vibration is also indispensable in practice. This is because 0.1-1% of the vertical motion is transferred to the horizontal direction by mechanical imperfections in each attenuation stage and ultimately by the non-parallelism of the verticality at locations kilometers apart in the interferometer. As shown in figure 2.5, the front and end mirrors of the Fabry-Perot cavities form an angle of $\alpha = L/2R_\oplus$ with the interferometer's global vertical direction. Here L is the cavity length and $R_\oplus$ is the radius of Earth. Hence, a vertical displacement δz has an effect along the beam direction, producing a variation $\alpha\delta z$ of the cavity length. In the case of a 3-km length interferometer, the minimum coupling due to the Earth curvature is $\alpha \sim 2 \times 10^{-4}$.

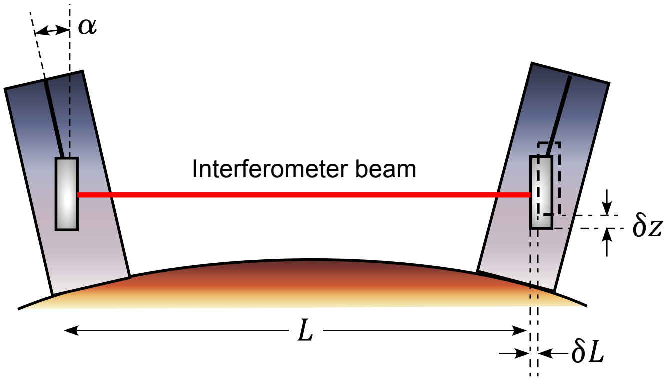

Figure 2.5: Effect of the Earth curvature.

Not only the vertical motions but the rotational motions of the mirror may affect the sensitivity of the interferometer. The rotational motion of a mirror does not change the optical path length if the laser beam illuminates the center of the mirror. However, the beam spot is off-center to some extent in reality, and an angular displacement causes a variation of the optical path length as shown in figure 2.6. When the beam spot is misaligned by a distance of d from the center, the rotation angle of the mirror $\delta\theta$ couples to the length variation along the beam axis by $d\delta\theta$.

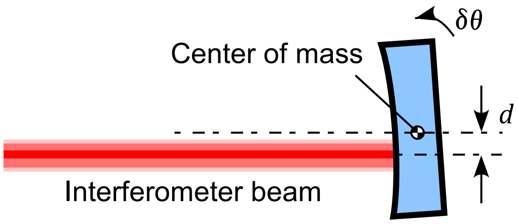

Figure 2.6: Coupling from the rotational motion of the mirror due to misalignment.

The coordinate system used in this thesis is defined in figure 2.7. The longitudinal direction coincides with the beam axis of the interferometer. The names for the rotation degrees of freedom are taken from aircract terminology.

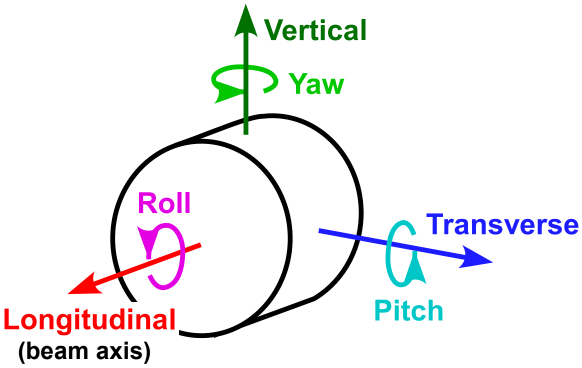

Figure 2.7: Definition of the coordinate system.

2.3 Damping of suspension system

2.3.1 Stable Operation of interferometers

Seismic motion affects not only the sensitivity of the interferometer, but also its stability. Although the chains of mechanical filters isolate the optics from seismic motion in a high frequency region, the mirror motions can be largely excited at low frequencies, especially at the resonant frequencies of the mechanical components. As the Michelson interferometer and the Fabry-Perot cavities must be kept in the dark fringe / the resonant condition by feedback controls, the RMS (Root Mean Square) amplitude of the mirror displacement and velocity have to be suppressed within the limited range of the controls.

The RMS amplitude of the ground motion displacement (integrated down to $\lesssim 0.1$ Hz) is typically in the order of microns at the surface and submicrons for underground. As the main contribution to the RMS amplitude is concentrated in the low frequency band ($\lesssim 1$ Hz), the resonant peaks of the mechanical system in this frequency region must be suppressed. The microseismic peak between 0.2-0.5 Hz contributes most to the seismic RMS amplitude, therefore one tries to place the mechanical resonances away from this region. In underground locations, the microseismic motion itself is largely coherent across the entire interferometer, therefore it would be of little ill effect on the interferometer stability. The actual problem is that the resonances of the seismic isolation system can be excited with different and varying phases, thus resulting in large relative motions of the interferometer mirrors. Therefore the resonances of the seismic attenuation chains must be damped strongly.

Another reason for introducing damping mechanisms is to enhance robustness to unwanted acceleration disturbances such as earthquakes and miscontrol actuation forces. Such disturbances excite the mechanical resonances and the oscillation at the resonant frequencies remains for a long period unless they are appropriately damped. The interferometer cannot be operated while the mirrors are swinging in large amplitudes and thus the time for observation is reduced. It is essential to suppress the decay time of mechanical resonances which may be excited by external disturbances and affect the operability of the interferometer.

2.3.2 Passive damping

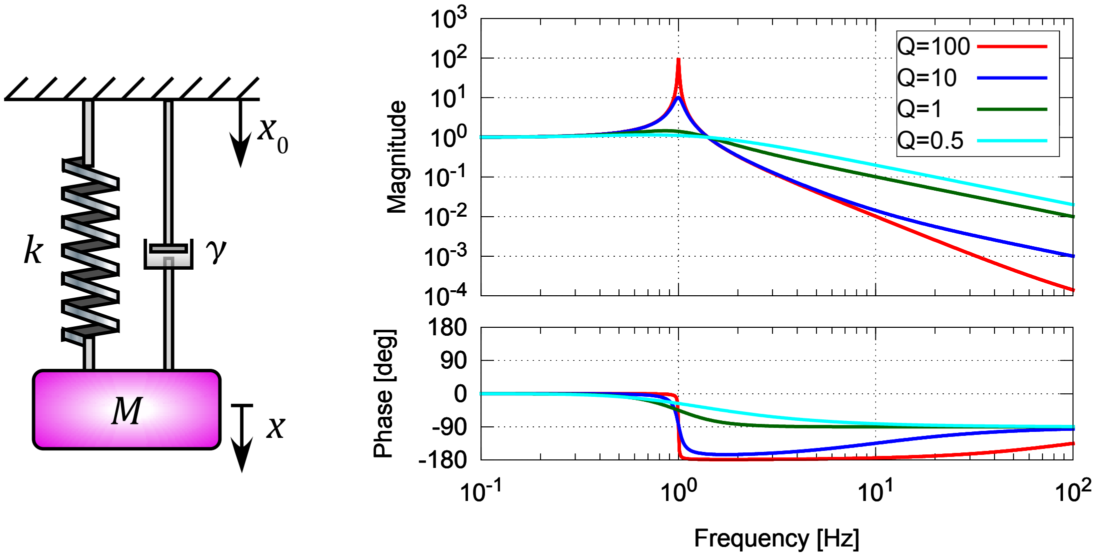

Figure 2.8: (*Left*)A mechanical oscillator with a viscous damping mechanism represented by a dashpot. (*Right*) Bode plots of the transfer function with various quality factors.

There are fundamentally two ways of damping the mechanical resonances: passive and active damping. Passive damping can be achieved by adding a viscous damper which outputs a braking force proportional to the relative velocity between the damper and the object to be damped. Figure 2.8 shows a conceptual design of a viscously damped mechanical oscillator. The equation of motion of the system is

$$M\ddot{x} = -k(x - x_0) - \gamma(\dot{x} - \dot{x}_0), \tag{2.4}$$

where γ is the damping coefficient of the damper. The damping force provides dissipation to the system in addition to structural damping caused by the spring's internal friction. The structural damping contribution is typically much smaller than that from a deliberately implemented damper. From the Fourier transform of this equation, the frequency response of the suspended mass displacement to the ground vibration is

$$H(\omega) = \frac{1 + 2i\eta(\omega/\omega_0)}{1 + 2i\eta(\omega/\omega_0) - (\omega/\omega_0)^2}, \tag{2.5}$$

where the damping ratio η is given by $\eta = \gamma/2M\omega_0$. A system with dissipation is often characterized by the quality factor of the resonance, which is given by $Q = \frac{1}{2\eta}$.

The amplitude and the phase of the transfer function $H(\omega)$ with various quality factors are plotted in figure 2.8. There are two important characteristics in the transfer function of the viscously damped system. First, the height of the peak at the resonance ($f = f_0$) gets smaller when the damping gets stronger, and is roughly equal to Q in the case of $Q \gg 1$. Second, the amplitude of the transfer function rolls off in proportion to only f^{-1} above the frequency Qf_0, instead of f^{-2} observed in the system with no dissipation. Hence, the performance of the mechanical filter is degraded at high frequencies in a viscously damped system.

The robustness of the mechanical filter to acceleration disturbances can be seen in an impulse response to a driving force on the suspended mass. Figure 2.9 shows the impulse response of a viscously damped mechanical oscillator with various damping factors. When the system has small dissipation, the suspended mass shows a sinusoidal oscillation with decaying amplitude. The oscillation amplitude decays faster as the damping factor increases. The decay time τ, in which the oscillation amplitude decreases by a factor of $1/e$, becomes $\tau = \frac{1}{\eta\omega_0} = \frac{Q}{4\pi f_0}$. In the critical damping condition where the damping factor η reaches 1 (or $Q = 0.5$), the suspended mass no longer oscillates and the displacement decays with decay time $\tau = \frac{1}{\omega_0}$. When the damping becomes even stronger ($\eta > 1$, in the over-damped condition), the suspended mass becomes harder to displace but the decay time becomes longer than that of the critically damped oscillator, since the damper resists the suspended mass returning to its original condition.

The degradation of vibration isolation performance due to a damper can be avoided by isolating the damper from the ground vibration by means of another mechanical filter as shown in figure 2.10. This technique is called flexible damping. Although the additional spring introduces another resonance to the system, the amplitude of the transfer function falls in proportion to f^{-2} at high frequencies as in the case without dissipation (see the plots in figure 2.10).

2.3.3 Actual implementation of viscous dampers

One simple way to implement viscous damping in the suspension system is the use of an eddy current damper [47], which is composed of permanent magnets on the mechanical ground acting on conductive objects placed on the oscillator to be damped. When a conductive material experiences a time-varying magnetic field, eddy currents are generated in the conductor. These currents generate a magnetic field with opposite polarity of the applied field and a delay due to the induced field decay, causing a resistive force. Figure 2.11

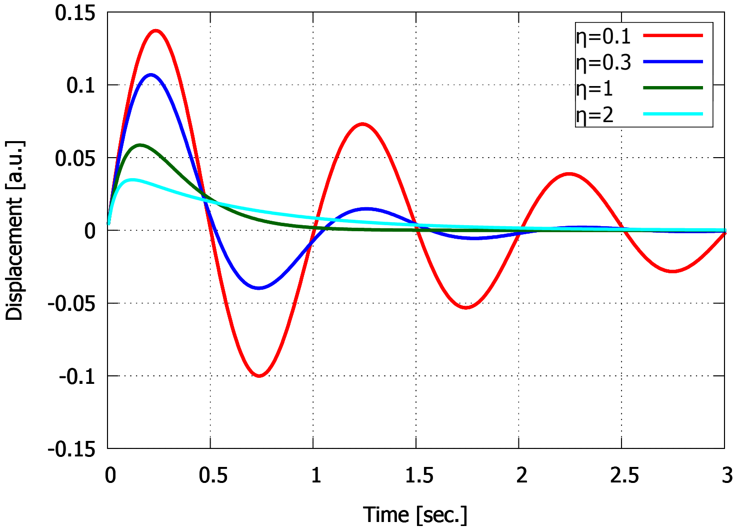

Figure 2.9: Response of a viscously damped mechanical oscillator with various damping factors to an impulsive force exerted to the suspended mass.

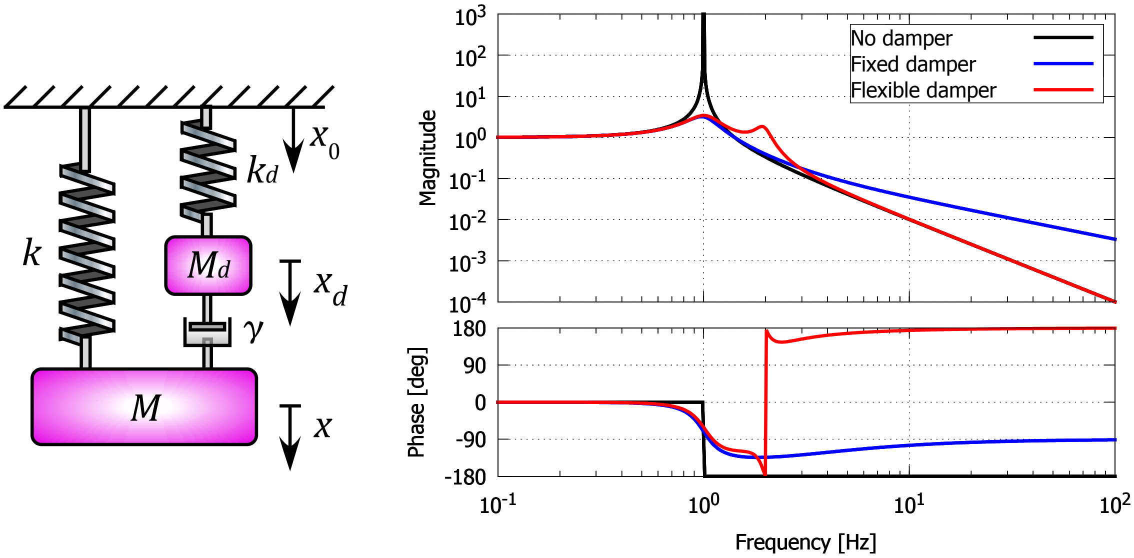

Figure 2.10: (*Left*)A mechanical oscillator with a flexible damping mechanism. (*Right*) Comparison of the transfer functions of the mechanical filter with no damper, a fixed damper, and a flexibly supported damper.

illustrates the working mechanism of an eddy current damper. The damping coefficient caused by an eddy current damper is

$$\gamma_x = A\sigma B\frac{\partial B}{\partial x}, \tag{2.6}$$

where B is the magnetic field from the permanent magnet, σ is the electrical conductivity of the conductor and A is a factor determined from the geometry of the conductor. In general, a large damping strength is obtained by the use of a permanent magnet with strong magnetic field and a conductive object with large electric conductivity.

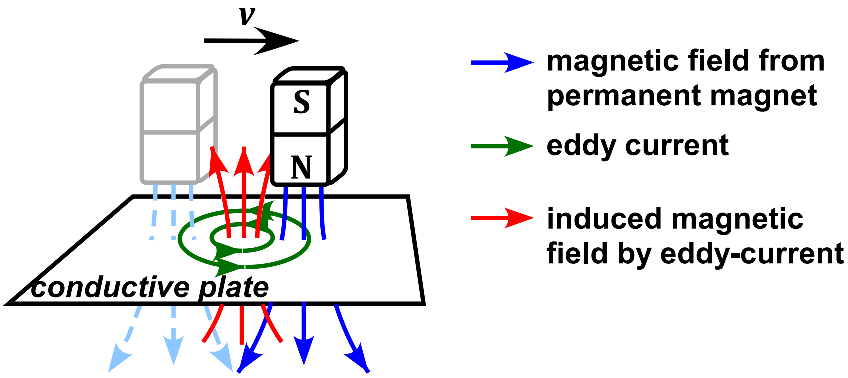

Figure 2.11: An illustration of the working mechanism of an eddy current damper.

A chief advantage of using eddy current dampers is that there is no contact between the damper and the damped objects and thus there is no risk of hysteretic noise caused by mechanical friction. A possible drawback of using eddy current dampers is direct transmission of the damper motions to the mirror motions through the magnetic field couplings, since most mirrors in the interferometer possess permanent magnets for actuators. Suspension systems with eddy current dampers have been developed for TAMA [48] and their effectiveness has been demonstrated.

2.3.4 Suspension thermal noise

Although viscous damping contributes to suppression of RMS displacement or velocity of the suspended optics and stable operation of the interferometer, it can degrade the detector sensitivity by inducing thermal fluctuation of the suspended mirrors in the detection band of gravitational waves. The fluctuation dissipation theorem provides a general relation between the frequency response of systems in equilibrium to external perturbation forces ($H_{\rm f}(\omega)$) and the power spectral density of their spontaneous fluctuations ($S_{\rm th}(\omega)$):

$$S_{\rm th}(\omega) = -\frac{4k_BT}{\omega}{\rm Im}[H_{\rm f}(\omega)]. \tag{2.7}$$

Here k_B is the Boltzmann constant and T represents the temperature. In a viscously damped system, the power spectrum density of the harmonic oscillator's thermal fluctuation can be calculated as

$$S_{\mathrm{th}}(\omega) = \frac{4k_BT}{M}\frac{2\eta\omega_0}{(\omega_0^2-\omega^2)^2+4\eta^2\omega_0^2\omega^2}. \tag{2.8}$$

Figure 2.12 shows spectra calculated from the equation. The amplitude spectral density is in proportion to f^{-2} in the detection band and reaches 10^{-17}-10^{-16} $[\mathrm{m}/\sqrt{\mathrm{Hz}}]$ at 100 Hz. This is not applicable in gravitational wave detectors since expected gravitational wave signals are in the order of 10^{-20} $[\mathrm{m}/\sqrt{\mathrm{Hz}}]$.

In a multi-stage suspension, the impact from thermal fluctuations induced by viscous dampers can be mitigated by placing the dampers on upper stages, since like seismic vibration, the thermal vibration is filtered out by mechanical filters. Passive dampers should be set well apart from the optics so that thermal fluctuations due to their dissipation do not limit the detector sensitivity.

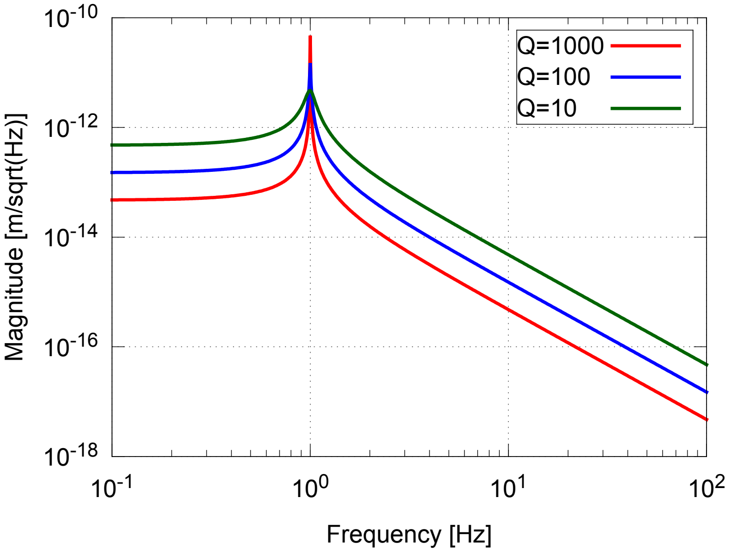

Figure 2.12: Predicted amplitude spectrum densities of thermal displacement fluctuation of viscously damped harmonic oscillators, assuming $T = 300$ K, $M = 30$ kg and $f_0 = 1$ Hz.

2.3.5 Active damping

Passive damping has advantages such as low cost, robustness, low complexity and ease of implementation. However, the magnetic field from permanent magnets diverges in all directions and an eddy current damper implemented for one degree of freedom (DoF) also affects the damping strengths in other DoFs. Therefore it is difficult to design the passive dampers so that the resonances of all the translational/rotational motions of the suspended mass are damped sufficiently. In addition, suspension systems with eddy current dampers suffer from severe suspension thermal noise at high frequencies as described above, therefore one needs to avoid using them near the optics of the interferometer.

In actively damped systems, the vibration of the suspended mass is suppressed by feedback controls with vibration sensors and actuators. The active damping strength can be tuned flexibly and the frequency response can be controlled by designing the servo filters. If one places sensors and actuators in sufficient numbers and proper configuration, the motion of the suspended mass can be controlled in all translational/rotational DoFs individually. The servo filters of the feedback controls have to be designed carefully so that they no sensor, actuator and electric circuit noise are injected in the form of random motion of the suspended mass. An advantage of active damping is that it can be switched off after the unwanted oscillations have been damped, thus eliminating the control noise.

2.4 Active vibration isolation

Passive isolation systems rely on natural characteristics of mechanical oscillators for vibration reduction of suspended objects. Since a mechanical oscillator can filter out vibration components only above its natural resonant frequency, reduction of low frequency vibration such as motion induced by microseismism (between 0.2-0.5 Hz) is not easily achieved by passive systems. Active isolation systems, which implement vibration sensors, actuators and controllers (servos), isolate the target objects from seismic vibration actively with feedback and feedforward controls. Active systems in principle can reduce the targets' vibration in any frequency band, if vibration sensors with sufficient sensitivities and low noise levels are used.

Figure 2.13 shows a typical control topology of an active isolation system. The isolation platform is supported by suspension springs so that the motion can be controlled with actuators. Vibration of the platform is measured by inertial sensors (seismometers), which sense the platform accelerations relative to an inertial frame, and the signals are sent to the feedback controller. Since inertial sensors have poor sensitivities at low frequencies, the platform is positioned at DC with respect to the support structure by using relative position sensors. In the feedback controller, signals from inertial sensors and position sensors are blended to connect the two control loops. Additional isolation performance is obtained by using feedforward inertial sensors measuring the ground vibration. Detailed discussion on the active isolation system can be found in reference [49].

2.5 Vibration isolation systems in detector projects

This section briefly introduces various vibration isolation systems implemented for large-scale terrestrial gravitational wave detectors.

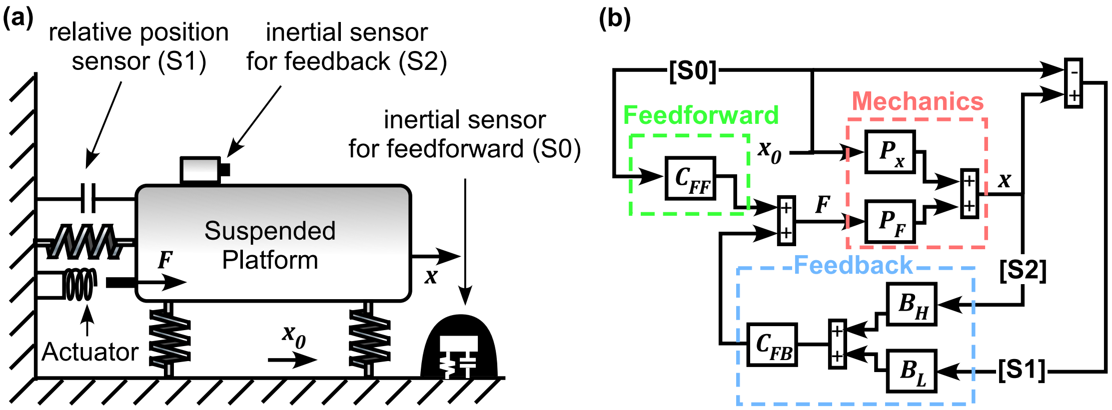

Figure 2.13: (a) A schematic drawing of an active isolation system . (b) A block diagram of the active control scheme.

2.5.1 Vibration isolation stack

LIGO, GEO and initial configuration of TAMA employ a multiple-stage vibration isolation system called a stack, which consist of alternating layers of metallic masses and elastomer springs, for core optics of the interferometers [50, 51]. Its visual impression is shown in figure 2.14. Elastomers have internal viscoelastic damping, which reduces the quality factors of the mechanical resonances by a factor of 1-10. The resonant frequencies are typically 2-10 Hz for horizontal modes and 5-20 Hz for vertical modes. It can attenuate seismic vibration above several tens of Hz and provide attenuation factors of 10^{-3}-10^{-6} at 100 Hz. The stack supports a breadboard from which a core optic of the interferometer is suspended through a single or multiple-stage suspension.

The vibration isolation stack is a fully passive and simple system and thus has an

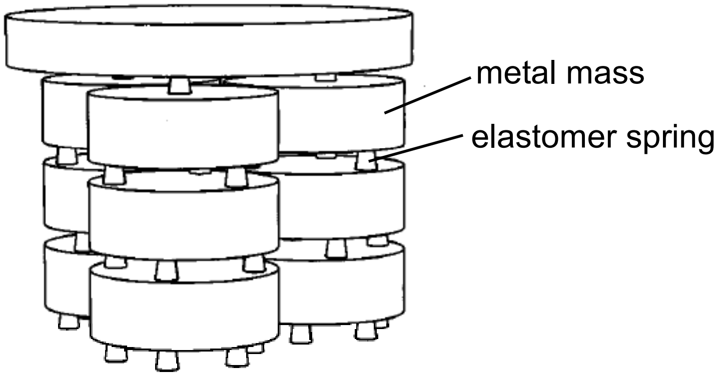

Figure 2.14: Perspective drawing of a vibration isolation stack [50].

advantage in easy implementation. However, the resonant frequencies are relatively high and vibration isolation performance at low frequencies (10-50 Hz) is not sufficient for allowing gravitational wave detection in that frequency band. Additionally, elastromer springs suffer from large creep, which requires periodic adjustment of the height and tilt of the structure.

2.5.2 Superattenuator

Virgo pioneered in developing low-frequency vibration isolation systems aiming to extend the detection band of gravitational waves to lower frequencies. Each core optic of the interferometer is suspended from a vibration isolation system called a Superattenuator [52], which consists of a pre-isolation stage with inverted pendulums and a chain of mechanical filters (see figure 2.15). Each mechanical filter attenuates vertical vibration by the use of metal cantilever springs with its resonant frequency lowered by magnetic antispring technology [53]. The penultimate stage of the suspension chain is called the marionette, which supports the mirror by four wires and can be steered by coil-magnet actuators from the stage above.

The performance of the superattenuator has been tested in the facility with the interferometer, by actuating the top stage vibration with sinusoidal excitation and measuring the resulting output signals from the interferometer. The experiment demonstrates that the superattenuator succeeds in attenuating the vibration by more than 10 orders of magnitude in the detection band of gravitational waves (> 10 Hz) [54]. Virgo reached the design sensitivity in the second science run (VSR2 in 2009) and achieved a noise level of 10^{-20} $[1/\sqrt{\mathrm{Hz}}]$ at 10 Hz in spacetime strain equivalent.

2.5.3 Seismic attenuation system

TAMA replaced its vibration isolation systems for the core optics in 2005-2006 from conventional vibration isolation stacks to low-frequency vibration isolation systems called the TAMA-Seismic Attenuation System (SAS) [55]. SAS features mechanical filters with low natural frequencies, i.e. inverted pendulums (IPs) and Geometric Anti-Spring (GAS) filters. The low frequency oscillators contribute in cutting off the seismic noise from a frequency as low as a few Hz and extending the detection band of gravitational waves to low frequencies. The second generation detector KAGRA will hold similar systems for core optics of the interferometer. More details on SAS will be given in the following chapter.

2.5.4 Active isolation platform

Vibration isolation systems in advanced LIGO feature active isolated platforms using various vibration sensors and actuators for feedback and feedforward controls. Figure 2.16 shows schematic and CAD drawings of the vibration isolation systems for the core optics, which are placed inside and around vacuum envelops called the Basic Symmetric Chambers

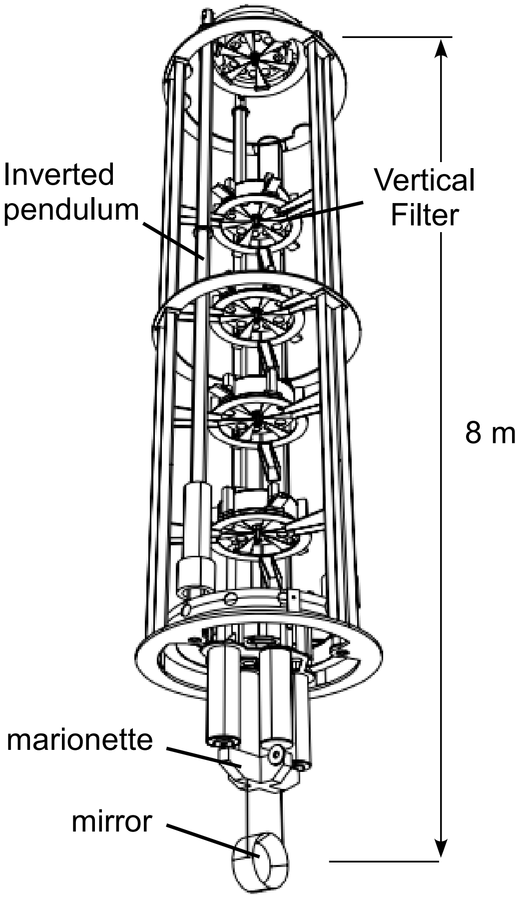

Figure 2.15: An illustration of the Virgo Superattenuator [54].

(BSC). Three systems are cascaded to provide up to seven stages of seismic isolation to the core optics; the Hydraulic External Pre-Isolator (HEPI), the Internal Seismic Isolation platform (ISI) and the quadruple pendulum suspension. HEPI and ISI provide precise positioning and active isolation of a suspension platform, from which the core optic is suspended. The platform is isolated from the seismic vibration from low frequency ($\lesssim$ 0.1 Hz) down to the level of $\sim 10^{-12}$ m/$\sqrt{\text{Hz}}$ at 10 Hz. The seismic isolation systems were installed in the detectors and their robustness and effectiveness have been proved through years of commissioning on the interferometers. The detailed control strategy and measured performance of this active isolation system can be found in reference [49].

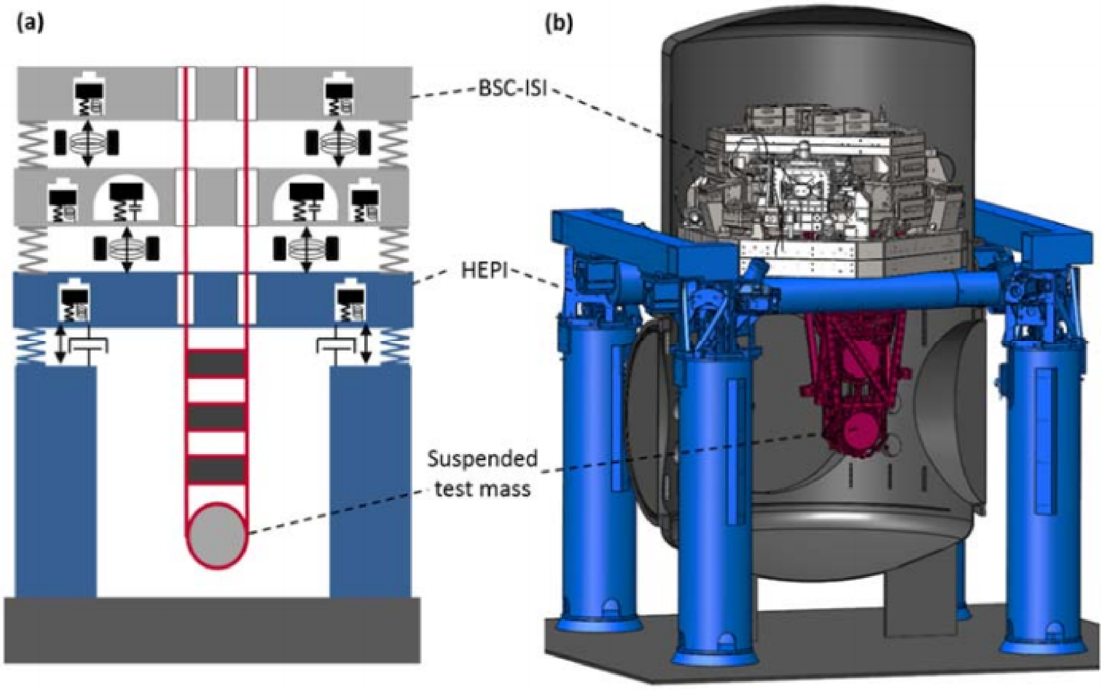

Figure 2.16: (a) Schematic and (b) CAD drawings of the vibration isolation systems supporting the core optics of the advanced LIGO interferometer [49].

Seismic Attenuation System

Chapter 3

Vibration isolation systems invented for various gravitational wave detectors were introduced in the previous chapter. This chapter focuses on the low-frequency vibration isolation system called the Seismic Attenuation System (SAS). Its general concept and the working principles of key mechanical components are briefly introduced in sections 3.1-3.3.

3.1 General concept

As explained in chapter 2, a mechanical oscillator can provide vibration isolation at frequencies higher than its natural resonant frequency, and thus one of the simplest way to improve the attenuation performance is reducing the natural frequency of the mechanical filter. The Seismic Attenuation System (SAS) aims to improve its seismic attenuation performance at low frequencies by pushing down the natural frequencies of mechanical resonators with the aid of anti-spring technologies.

SAS contains two key mechanical components called the Inverted Pendulum (IP) and the Geometric Anti-Spring (GAS) filter, which provide horizontal and vertical vibration isolation respectively. The resonant frequency of the IP can be lowered to ∼30 mHz and thus it can passively attenuate the ground motion at the microseismic peak (0.2-0.5 Hz), which contributes most of the RMS amplitude of the mirror displacement/velocity. The resonant frequency of the GAS filter can be lowered to ∼200 mHz and it enable us to achieve vertical attenuation performance comparable to that obtained by pendulums in the horizontal direction. Note that the lowest natural frequencies of the IP and GAS filters are limited by hysteretic behaviors of elastic components and thus can be potentially improved by investigating better elastic material in the future.

SAS is basically a passive system and thus has advantages in robustness and ease of maintenance once it is installed. Nevertheless the system cannot be completely passive and active controls are required for compensating thermal drift and damping the mechanical resonances.

3.2 Inverted pendulum

3.2.1 Basic working principle

An Inverted Pendulum (IP) is a horizontal mechanical oscillator whose resonant frequency is tunable and can be reduced lower than 0.1 Hz. It provides seismic attenuation at the microseismic peak frequency (0.2-0.5 Hz) by one order of magnitude and horizontal mobility of the suspended platform in soft manners. A simple model of the IP is shown in figure 3.1. The IP consists of a flexure fixed to the ground, a rigid cylindrical leg connected onto it and a mass on the top of the leg. When the mass is displaced horizontally from the vertical point, a restoring force acts on it with an effective spring constant of

$$k_{\mathrm{eff}} = \frac{k_\theta}{L^2} - \frac{Mg}{L}. \tag{3.1}$$

k_θ is the bending spring constant of the flexure (the torque induced by unit bending angle), M is the mass of the payload and L is the length of the leg. Here the mass of the leg m is assumed to be negligibly small, i.e. $m \ll M$. The first term of k_{eff} corresponds to the elastic restoring force of the flexure and the rest represents a repulsive force with gravitational anti-spring effect. The effective stiffness of the IP decreases as the mass of the payload increases and it vanishes when the mass reaches $M_{\mathrm{c}} = k_\theta/gL$. This mass is called the critical mass. Within the stable region ($M < M_{\mathrm{c}}$) the resonant frequency of the IP is

$$\omega_{\mathrm{IP}} = \sqrt{\frac{g}{L}\left(\frac{M_{\mathrm{c}} - M}{M}\right)}. \tag{3.2}$$

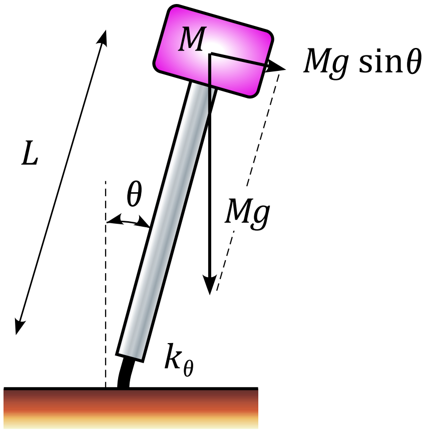

Figure 3.1: An illustration of the IP.

3.2.2 Anelasticity and quality factors

In the case of real IPs, inelastic damping effect due to the internal friction of the flexure must be taken into account. Introducing an imaginary part with an intrinsic loss angle ϕ to the flexure spring constant, the effective spring constant becomes

$$k'_{\mathrm{eff}} = \frac{k_\theta}{L^2} \times (1 + i\phi) - \frac{Mg}{L}. \tag{3.3}$$

One can define the effective loss angle of the system as

$$\phi_{\mathrm{eff}} = \frac{k_\theta}{L^2 k_{\mathrm{eff}}} \phi. \tag{3.4}$$

The quality factor of the IP resonance decreases as the real part of the effective spring constant is reduced by the gravitational anti-spring effect. This is an important and useful property of the IP, because an IP tuned at sufficiently low frequency needs no external damping. Figure 3.2 shows the measured quality factor with the resonant frequency of the IP which has been developed for LIGO [56]. The downside of this loss mechanism is that when the IP is tuned to extremely low frequency and the quality factor approaches $Q \sim 1$, the IP shows hysteretic behaviors and instability. Therefore in most cases the IP is tuned to not lower than 30 mHz when it is used as a seismic isolator in gravitational wave detectors. This practically limits the seismic attenuation at very low frequencies with IPs.

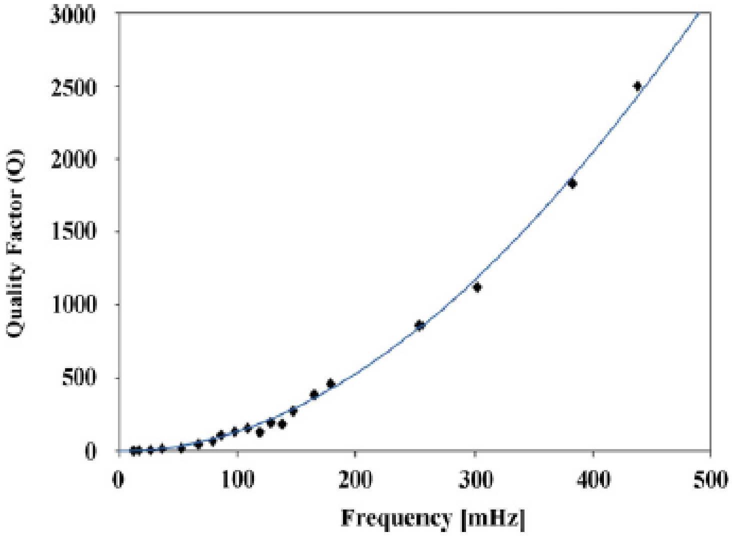

Figure 3.2: Measured quality factor versus resonant frequency of the HAM-SAS IP developed for LIGO [56]. The measurement data fit with a quadratic function.

3.2.3 Attenuation performance

When calculating the frequency response of the IP to the ground motion, one has to take into account the mass distribution of the IP leg. Assuming that the leg has uniform mass distribution between the flexure and the payload with total mass of m and moment of inertia of I, the transfer function from the ground displacement to the payload displacement is [55]

$$H_{\mathrm{IP}}(\omega) = \frac{A + B\omega^2}{A - \omega^2}, \tag{3.5}$$

$$\text{where} \quad A = \frac{k_{\mathrm{eff}}}{M + \frac{m}{4} + \frac{I}{L^2}}, \quad B = \frac{\frac{m}{4} - \frac{I}{L^2}}{M + \frac{m}{4} + \frac{I}{L^2}}. \tag{3.6}$$

Figure 3.3 shows the amplitude of $H_{\mathrm{IP}}(\omega)$ as a function of frequency. The attenuation ratio saturates at high frequencies due to the coefficient B in equation (3.5). This behavior is physically related to the Center of Percussion (CoP) effect [57, 55]. The IP legs should be made as light as possible to minimize the CoP effect and improve the attenuation performance at high frequencies. In order to further compensate the CoP effect, the mass distribution of the leg can be changed by introducing a counter weight at the bottom of the leg (figure 3.4).

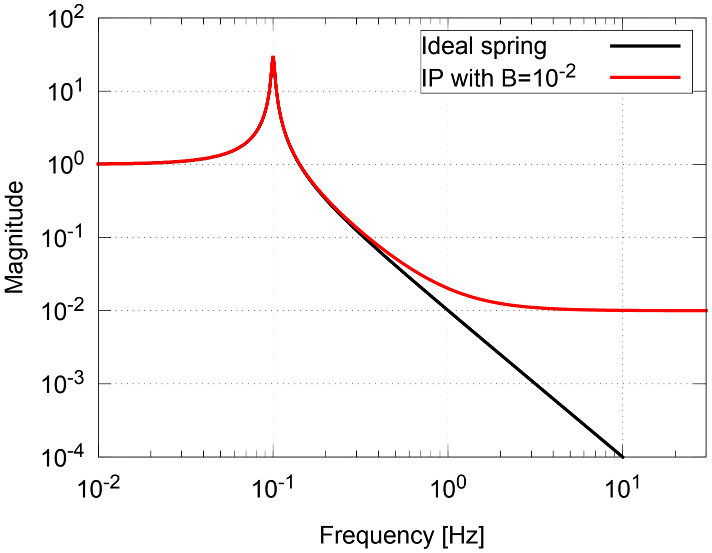

Figure 3.3: The transfer function of an IP with the resonant frequency of 0.1 Hz and the saturation level of 10^{-2}.

The IP of the HAM-SAS developed for Advanced LIGO [58] has an aluminum pipe with 1 mm thickness and 50 cm length as a leg. With the aid of the lightness of the leg ($m \sim 0.2$ kg), the attenuation performance reaches $\sim 10^{-3}$ without counter-weights and 10^{-5}-10^{-4} with them.

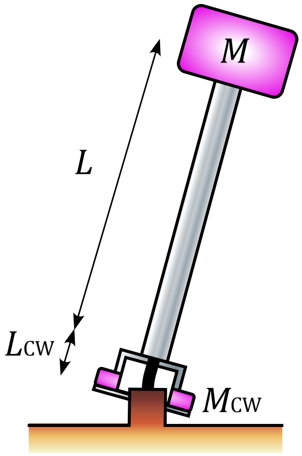

Figure 3.4: An illustration of the IP with the counter weight mounted at the bottom of the leg.

3.2.4 Horizontal modes of the IP stage

In the Seismic Attenuation System for gravitational wave detectors, IPs are used in the primary isolation stage, which provides pre-isolation of seismic vibration in the horizontal directions with a platform supported by three IP legs. Neglecting the vertical elasticity of the IP legs, the platform has three normal modes with two translational and one rotational DoFs. A model of the isolation platform is illustrated in figure 3.6. There is a round rigid-body platform connected to three horizontal springs, which correspond to the IPs with effective spring constants of k_1, k_2 and k_3. The IPs are arranged at a distance of R from the central point and separated by 120° from each other. The motion of the rigid body is characterized by a vector defined by the position and rotation angle $(x, y, R\phi)$ in the Cartesian coordinate system. By applying a small perturbation in each degree of freedom, one obtains the following stiffness matrix of the system:

$$K = \begin{bmatrix} k_1+k_2+k_3 & 0 & \frac{\sqrt{3}}{2}(-k_2+k_3) \\ 0 & k_1+k_2+k_3 & \frac{1}{2}(2k_1-k_2-k_3) \\ \frac{\sqrt{3}}{2}(-k_2+k_3) & \frac{1}{2}(2k_1-k_2-k_3) & k_1+k_2+k_3 \end{bmatrix}. \tag{3.7}$$

In the symmetric system with $k_1 = k_2 = k_3$, the non-diagonal elements of the stiffness matrix vanish and the eigen modes are separated into pure translation modes in the x, y directions and a rotation mode about ϕ. In actual system, there exists asymmetry in the effective stiffness and thus the translational and rotational modes are coupled with each other.

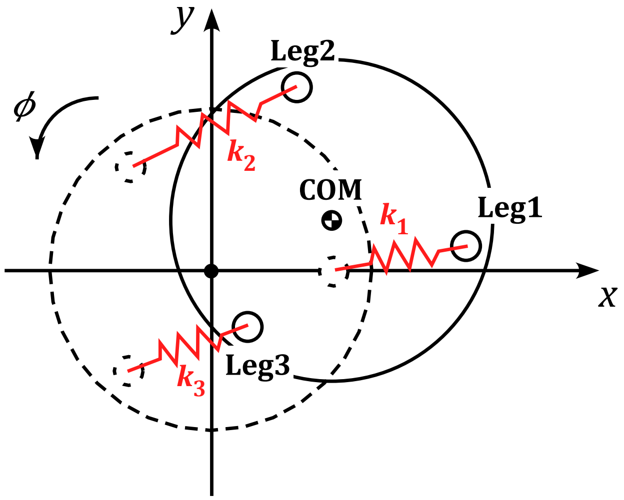

Figure 3.5: A rigid-body model of the isolation platform with three IP legs.

3.2.5 Response to ground tilt

When the ground tilts by an angle of θ, it introduces additional force of $\frac{k_\theta \theta}{L}$ to the suspended payload. The transfer function from the ground tilt to the induced payload displacement is then described as

$$H_{\mathrm{IP,tilt}}(\omega) = \frac{AC}{A-\omega^2},, \quad \text{where} \quad C = \frac{k_\theta}{L k_{\mathrm{eff}}}. \tag{3.8}$$

In the low frequency limit, the transfer function approaches C. The coupling coefficient increases as the effective spring constant k_{eff} is reduced by gravitational anti-spring effect. This means the system with the lower resonant frequency gets more sensitive to the DC ground tilt. The DC tilt of the IP support structure may reach 10^{-5} rad, which would be induced by crustal movement of the earth, human activities around the system and thermal deformation of the structure. It would induce payload displacement of tenths of millimeters and thus should be compensated by active control systems.

In an isolation platform supported by multiple IP legs, couplings by the ground tilt at high frequencies would be dominated by contribution from the rigid-body motion of the platform. Since the IP legs are rigid in the vertical direction, the ground tilt induces tilt of the platform in the same rotational DoF. When the measurement point is vertically separated from the center of platform rotation by a distance of d, the rotational displacement $d\theta$ directly couples to the displacement at the measurement point. Therefore the transfer function from the ground tilt becomes

$$H_{\mathrm{IP,tilt}}(\omega) = \frac{AC}{A-\omega^2} + d \tag{3.9}$$

in the frequency region where the IP legs and the payload can be regarded as rigid bodies. Figure 3.7 shows the amplitude of the transfer function with the coupling coefficient of $C = 30$ m/rad and $d = 50$ mm.

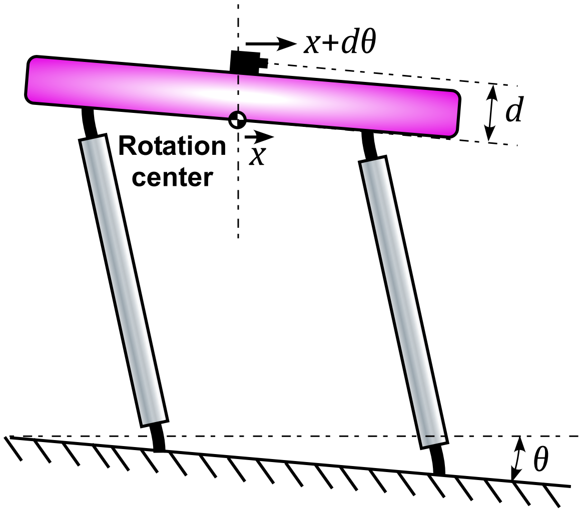

Figure 3.6: Ground tilt coupling through rigid-body motion of the platform.

3.3 Geometric Anti-Spring (GAS) Filter

3.3.1 Low-frequency vertical isolator

One of the major difficulties in designing vibration isolation systems for gravitational wave detectors is to achieve vertical attenuation performance comparable to that obtainable in the horizontal direction. For achieving low frequency seismic isolation one needs to implement soft springs, while at the same time the springs must support the weight of the suspended payload.

One solution to the problem is based on magnetic anti-spring technology [53], which has been implemented in the superattenuator for the Virgo detector. It utilizes permanent magnets faced each other in a horizontal plane with the same magnetic pole. These magnets produce a repulsive force and it transmits to the vertical direction as they are displaced vertically. This repulsive force works as an anti-spring force and reduces the effective stiffness of the vertical spring. A drawback of using the technology is that the resonant frequency fluctuates by temperature shift, since the magnetic field strength strongly depends on the temperature. Also the additional components such as permanent magnets and centering devices induce unwanted mechanical resonances around few tens of Hz, which degrade the attenuation performance in the detection band of gravitational waves.

A considerable improvement on the magnetic anti-spring is the Geometric Anti-Spring (GAS) technique [59], which allows increases of attenuation performance, thermal stability

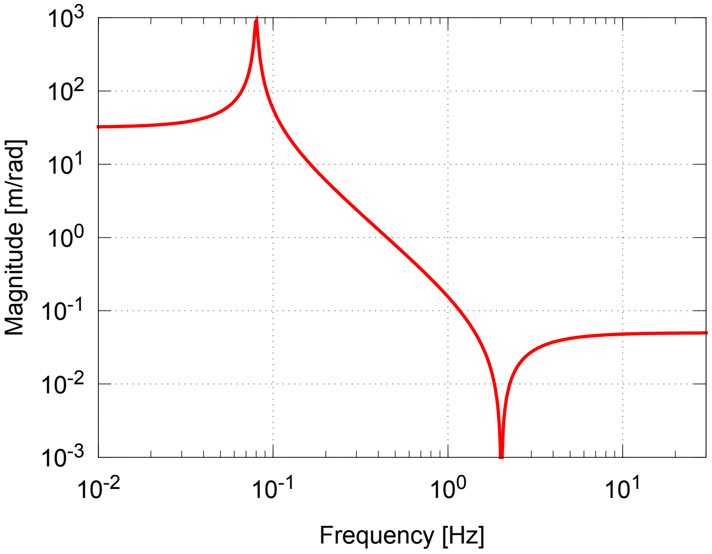

Figure 3.7: Expected ground tilt coupling of the IP as a function of frequency, assuming $C = 30$ m/rad and $d = 50$ mm.

and simplicity of the mechanics. This section briefly explains the mechanism and expected mechanical properties of the vertical isolator with GAS technology, called the GAS filter.

3.3.2 Basic working principle

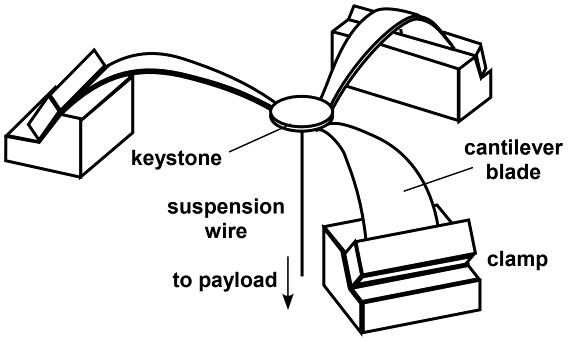

Figure 3.8: A schematic drawing of the GAS filter.

The GAS filter consists of a set of radially-arranged cantilever blades clamped on the base frame and to the central disk called the keystone. (figure 3.8). The blades are flat when they are manufactured and bend like fishing rods when they are loaded. The working principle of the GAS filter is mathematically described in reference [59], while its behavior can be understood by means of a simple analytical model shown in figure 3.9. In this model, a cantilever spring is represented as a combination of vertical and horizontal linear springs. Due to the symmetry of the system, one can simplify the model to a single blade model with the constraint that the tip of the blade moves only along the vertical axis.

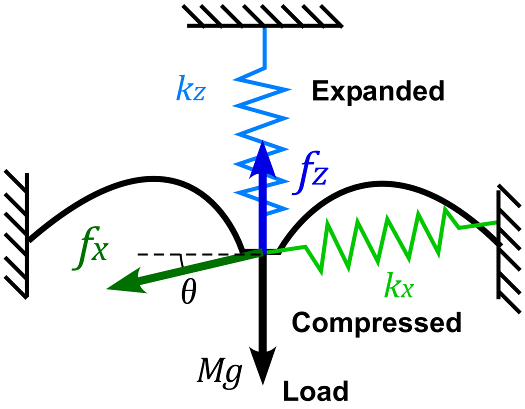

Figure 3.9: An analytical model of the GAS filter.

The payload of mass M is suspended by a vertical spring of elastic constant k_z and a horizontal spring of elastic constant k_x. The angle formed by the horizontal spring and the horizontal axis θ is zero when the tip of the blade is at the equilibrium position ($z = z_{\mathrm{eq}}$). Then the equation of motion in the vertical axis is written as

$$M\ddot{z} = -k_z(z - z_{\mathrm{eq}}) - k_x(l - l_{0x})\sin\theta, \tag{3.10}$$

where l is the actual length of the horizontal spring and l_{0x} is its natural length. Expanding the equation of motion around the working point z_{eq} to first order in z, one obtains the following linearized equation of motion:

$$M\ddot{z} = -\left[k_z - \left(\frac{l_{0x}}{x_0} - 1\right)k_x\right](z - z_{\mathrm{eq}}) = -k_{\mathrm{eff}}(z - z_{\mathrm{eq}}). \tag{3.11}$$

Here x_0 is the horizontal distance between the central keystone and the support point of the horizontal spring. When the horizontal spring is under compression ($x_0 < l_{0x}$), it causes a repulsive force in the vertical direction and therefore the effective spring constant is reduced from the spring constant of the vertical spring ($k_{\mathrm{eff}} < k_y$). This is the principle of the anti-spring effect in the GAS springs. The name of Geometric Anti-Spring stands for the fact that the anti-spring is realized by a specific geometry of the cantilever blade. The effective stiffness and the resonant frequency can be reduced by increasing the compression of the blades (decreasing x_0).

3.3.3 Quality factor

When the GAS filter is tuned toward lower resonant frequencies, its quality factor decreases progressively, as observed in the IP. Figure 3.10 shows measurement results of the quality factor versus resonant frequency of the GAS filters [60]. In contrast to the quality factor of the IP, the measurement data do not show quadratic behavior with the structural damping model. This indicates contribution of other damping mechanisms such as thermoelastic damping. One possible explanation of the behavior by the Self Organized Criticality (SOC) of the dislocation can be found in reference [61].

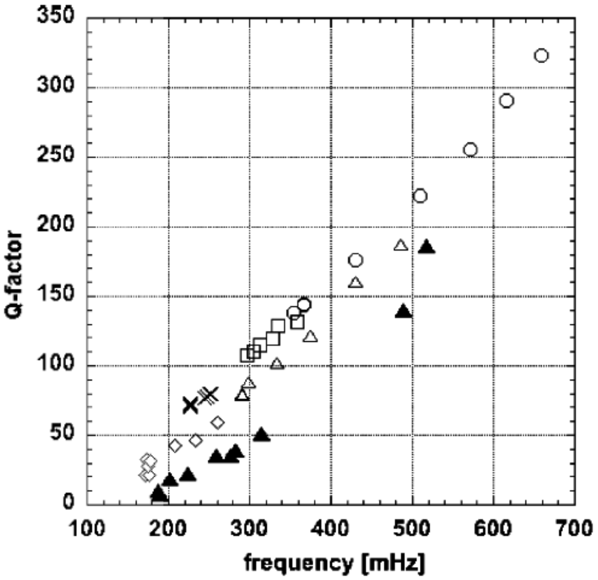

Figure 3.10: The measured quality factor versus resonant frequency of the GAS filters [60].

3.3.4 Attenuation performance

The transfer function of the GAS filter from the vertical displacement of the frame to that of the keystone is written in the same form as that of the IP, equation (3.5). Due to the CoP effect, the attenuation performance saturates at high frequencies and is typically limited to $\sim 10^{-3}$ (see figure 3.11). It can be compensated by adding a wand with a counter-weight in parallel with the blades, the so-called magic wand (figure 3.12), which allows the attenuation level to be improved down to 10^{-4} [62].

3.3.5 Thermal drift

The GAS filter achieves significant softness by balancing the anti-spring effect by horizontal compressive force and intrinsic vertical stiffness of the cantilever blade. Due to the softness, the vertical position of the keystone moves easily in response to a small change of the payload mass and the blade springs' physical properties. The thermal drift due to the temperature dependence of the Young's modulus of the spring material is an especially big issue in operating the GAS filter. If the GAS filter is balanced at the working point

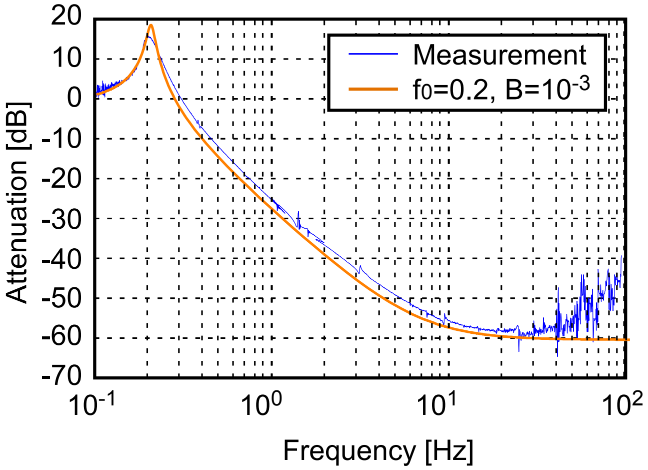

Figure 3.11: Attenuation performance of the GAS filter without the magic wand [62].

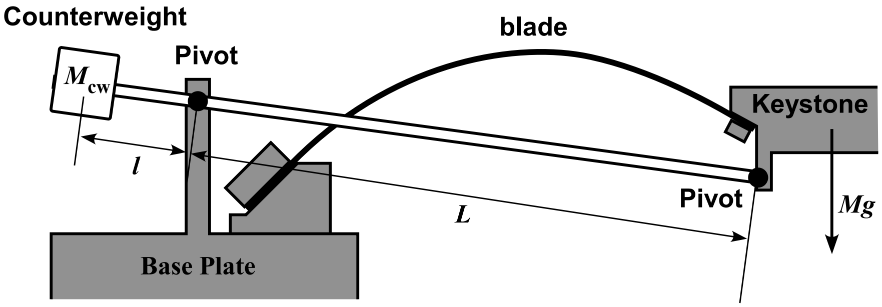

Figure 3.12: The magic wand used to compensate the CoP effect.

with a payload mass of M, the optimal load to keep the keystone at the working point is shifted with the temperature change by:

$$\varDelta M \approx \frac{M}{E}\frac{\partial E}{\partial T}\varDelta T. \tag{3.12}$$

Here E is the Young's modulus of the spring material and $\varDelta T$ is the shift of the temperature. For small perturbations, this change is equivalent to an additional force applied to the keystone, $\varDelta F = \varDelta M g$. Since the system has an effective spring constant of k_{eff}, the displacement caused by thermal shift is

$$\varDelta z = \frac{\varDelta F}{k_{\text{eff}}} = \frac{g}{E\omega_0^2}\frac{\partial E}{\partial T}\varDelta T. \tag{3.13}$$

Here the resonant frequency of the GAS filter is tuned at ω_0 and thus the effective spring constant is calculated as $k_{\text{eff}} = M\omega_0^2$. The system becomes more sensitive to the temperature change as the resonant frequency is reduced by the anti-spring effect. With typical parameters, the temperature dependence is

$$\frac{\varDelta z}{\varDelta T} = 0.69\ [\text{mm/K}]\ \left(\frac{0.33\ \text{Hz}}{\omega_0/2\pi}\right)^2 \left(\frac{\frac{1}{E}\frac{\partial E}{\partial T}}{3.0\times 10^{-4}\ [1/\text{K}]}\right). \tag{3.14}$$

3.4 SAS for gravitational wave detector

3.4.1 Various SASs in detector projects

The SAS technology has been adopted by several vibration isolation systems for gravitational wave detectors, such as HAM-SAS developed for Advanced LIGO [58], AEI-SAS for 10-m prototype detector in Hannover [63], and EIB-SAS and Multi-SAS for Advanced Virgo [64]. A rendering of one of the systems is shown in figure 3.13. They are designed to provide seismic attenuation for optical benches which various optics for the interferometers are fixed to or suspended. They provide 1-2 stages of seismic attenuation for all six DoFs of the bench rigid-body motions, with attenuation factors of 10^{-2}-10^{-6} in the detection band of gravitational waves.

A version of SAS that directly suspends the core optics of the interferometer was developed for TAMA and called the TAMA-SAS [55]. A schematic drawing of the TAMA-SAS is shown in figure 3.14. The TAMA-SAS provides 5-stage attenuation (including the IP stage) for the horizontal motions and 3-stage attenuation for the vertical motions to the suspended optic. The top stage supported by three IPs is actively controlled using position sensors and accelerometers. The internal modes of the suspension system are passively damped by an eddy-current damper just above the optic. The TAMA-SAS should provide enough seismic attenuation performance at 10 Hz so that the contribution from seismic noise gets much less than that from other fundamental noise sources.

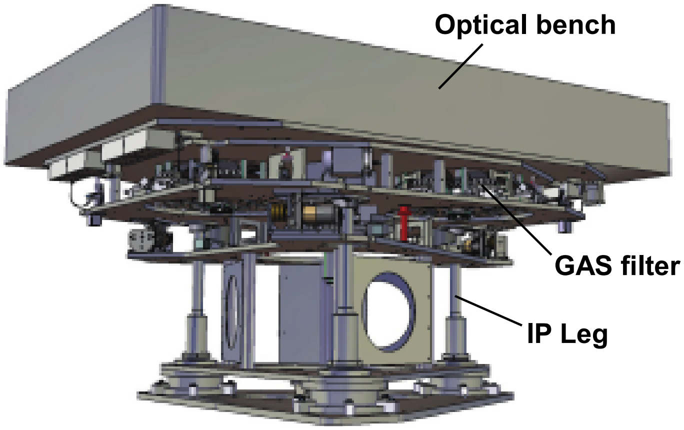

Figure 3.13: A rendering of the EIB-SAS developed for advanced Virgo [65].

3.4.2 Interferometer operation with TAMA-SAS

The vibration isolation systems for TAMA were replaced from conventional vibration isolation stacks to TAMA-SAS, and the interferometer started its operation with TAMA-SAS from 2006. Figure 3.15 shows the achieved displacement noise level of the detector and the noise budget. The noise level below 200 Hz was improved by introducing TAMA-SAS, owing to reduced alignment control noise of the interferometer. This was achieved by reduction of angular motion of the test mass in the 1-10 Hz band.

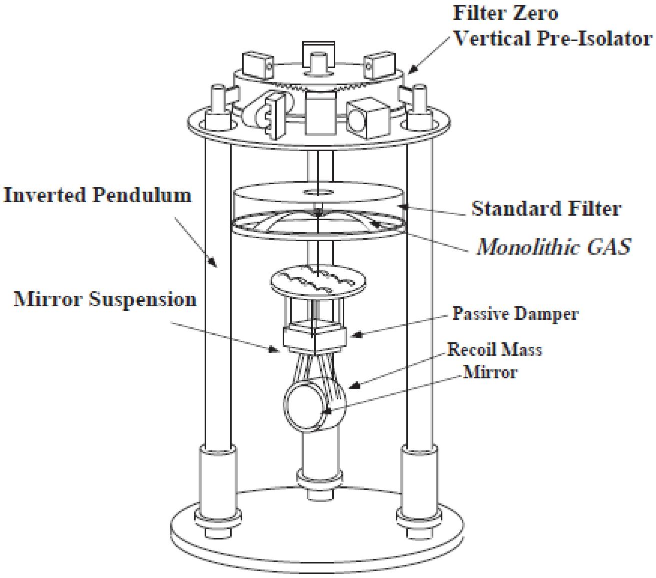

Figure 3.14: A schematic drawing of the TAMA-SAS [55].

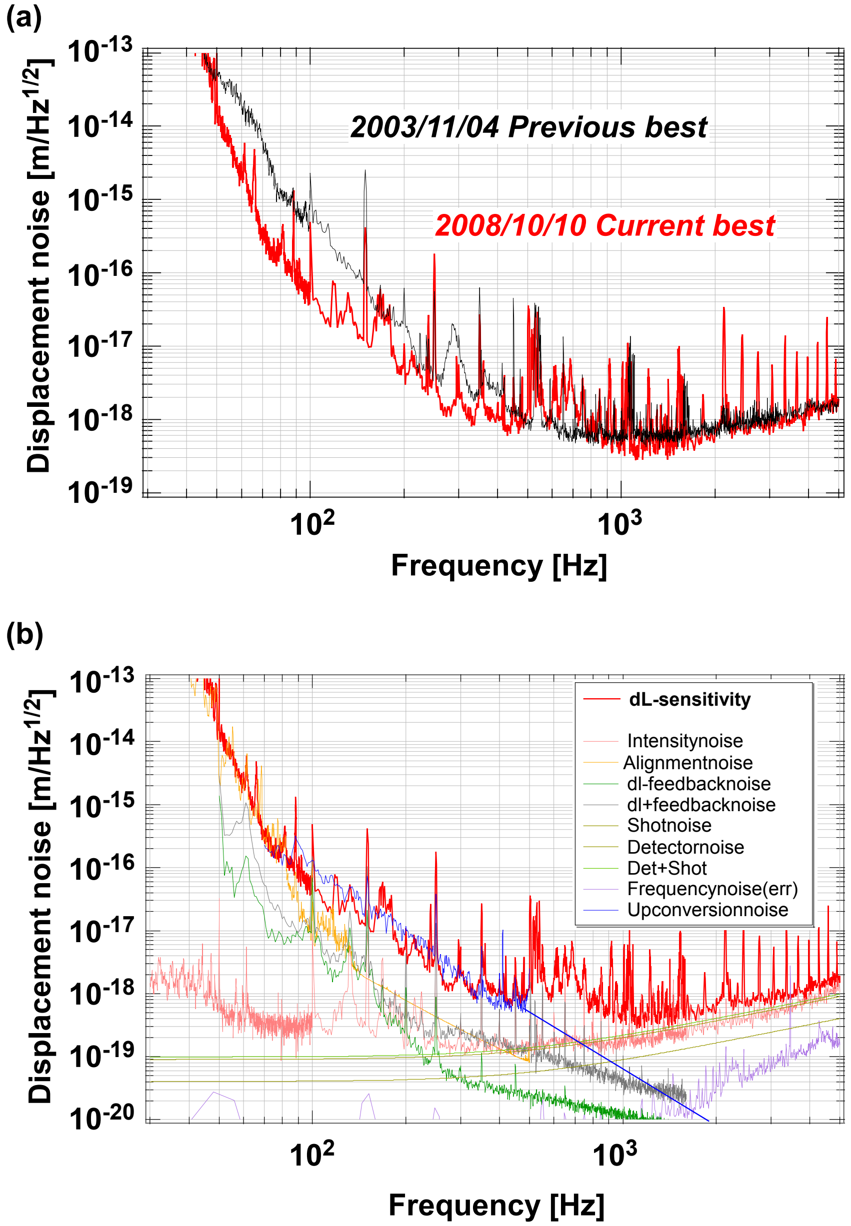

Figure 3.15: (a) Comparison of the detector sensitivity before and after the TAMA-SAS installation. (b) Noise budget of the interferometer with TAMA-SAS [24].

Although the noise level was improved by introducing SAS, the detector sensitivity of TAMA is still limited by technical noises rather than fundamental noises such as thermal noise and quantum noise. The main contribution in the 100-500 Hz band comes from upconversion, which is induced by feedback forces applied on the test masses in the low frequency band (< 1 Hz). The noise is expected to be related to acoustic noise emission from Nd-Fe-B magnets attached to the mirrors, due to discontinuous jumps of the magnetization (Barkhausen effect [66]). The alignment control noise limits the sensitivity below 100 Hz and further reduction of control bandwidth is required to expand the detection band of gravitational waves down to $\sim$10 Hz. Experience in TAMA indicates that it is essential to reduce low frequency fluctuation of the mirror displacements and angles with appropriate control loops. Otherwise, the attenuation performance of SAS is spoiled by control-noise couplings and upconversion noise.

Another finding from the operation of TAMA-SAS was that one has to make sure that all the low-frequency resonances are appropriately damped by passive/active damping mechanisms. In case of TAMA, the operation of the interferometer was often disturbed by yaw rotation of the suspended optics, which arises through excitation of the torsion modes of the suspension wires. Since the GAS filters and the lower stages are connected through single-wire suspensions, they form a multi-stage torsion pendulum with very low resonant frequencies (in the order of $\sim$ 10 mHz). The torsion modes have long decay times (in the order of 10^3-10^4 sec) unless they are appropriately damped. Consequentyly, TAMA-SAS retrofitted motion sensors to detect the torsion modes and actively damp them [67].

Seismic attenuation in KAGRA

Chapter 4

The previous section introduced the general concept of SAS and the basic working principles of the mechanical components. This section focuses on the SAS developed for KAGRA, the Japanese second-generation detector. As described in chapter 1, the second generation detectors aim to expand the detection band of gravitational waves toward ∼10 Hz in the low frequency region. To achieve this goal, KAGRA employs SAS technologies for core optics vibration isolation, based on the results obtained in the TAMA-SAS operation. This chapter describes the conceptual design of KAGRA-SAS, mechanical simulations for verifying the performance and some detailed design of mechanical components.

4.1 Basic requirement

4.1.1 General consideration

Seismic isolation systems for the core optics of the interferometric gravitational wave detectors must possess the following features in general:

- Passive attenuation of the seismic noise level well below the gravitational wave signal level or other noise levels in the detection band of gravitational waves.
- Suppression of the RMS velocity/displacement of the suspended optics, which are typically concentrated at low frequencies below 1 Hz, for fast lock acquisition and stable operation of the interferometer.
- Active/passive damping of low-frequency mechanical resonances for fast recovery from unwanted excitation states.
- Sufficient actuation range of the suspended optics to allow lock acquisition, alignment tuning and beam-spot optimization of the interferometer.
- Stability of the mechanics and active components to allow long-term observation of gravitational waves.

- Ultra-High Vacuum (UHV) compatibility so as not to degrade the detector sensitivity through the residual gas noise or contamination on the mirror surfaces.

This section mainly discusses the in-band requirement of the seismic attenuation performance at frequencies above $\sim$ 10 Hz. The out-band requirement below 10 Hz, damping capability and mobility of the optics will be further discussed in chapter 5.

4.1.2 Displacement noise requirement

As described in section 1.4, the second generation detectors employ dual-recycled Fabry-Perot Michelson interferometers for enhancing and optimizing the detector sensitivities. Differential length variation of the long Fabry-Perot cavities (the so-called DARM signal) contains gravitational wave information and thus it is the most important DoF in the gravitational wave detectors. Since the displacement noise of the test masses directly couples to the DARM signal, they have the strictest requirement on their displacement noise. Displacement noise of auxiliary optics also affects the detector sensitivity due to the couplings in the length sensing and control schemes of the interferometer [68], but to a much lower extent than the test masses.

Besides the seismic noise, the sensitivity of the interferometer is fundamentally limited by the thermal noise and the quantum noise (see figure 1.8). The goal of the vibration isolation system is suppressing the seismic noise level well below these noise levels in the detection band of gravitational waves. More specifically, the requirement for the seismic noise level is to be lower by a factor of 10 in amplitude spectrum densities than other noise levels in the frequency region above 10 Hz. Required displacement noise level of the core optics of the KAGRA interferometer in two different detection modes is shown in figure 4.1 [69]. KAGRA has two optional detection modes called BRSE (Broadband Resonant Sideband Extraction) and DRSE (Detuned Resonant Sideband Extraction) [32]. These two modes can be switched by changing the resonant condition of the signal recycling cavity. The DRSE mode has better sensitivity around 100 Hz, for detecting gravitational waves from binary neutron stars, but less in the high frequency region.

The maximum permitted displacement noise level at 10 Hz is summarized in table 5.3. It takes lower values of the displacement noise required in the two detection modes. The auxiliary optics are allowed to have larger displacement noise than test masses, by a factor of $\sim 10^2$ for the beam splitter and signal recyclers, and by a factor of $\sim 10^4$ for the power recyclers. Folding mirrors for the power/signal recycling cavity have stricter requirements than PRM/SRM, since their longitudinal displacement alters the cavity length by twice of the distance.

As described in chapter 2, 0.1-1% of the vertical motion is transferred to the longitudinal direction by mechanical cross-couplings, therefore vertical seismic attenuation is also required. Even without mechanical couplings, the vertical motion is coupled to the longitudinal direction at least by 0.3% in the KAGRA detector. This coupling comes from the fact that the KAGRA interferometer is not constructed in the horizontal plane for a practical reason. As there are many groundwater sources in the Kamioka mine (the site of

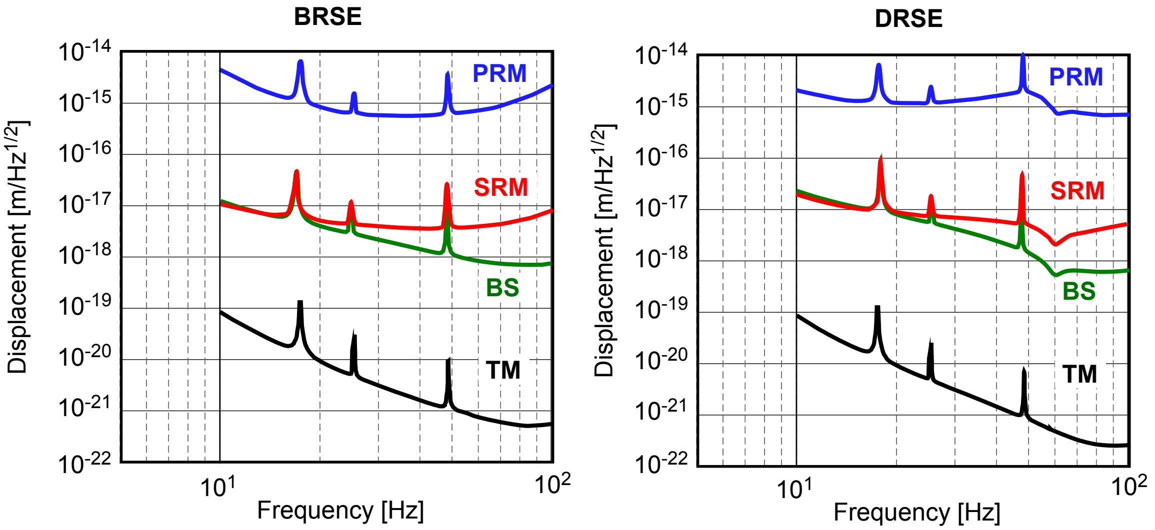

Figure 4.1: Longitudinal displacement noise requirements on core optics of the KAGRA interferometer, in two different detection modes. [69].

	spectrum density at 10 Hz
TM	1×10^{-19} m/$\sqrt{\text{Hz}}$
BS	1×10^{-17} m/$\sqrt{\text{Hz}}$
PRM	2×10^{-15} m/$\sqrt{\text{Hz}}$
PR2, PR3	1×10^{-15} m/$\sqrt{\text{Hz}}$
SRM	1×10^{-17} m/$\sqrt{\text{Hz}}$
SR2, SR3	5×10^{-18} m/$\sqrt{\text{Hz}}$

Table 4.1: Requirement on longitudinal displacement noise of the core optics for the KAGRA interferometer.

the KAGRA detector), the interferometer arm tunnels have been bored with a tilt of 1/300 for drainage. In the following discussion, vertical-horizontal coupling of 1% is assumed.

4.1.3 Seismic vibration in the Kamioka mine

KAGRA features an underground environment with very low seismic vibration as described in section 2.1. The seismic vibration in the Kamioka mine has been monitored over a long period as a joint research project of the Disaster Prevention Research Institute and Cryogenic Laser Interferometer Observatory (CLIO) [70] Project. Analysis of a 1.5-year (2009.9-2011.2) data of ambient seism motion, taken by a Güralp CMG-3T seismometer located at the CLIO site, gives the noise spectrum models shown in figure 4.2.

The plots below 1 Hz show measured seismic spectra at the 10, 50 and 90th percentile levels and the spectra above 1 Hz are fitted curves proportional to f^{-2}. The seismic

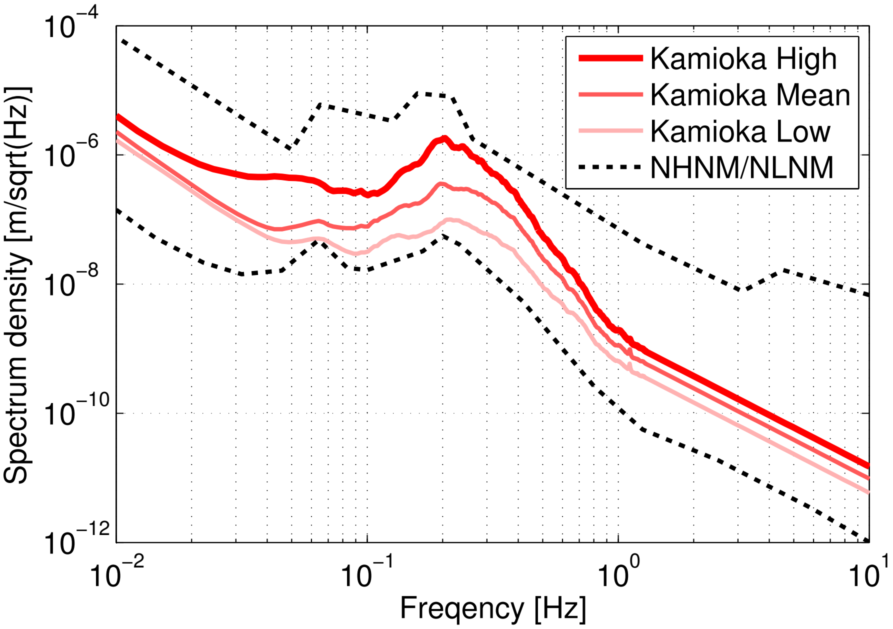

Figure 4.2: Seismic vibration spectrum of the Kamioka site.

spectrum around the microseismic peak widely spreads in magnitude, since the amplitude highly depends on the oceanic activities and thus on the weather conditions. The RMS displacement of the seismic motion (integrated down to 10^{-2} Hz) varies from 0.08 to 0.5 μm, in the 10-90 percentile range. Although CMG-3T is not sensitive enough to measure the seismic vibration of the Kamioka site in the high frequency region above 1 Hz, another measurement set out with a Trillium 240 seismometer confirms the displacement spectrum in proportion to f^{-2} at high frequencies. More details on the analysis of the seismic spectrum measurement in the Kamioka mine are described in reference [71]. In the following investigation, the high noise model in figure 4.2 is taken as the seismic vibration for a conservative estimate.

Since the seismic vibration level of the Kamioka site is $\sim 10^{-11}$ [m/$\sqrt{\text{Hz}}$] at 10 Hz, required attenuation ratio at that frequency is roughly 10^{-8} for the test masses, 10^{-6} for the beam splitter and signal recycling mirrors, and 10^{-4} for the power recycling mirrors.

4.2 System Overview

4.2.1 Conceptual design

To meet the requirements described above, KAGRA employs several types of suspension systems for the core optics depending on the required seismic attenuation levels. The conceptual designs of three types of KAGRA-SAS are illustrated in figure 4.3 and their disposition is shown in figure 4.4. Table 4.2 shows their basic specifications.

The largest suspension system, the so-called type-A SAS, provides 8 stages of horizontal attenuation and 6 stages of vertical attenuation for the test masses. To take advantage of the underground environment, the type-A SAS is constructed in a separately bored tunnel at a higher elevation and the base of the suspension system sits directly on the upper floor. The IP stage at the top of the chain provides pre-isolation and static control of the whole suspension system. The attenuation chain resides inside a borehole of 1.2 m diameter and

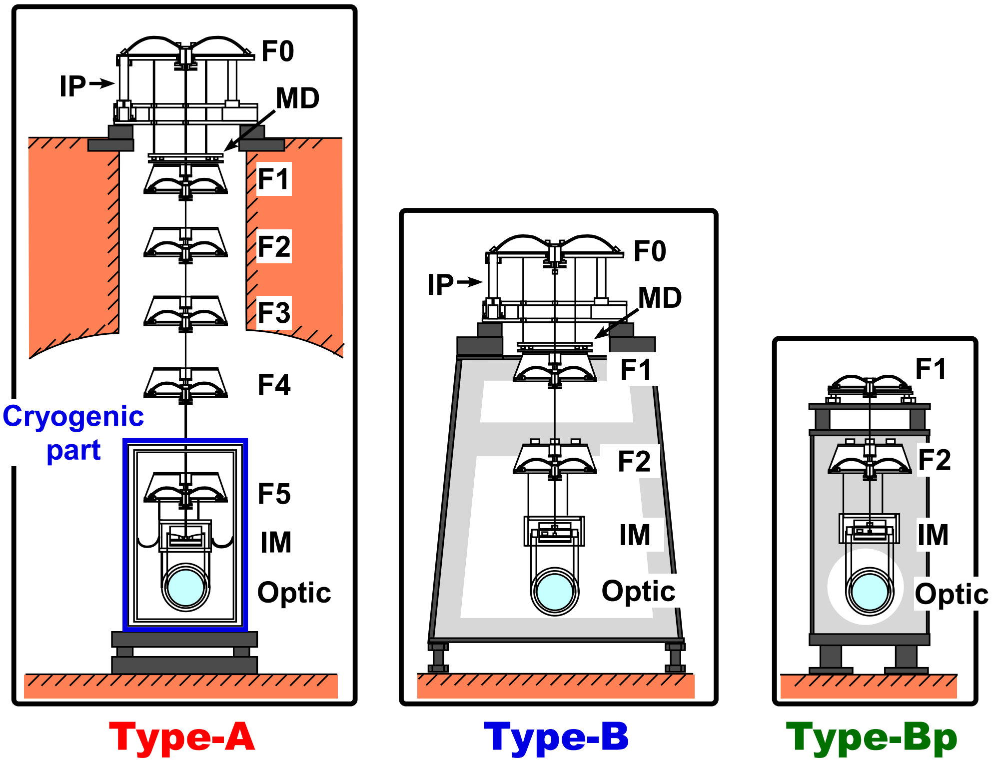

Figure 4.3: Conceptual designs of SAS for the KAGRA detector. The vacuum envelopes are not illustrated for simplicity. F0-F5 denote the GAS filters for vertical seismic attenuation. MD represents the magnetic damper, which is placed just above F1 and aims to damp the torsion modes of the attenuation chain. IM represents the intermediate mass, from which the optic is hung with suspension wires.

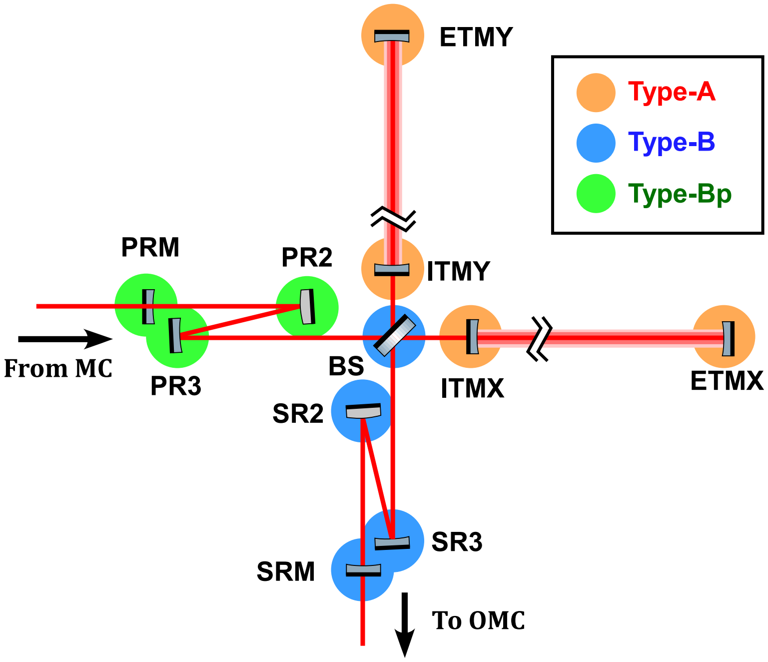

Figure 4.4: Disposition of SAS in the KAGRA main interferometer.

connected to the mirror suspension located in the lower tunnel. Several lower stages are cooled down to cryogenic temperature for thermal noise reduction. The cryogenic part is covered with aluminum boxes to shield black-body radiation from room temperature components.

The type-B SAS, used for seismic isolation of the BS and signal recycling mirrors, has smaller number of attenuation stages and a room temperature payload. The base of the suspension system sits on an external support frame enveloping the attenuation chain. The support frame is supposed to be a rigid structure and transmit the seismic vibration to the suspension system directly. However, in practice, it has inevitable mechanical resonances and thus enhances the vibration entering the suspension system. The type-B SAS also has the IP stage for pre-isolation and static control of the suspension chain, as for the type-A SAS. Three stages of GAS filters provide vertical seismic attenuation in the detection band of gravitational waves. The optic is suspended from the penultimate stage, called

	Type-A	Type-B	Type-Bp
suspended optics	TM	BS, SRM, SR2, SR3	PRM, PR2, PR3
horizontal stage #	8 (include IP)	5 (include IP)	3
vertical stage #	6	3	2
payload temperature	cryogenic (< 20 K)	room-temperature	room-temperature

Table 4.2: Basic specification of three types of KAGRA-SAS.

the intermediate mass, by two loops of wires. It works as a marionette and the alignment of the optic can be adjusted through rotating the intermediate mass.

The type-Bp SAS is a reduced version of the type-B SAS used for the optics in the power recycling cavity. Although the power recyclers were to have employed the type-B SAS in the preliminary design of the KAGRA detector, their suspension systems were reduced due to budgetary constraints. The type-Bp system does not contain the pre-isolation stage with IP and has only two stages of GAS filters for vertical isolation. In order to control the horizontal static position of the suspended optic, a motorized stage called the traverser is implemented on the top of the chain. This system however does not provide pre-isolation of horizontal vibration in contrast to the IP stage, and thus the suspended optics are expected to suffer from large RMS displacement/velocity.

4.2.2 Expected isolation performance

The seismic attenuation performance of the KAGRA-SAS was calculated by mechanical simulation with rigid-body models [72]. The rigid-body modeling treats the suspension system as a combination of rigid-bodies and elastic elements connecting with them. The rigid-body approximation is valid only at low frequencies ($\lesssim 50$ Hz in KAGRA-SAS), and thus one has to keep in mind that the predicted performance can be degraded to some extent in the high frequency region due to internal resonances of the suspension components. Details of the modeling and the parameters of the suspension systems are further described in appendix A.

Figure 4.5 shows the predicted displacement noise level of the suspended optics with the three types of KAGRA-SAS in comparison with the requirement. The seismic vibration curve assumes the high noise model of the Kamioka site as described in section 4.1. The graphs show the displacement noise spectra of the ground vibration, horizontal vibration of the suspended optics, contribution from the vertical vibration of the optics assuming 1% vertical-longitudinal couplings, and the requirements described in section 4.1. Since the systems have a smaller number of attenuation stages in the vertical direction, the couplings from vertical vibration dominate the displacement noise at high frequencies ($\gtrsim 2$ Hz for type-A and type-B, and $\gtrsim 10$ Hz for type-Bp). The suspension systems meet the seismic attenuation requirement in the frequency region above 10 Hz, and even widen the detection band toward the few-Hz level. The type-A SAS has a safety margin of roughly 8 orders of magnitude at 10 Hz, and others have safety margins of 2 orders of magnitude. Taking into account that attenuation performance is degraded by internal resonances above 50 Hz, it is prudent to have large safety margins in that frequency region.

4.3 Detailed mechanical design

This section describes more details of the mechanical designs of the suspension components of KAGRA-SAS. The isolation system can be generally divided into the following three distinct parts:

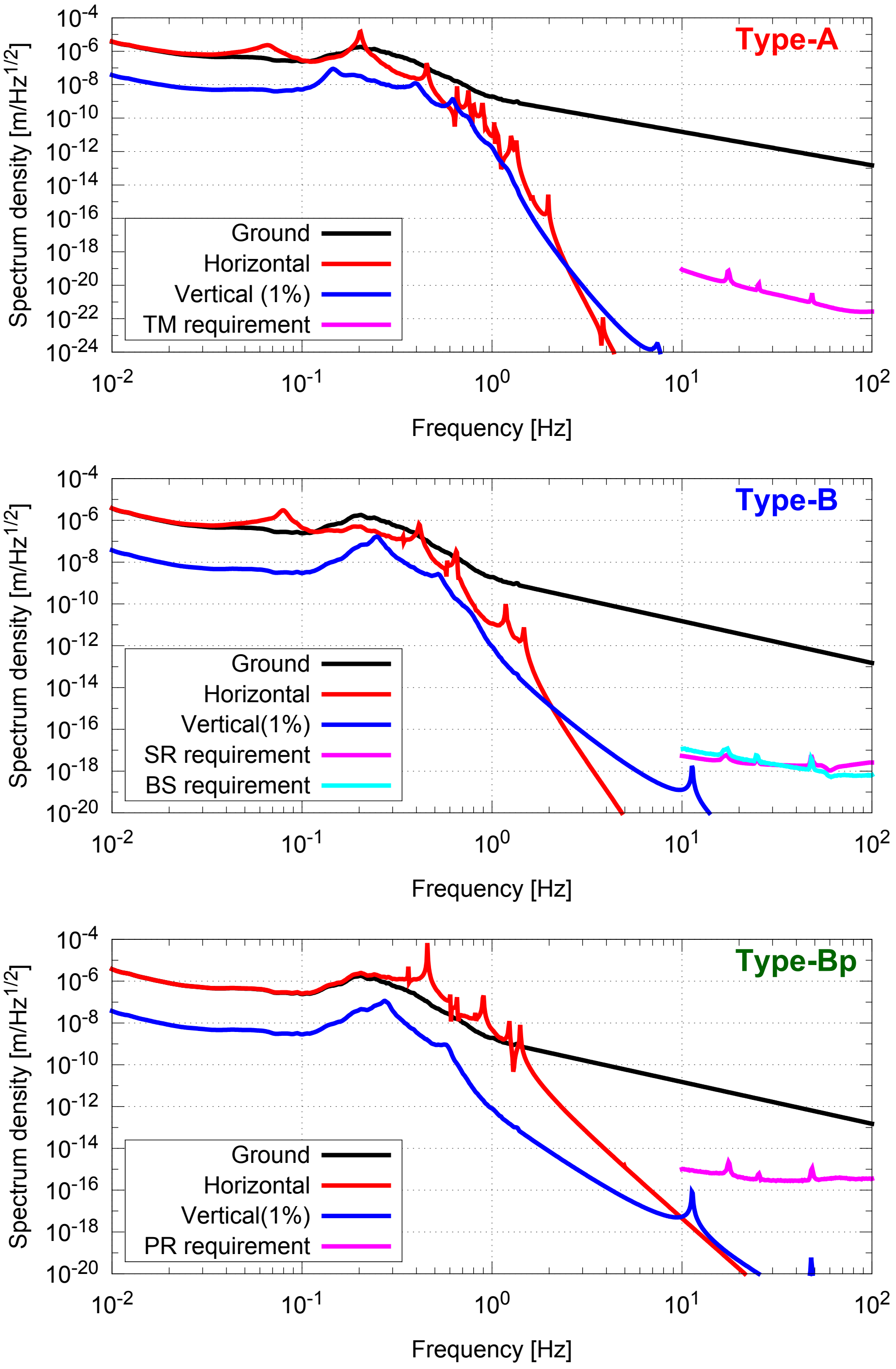

Figure 4.5: Predicted seismic attenuation performance of the three types of KAGRA-SAS in comparison with the requirement.

1. The pre-isolation and static-control stage at the top of the chain.
2. The chain of mechanical filters to achieve the required seismic attenuation.
3. The mirror suspension providing control forces for lock acquisition and alignment.

Although there is no actual physical separation, the first and second parts are conventionally known as SAS, and the last part is often called the payload of the seismic attenuation chain. The first part comprises the IP stage in the type-A and type-B, while the type-Bp system has instead a motorized stage called the traverser at the top of the chain for static-control. The second part comprises the cascaded GAS filters in all the systems. The design of the third part (payload) is substantially different in the type-A and other systems, since the payload in the type-A SAS has to be cooled down for thermal noise reduction.

4.3.1 IP pre-isolation stage

This stage is in charge of seismic attenuation starting from ~ 0.1 Hz and static control of the suspension point position and yaw orientation of the chain. Figure 4.6 shows the overview of the pre-isolator. The stage is supported from the ground or the support structure by three IP legs, which provide seismic attenuation in the horizontal plane. At the top of the stage, there is a large GAS filter for vertical seismic attenuation. It is twice as large in diameter as the lower GAS filters, and called the top filter or the Filter 0 (F0). In order to achieve seismic attenuation at the microseismic peak (0.2-0.5 Hz) and reduce the RMS amplitude of the mirror displacement, the IP is tuned at resonant frequencies lower than 0.1 Hz.

The horizontal motion of the top stage is controlled by the use of three single-axis seismometers, three Linear Variable Differential Transducers (LVDTs) [73] and three coil-magnet actuators [74]. The LVDT measures the relative motion of the stage with respect to an external frame fixed to the ground, while the seismometer measures the acceleration of the top stage with respect to an inertial frame. The static position of the top stage is tuned using three motorized springs with thin cantilever blades. The design of the control system is essentially the same as developed for the TAMA-SAS and the Virgo Superattenuator [75, 76].

Mechanical design of IP

The IP for the KAGRA-SAS is essentially a copy of that for the HAM-SAS (developed for the Advanced LIGO detector) [58]. Figure 4.7 shows the cross section view of an IP leg. An aluminum pipe with 1 mm thickness and about 50 cm length is supported from the base structure with a thick metal pillar which works as a flexure providing the elastic stiffness of the IP. The isolation stage is suspended from the top of the pipe by a thin flexure with 3 mm diameter. The flexures are made of maraging steel [77], which is known for possessing superior strength and a particularly good creep characteristic [78]. The lightness of the leg (about 0.2 kg) mitigates the saturation of the attenuation performance due to the CoP effect (see section 3.2). The attenuation ratio naturally reaches $\sim 10^{-3}$ and can be improved to 10^{-5}-10^{-4} by introducing counter weights.

The length and thickness of the bottom flexure are tuned to match the critical load of the IP to the weight of the suspension system. The bending stiffness of the flexure is calculated by the following formula:

$$k_\theta \approx \frac{\pi E d^4}{32\ell}, \tag{4.1}$$

where ℓ and d represent the length and diameter of the cylinder respectively, and E is the Young's modulus of the flexure material. Since the spring constant is proportional to the fourth power of the diameter, the critical load of the IP dramatically increases as the flexure thickness increases. The IP in the KAGRA-SAS utilizes flexures of about 10 mm in diameter and about 50 mm in length, which results in about 1000 kg optimal load with three flexures.

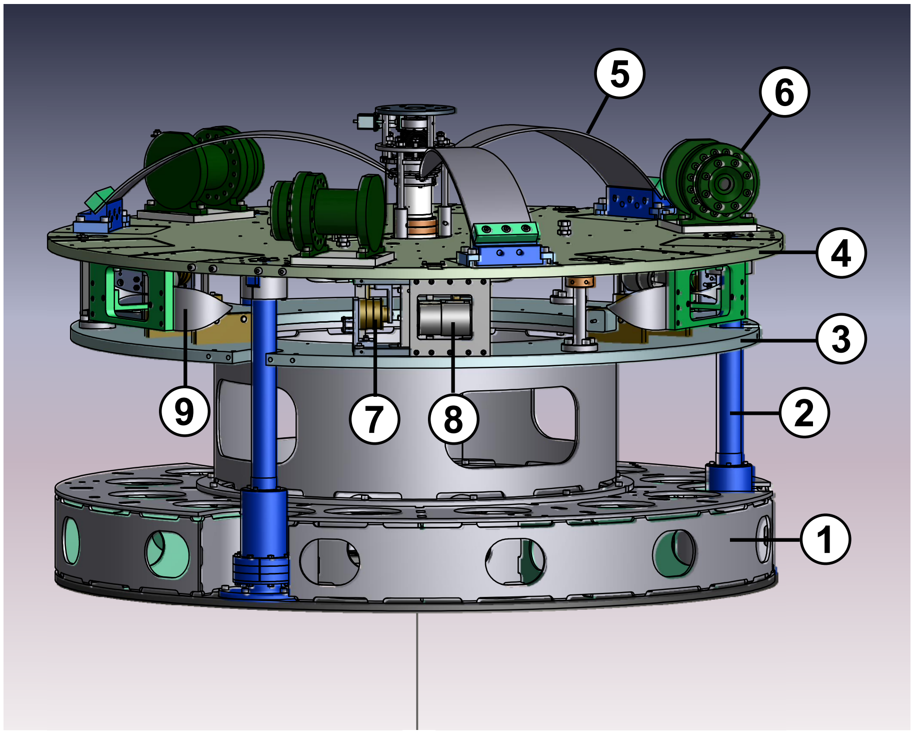

Figure 4.6: A 3D CAD drawing of the pre-isolator. 1) The base ring, 2) the IP leg, 3) the coil support frame rigidly connected to the base ring, 4) the top stage isolated by the IP, 5) the top filter for vertical isolation, 6) the seismometer (L-4C geophone) capsulated in the vacuum canister, 7) the Linear Variable Differential Transducer (LVDT), 8) the coil-magnet actuator, 9) the motorized spring for the static position control of the top stage, 10) the locking and range-limiting screw.

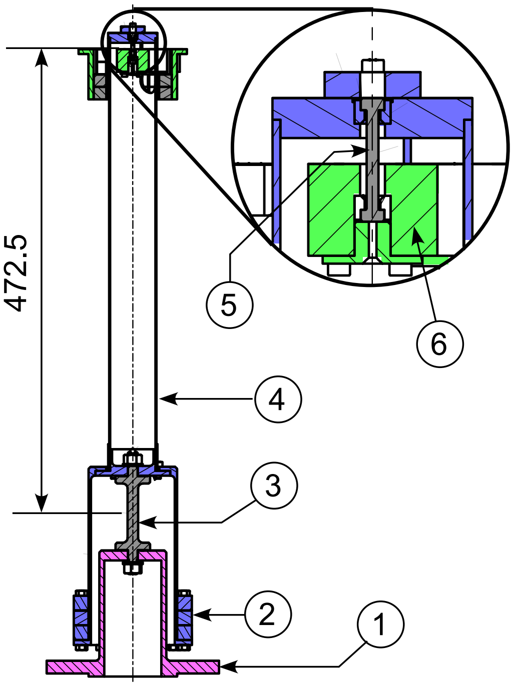

Figure 4.7: A cutaway drawing of the IP leg. 1) The support structure of the IP, 2) the counter-weight for compensating the CoP effect, 3) the main flexure of the IP, 4) the IP leg; an aluminum pipe with 1 mm thickness, 5) the top flexure, 6) a metal block rigidly connected to the top stage.

4.3.2 GAS filter chain

Standard GAS filter

In order to achieve the required seismic attenuation both in horizontal and vertical directions, a chain of standard GAS filters is suspended from the top stage. A drawing of the filter is shown in figure 4.8. Each GAS filter is suspended by a single wire, and its suspension points are placed nearby to its center of mass. In this configuration, the motion of the filter is attenuated in every translational and rotational DoF. The cantilever blades and the suspension wires are made of maraging steel [77] as well as the IP flexures, to avoid creep under highly stressed conditions. The cantilever blades are clamped to the base plate at a 45° inclination and their tips are attached to the central keystone with an incidence angle of $-33°$. The relative position of the keystone and the outer frame is controlled by the use of an LVDT and a coil-magnet actuator. The static position can be tuned by a motorized spring with a thin cantilever blade.

Blade design

The width and number of the cantilever blades are adjusted so that the optimal load of the GAS filter coincides with the weight of the payload. The shape and dimension of a cantilever blade for the standard GAS filter are shown in figure 4.9. The blades are designed to have uniform stress distribution in the working configuration. All the GAS blades in the KAGRA-SAS have a similar shape to the standard one, while the overall size is adjusted depending on the required load. The optimal load of a GAS blade is estimated

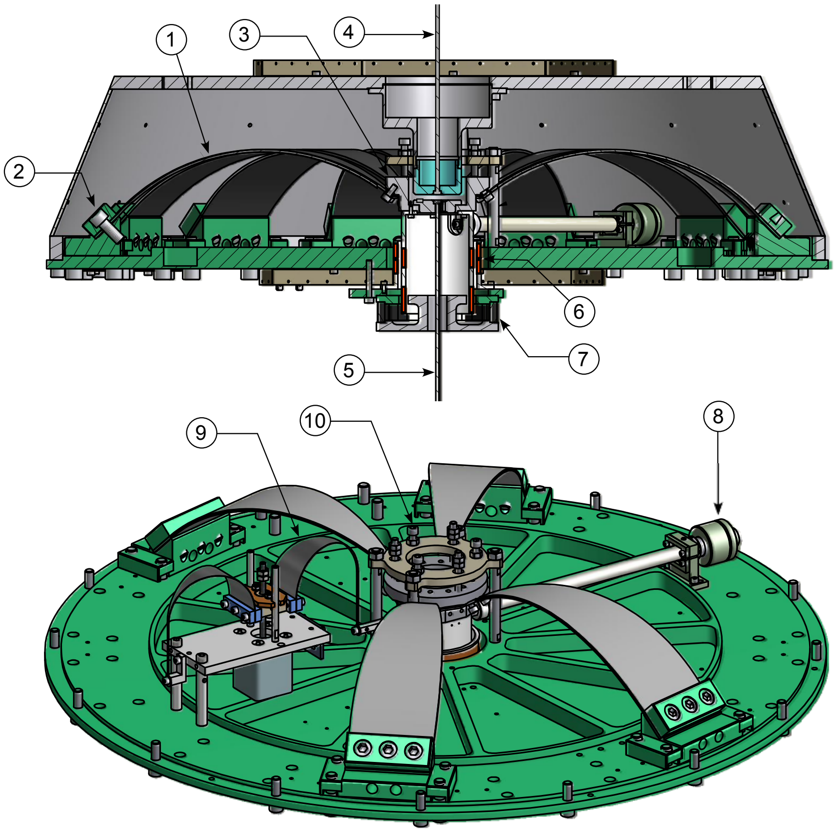

Figure 4.8: A cross section view of the standard GAS filter and the oblique view without the cap. 1) The cantilever blade, 2) the blade clamp, 3) the keystone, 4) the upper suspension wire, 5) the lower suspension wire, 6) the LVDT to measure the displacement of the keystone, 7) the coil-magnet actuator, 8) the magic-wand for compensating CoP effect, 9) the motorized spring for static-positioning of the keystone, 10) the locking and range-limiting screws.

to be [59]

$$F_{\text{opt}} = G\frac{Et^3w_0}{12L^2}, \tag{4.2}$$

where t, L and w_0 represent the thickness, length and base width of the cantilever blade. E is the Young's modulus of the blade material. G is the geometry factor depending on the blade shape, which is 1.71 in the standard blade. Note that the surface stress σ is proportional to the thickness and inversely proportional to the length ($\sigma \propto t/L$) and thus the blade is normally designed to keep this ratio constant.

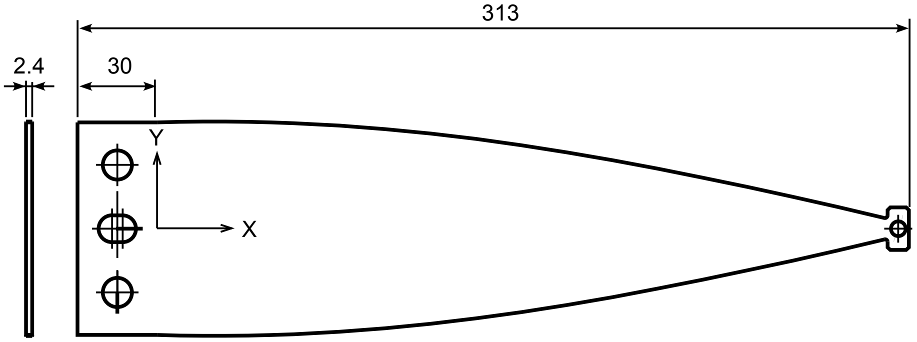

X	Y
0.00	40.00
27.26	40.31
54.52	39.58
81.78	37.84
109.04	35.13
136.30	31.53
163.56	27.15
190.82	22.12
218.08	16.57
245.34	10.67
273.80	4.01

Figure 4.9: Dimension of the standard GAS blade.

The following figures show the mechanical simulations of the standard GAS blade using Finite Element Analysis (FEA). Figures 4.10 shows the load on the blade versus the vertical position of the tip (keystone) with various horizontal compressions. x/L denotes the horizontal distance between the base and tip of the blade, normalized by the blade length. The slope of the curve gets steep around the optimal load (39.5 kg) and the steepness increases as the horizontal compression increases (x/L decreases). In the steep region, a small change of vertical force induces a large vertical movement around the equilibrium point, and thus the spring has a small restoring force. The gradient diverges with the critical compression $x/L = 0.896$ and the spring shows a bistable characteristic with further compression. Figure 4.11 shows the stress distribution in a standard GAS blade at the optimal working point. The maximum stress on the top surface of the blade reaches 1.7 GPa, which is lower than the tensile strength of maraging steel (2.0 GPa).

Torsion mode damping

The attenuation chain of single-wire suspensions forms a multi-stage torsion pendulum with very low resonant frequencies (in the order of 10 mHz). Although the yaw motions of the attenuation chain are isolated well in this configuration, these modes naturally have long decay time due to their high quality factors ($\gtrsim 100$) and thus the filters will keep

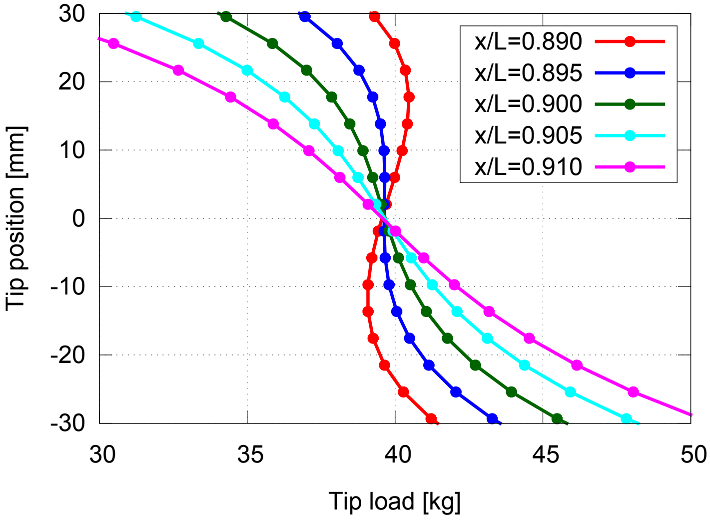

Figure 4.10: The equilibrium points of a GAS blade as a function of the vertical load predicted from an FEA. Several loci with various horizontal compressions (x/L) are plotted.

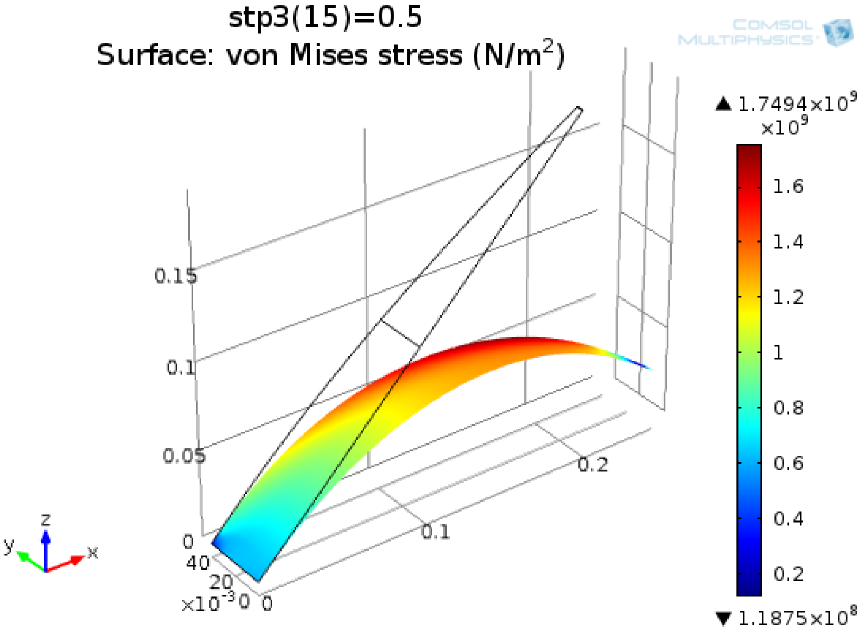

Figure 4.11: The top-surface stress distribution of a standard GAS blade at the optimal working point with horizontal compression of $x/L = 0.900$, calculated by COMSOL Multiphysics. The image only shows half of the blade, which is symmetric with respect to the xz plane.

oscillating once these modes are excited. So as not to disturb the interferometer operation by these motions, the torsion modes are passively damped by eddy-current dampers. The conceptual design of the torsion mode damper is illustrated in figure 4.12. A disc with a number of permanent magnets is suspended from the pre-isolation stage by three wires and placed just above the first standard filter (written as F1). A conductive plate attached to F1 and the permanent magnets attached to the damper produce breaking torque between the damper and F1.

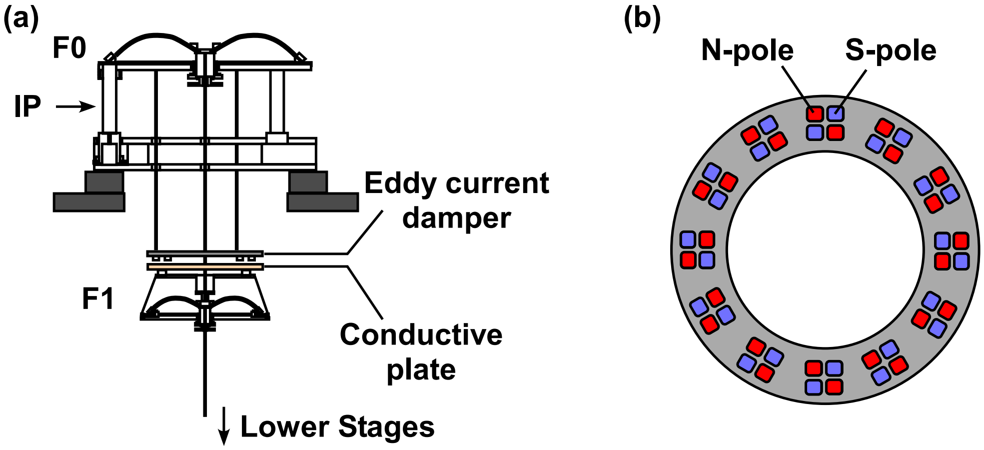

Figure 4.12: (a) Disposition of the eddy current damper in the type-A and type-B attenuation chain. (b) A bottom view of the eddy current damper showing the arrangement of the permanent magnets.

The thickness of the suspension wires is adjusted so that all the torsion modes are coupled to the movement of F1 and effectively damped by the eddy current damper [72]. The torsional stiffness constant of a suspension wire is expressed as

$$k_{\mathrm{t}} = G\frac{\pi d^4}{32L}, \tag{4.3}$$

where d and L are the diameter and length of the wire, and G is the shear modulus of the wire material. Although the torsional stiffness of the wires can be increased by thickening them, wires with large thickness may possibly degrade the horizontal attenuation performance of the suspension system due to the bending elasticity [79]. The bending elasticity of a wire depends on the wire thickness in the first few cm from the suspension points, while the torsional stiffness depends on the thickness integrated over the wire length. Therefore, the wires are designed with large thickness in the middle and small thickness at the ends as illustrated in figure 4.13. The suspension wire is hooked to the suspension bodies by the nail head shapes machined into both ends of the wire.

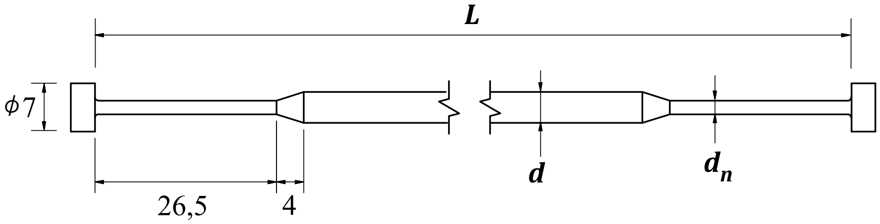

Figure 4.13: Design of the suspension wire.

4.3.3 Mirror suspension (payload)

This part is located at the very bottom of the attenuation chain. It precisely controls the mirror position and orientation and provides additional seismic attenuation. As it holds directly the optics of the interferometer, the pyaload must be carefully designed so that it does not generate thermal noise or acoustic noise above the acceptable level.

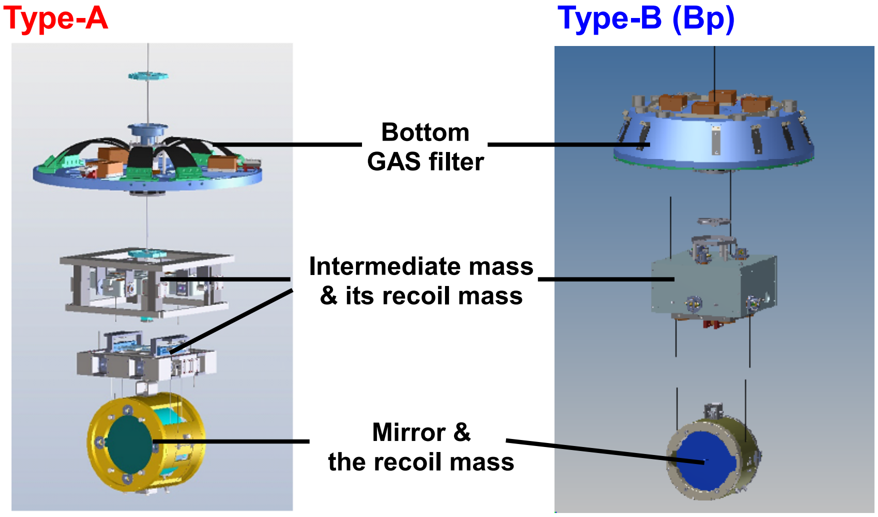

Figure 4.14: Renderings of the payloads in the type-A and type-B systems.

Figure 4.14 shows renderings of the payloads in the type-A and type-B systems. The mirror is suspended from the penultimate stage, called the intermediate mass, by four wires, and the intermediate mass is suspended from the bottom GAS filter by a single wire. This configuration allows us to adjust the mirror orientation by rotating the intermediate mass like a marionette. The control force and torque are exerted onto the mirror from the coil-magnet actuators on its recoil mass, which is also suspended from the upper stage. The intermediate recoil mass hanging from the bottom GAS filter is added to provide actuation to the intermediate mass. A two level control is necessary because only very delicate forces can be applied on the mirror, while larger authority can be applied on the intermediate mass. The concept of using a recoil mass (reaction mass) hung in parallel to the mirror suspension was introduced in the Virgo last-stage suspension system [80] and adopted in TAMA-SAS [81]. There are several technical advantages of using a recoil mass:

- The actuator is isolated from seismic disturbance, and therefore the fluctuation of the actuation efficiency due to the change of the relative position between the mirror and actuation mass is suppressed.
- The actuation on the mirror is isolated from the upper stages, because the reaction from the mass and its recoil mass compensate each other at the upper stage. It simplifies the servo design for the control.

The recoil mass for the intermediate mass is equipped with actuators and position sensors to control the motion of the intermediate mass. In the type-B system, Optical Sensor and Electro-Magnetic actuator (OSEM) [82], similar to developed for Advanced LIGO, will be used for the position sensing and controls.

Cryogenic issues

In type-A system, the payload is cooled down to cryogenic temperature to reduce the thermal noise. In order to transfer the heat absorbed in the mirror from the laser beams, the test mass is suspended by four sapphire fibers with 1.6 mm diameter and 350 mm length. The heat is transferred to the upper stage, and then finally transferred to the inner shield of the cryostat via heat links made of pure aluminum [83]. The heat flow in the cryogenic payload is illustrated in figure 4.15. Due to the large thickness of the sapphire fibers, the mirror suspension is significantly stiff in the vertical direction, which results in large suspension thermal noise in the detection band of gravitational waves. In order to mitigate the vertical stiffness, blade springs made of sapphire are designed and used in the mirror suspension, which lowers the vertical bounce mode frequency to $\sim$14 Hz [84].

Since the heat links are mechanically connected to the cryostat, which is firmly fixed to the ground, extra vibration from the cryostat is introduced to the suspension system through the heat links. Although the heat links are loosely connected so that they do not provide much DC stiffness, the vibration transmissivity is enhanced at high frequencies by the internal resonances of the wires. Figure 4.16 shows the calculated vibration transmissivity of an aluminum wire configured in a semi-ellipsoidal shape, assuming that the wire is attached to a 50-kg mass. The resonant peaks appearing above 4 Hz affect the transmissivity and result in 10^{-3}-10^{-4} vibration transmission in the detection band of gravitational waves.

Figure 4.17 shows the estimated displacement noise level of the test mass due to the vibration transmission via heat links. The simulation assumes that the intermediate recoil mass and the cryostat inner shield are connected by eight aluminum wires with the same parameters as assumed in figure 4.16. It also assumes that the vibration of the cryostat is at the same level of the ground vibration. The vibration from the cryostat exceeds the vibration from the upper floor at frequencies above 1.5 Hz, and the coupling from

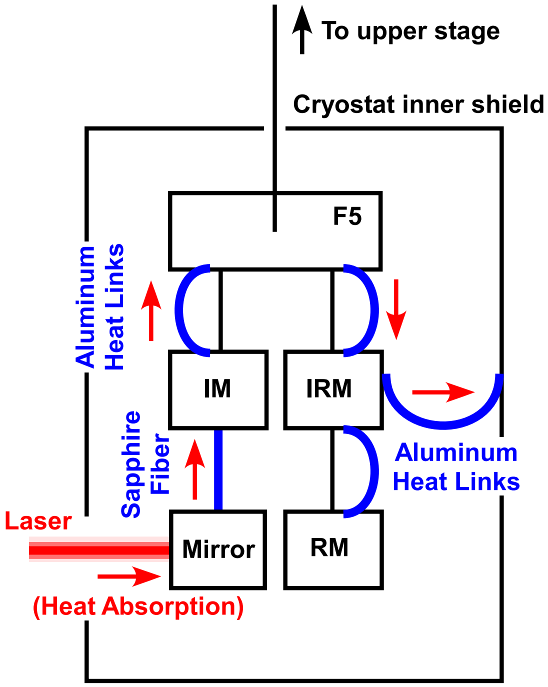

Figure 4.15: Schematic heat-flow diagram in the cryogenic payload.

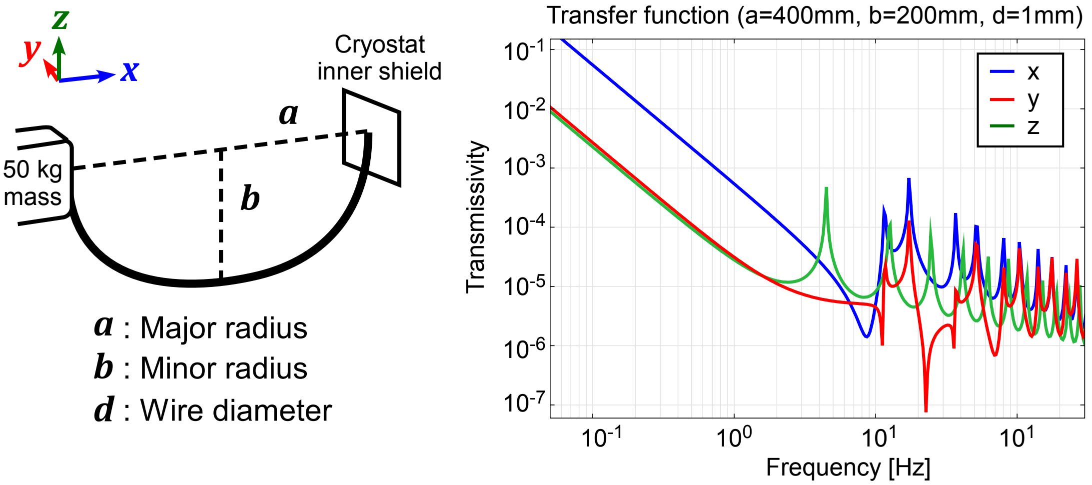

Figure 4.16: An illustration of the heat link wire and its vibration transmissivity predicted from an FEM analysis using COMSOL Multiphysics.

the vertical vibration exceeds the required noise level in the detection band. Note that vibration of the cryostat may be enhanced due to its internal resonances and cryocooler operations by 1-2 orders of magnutude in the detection band, as observed in the CLIO cryostat [85]. It means that vibration from the heat links needs to be further suppressed by 3-4 orders of magnitude in the detection band. This can be achieved by pre-isolating the heat link vibration before connecting to the suspension system, with 2-3 attenuation stages having few-Hz natural frequencies. The pre-isolation system for the heat links is currently under development.

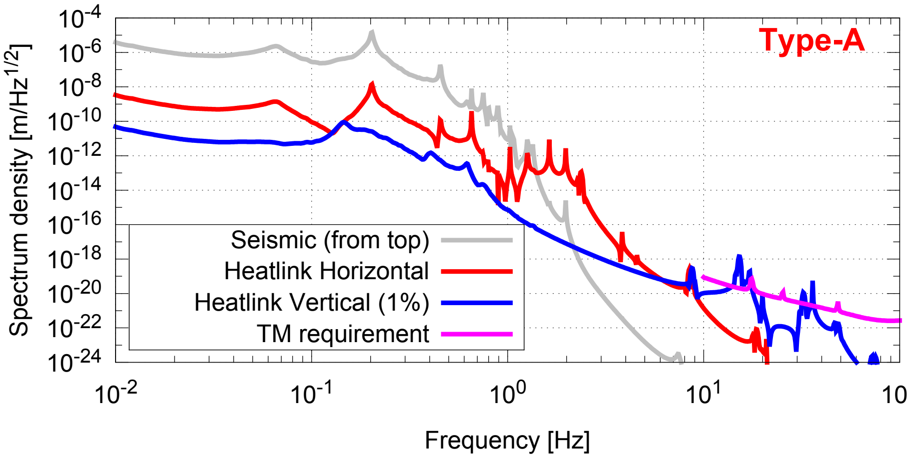

Figure 4.17: Impact of vibration transmission via heat links in the type-A SAS.

Active suspension controls

Chapter 5

The previous section explained the mechanical design and passive attenuation performance of the KAGRA-SAS. This section focuses on the active control systems of the suspension systems, which suppress the low frequency fluctuation of the suspension components and are required for stable operation of the interferometer.

5.1 Motivation for active controls

The mechanics of suspension systems are designed so that they achieve sufficient vibration isolation in the frequency band of gravitational wave observation. On the other hand, the suspension systems also have to suppress the out-of-band mirror vibration, for smooth and stable operation of the interferometer. Without any damping mechanisms, mirror vibration tends to be enhanced at low frequencies by mechanical resonances which typically possess high quality factors. Also, the low frequency oscillators of SAS such as IP and GAS filters often suffer from thermal drifts or creep, which bring the suspended mirrors away from the operation point of the interferometer.

In order to suppress the low frequency motion due to these mechanical characteristics, active control is applied by the use of vibration sensors, actuators and servo systems. The damping of mechanical resonances can be also achieved by passive dampers such as eddy-current dampers, which have advantages in stability and ease of maintenance once they are installed to the suspension systems. Active control systems are rather delicate and one has to design the control servo carefully for stable operation. On the other hand, active systems are more flexible and can be switched easily after installation in the suspension systems. We often need the flexibility since different controls are required depending on the states of the interferometer and surrounding environment such as temperature and seismic vibration levels. This becomes a big motivation for using active control systems regardless of the complexity.

Another point which has to be taken care of regarding the active control systems is the control noise. The control noise is introduced by electronics of sensors and actuators, and also by digital servo systems, which for instance bring quantization errors in the digitization processes. One has to make sure that the control noises do not degrade the interferometer sensitivity beyond the acceptable level in the detection band.

5.2 Requirement on active controls

5.2.1 Interferometer phases and requirements

As mentioned in the previous section, there are different requirements on the active controls depending on the operation status of the interferometer. The status of the interferometer can be categorized into three phases:

1. the calm-down phase,
2. the lock-acquisition phase,
3. the observation phase.

In the calm down phase, the suspension systems are undergoing large disturbances and the optics are swinging with large amplitudes. In this phase, signals for some delicate sensors and weak actuators may saturate due to the large oscillation. One has to calm down the vibration using sensors and actuators with sufficient range, and restore the position or orientation of masses back to the nominal places. Active suspension controls in this phase require robustness rather than quietness, and mainly need to exert damping control on mechanical resonances. The requirement has been set that the $1/e$ decay time of the mechanical resonances regarding the interferometer operation has to be less than 1 minute.

In the lock acquisition phase, the optics in the interferometer are brought to their operation points to get ready for gravitational wave observation. For smooth lock acquisition of the interferometer, the mirrors have to be slowed so that control forces can freeze their motion and trap them into the linear regime of the interferometer signals. Thus in the lock-acquisition phase, the active suspension controls are required to minimize the velocities of the suspended optics. Typically the RMS velocities of the suspended mirrors have to be less than 1 μm/sec for smooth lock acquisition of optical cavities. Note that the RMS velocity of the ground vibration is roughly 1 μm/sec and the RMS velocities of the suspended mirrors tend to be enhanced by mechanical resonances with high Q factors at low frequencies. The mirror rpitch and yaw should be also suppressed, since these mirror rotations cause fluctuations of the beam spot and contaminates the length control signals of the interferometer. The requirements on the mirror velocities and rotation angles will be further discussed later.

After the interferometer is locked successfully, it moves into the observation phase in which gravitational wave observations are made. In this phase, very low-noise controls are required so that the control noises do not degrade the detector sensitivity in the detection band of gravitational waves(> 10 Hz). Some noisy control loops should be opened or their control gains should be reduced. At the same time, the mirror displacements and orientation have to be kept in a certain range so that the interferometer maintains good sensitivity to gravitational waves. The operation phases of the interferometer and requirements on the active suspension controls are summarized in figure. 5.1.

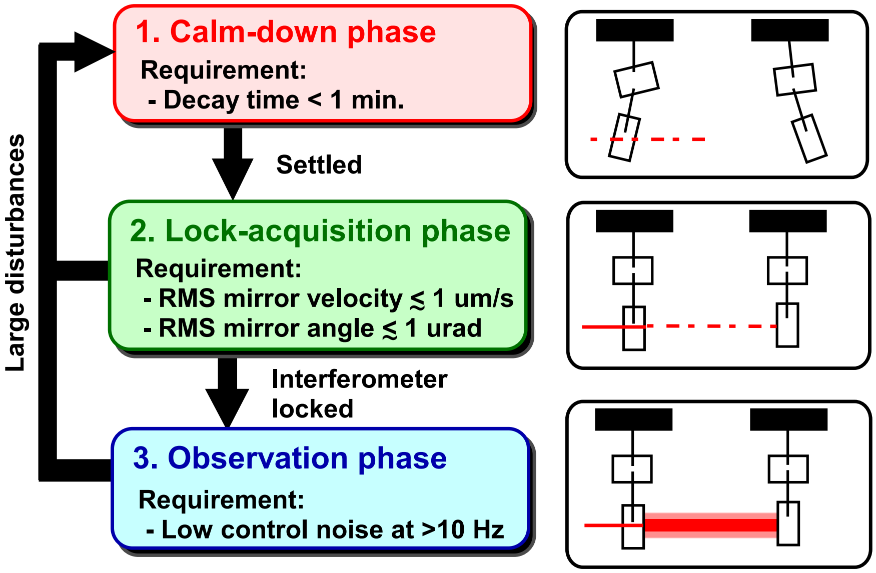

Figure 5.1: Operation phases of the interferometer and the basic requirements on the active suspension controls.

5.2.2 Mirror velocity requirement

Interferometer lock acquisition

The length sensing and controls of the interferometer adopts the so-called frontal modulation techniques [86], in which the laser frequency or amplitude is modulated at radio frequencies before injected to the interferometer. By demodulating detected laser power in the proper phase, one can obtain a control signal proportional to the length variation around the operation point. Figure 5.2 shows a typical sensing signal with respect to the length variation of an optical cavity. The width of the linear regime is calculated from the finesse of the cavity ($\mathcal{F}$) and wavelength of the laser light (λ) as

$$\mathit{\Delta} L_{\mathrm{lin}} = \frac{\lambda}{2\mathcal{F}}. \tag{5.1}$$

The finesses of the cavities are 38 for the signal recycling cavity, 57 for the power recycling cavity and 1550 for the arm cavities (and 1 for the Michelson interferometer) in the KAGRA interferometer. The wavelength of the laser is 1064 nm. For supporting the lock acquisition of the arm cavities, the KAGRA detector employs the so-called green-lock scheme [87], which introduces an auxiliary green laser with half wavelength of the main laser ($\lambda = 532$ nm). The auxiliary laser resonates in the arm cavities with lower finesse (∼50).

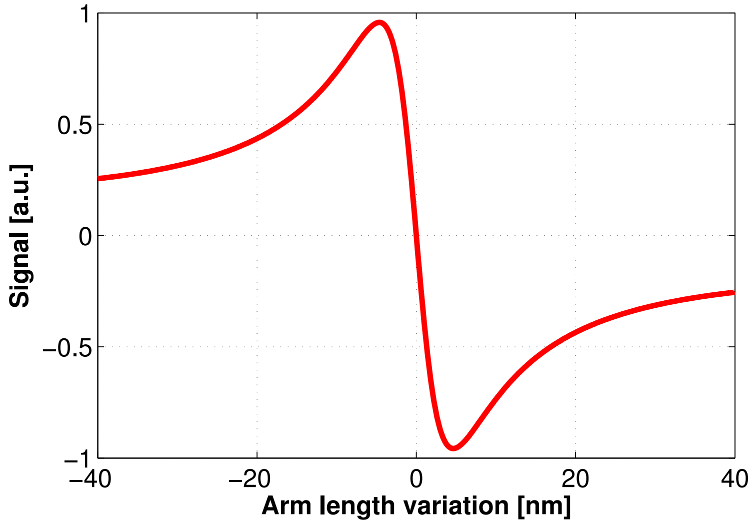

Figure 5.2: A typical length sensing signal around the operation point of a linear optical cavity with finesse of 57.

In order to acquire the lock of an optical cavity, the velocity of cavity length change should be nulled by feedback forces applied to suspended mirrors while the mirrors pass through the linear regime. The momentum applicable to the suspended mirror by feedback force is limited by the dwell time of mirrors in the linear regime, the control bandwidth and the maximum actuation power.

Bandwidth limit

When the control bandwidth is not large enough, the servo responds too slowly and fails to apply sufficient feedback force before the mirrors pass through the linear regime. The control bandwidth is limited by the response of the actuators and existence of mechanical resonances. The violin modes of the mirror suspension wires produce resonant peaks around 200 Hz and thus the control bandwidth with coil-magnet actuators is practically limited to ∼50 Hz.

For the lock acquisition of the arm cavities, the cavity length signals are fed back to Voltage Controlled Oscillators (VCOs) which modulate the frequencies of the auxiliary (green) laser. This means that the phase of the auxiliary laser is locked to the arm cavity length variation. The VCOs are free from mechanical resonances of the suspension systems and thus the control bandwidth can be set as high as 10 kHz. The frequency of the auxiliary laser is then compared to that of the main laser by measuring the frequency of their heterodyne beat. The beat frequency indicates how far the main laser is from resonating in the arm cavity. Feedback controls derived from these signals are applied to the coil-magnet actuators on the test masses. This scheme significantly expands the linear range of the cavity length measurement and thus moderates the velocity requirement of the test masses.

If the actuators have sufficient actuation power and feedback controls are applied only during the time mirrors are in the linear regime, the requirement on the incident velocity to acquire the cavity lock is

$$v_{\mathrm{in}} \lesssim \omega_b \mathit{\Delta} L_{\mathrm{lin}} = \frac{\omega_b \lambda}{2\mathcal{F}}. \tag{5.2}$$

Here ω_b denotes the control bandwidth. A typical velocity limit in this model is 3.3 μm/sec for $\omega_b/2\pi = 50$ Hz, $\lambda = 1064$ nm and $\mathcal{F} = 50$.

Actuation power limit

In practice, maximum forces applicable from the mechanical actuators are limited because of control noise requirement. The stronger the actuators become, the more noise is introduced from the electronics of the actuators in the detection band of gravitational waves. Typically the voltage applied on the coil magnet actuators has a noise level $\tilde{V}_{\mathrm{n}} \sim 10^{-8}$ V/$\sqrt{\mathrm{Hz}}$ above 10 Hz and the maximum applicable voltage is V_{max} =10 V. The coil driving noise should be suppressed to lower than the required displacement noise of the mirrors. Thus the maximum acceleration that can be applied on the mirror is

$$a_{\mathrm{max}} = \frac{V_{\mathrm{max}}}{\tilde{V}_n} \tilde{x}_{\mathrm{req}} \omega_{\mathrm{obs}}^2. \tag{5.3}$$

Here $\tilde{x}_{\mathrm{req}}$ is the required displacement noise level (in m/$\sqrt{\mathrm{Hz}}$) due to the actuator noise and ω_{obs} is the frequency at which the noise requirement should be satisfied. In the case of KAGRA, the requirement is strictest at $f_{\mathrm{obs}} = 10$ Hz.

If on the other hand the control bandwidth is large enough but the actuators can only apply limited acceleration (a_{max}) on the mirrors, the requirement on the incident velocity to acquire the cavity lock is then calculated as

$$v_{\mathrm{in}} \lesssim \sqrt{2 a_{\mathrm{max}} \mathit{\Delta} L_{\mathrm{lin}}}. \tag{5.4}$$

RMS velocity requirement

Table 5.1 summarized the requirements on the velocity of cavity length variation calculated from equations (5.2) and (5.4). It assumes that control bandwidths are set 10 kHz for the arm cavities and 50 Hz for other cavities. The arm cavities are locked to the green laser and assumed to have finesse of 50 to it. The required displacement noise level from the coil drivers $\tilde{x}_{\mathrm{req}}$ is set 3 times lower than the required seismic noise level of the optics (see table 5.3). As the VCOs used for the locking arm cavities have significantly large actuation range, the velocity limit due to maximum actuation power is not defined for the arm cavities.

Cavity/interferometer	BW limit [μm/s]	$a_{\max}$ limit [μm/s]
Arm cavities	330	–
Power recycling cavity	2.9	4.7
Signal recycling cavity	4.4	0.6
Michelson interferometer	170	3.5

Table 5.1: Requirements of the velocity of the cavity length variation.

As the mirrors comprising the optical cavity move randomly, the incident velocity varies each time the mirrors pass by the linear regime. On the assumption that the velocity of the mirrors has Gaussian distribution, the incident velocity of the optical cavity would have the following probability distribution [88]:

$$f(v) = \frac{v}{v_{\text{rms}}^2} \exp\left(\frac{v^2}{2v_{\text{rms}}^2}\right), \tag{5.5}$$

where v_{rms} denotes the RMS velocity of the cavity length variation. In order to achieve the lock acquisition with higher than 50% probability in this model, the RMS velocity of the length variation should be suppressed lower than $0.72v_{\text{req}}$, where v_{req} is the maximum permitted velocity to acquire the cavity lock. From these considerations, requirement on the RMS velocity of the suspended mirrors with the KAGRA-SAS is set to 0.5 μm/s for the type-A and type-B SAS, and 2 μm/s for the type-Bp system. Although the arm cavities have moderate requirement on the velocity, the motion of the input test masses also affects the length of power and signal recycling cavities and thus the type-A SAS needs a requirement as strict as that of the type-B SAS.

5.2.3 Angular motion requirement

The mirror angular motion causes the beam spot fluctuation and spatial mode mismatch in the interferometer. Since the test masses are kilometers apart, small fluctuations of the mirror angles produces large beam spot fluctuation. For operating the interferometer stably and avoiding degradation of the detector sensitivity due to the mode mismatch, the mirror RMS angles are to be suppressed so that they do not produce beam spot fluctuation on the optics larger than 1 mm in RMS [31]. Table 5.2 shows the maximum permitted mirror rotation angles to meet the above-mentioned requirement [89]. The requirement on the RMS angles of the mirrors suspended with the KAGRA-SAS is therefore set to 0.2 μrad for the type-A, 1 μrad for the type-B, and 2 μrad for the type-Bp system. The system should meet the requirement both in the lock-acquisition and observation phase.

Optics	Requirement [μrad]
TM	0.2
BS	4
PRM	45
PR2	20
PR3	2
SRM	25
SR2	10
SR3	1

Table 5.2: The requirements on the RMS mirror angles in the KAGRA interferometer.

5.2.4 Longitudinal displacement requirement

In the observation phase, the mirror longitudinal position should be kept locked with the interferometer control signals by coil-magnet actuators. In order to keep the interferometer lock, the amplitude of the control forces should be kept within the maximum forces of the coil-magnet actuators. The maximum force on the mirror is derived as $F_{\mathrm{max}} = M_{\mathrm{m}} a_{\mathrm{max}}$ using the maximum acceleration a_{rmmax} defined in equation (5.3), where M_{m} represents the mass of the mirror. As the mirror displacement RMS comes mainly from the low frequency ($<$ 0.5 Hz) components, the control force exerted on the mirror F_{c} can be derived from the seismically-induced mirror displacement x_{s} as approximately

$$F_{\mathrm{c}} \approx k_{\mathrm{sus}} x_{\mathrm{s}} = M_{\mathrm{m}} \omega_{\mathrm{sus}}^2 x_{\mathrm{m}}. \tag{5.6}$$

Here k_{sus} denotes the spring constant of the mirror suspension in the longitudinal direction, and ω_{sus} is the resonant frequency. The resonant frequency of the suspension is 1 Hz for the type-A SAS and 0.6 Hz for the type-B (type-Bp) SAS. The maximum permitted mirror displacement (before suppressed by the interferometer control) to keep the interferometer lock with the mirror actuators is then calculated as

$$x_{\mathrm{max}} = \frac{F_{\mathrm{max}}}{k_{\mathrm{sus}}} = \frac{V_{\mathrm{max}}}{\tilde{V}_n} \frac{\omega_{\mathrm{obs}}^2}{\omega_{\mathrm{sus}}^2} \tilde{x}_{\mathrm{req}}. \tag{5.7}$$

Table 5.3 shows the maximum applicable force on the mirror and the maximum permitted mirror displacement estimated from the equation. The mirror displacement RMS should be suppressed much lower than these values, to avoid saturation in actuators. Here the requirement on RMS is set 1/4 of the maximum permitted displacement[1]. Thence the requirements are 2 nm for the type-A, 0.4 μm for the type-B and 70 μm for the type-Bp system. The requirement on the long-term drift in the longitudinal direction is also set to the same value.

---

[1] In the Gaussian distribution, the fraction outside 4σ (σ =RMS) is 6×10^{-5}.

Optics	$F_{\max}$ [N]	$x_{\max}$ [μm]
TM	9×10^{-6}	0.010
BS	7×10^{-4}	3.3
SRM	4×10^{-4}	3.3
SR2,SR3	2×10^{-4}	1.6
PRM	9×10^{-2}	560
PR2,PR3	4×10^{-2}	280

Table 5.3: The maximum force applicable on the mirror and the maximum permitted mirror displacement to keep the interferometer lock with the mirror actuators.

Note that the requirement values are set with the assumption that the interferometer lock is maintained only by the actuators on the mirrors. On the other hand, one can distribute the low frequency component of the interferometer control signals to the upper-stage actuators, which are allowed to have larger actuation range. This scheme is called hierarchical control [94] and would be required especially for the type-A system, in which the applicable force by the mirror actuators is extremely weak.

5.2.5 Requirement in type-B SAS

The requirement set on the active controls for the type-B SAS is summarized in table 5.4. In the calm-down phase, the most important requirement is set on the $1/e$ decay time of the mechanical resonances and it should be suppressed lower than 1 min. The residual longitudinal displacement and angle of the mirror should be suppressed lower than ~ 50 μm and ~ 50 μrad, so that the control can be smoothly switched to that for the lock-acquisition phase. In the lock-acquisition phase, the mirror RMS velocity and RMS angle should be suppressed lower than the level for achieving the interferometer lock. Here the RMS values are defined as integration of the spectrum densities down to 0.01 Hz. The corresponding time scale (100 sec.) is long enough to cover the lock-acquisition process, and the integration cover the frequency band of microseismic peak (0.2-0.5 Hz), which largely contributes to the RMS velocity or angle.

In the observation phase, the longitudinal mirror displacement should be suppressed, to avoid saturation of actuation forces by the interferometer control. The mirror transverse/vertical displacement and mirror angle are to be suppressed at the same time to keep the beam spot centering. Not only the RMS displacement/angle in a relatively short time scale ($\lesssim$ min), but also long-term ($\gtrsim$ min) drift of the mirror displacement/angle should be suppressed, to allow the long-term observation. On the other hand, the control noise coupling to the mirror longitudinal displacement in the detection band ($> 10 Hz$) should be suppressed lower than the required vibration level of the type-B SAS. This practically limits the bandwidth of the active suspension control lower than ~ 1 Hz.

1. The calm-down phase		
items	requirements	references
$1/e$ decay time of mechanical resonances	< 1 min	§5.2.1
(residual) RMS displacement (longitudinal)	< 50 μm	§5.2.5
(residual) RMS displacement (transverse,vertical)	< 1 mm	§5.2.3
(residual) RMS angle (pitch, yaw)	< 50 μrad	§5.2.5
2. The lock-acquisition phase		
items	requirements	references
RMS velocity (longitudinal)	< 0.5 μm/sec	§5.2.4
RMS displacement (transverse, vertical)	< 1 mm	§5.2.3
RMS angle (pitch, yaw)	< 1 μrad	§5.2.3
3. The observation phase		
items	requirements	references
control noise at 10 Hz (longitudinal)	$< 5 \times 10^{-18}$ m/$\sqrt{\text{Hz}}$	§4.1.2
RMS displacement (longitudinal)	< 0.4 μm	§5.2.4
RMS displacement (transverse, vertical)	< 1 mm	§5.2.3
RMS angle (pitch, yaw)	< 1 μrad	§5.2.3
displacement long-term drift (longitudinal)	< 0.4 μm	§5.2.4
displacement long-term drift (transverse, vertical)	< 1 mm	§5.2.3
angle long-term drift (transverse, vertical)	< 1 μrad	§5.2.3

Table 5.4: Requirements on the active controls for the type-B SAS. The rightmost column shows the subsection explaining the reasons for the requirements. The RMS values are to be obtained by integrating the power spectrum density down to 0.01 Hz. The long-term drift is defined as the time scale longer than ~ 1 min.

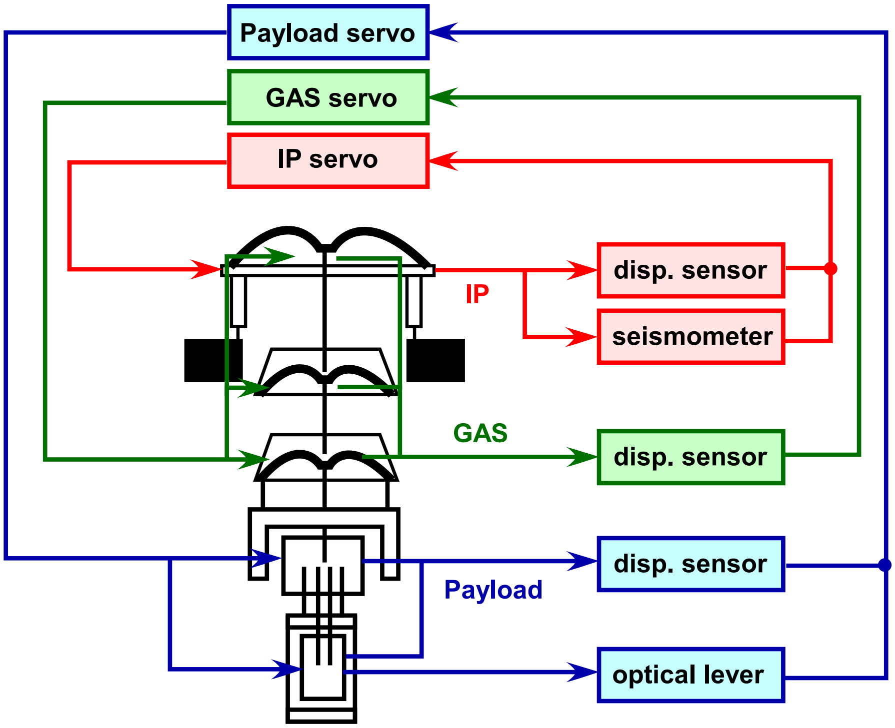

Figure 5.3: Schematics of the active control structure for the KAGRA-SAS.

5.3 Active control system for KAGRA-SAS

The active control system for the KAGRA-SAS plays roles in damping the mechanical resonances and compensating the drift of low-frequency oscillators. The schematic diagram of the active control system is illustrated in figure 5.3. It has three main control loops: the IP control, the GAS filter control, and the payload control. The IP control performs the static positioning of the top stage and damping of the pendulum modes of the attenuation chain. The GAS filter control mainly deals with compensation of the thermal drift of the GAS filters. The payload control performs damping of the mechanical resonances of the mirror suspension, and alignment control of the suspended optics. The design of the servo filters and expected performance of the controls are discussed in the following subsection. The simulations mainly focus on active controls of the type-B SAS, which are experimentally investigated in the prototype test as described in chapter 8.

5.3.1 IP controls

As shown in figure 4.6, the IP pre-isolation stage is equipped with three sets of LVDT position sensors, seismometers and coil-magnet actuators to control the top stage motion in three DoFs (longitudinal, transverse and yaw). The LVDT position sensors measure the relative position between the top stage and the outer frame fixed to the ground, while the seismometers measure the inertial vibration of the top stage. The KAGRA-SAS plans to use the L-4C geophones from Mark Products as seismometers. The geophone is a passive device that converts ground velocity into voltage and has good enough sensitivity to measure the seismic vibration in the KAGRA site. Figure 5.4 shows a conceptual block diagram of the IP control. The measurements of the LVDT and geophone are combined into one super-sensor using complementary blending filters (B_{HP} and B_{LP}). The combined sensor signal is then sent to the servo filter and to the coil-magnet actuators. Sensors and actuators have electronics noise from the driver circuits and that introduces additional vibration to the top stage and consequently to the suspended mirror.

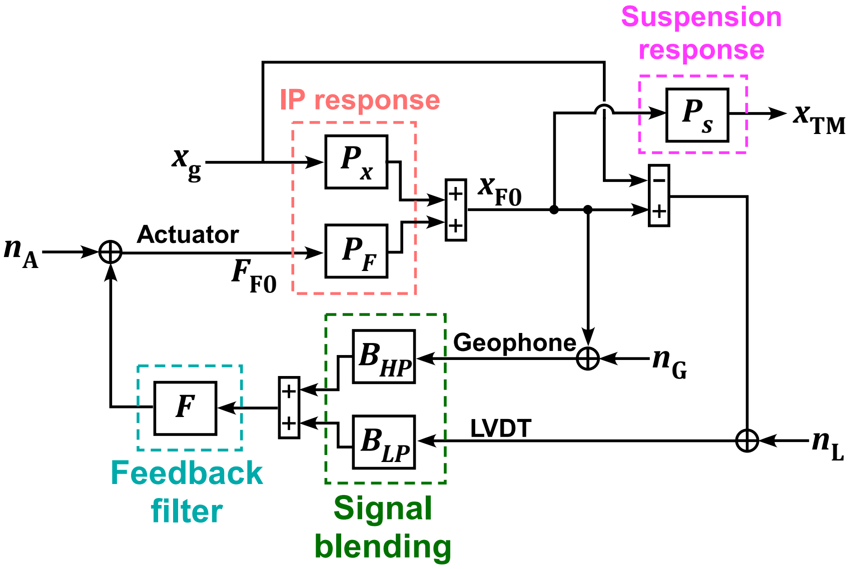

Figure 5.4: The block diagram of the IP control.

Servo filter

The servo filter for the IP control is designed so that it performs damping of the pendulum modes around 0.2-1 Hz and static positioning of the top stage below 10 mHz. Thence the servo should provide differentiation filter above 0.2 Hz to produce feedback signals proportional to the top stage velocity, and enough control gain below 10 mHz. Figure 5.5 shows the designed servo filter for the IP control in the type-B SAS and the expected open-loop gain. The resonant peaks at 0.41 and 0.64 Hz correspond to the pendulum mode of the attenuation chain. The control gain is raised at low frequencies and reaches 10^3 at 10^{-4} Hz.

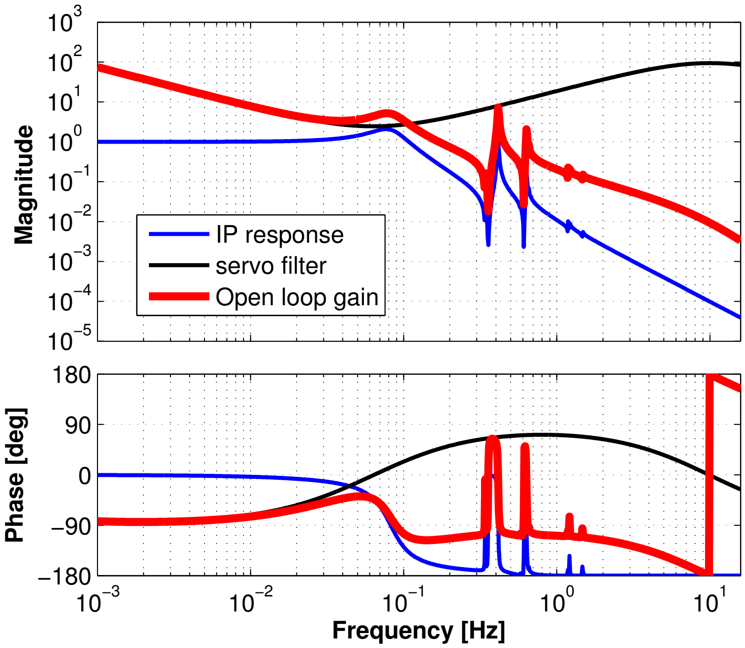

Figure 5.5: Servo filter design of the IP control in the type-B SAS. The IP response shows the calculated transfer function from external longitudinal force onto the top stage to the longitudinal displacement (normalized at DC).

Sensor blending

The super-sensor combines the low frequency LVDT signals with the high frequency geophone signal. This is done by applying a lowpass filter with frequency response $B_{\mathrm{LP}}(s)$ to the LVDT signal and a complimentary highpass filter $B_{\mathrm{HP}} = 1 - B_{\mathrm{LP}}$ to the geophone signal. This ensures that there is no phase distortion around the blending frequency. The blending filters are derived from seventh order polynomial function of the Laplace variable (s) as

$$B_{\mathrm{LP}}(s) = \frac{35\omega_b^4 s^3 + 21\omega_b^5 s^2 + 7\omega_b^6 s + \omega_b^7}{(s+\omega_b)^7}, \tag{5.8}$$

$$B_{\mathrm{HP}}(s) = \frac{s^7 + 7\omega_b s^6 + 21\omega_b^2 s^5 + 35\omega_b^3 s^4}{(s+\omega_b)^7}. \tag{5.9}$$

Here ω_b represents the crossover frequency of the two blending filters. Figure 5.6 shows the Bode plots of the blending filters with $\omega_b/2\pi = 0.1$ Hz. The seventh order polynomial is chosen so that the fourth-order highpass filter omits the low-frequency geophone noise, which rises as $\sim f^{-3.5}$ at low frequencies.

Since the LVDT measures the relative position between the top stage and the ground, the active control using the LVDT may re-introduce seismic vibration to the top stage. The blending crossover frequency should be set below 0.1 Hz, to avoid degradation of

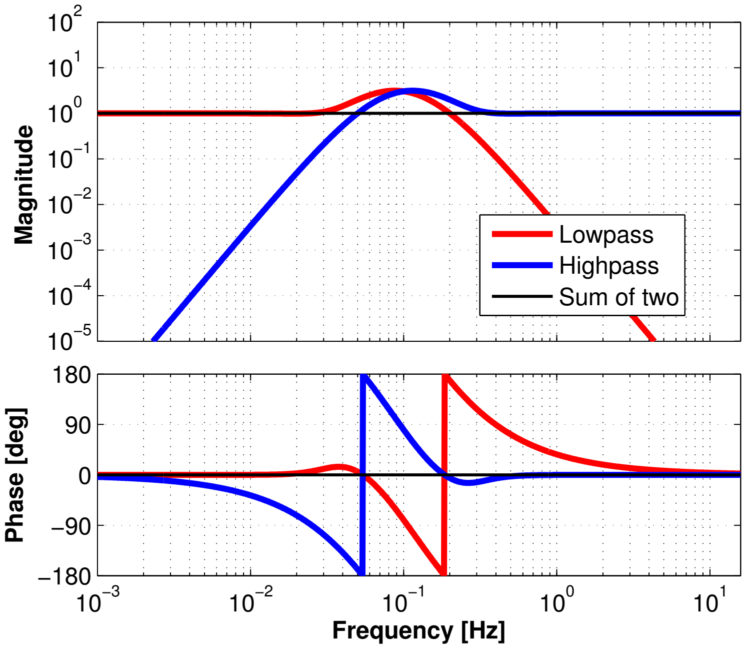

Figure 5.6: Bode plots of the blending filters with the crossover frequency of 0.1 Hz.

attenuation performance around the microseismic peak (0.2-0.5 Hz). Figure 5.7 shows the calculated seismic noise spectra in the actively controlled type-B SAS with various crossover frequencies. They are compared with the spectrum in the passive system (plotted in the black curves). The resonant peak at 0.41 Hz, which contributes to the RMS velocity of the mirror in the passive system, is suppressed successfully in the actively controlled system. On the other hand, when the blending frequency is set higher than ∼50 mHz, the attenuation performance around the microseismic peak is degraded and that worsens the mirror RMS velocity.

Sensor noise couplings

Although the crossover frequency of the sensor blending should be lowered for good seismic attenuation performance, using the geophone signal at low frequencies may introduce a large amount of control noise due to the poor sensitivity of the geophone at low frequencies. Figure 5.8 shows typical sensing noise curves of the LVDT and geophone L-4C (based on the measurement in the prototype, see section 6.1). The sensing noise of the geophone rapidly increases below 1 Hz, proportional to $\sim f^{-3.5}$. Since the noise curves of the LVDT and geophone cross at 80 mHz, the sensor noise coupling would be minimized when the crossover frequency is set around this frequency.

Figures 5.9 and 5.10 show the expected sensor noise couplings to the mirror velocity, with various crossover frequencies of the blending filters. When the crossover frequency is lower than 50 mHz, the sensor noise coupling from the geophone introduces low-frequency

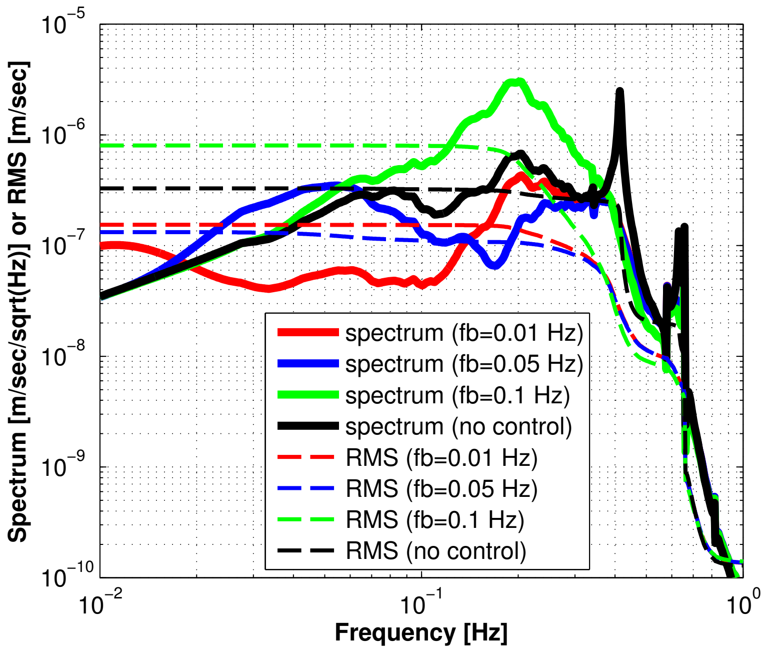

Figure 5.7: The seismically-induced mirror velocity spectra in the type-B SAS with and without the IP controls. The crossover frequency of the signal blending is altered.

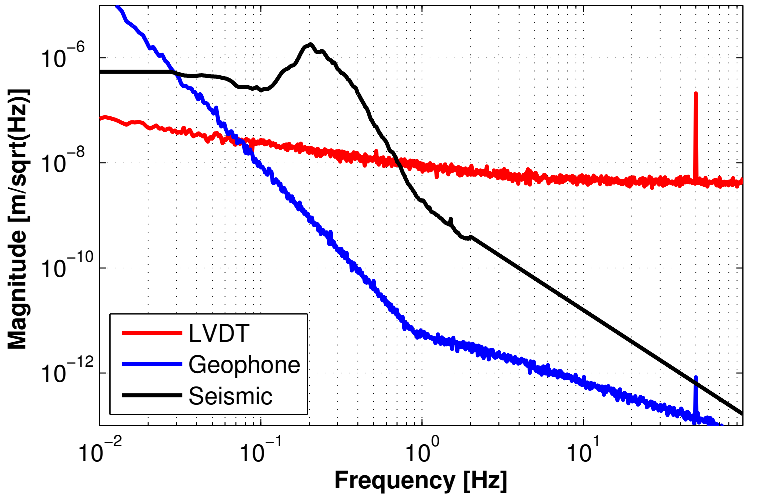

Figure 5.8: The sensing noise of the LVDT and geophone L-4C (compared with the seismic noise level in the Kamioka site).

fluctuation of the mirror position and that worsens the mirror RMS velocity. Taking the balance of the attenuation performance and the sensor noise coupling, the RMS velocity of the suspended mirror is minimized when the crossover frequency is set to 50 mHz.

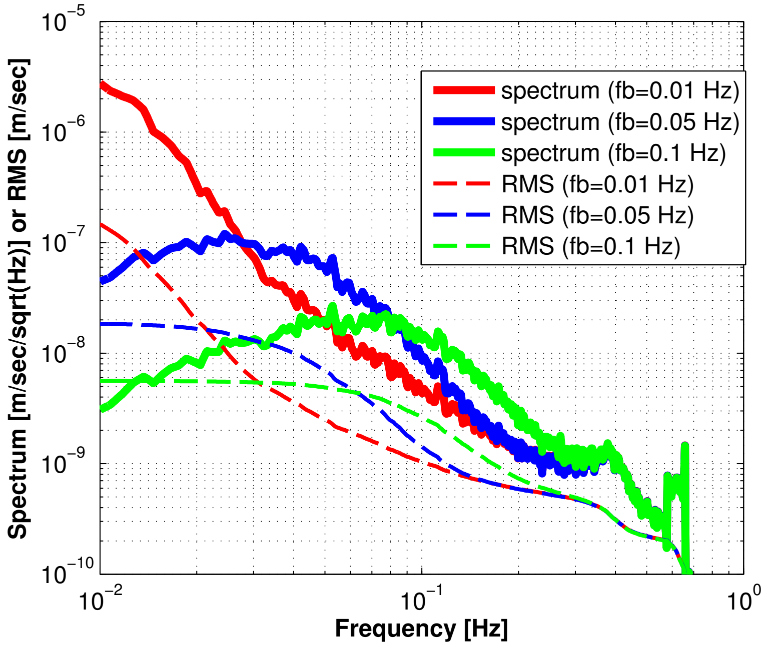

Figure 5.9: Predicted sensor (geophone) noise couplings to the mirror velocity, with various crossover frequency of the blanding filters.

The control noise of the IP control does not affect the detector sensivity in the detection band of gravitational waves, since control bandwidth is much lower ($<$ 1 Hz) and the type-A and type-B systems have sufficient attenuation performance in the horizontal direction.

5.3.2 GAS filter control

Servo design

The GAS filter control mainly deals with the static control of the GAS filters, which tend to drift by a large amount with temperature change. Each GAS filter is equipped with a set of LVDT position sensors and coil-magnet actuators as illustrated in figure 4.8. The control loop is closed around each LVDT/actuator pair so that the position of the keystone is statically locked in each GAS filter. Figure 5.11 shows the designed servo filter for thermal drift compensation and expected open loop gain (for the top GAS filter, F0). The bandwidth is set around 20 mHz, well below the resonant frequencies of the GAS filters (0.2-0.8 Hz). The DC control gain is about 100. As discussed in section 3.3, the GAS filter has an intrinsic thermal response of $\sim$ 0.8 [mm/K]. When the GAS filter control

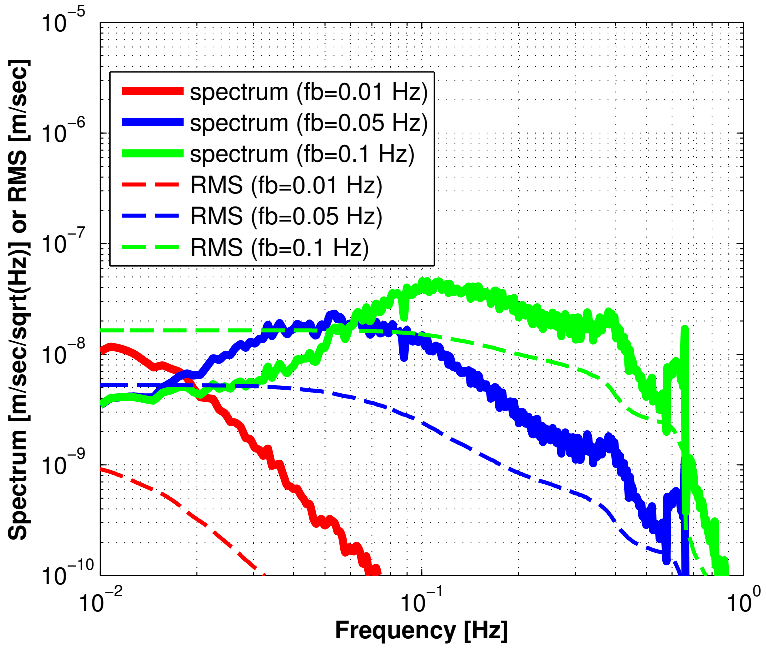

Figure 5.10: Predicted sensor (LVDT) noise couplings to the mirror velocity, with various crossover frequency of the blanding filters.

is applied, it is reduced to the level of ∼ 8 [μm/K], which is sufficiently low for keeping the mirror vertical position in ∼1 mm precision.

Sensor noise couplings

The GAS filter control loops should be constantly closed in any operation phase of the interferometer, and thus the control noise in the observation phase is important. Vertical vibration introduced to the lower-stage GAS filter is transmitted to the mirror with small attenuation, and thus the noise from the control system can affect the in-band detector sensitivity. Figure 5.12 shows the estimated sensor noise coupling from LVDT on each GAS filter stage in the type-B SAS, assuming 1% vertical-horizontal couplings. The simulation confirms that control noise due to the LVDT sensing noise is well below the required noise level in the type-B SAS.

5.3.3 Payload control

Damping with position sensors

The vibration of the payload is observed by the use of displacement sensors which measure the relative displacements of the intermediate mass and mirror with respect to their recoil masses. They are used to damp mechanical resonances of the payload which cannot be damped by the IP control. In particular, tilt motions of the mirror can be only

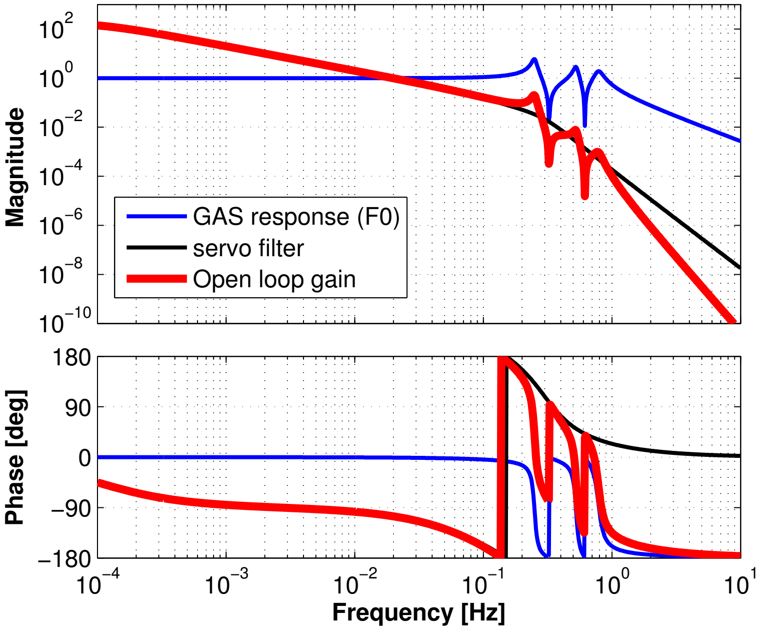

Figure 5.11: Design of the servo filter for the GAS filter control. The mechanical response shows the (normalized) transfer function from the coil-magnet actuator to the LVDT mounted on the top GAS filter (F0).

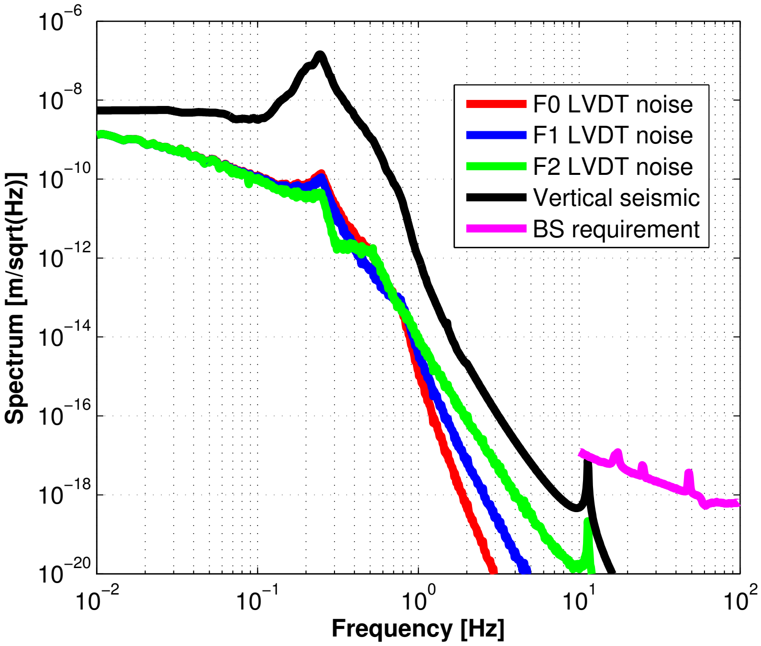

Figure 5.12: Sensor noise couplings of the GAS filter controls in the type-B SAS.

controlled in this part since the intermediate mass is suspended by a single wire and the tilt motions are separated from the tilt of upper stages.

In the type-B and type-Bp system, Optical Sensor and Electro-Magnetic actuators (OSEMs) [82] are used for the position sensing and controls. The OSEMs are arranged so that they can control the intermediate mass motions in six DoFs and the mirror motions in three DoFs (longitudinal, pitch and yaw). The sensor signal about a DoF is fed back to the actuator about the corresponding DoF (longitudinal to longitudinal, for instance), and thus the control system has nine individual control loops. Figure 5.13 shows the designed servo filters and expected open loop gains for the intermediate mass longitudinal and pitch controls. To apply damping forces, signals from the position sensors are converted to the velocity signals with differentiation filters. The gains of the differentiation filters are tuned to provide sufficient damping strength to all the mechanical resonances with frequencies below 20 Hz.

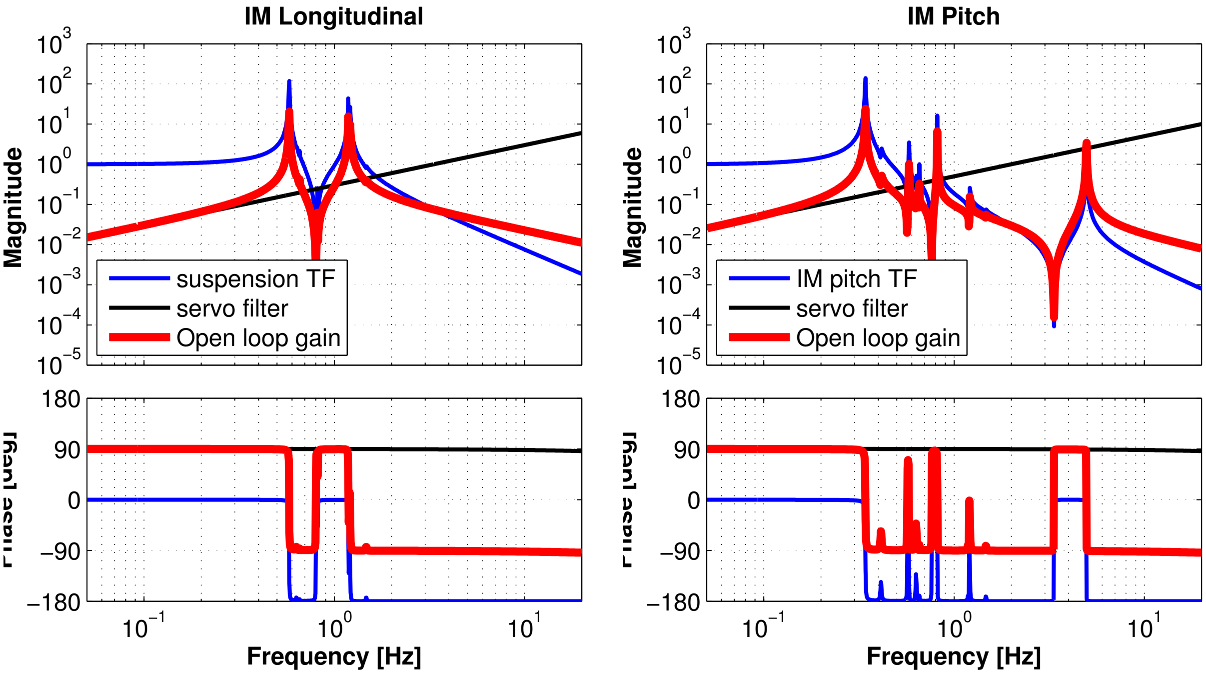

Figure 5.13: Servo filter design of the payload control in the type-B SAS.

To see the performance of the damping controls, the $1/e$ decay time of the mechanical resonances is investigated. The plot in figure 5.14 shows the predicted $1/e$ decay time of mechanical resonances versus the resonant frequencies in the type-B SAS, with and without active controls. The active controls also include the IP control, which provides the pendulum mode damping of the attenuation chain. In the passive system, there are many mechanical resonances with long decay time in the 0.1-1 Hz region. The active controls efficiently damp these modes and suppress the $1/e$ decay time of most resonances to lower than 1 minute, which is the requirement in the calm-down phase. There exists one resonance whose decay time exceeds 1 minute in the actively controlled system, but the mode is related with the transversal motions of the mirror (the mode shape is illustrated in figure 5.14) and does not disturb the interferometer operation.

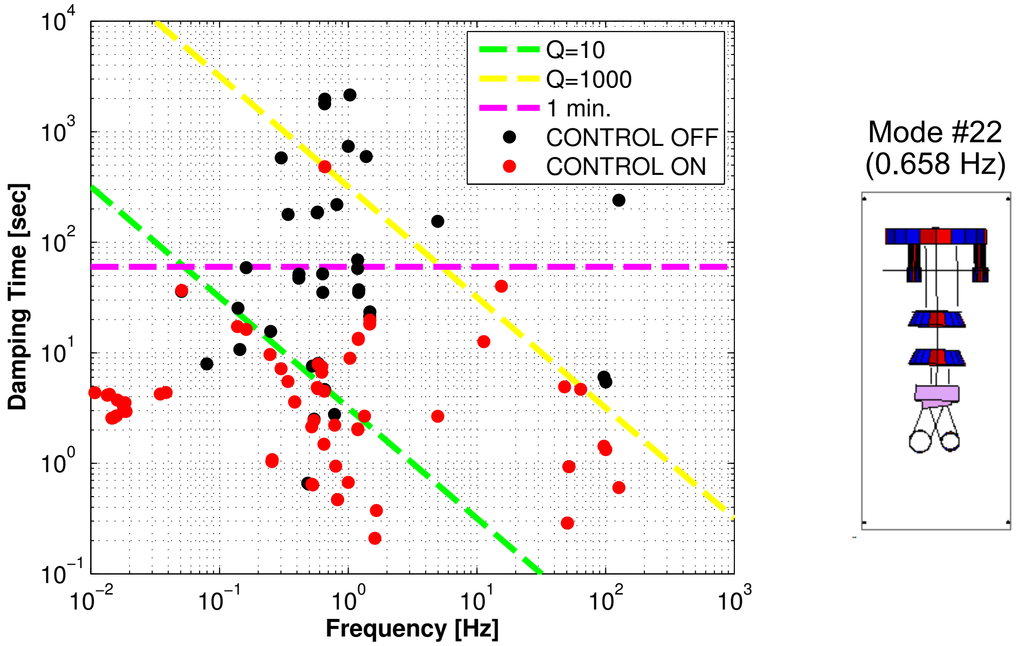

Figure 5.14: Predicted decay time versus the resonant frequencies of the mechanical responces in the type-B SAS with and without active controls.

Sensor noise couplings in damping control

The OSEM position sensor typically has the noise level of $\sim 10^{-9}$ m/$\sqrt{\text{Hz}}$ in the detection band of gravitational waves. Figure 5.15 shows expected noise couplings from the OSEM position sensors implemented in the intermediate mass and mirror levels. The sensor noise induces mirror displacement noise much larger than the acceptable level. Therefore the control loops should be opened in the observation phase.

Alignment control

Another important role of the payload control is aligning the mirror to the interferometer beam and reducing the RMS pitch and yaw angular displacements. The mirror pitch and yaw are monitored by the optical lever, which is a device composed with a light source illuminating the mirror and a Quadrant Photo-Diode (QPD) to detect the beam spot position of the reflected light. After the lock acquisition of the interferometer, the sensor signals are replaced by the signals from the Wave-Front Sensors (WFSs), which use

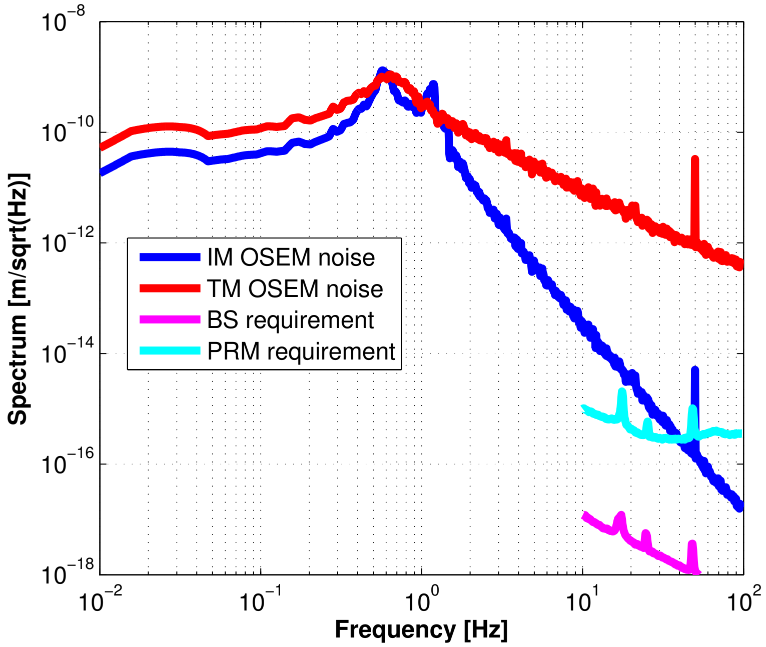

Figure 5.15: Sensor noise couplings of the payload damping controls in the type-B SAS.

the interferometer beam as a reference and have better sensitivity. The feedback signals are applied to the actuators on the intermediate mass, since the mechanical resonances of the intermediate mass contribute a lot to the RMS angles of the mirror and thus the motions should be suppressed on that level. The conceptual design of the mirror alignment control system is illustrated in figure 5.16.

Figure 5.17 shows the designed servo filters for the alignment control in the type-B (Bp) system. The servo filters get rather complicated, since the angles observed in the mirror level are fed back to the upper stage and thus one needs to compensate the phase delay in the mechanical response. In the high frequency region, the amplitude of the mechanical response drops by $\sim f^{-4}$ and the phase is delayed by 360 deg. The servo filter gain is raised around the unity gain frequency ($\sim$ 1 Hz) by $\sim f^3$ to compensate this mechanical response. The sharp notch at 4.9 Hz in the pitch servo filter is introduced to avoid the instability due to the mechanical resonance corresponding to the pitch mode of the recoil mass. The shallow notch at 10 Hz is introduced to mitigate the sensor noise coupling around this frequency.

Alignment control noise

In order to allow the gravitational-wave detection in the low frequency region down to 10 Hz, it is required to suppress the bandwidth of the alignment control lower than $\sim$1 Hz so that the sensing noise from WFS does not contaminate the detector sensitivity [31]. The WFS would have a sensing noise level of 10^{-12}-10^{-14} rad/$\sqrt{\mathrm{Hz}}$ which is limited

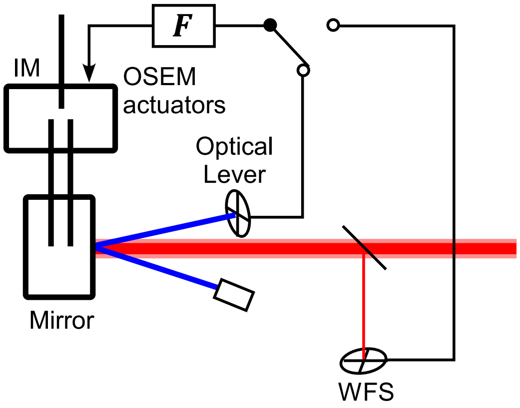

Figure 5.16: A conceptual diagram of the payload alignment control system.

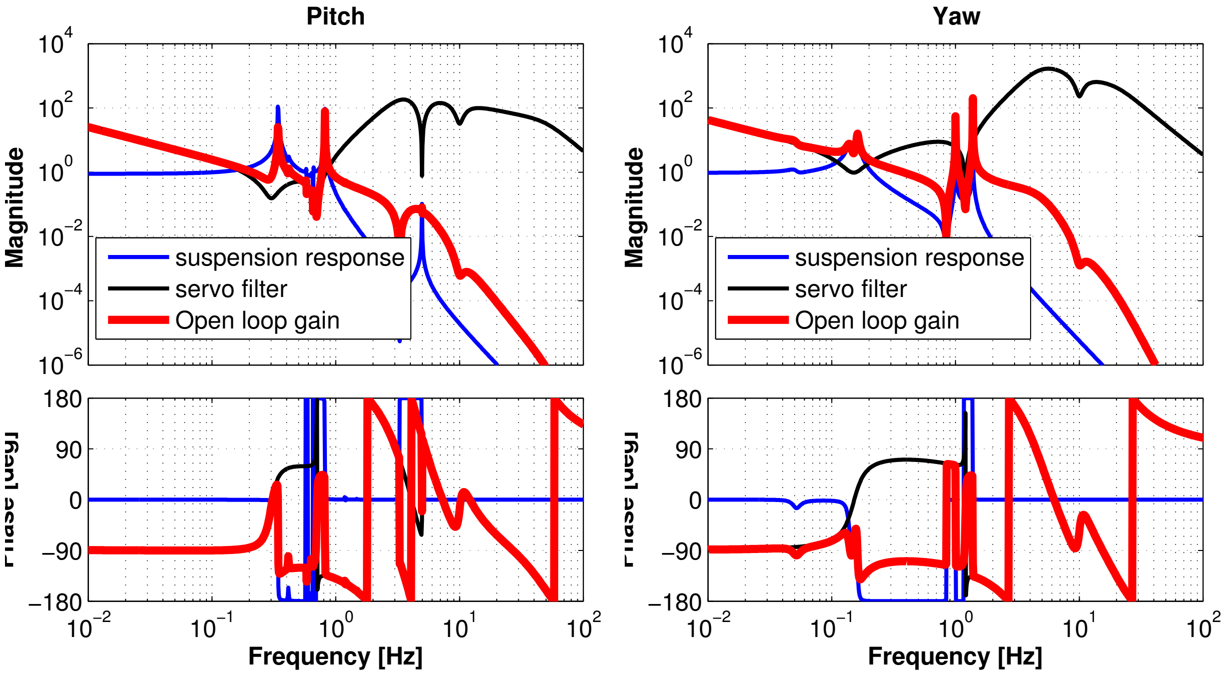

Figure 5.17: Servo filter design of the alignment control in the type-B (Bp) system.

by the shot noise of the photodetectors. The sensing noise couples to the mirror angular motion through the alignment control, and the angular motion induces the longitudinal displacement of the interferometer due to the mis-centering of the beam spot as discussed in subsection 2.2.3. More details on the alignment sensing and control of the KAGRA interferometer are found in reference [31]. From these considerations, the bandwidth of the alignment control is set 0.9 Hz for the pitch control and 1.3 Hz for the yaw control.

Figure 5.18 shows an estimate of the alignment control noise coupling to the interferometer signal. The simulation assumes sensing noise of 10^{-12} rad/$\sqrt{\text{Hz}}$ as a typical shot noise level of the WFS. It also assumes miscentering of the interfermeter beam spot by 1 mm. The calculated control noise coupling is lower than the required vibration level in the detection band.

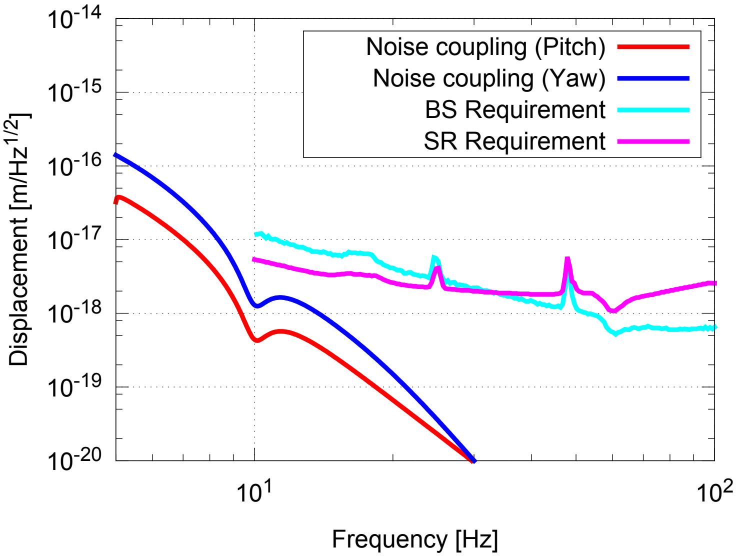

Figure 5.18: Alignment control noise coupling estimation, assuming the sensing noise of the WFS as 10^{-12} rad/$\sqrt{\text{Hz}}$.

Mirror rotation and control performance

The rotational motion of a suspended mass is coupled to the translation motion by the mismatch of the suspension point and the center of mass. The longitudinal and pitch motion is inevitably coupled into the suspension system, since the clamp point and center of mass have to be vertically separated so that the suspended mass is stably balanced. On the other hand, the yaw motion is coupled to the translation motion through the asymmetry of the system such as variation in the IP stiffness (see section 3.2) and misbalance in the suspended mass. Figure 5.19 shows illustrations of the translation-rotation couplings induced in the suspension system. As the amount of the yaw rotation depends on the level of the asymmetry, the precise rotation spectrum is not easily predicted. In the following simulation, 1 mm horizontal separation between the suspension point and the center of mass is assumed in each suspension, and about 30% variation of the effective stiffness of IP is assumed for estimating the yaw motion spectrum.

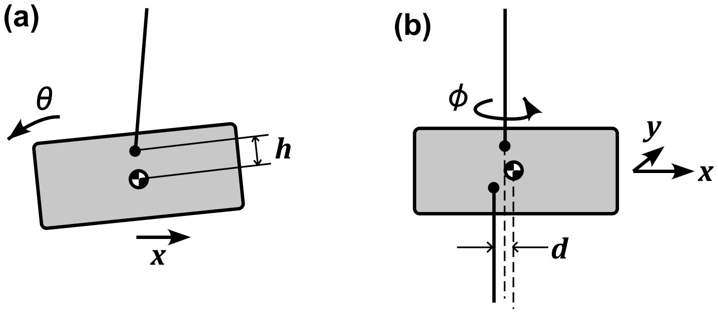

Figure 5.19: Illustrations about (a) the translation-pitch coupling and (b) the translation-yaw coupling induced in the suspension system.

Figure 5.20 shows the predicted angular noise spectrum in the type-B SAS with and without active controls. The active controls also include the IP control, which suppresses the microsesmic vibration at 0.2-0.5 Hz and contributes to the reduction of the mirror RMS angles. Without the active controls, the RMS mirror angle reaches 0.6 μrad for the pitch rotation and 1.5 μrad for the yaw rotation. The active controls suppress the RMS angles by about one order of magnitude, which is below the required level of the type-B system (1 μrad).

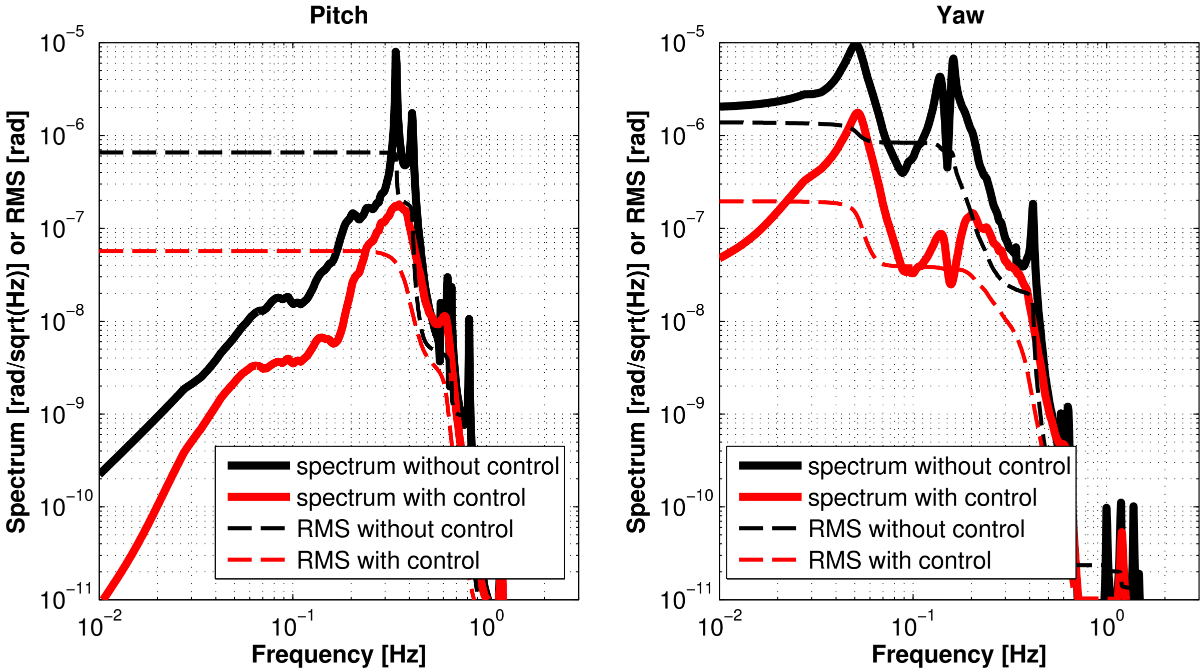

Figure 5.20: Predicted angular noise spectrum of the suspended mirror in the type-B SAS, with and without active controls.

Performance test of SAS components

Chapter 6

This chapter describes experimental tests on the individual SAS components which are going to be implemented in the type-B SAS prototype described in chapter 7. The type-B SAS is divided into three parts and respective parts were tested separately; the IP pre-isolation stage, the standard GAS filter and the payload.

6.1 IP pre-isolation stage

The performance and controllability of the IP pre-isolation system were investigated in a simplified configuration as illustrated in figure 6.1. This section describes the basic mechanical properties of the IP, characterization of the sensors and actuators, vibration isolation performance of the pre-isolation system, and demonstration of the active controls with a simplified servo filter.

6.1.1 Experimental setup

Figure 6.1 shows the experimental setup of the test of the IP pre-isolation system. The pre-isolation system is supported from the ground by a rigid metal frame and hydraulic pistons which are driven by an oil pump and used to level the pre-isolation system. The top stage containing the top GAS filter is supported by the IP, and a dummy payload is suspended from it by a suspension wire made of maraging steel. The top stage motion is sensed by three sets of LVDTs and L-4C geophones. The sensing signals are introduced to the digital system and the processed signals are sent back to the coil-magnet actuators. Details of the digital system are described in section 7.4.

The disposition of the sensors and actuators is illustrated in figure 6.2. The LVDTs and geophones were arranged in a pinwheel configuration with an angular separation of 120° to sense the top stage motion in three DoFs. The coil-magnet actuators were placed coaxially with the LVDTs. The static positioning of the IP was achieved by the three sets of motorized springs driven by stepper motors. A geophone in the longitudinal direction was added to monitor the top stage motion as an out-of-loop observer,

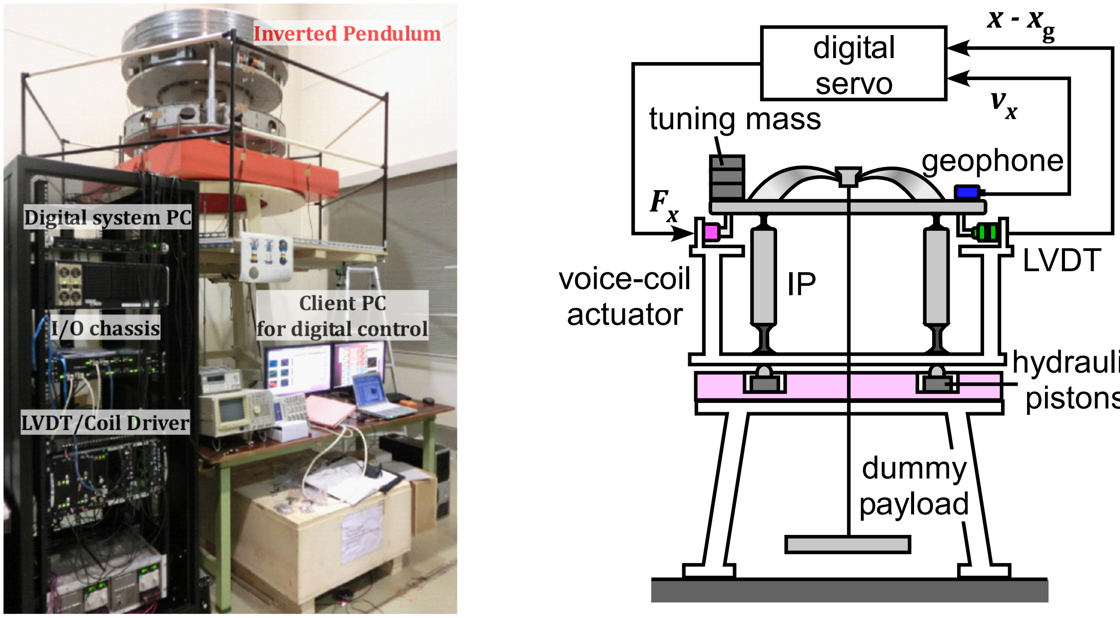

Figure 6.1: Experimental setup of the pre-isolator test.

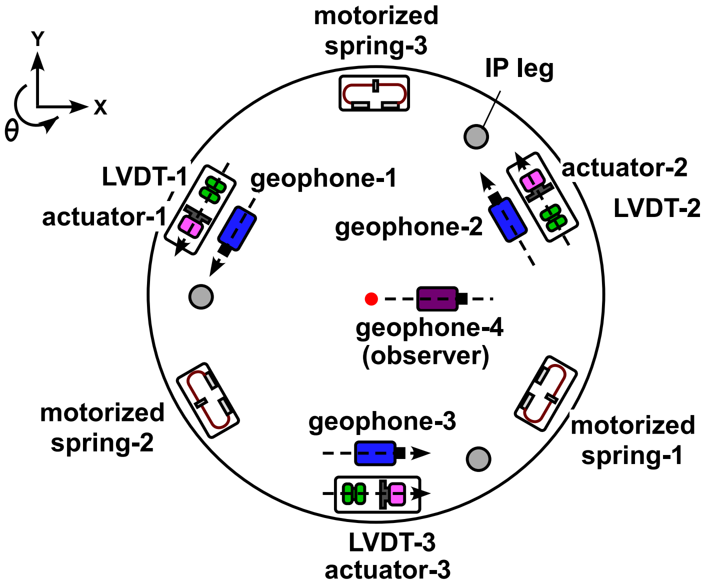

Figure 6.2: Disposition of the sensors and actuators on the top stage.

6.1.2 Tuning of IP

The resonant frequencies of the IP are tuned by adjusted the total weight of the top stage and the suspended payload. The thickness of the IP flexures (10.50 mm in diameters) is chosen so that they support about $\sim$ 1000 kg mass when the IP is critically loaded. Figure 6.3 shows the resonant frequency transition about the translation mode versus the load on the IP. The measurement result is fitted by equation (3.2) with $L = 0.48$ m. The critical load of this IP is estimated as $M_c = 1096 \pm 5$ kg from the fitting result.

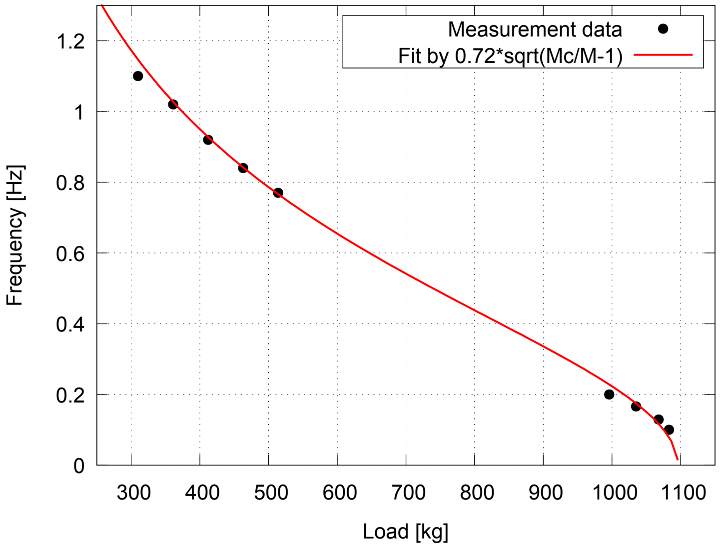

Figure 6.3: The resonant frequency of the IP translation mode versus load on the IP.

6.1.3 Senors and actuators

LVDT

The LVDT is a relative position sensor utilizing coil inductance and modulating magnetic fields. Figure 6.4 shows the working principle of the LVDT. A sinusoidal excitation signal of $\sim$10 kHz is sent to the central emitter coil which produces oscillating magnetic field around. The two receiver coils coaxially mounted to the emitter coil sense the magnetic field and provide oscillating voltages. Since the two receiver coils are identical and counter-wound, the induced voltage is cancelled when the emitter coil is at the center of the two coils. When the emitter coil is displaced from the center, the mutual inductance is changed and that makes a difference in the induced voltages. The induced differential voltage is then introduced to a mixer which demodulates the oscillation signals and produce DC signals proportional to the oscillation amplitude.

In the pre-isolator, the LVDT is arranged coaxially with the coil-magnet actuator as illustrated in figure 6.5. The emitter coil is fixed to the top stage and the receiver coils

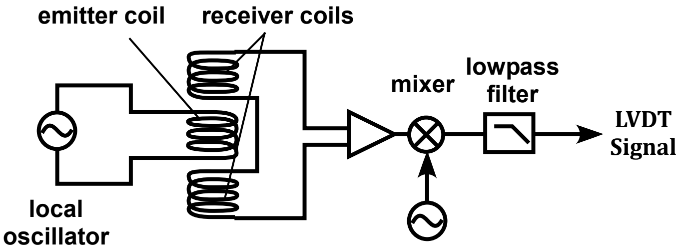

Figure 6.4: Working principle of the LVDT.

are fixed to the outer frame rigidly connected to the ground. The driving circuit of the LVDT used in the experiment is the one developed for advanced Virgo, and the details are described in [90].

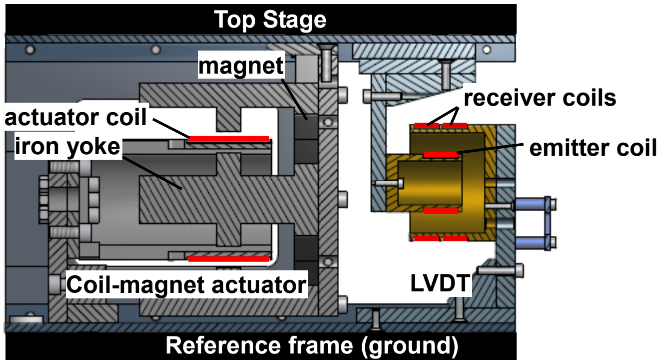

Figure 6.5: A unit of LVDT and coil-magnet actuator mounted on the pre-isolator.

Figure 6.6 shows the calibration result and the readout noise of an LVDT. The LVDT shows a linear response in the range of ±5 mm from the central position with the sensitivity of $\sim$ 2 V/mm. The readout noise of the LVDT is currently limited by the noise in the data acquisition system of the digital system (quantization error in the Analog-to-Digital Converter). The measured noise level at 10 Hz is 4 $\mu\mathrm{V}/\sqrt{\mathrm{Hz}}$, which corresponds to 2 $\mathrm{nm}/\sqrt{\mathrm{Hz}}$ in the displacement noise level.

Geophone

The geophone is a transducer which converts the velocity to voltage signals using electromagnetic induction. The geophone has a mechanical oscillator with a coil inside, and the relative movement between the coil and the permanent magnets attached to the outer frame induces electromotive force in proportion to the relative velocity. In the frequency region higher than the resonant frequency of the oscillator, the induced voltage

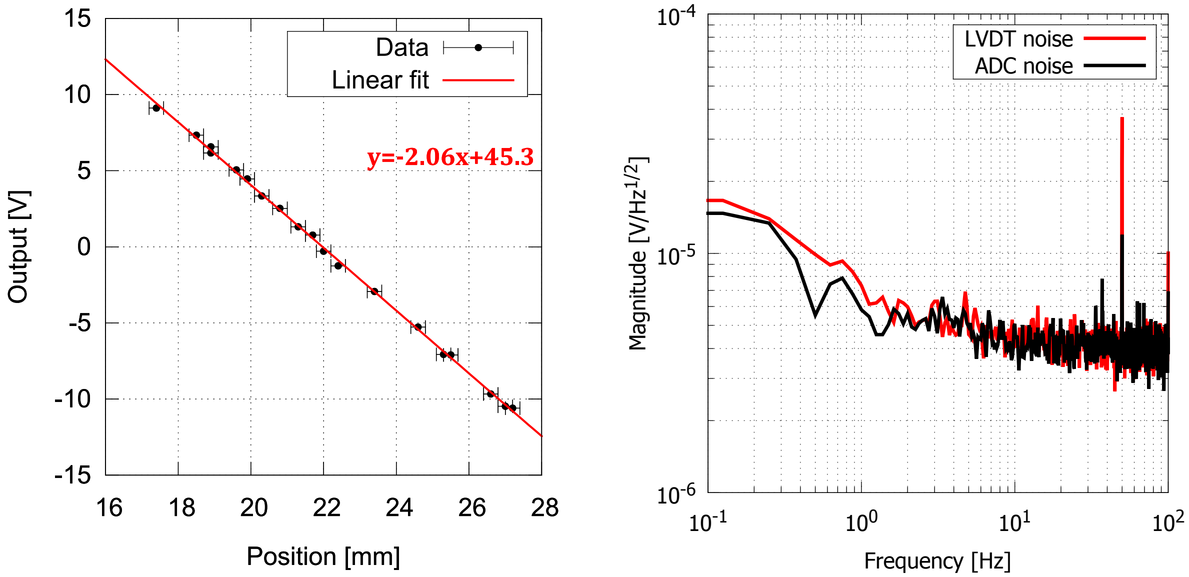

Figure 6.6: (*left*) The calibration result and (*right*) the measured noise level of an LVDT for the IP control.

is proportional to the ground velocity. The geophone itself is a passive device and does not need any controls for the internal oscillator. The frequency response of the geophone to the ground velocity is expressed as

$$H_{\text{geo}}(\omega) = \frac{G_e\omega^2}{\omega_0^2 + 2i\eta\omega_0\omega - \omega^2}, \tag{6.1}$$

where G_e is the generator constant which denotes the sensitivity in the high frequency region, ω_0 is the resonant frequency of the internal oscillator and η is its damping ratio. The nominal parameter of the L-4C geophone and the frequency response are shown in table 6.1 and figure 6.7.

Generator constant (sensitivity)	276 V/(m/sec)
Mass of the oscillator	0.970 kg
Resonant frequency of the oscillator	1.0 Hz
Intrinsic damping ratio	0.28
Coil resistance	5500 Ω

Table 6.1: Nominal parameters of the L-4C geophone.

The induced voltage is amplified by an amplification circuit before being introduced to the control system, and it mostly determines the sensing noise of the ground velocity. The pre-amplifier used in KAGRA-SAS is the one designed in NIKHEF for the advanced Virgo

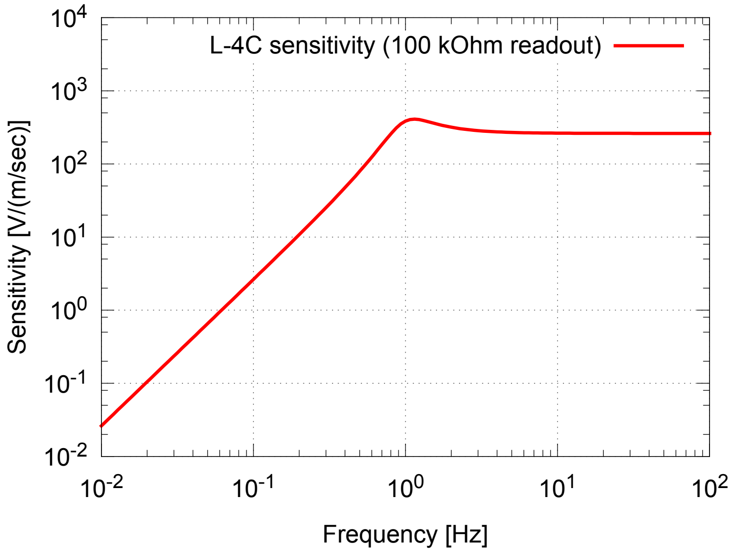

Figure 6.7: Nominal frequency response of the L-4C geophone to the ground velocity.

detector. Figure 6.8 shows a photo of the preamp and the conceptual circuit diagram of the primary amplification stage. The signal from the geophone is amplified by a factor of 376 in the primary stage and then converted to a differential signal with a gain of 5 in the second amplification stage. The operational amplifier CS3002 was chose since it has low voltage noise in the low frequency region (< 0.1 Hz).

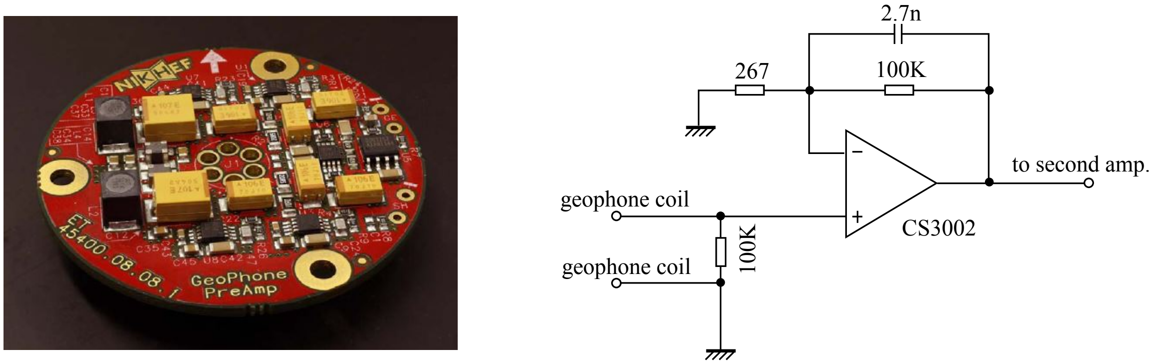

Figure 6.8: (*Left*) A picture of the geophone preamp. (*Right*) The conceptual circuit diagram of the primary amplification stage.

The detection noise is determined by the voltage and current noise of the primary-stage operational amplifier (CS3002), and the thermal noise of the resistance. The power spectrum of the pre-amplifier in the input voltage noise $P_{nn}(f)$ is calculated as follows:

$$P_{nn}(f) = V_{nn}\left(1 + \frac{f_{cv}}{f}\right) + I_{nn}\left(1 + \frac{f_{cc}}{f}\right)R^2 + 4\pi k_B RT. \tag{6.2}$$

The first and second terms are the contribution from the voltage and current noise of the operational amplifier respectively, and the third term is the thermal noise from the resistance (Johnson noise). Here R is the input resistance of the circuit, k_B is the Boltzmann constant and T is the temperature. The noise spectrum of the operational amplifier typically increases in proportion to $1/f$ at the low frequencies and f_{cv}, f_{cc} represent the corner frequencies.

Figure 6.9 shows the noise budget and the measured input voltage noise of the preamp. The measurement is done by closing the pre-amplifier inputs by a resistor of 5500 Ω, which is the resistance of the coil in the L-4C geophone. The curve (1) shows the measurement result when the preamp is exposed to the air and (2) is the result with the preamp packed in a heat insulation box. It is believed that the temperature fluctuation of the preamp due to the thermal ejection from the circuit introduces excess noise below 0.1 Hz due to thermocouple effect or fluctuation of the resistance values. When the preamp is well thermally insulated, the measurement noise fits well with the prediction.

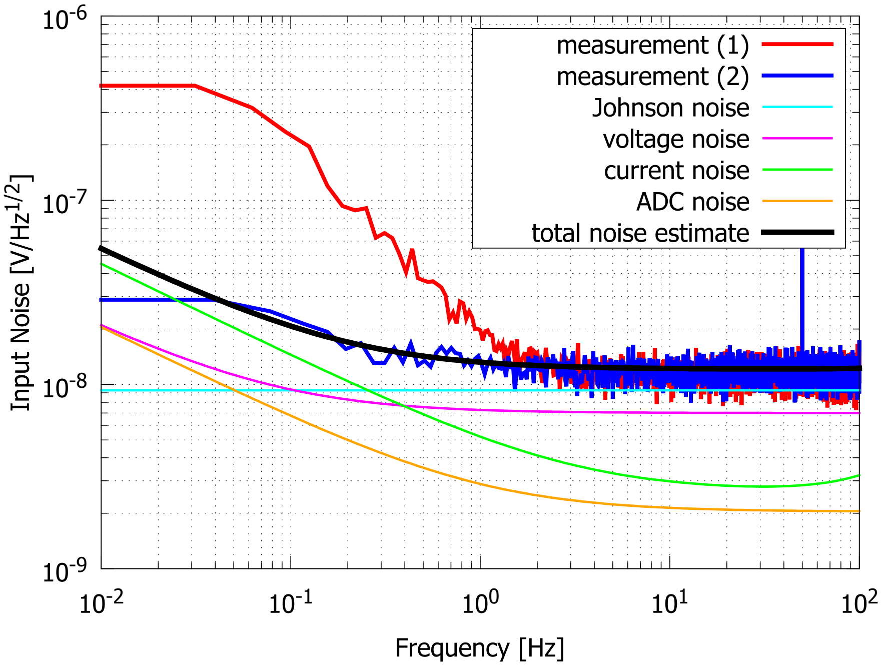

Figure 6.9: The input voltage noise of the geophone preamp. The red and blue lines show the measurement data, while the others show the expected noise spectra.

Coil-magnet actuators

The coil-magnet actuators for the IP control illustrated in figure 6.5 is designed to have constant actuation efficiency over the top stage displacement [74]. The efficiency of each actuator is about 9 N/A. The actuators are driven by homemade coil-driver circuits developed for TAMA-SAS, whose conceptual diagram is shown in figure 6.10. Each actuator provides the maximum force of ∼ 1.4 N, which can move the top stage statically by ±7 mm when the resonant frequency of the IP is tuned at 0.1 Hz.

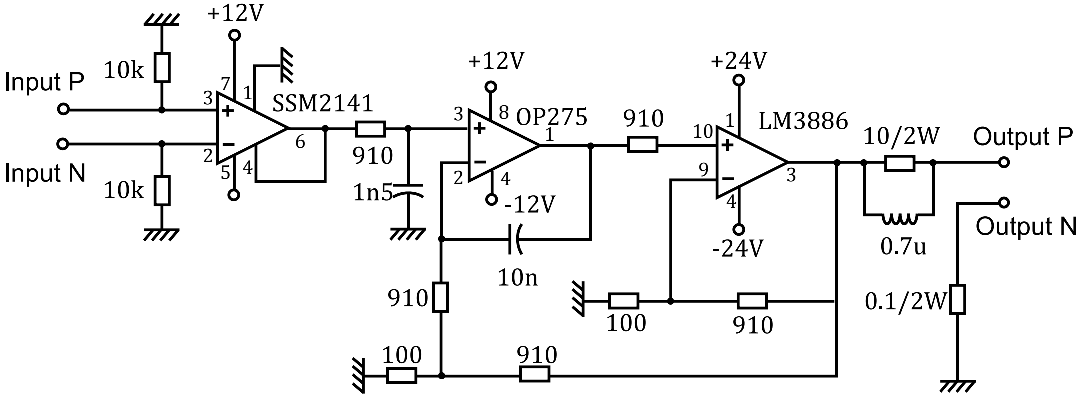

Figure 6.10: Circuit diagram of the coil driver.

6.1.4 Control diagram

The control diagram of the IP pre-isolation stage is shown in figure 6.11. The signals from the LVDTs and geophones are converted to displacement signals by multiplying by calibration factors or the frequency response. The signals are then converted to the top stage displacements in the Cartesian coordinate (x, y, θ) by the 3 × 3 sensor matrix. The signals from two kinds of sensors are blended and sent to the servo filters. The actuation signals in the Cartesian coordinate are converted to the individual actuator signals by the 3 × 3 coil matrix, and then sent to the coil-magnet actuators.

6.1.5 Top stage displacement spectrum

The individual sensor signals (S_1, S_2, S_3) are converted to the displacement vectors in the Cartesian coordinate system (x, y, θ) with the following sensor matrix:

$$\begin{bmatrix} x \\ y \\ r\theta \end{bmatrix} = \underbrace{\begin{bmatrix} 1/3 & 1/3 & -2/3 \\ 1/\sqrt{3} & -1/\sqrt{3} & 0 \\ 1/3 & 1/3 & 1/3 \end{bmatrix}}_{\boldsymbol{S}} \begin{bmatrix} S_1 \\ S_2 \\ S_3 \end{bmatrix}. \tag{6.3}$$

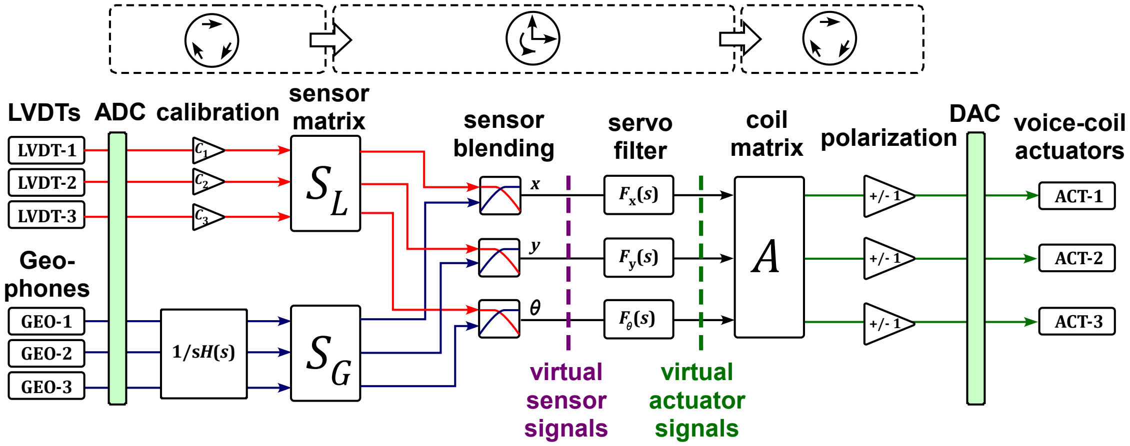

Figure 6.11: Control diagram of the IP.

Here r denotes the distance of the sensor position from the stage center. The distance is $r = 0.7$ m for the LVDTs and $r = 0.5$ m for the geophones.

Figure 6.12 shows the spectra of the top stage vibration induced by seismic vibration and measured by LVDTs, when the IP is tuned at 0.12 Hz. The upper graph shows the displacement spectra in the sensor basis and the lower graph shows the spectra in the Cartesian coordinate. The resonant peaks are separated in the Cartesian coordinate and thus one can extrapolate the eigenmodes corresponding to the resonant peaks. At the bottom right of figure 6.12, the eigenmodes predicted from the rigid-body model are illustrated. The sharp resonance at 0.37 Hz corresponds to the pendulum modes of the payload, and that mainly contributes to the RMS displacement of the top stage.

6.1.6 Actuator diagonalization

In order to control the top stage motion in the Cartesian coordinate basis (x, y, θ), it is necessary to know the required contributions from individual actuators for moving the top stage in each direction. The process of determining the weights is often called the actuator diagonalization. The desired displacement induced by the virtual actuators in respective DoFs (u_x, u_y, u_θ) is converted to the real actuators signals (A_1, A_2, A_3) by the diagonalization matrix (coil matrix) $\boldsymbol{D}$ as

$$\begin{bmatrix} A_1 \\ A_2 \\ A_3 \end{bmatrix} = \underbrace{\begin{bmatrix} D_{1,x} & D_{1,y} & D_{1,\theta} \\ D_{2,x} & D_{2,y} & D_{2,\theta} \\ D_{3,x} & D_{3,y} & D_{3,\theta} \end{bmatrix}}_{\boldsymbol{D}} \begin{bmatrix} u_x \\ u_y \\ u_\theta \end{bmatrix}. \tag{6.4}$$

When A_1-A_3 represents the voltages sent to the actuator, the matrix elements have units of [V/m]. The matrix $\boldsymbol{D}$ is determined by the following procedure:

1. The diagonalization matrix $\boldsymbol{D}$ is chosen arbitrarily. One can for instance plug in the 3×3 identity matrix for $\boldsymbol{D}$ as a first guess.

2. Each virtual actuator is driven by a sinusoidal wave with a frequency f_{D} well below the resonant frequencies of the suspension system ($f_{\mathrm{D}} = 10$ mHz is adopted in this experiment), and the induced displacements (x, y, θ) are measured. The magnitude of the transmission between the measured displacements and the excitation signals is calculated and used to populate the following transfer coefficient matrix $\boldsymbol{E}$:

$$\boldsymbol{E} = \left[\begin{array}{ccc} \tilde{x}/\tilde{u}_x & \tilde{x}/\tilde{u}_y & \tilde{x}/\tilde{u}_\theta \\ \tilde{y}/\tilde{u}_x & \tilde{x}/\tilde{u}_y & \tilde{x}/\tilde{u}_\theta \\ \tilde{\theta}/\tilde{u}_x & \tilde{\theta}/\tilde{F}_y & \tilde{\theta}/\tilde{u}_\theta \end{array} \right]_{f=f_D} . \tag{6.5}$$

3. The diagonalization matrix is updated by multiplying with the inverse of $\boldsymbol{E}$: $\boldsymbol{D}_{\mathrm{new}} = \boldsymbol{E}^{-1}\boldsymbol{D}_{\mathrm{old}}$.

4. Steps 2 and 3 are repeated until the couplings between the different DoFs are well suppressed. When the system is perfectly diagonalized, $\boldsymbol{E}$ becomes the identity

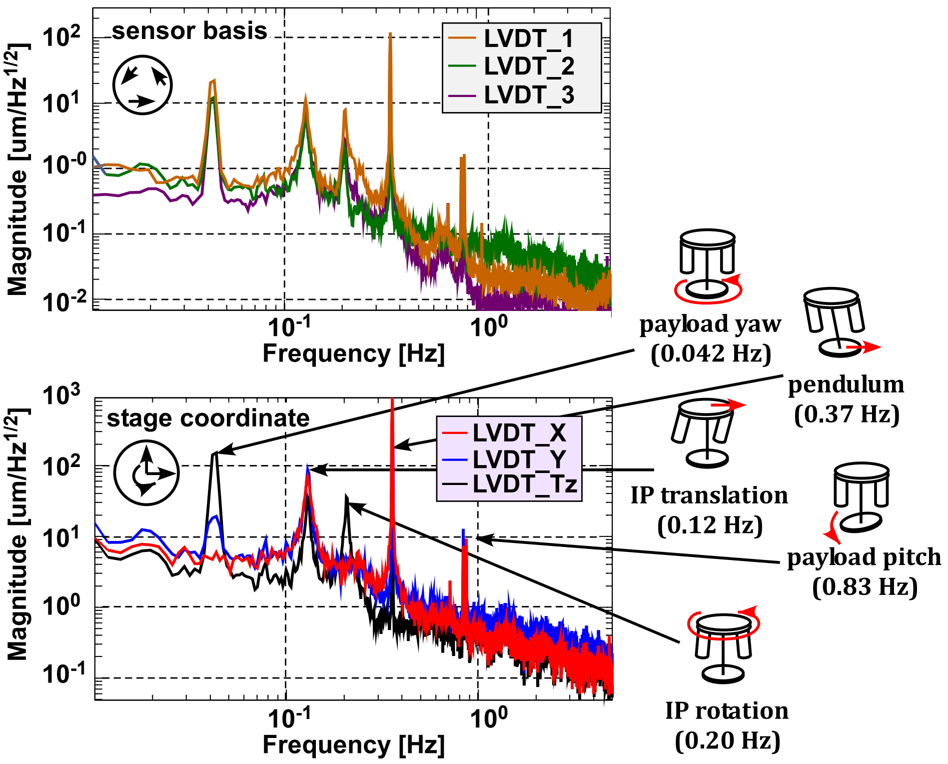

Figure 6.12: The top stage vibration measured by LVDTs and identification of the mechanical resonances.

matrix and the excitation signal $\tilde{u}_x$ coincides with the induced displacement $\tilde{x}$. In the prototype test, the diagonalization process was repeated until the non-diagonal elements of the matrix $\boldsymbol{E}$ were suppressed below 10^{-2}.

Figure 6.13 shows the transfer functions from the diagonalized virtual actuators to the top stage displacements, measured by injecting white noise into the virtual actuators. The couplings at low frequencies were suppressed to lower than 1%, while the couplings were larger around and above the resonant frequencies. Since the effective stiffness of the three IP flexures had asymmetry, the actuators diagonalized at a low frequency does not provide pure translation forces in x, y directions or torque around the vertical axis.

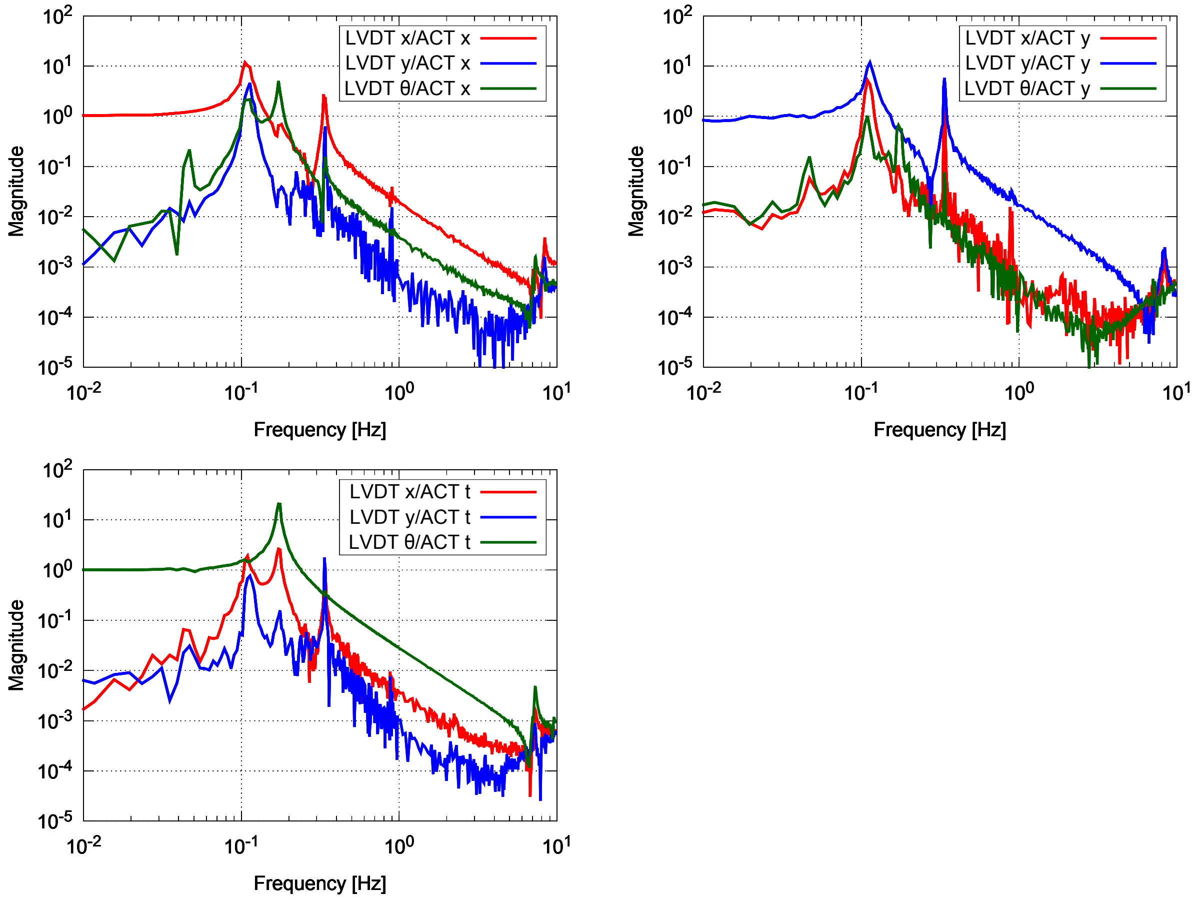

Figure 6.13: Measured transfer functions from the diagonalized virtual actuators to the top stage displacements.

6.1.7 Isolation performance of IP

The passive vibration isolation performance of the IP stage is measured by comparing the top stage vibration with the IP base vibration taken by L-4C geophones. Figure

6.14 shows the measurement results. The measured transfer function fits well with the predicted curve below 5 Hz and the isolation ratio reaches $\sim 10^{-3}$ around 5 Hz. However, the measured transfer function deviates from the prediction and the vibration isolation ratio is degraded in the high frequency region. A possible reason is that the vibration at high frequencies is dominated by the coupling from the tilt of the IP base and the top stage.

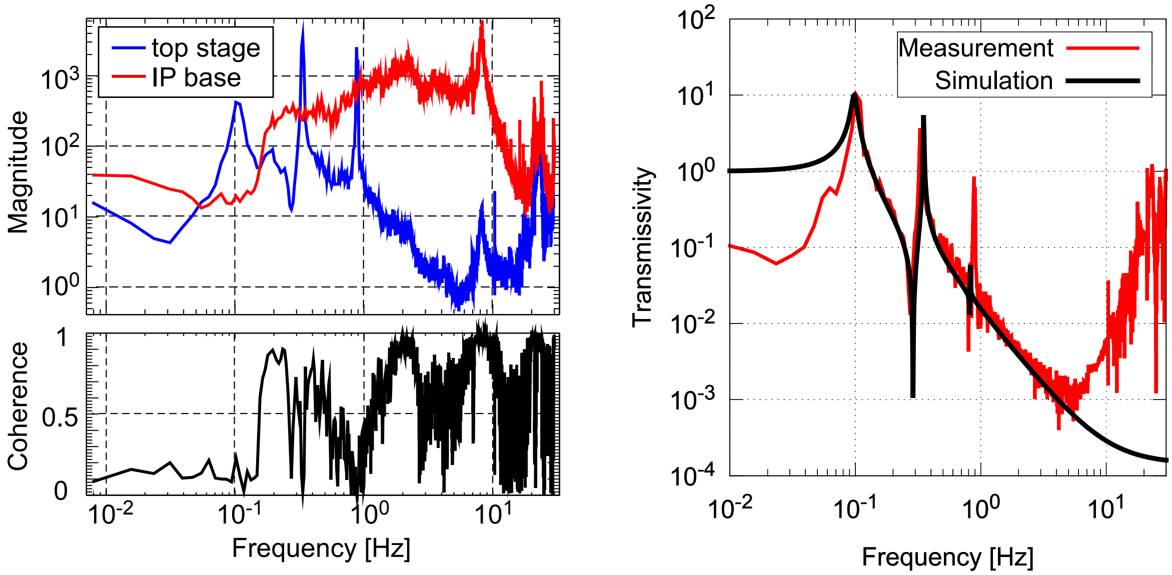

Figure 6.14: The isolation performance measurement of the IP pre-isolation stage. (*Left*) Measured vibration spectra of the top stage and the IP base, and the coherence between the signals. (*Right*) The measured vibration transfer function and the prediction by the rigid-body model.

6.1.8 Damping control demonstration

As a simple demonstration of the IP control, simple damping filters were introduced to the servo loops for the respective DoFs. Figure 6.15 shows the design of the servo filter used for the control test. It has a frequency response proportional to f at low frequencies, aiming to damp the mechanical resonances in the 0.1-1 Hz band, and the gain is cut off above 10 Hz to avoid noise injection at high frequencies.

Figure 6.16 shows the displacement noise spectra of the top stage in a stationary state, with and without the damping control. The control signals are taken only from LVDTs and the sensor blending filters are switched off in this measurement. Mechanical resonances at 0.1-1 Hz are nicely suppressed and some of them are critically damped by the active controls.

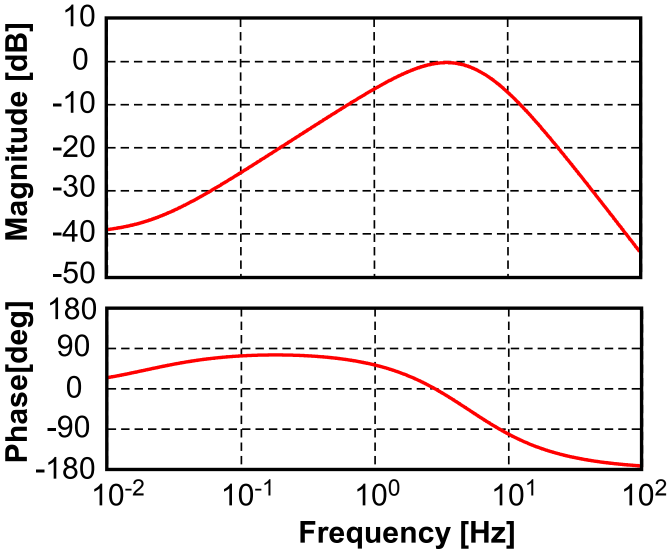

Figure 6.15: The servo filter designed for the simple damping test.

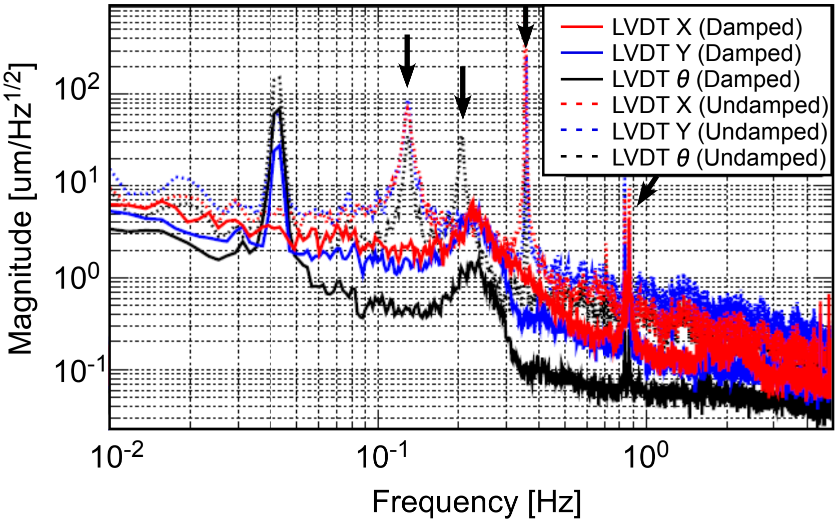

Figure 6.16: The top stage displacement measured by LVDTs, with and without the damping control using LVDT signals.

Figure 6.17 shows the longitudinal displacement spectra of the top stage measured by the out-of-loop geophone sensor. In this measurement, two kinds of control loops are tested; one utilizing LVDTs and the other utilizing geophones as feedback sensors. When the LVDTs are used for the feedback controls, re-injection of the seismic vibration occurs and thus the attenuation performance above 0.1 Hz is degraded. Such degradation of the attenuation performance does not occur when the geophones are used as feedback sensors. Owing to the suppression of the resonant peaks at 0.10 and 0.34 Hz, the RMS displacement of the top stage (integrated down to 0.1 Hz) is suppressed by a factor of ~ 3 with the LVDT controls and ~ 10 with the geophone controls.

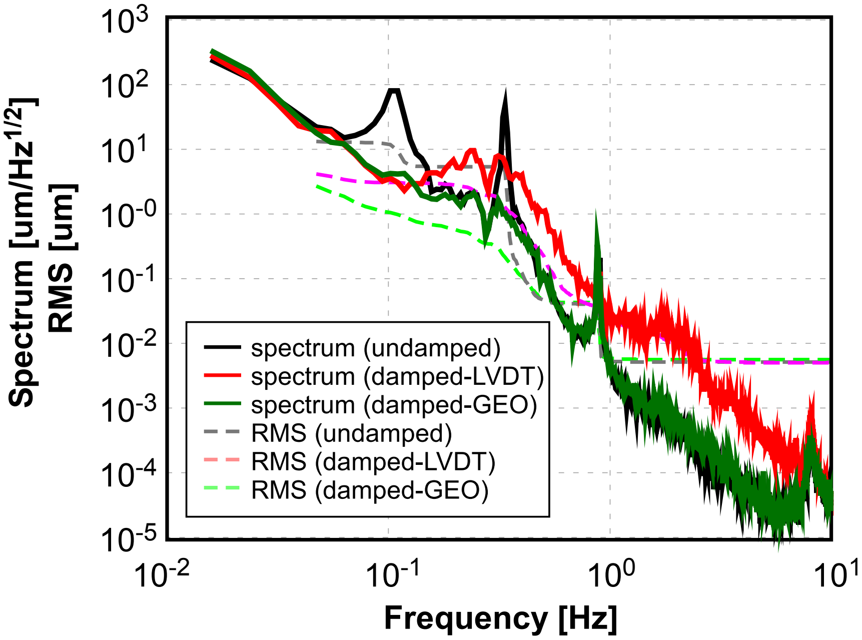

Figure 6.17: The top stage longitudinal displacement measured by the observer geophone, with and without the damping control.

6.2 Standard GAS filter

The experiment described in this section checks out the mechanical properties of the standard GAS filter and its vibration isolation performance. The capability to damp the torsion modes of the GAS filter chain is also investigated.

6.2.1 GAS filter setup and basic characteristics

Figure 6.18 shows a picture of the prototype standard GAS filter investigated in the following tests. The prototype filter equips with six standard GAS blades made of maraging steel (see figure 4.9). The blades are connected to the central keystone, and a dummy payload is suspended from it with a maraging steel wire. The weight of the payload is tuned so that the keystone stays in the operation point. The optimal load for the prototype GAS filter is measured as 232 kg, and thus the nominal load for one GAS blade is 38.7 kg, which is ∼2% lighter than the expected value from an FEM.

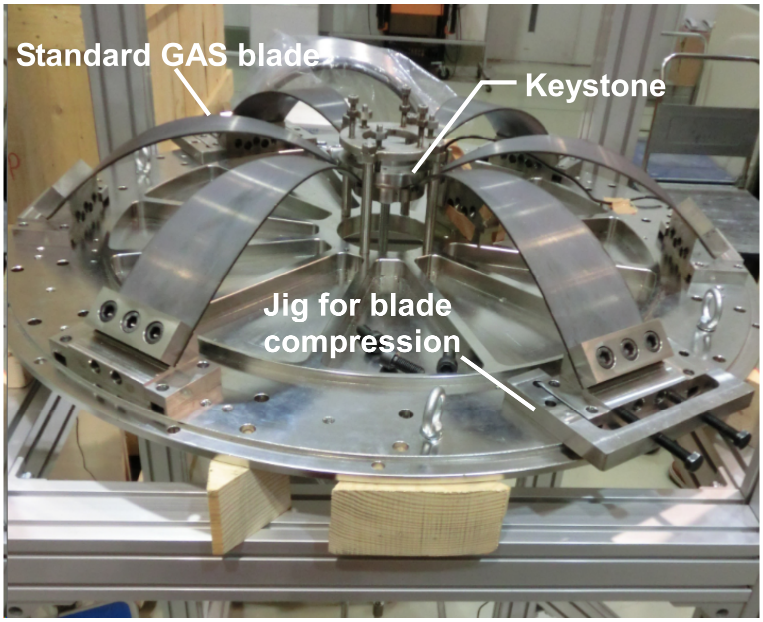

Figure 6.18: A picture of the prototype GAS filter.

The horizontal compression of the blades was adjusted by using a jig which pushes the blade base in the radial direction with two screws. The blades were compressed symmetrically so that the keystone is not horizontally displaced or tilted. As the blade is radially compressed, the resonant frequency of the GAS filter is lowered by the anti-spring effect. Figure 6.19 shows the measured resonant frequency versus the average radial compression distance of the blades. The resonant frequency would be nulled when the compression reaches 17 mm, but in practice the frequency was not able to be decreased lower than ∼0.15 Hz as the GAS filter showed hysteretic behavior and instability.

Figure 6.20 shows the temperature dependence of the vertical working point of the GAS filter, taken by monitoring the keystone position and temperature in a long term. The resonant frequency of the GAS filter was tuned at 0.33 Hz in this measurement. The vertical displacement of the keystone was measured by the LVDT. The measured temperature dependence was 0.70 mm/K, which is consistent with the expected value from equation (3.14).

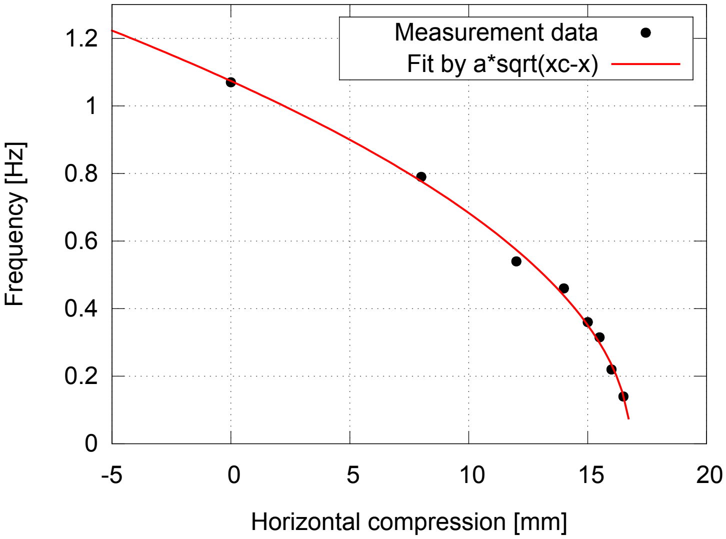

Figure 6.19: Transition of the resonant frequency as a function of radial compression of the GAS blades.

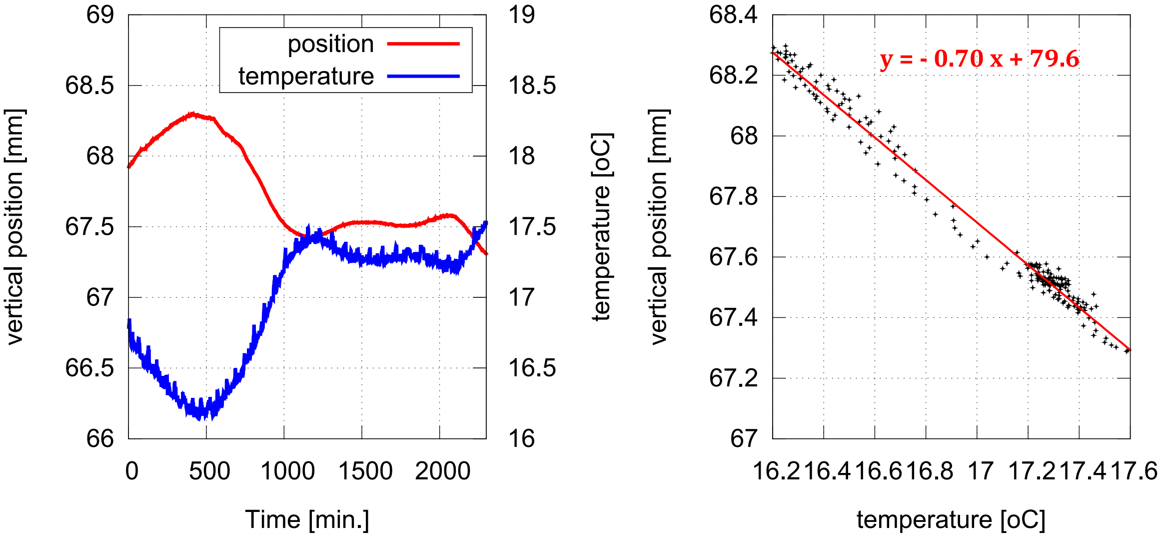

Figure 6.20: The thermal drift measurement of the GAS filter.

6.2.2 Vibration isolation performance measurement

In order to investigate the vibration isolation performance of the prototype GAS filter, a measurement setup illustrated in figure 6.21 was constructed. The base plate of the GAS filter was suspended from a rigid metal frame by four coil springs and its vertical motion was driven by a voice-coil actuator with a sinusoidal excitation signal. Vibration at the filter and the suspended payload was measured by piezoelectric accelerometers SA-710 from TEAC. These accelerometers contain FET pre-amplifiers inside, and the power supply to the preamp and signal readout are done by a TEAC SA-610 amplifier box. In order to avoid couplings from tilt modes, the accelerometers were attached in the same axis as that of the suspension wire. The attenuation performance of the GAS filter was obtained by taking the ratio of the two acceleration signals. The frequency of the excitation signal was swept so that the frequency response of the attenuation ratio was obtained. The measurement was taken by an HP35670A spectrum analyzer.

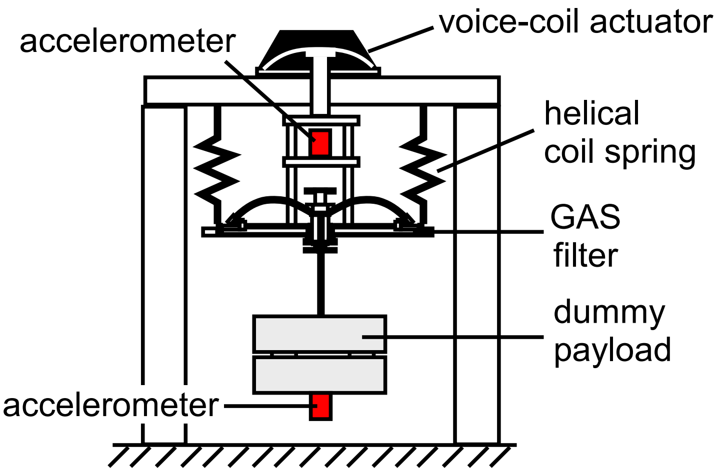

Figure 6.21: Experimental setup of the attenuation ratio measurement of the prototype GAS filter.

Figure 6.22 shows the measured transfer function of the prototype GAS filter, when the resonant frequency was tuned at 0.58 Hz. The measurement data fit well with the prediction curve below 30 Hz, and the attenuation ratio reaches $\sim 10^{-3}$. The performance is degraded in a high frequency region due to the internal resonances of the GAS filters and measurement systems. The large resonant peak observed at 70 Hz corresponds to the drum mode of the base plate, which affected the measurement since the accelerometer was attached to the center of the base plate while the GAS blades are clamped to the base plate at the circumference. Note that this drum mode would not affect the attenuation performance in actual suspension systems, since the vibration from the upper stage is transmitted to the circumference of the base plate through the outer shielding (the cap of the GAS filter, see figure 4.8).

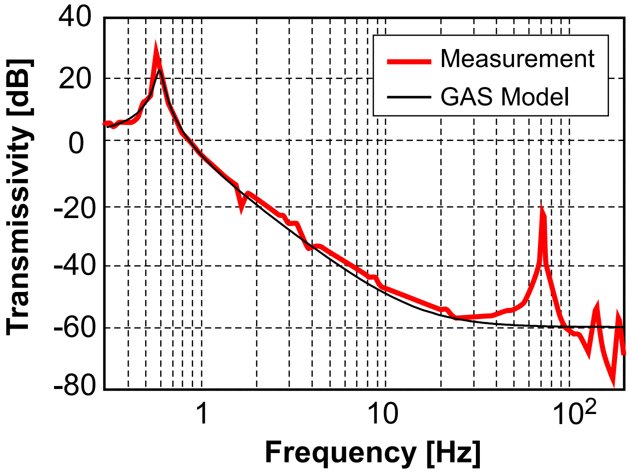

Figure 6.22: Measured transfer function of the prototype GAS filter.

6.2.3 Magic wand and attenuation ratio improvement

In order to improve the attenuation performance of the GAS filter, the compensation wand with counter weights (the so-called magic wand) is introduced. Figure 6.23 shows a picture of the magic wand on the prototype system. A rigid cylindrical bar made of silicon carbide is hinged to the central keystone, and a counter-weight M_{cw} is attached to the other end of the cylindrical bar. The bar is hinged to the based plate in the middle point which divides the segment between the keystone and the counter-weight by $L : l$. When the mass of the bar m_{w} is neglected, the transfer function of the GAS filter with the magic wand is [62]

$$H_{\mathrm{GAS}}(\omega) = = \frac{{\omega_0}^2(1+i\phi) - \beta\omega^2}{{\omega_0}^2(1+i\phi) - \omega^2} \tag{6.6}$$

$$\beta = \frac{1}{M}\left[m_b - M_{\mathrm{cw}}\frac{l(L+l)}{L^2}\right] \tag{6.7}$$

Here M is the payload mass supported by the GAS filter, ω_0 is the resonant frequency, m_b is the effective mass of the GAS blades affecting the attenuation performance. The parameters used in the prototype test is summarized in table 6.2. The effective mass of the blade is estimated from the saturation level without the magic wand ($\beta = m_b/M \sim 10^{-3}$).

Figure 6.24 shows the measured transfer function amplitudes with the magic wand. In this measurement, the top accelerometer is moved to the circumference of the base plate, to avoid the drum mode coupling at 70 Hz. The attenuation ratio in the 20-100 Hz region is improved by ~ 10 dB by introducing the magic wand and could be further improved by adding more counter-weight. The attenuation performance in the high frequency region (>100 Hz) is not improved, since the transfer function is dominated by internal resonance

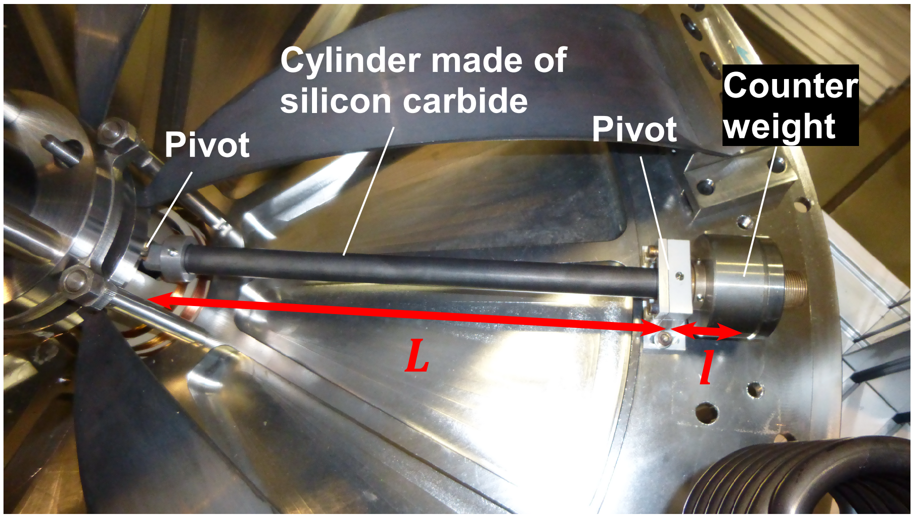

Figure 6.23: Magic wand introduced to the prototype GAS filter.

M	Payload mass	232 kg
m_b	Effective mass of blade	0.23 kg
m_w	Magic wand mass	0.053 kg
M_{CW}	Counter-weight mass	$0.3 - 0.5$ kg
L	Length between keystone and pivot	280 mm
l	Length between pivot and CW	50-65 mm

Table 6.2: The parameters about the magic wand

couplings in this region. Note that the notch and peak appearing at 100 Hz are caused by the internal resonances of the helical coil springs, and would not appear in an actual system. The resonances at higher frequencies would be related to the mechanical resonances of the suspension system, such as violin modes and bounce modes of the suspension wire.

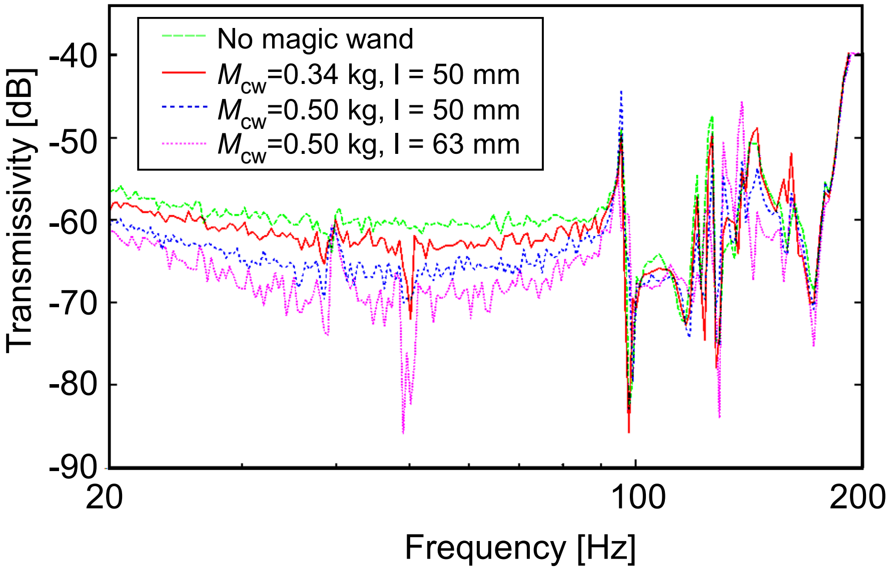

Figure 6.24: Measured transfer function of the GAS filter with magic wands.

6.2.4 Torsion mode damping

The magnetic damper introduces braking torques on the standard GAS filter for damping the torsion modes of the attenuation chain. The efficiency of the torsion mode damper was experimentally checked using the prototype GAS filter suspended by a single wire as illustrated in figure 6.25. The GAS filter was suspended from the top plate by a single wire made of maraging steel. The diameter and length of the wire were 4.5 mm and 0.7 m, respectively. The prototype GAS filter had a copper ring with 8 mm thickness on top of it. The magnetic damper was suspended from the top plate by three maraging-steel wires and placed just above the copper ring. The damper consisted of an iron ring with 15 mm thickness and a number of 1-cm cubic neodymium magnets attached on the bottom of it. The yaw motion of the GAS filter was sensed by a handmade photo-reflective sensor, whose working principle is illustrated in figure 7.13. The sensor signals were sent to the SR560 pre-amplifier to remove the unnecessary high frequency components and then introduced to the DL850 logger to acquire the data with a sampling rate of 10 Hz.

Figure 6.26 shows a typical decay signal of the torsion mode. The resonant frequency of the mode was about 0.14 Hz. The signal was fitted to an exponentially decaying sine

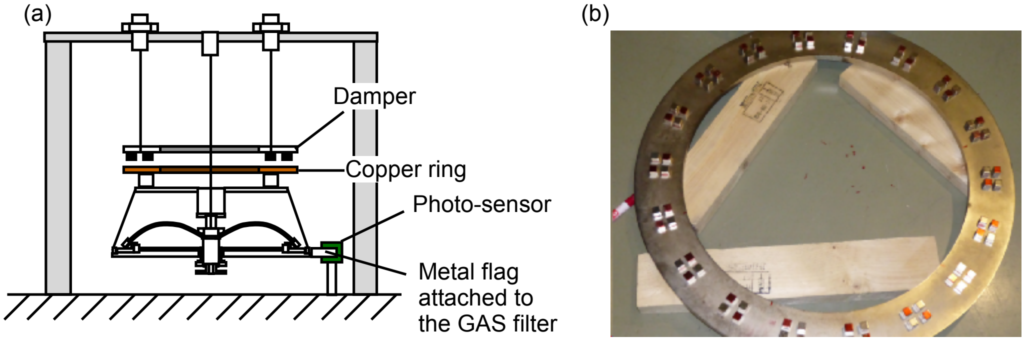

Figure 6.25: (a) Experimental setup of the torsion mode damping test. (b) A picture of the magnetic damper with 72 neodymium magnets attached.

wave and the $1/e$ decay time constant (τ [sec]) was extracted. The damping coefficient of the magnetic damper γ [kgm^2/sec] can be calculated from the decay time constant:

$$\gamma = \frac{2I_z}{\tau}, \tag{6.8}$$

where I_z is the moment of inertia of the GAS filter, which was estimated from the 3D CAD drawing as 6.7 kg m^2. Note that the decay time of the torsion mode without the magnetic damper is $\tau = 9.1 \times 10^3$ sec.

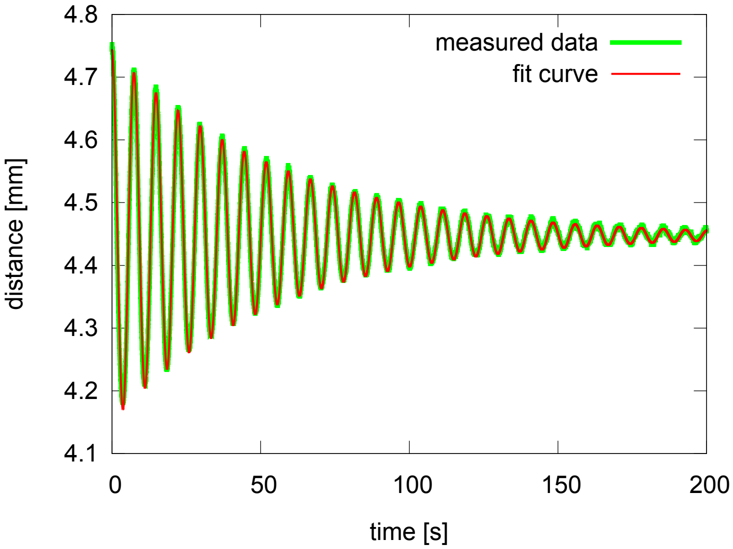

Figure 6.26: A typical decay signal of the torsion mode.

Figure 6.27 shows the measured damping coefficients with different numbers of magnets and different distances between the magnets and the copper ring. The damping strength depends on the relative distance, because the magnetic field on the copper ring increases as it approaches the magnets. The torsion mode is damped in a few cycle when the damping coefficient reaches $\sim$ 2 kgm^2/sec. For the efficient damping of the torsion modes of the GAS filter chain, the damping coefficient of 2-4 kgm^2/sec is required. This can be achieved by placing 72 magnets on the damper and setting the distance between the magnet and copper plate at $\sim$ 5 mm.

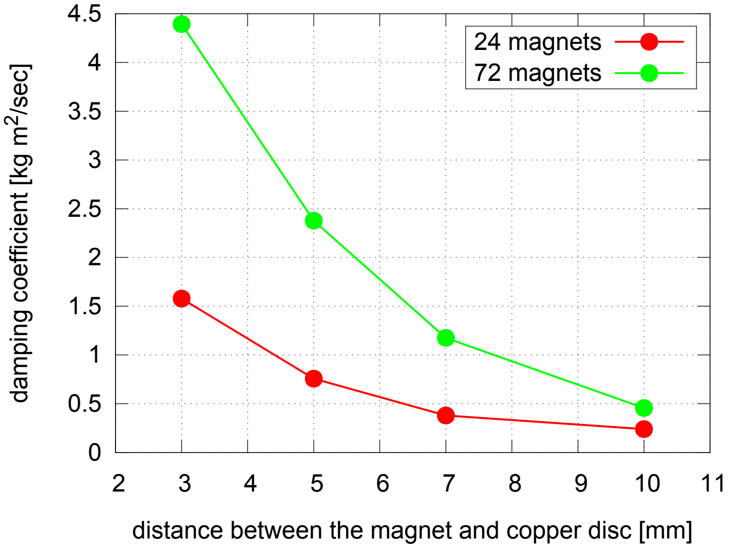

Figure 6.27: Measured damping coefficients of the magnetic damper about yaw motions.

6.3 Payload prototype

This section describes the mechanics and electronics of the payload prototype, and some preliminary tests for verifying the soundness of the mechanical responses and control systems.

6.3.1 Mechanical overview

Figure 6.28 shows a picture and 2D drawing of the payload prototype constructed for the performance test. It consists of a dummy mirror made of aluminum instead of silica, the recoil mass (RM), the intermediate mass (IM), the intermediate recoil mass (IRM) and the bottom GAS filter. The mass of the dummy mirror is adjusted to that of the actual mirror (10.7 kg), by adding a number of bore holes for compensating the density difference of glass and aluminum.

The dummy mirror, which is conventionally called the test mass (TM) in this section, and RM are each suspended by two loops of metal wires. The wires for TM are 0.2 mm

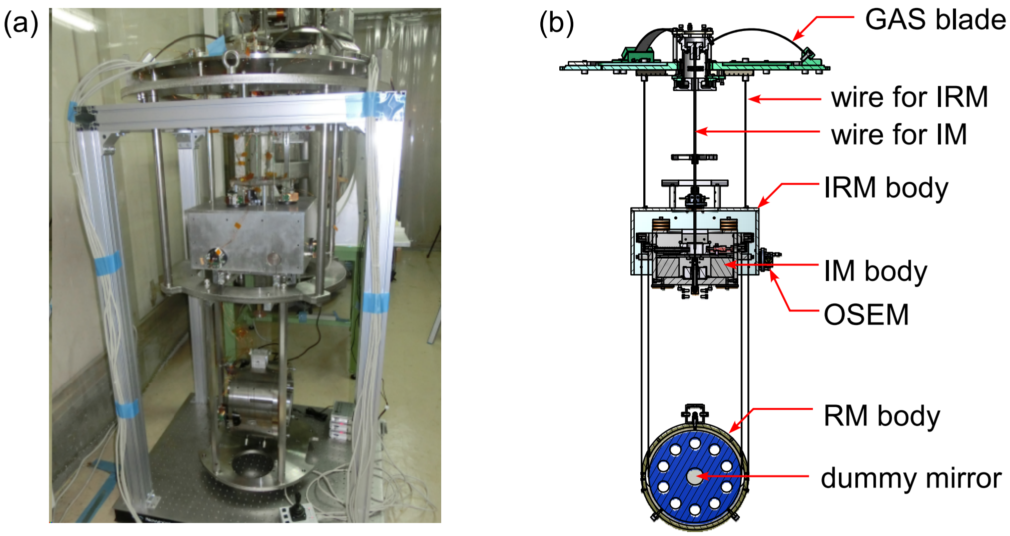

Figure 6.28: (a) The picture and (b) 2D rawing of the payload prototype.

in thickness and made of high-carbon steel (piano-wire). The wires for RM are 0.6 mm in thickness and made of tungsten. The length of the wires is about 580 mm. The two loops of wires are separated by a distance of 10 mm in the TM suspension and 20 mm in the RM suspension, which determines the pitch stiffness of the TM and RM. The suspension wires are clamped onto the IM body at the same height of the nominal center of mass of IM.

Figure 6.29 shows a cross section view of the IM. The IM is suspended from the bottom filter with a single maraging steel wire to allow softness in controlling the three rotational DoFs. The suspension wire is hooked into a piece whose lower section is screwed into the IM floor. This device provides the means to adjust the height of the suspension point and thus to change the stiffness in the pitch and roll motions. The height of the suspension is adjusted so that the resonant frequency of the IM pitch mode becomes 0.3-0.4 Hz. The IM houses mechanisms for remotely tuning the IM tilt in pitch and roll. The mechanism is composed of a stainless steel body of $\sim$ 1 kg mass that moves back and forth under the action of a picomotor and a spring compressing the body against the picomotor. The mechanism for tuning the roll angle is illustrated in figure 6.29. The tuning masses attached on the top of the IM are used for adjusting the total weight of IM, RM and TM to the optimal load of the GAS filter ($\sim$ 50 kg). The IRM is suspended from the base plate of the bottom GAS filter by three maraging steel wires.

6.3.2 OSEM

In order to monitor the movement of the suspended bodies and damp the mechanical resonances, the payload is provided with Optical Sensor and Electro-Magnetic actuators

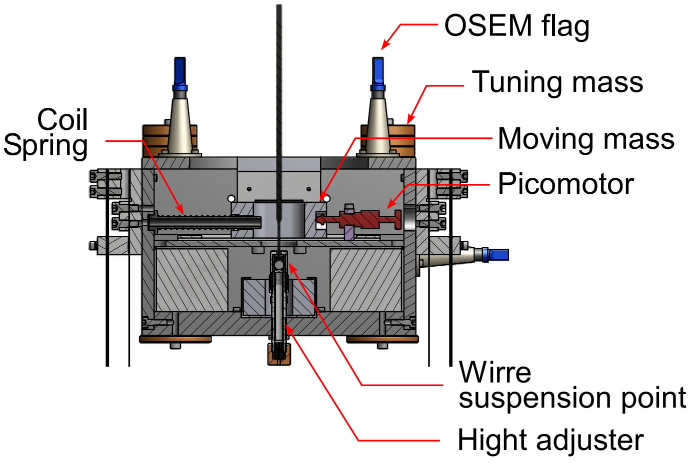

Figure 6.29: A cross section view of the IM.

(OSEMs). The payload contains ten OSEMs in total; six mounted on the IRM and four on the RM. They are used for controlling the rigid-body motions in three DoFs (longitudinal, pitch and yaw) at the TM level and six DoFs (longitudinal, transverse, vertical, pitch, roll and yaw) at the IM level. Disposition of the OSEMs at the IM and TM levels is illustrated in figure 6.30.

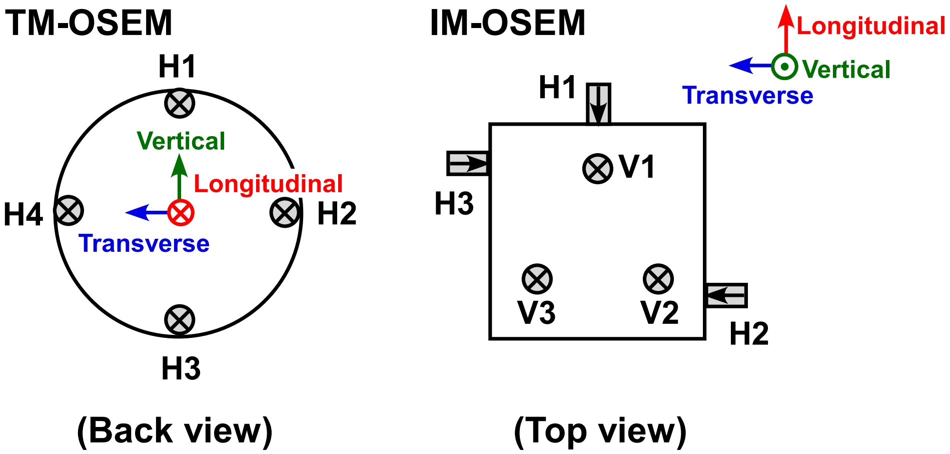

Figure 6.30: Disposition of the OSEMs at the IM and TM levels.

Figure 6.31 shows drawings of the OSEM. The OSEM is a shadow sensor and coil-magnet actuator. The sensing part consists of an LED (Optek OP232), a photodiode (Hamamatsu S1223-01), a collimation lens, and an aluminum flag which shadows the light emitted from the LED. The optics are fixed to the OSEM body which is attached to the RM or IRM, while the flag is attached to the TM or IM. The movement of the flag along the longitudinal axis changes the amount of light reaching the photodiode and thus one can detect the relative displacement between the OSEM body and the flag. The flag also contains a permanent magnet inside and the force can be applied by an actuator coil wounded on the OSEM body. The OSEMs for the TM and IM use different sizes of neodymium magnets: $\phi 6 \times$ t3 mm for TM and $\phi 10 \times$ t10 mm for IM, since the actuators on the IM require stronger control forces.

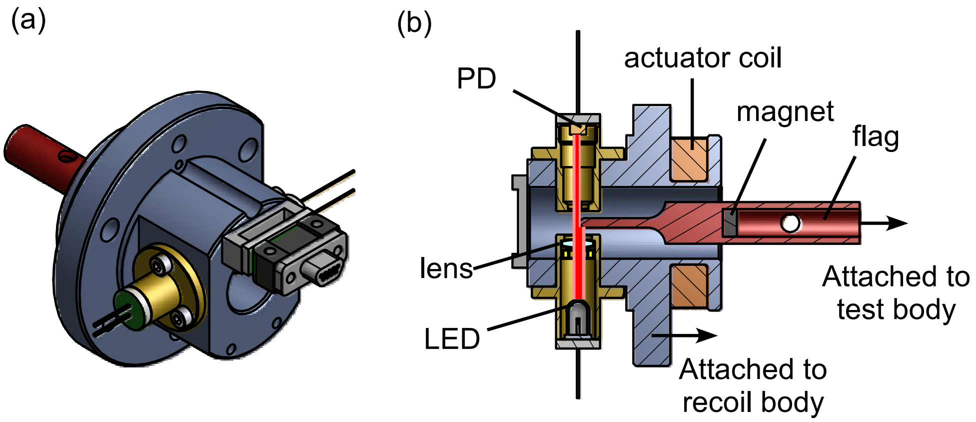

Figure 6.31: (a) An isometric and (b) cutaway drawings of the TM-OSEM.

Figure 6.32 shows the calibration results of several OSEM shadow sensors. The shadow sensor provides linear response and maximum sensitivity around the point where the flag blocks half of the LED light. The obtained sensitivity around the point is 7-8 V/mm in the linear range of ±0.5 mm. Figure 6.33 shows the noise spectra of the sensors taken by the digital system. The achieved noise level is 2 nV/$\sqrt{\text{Hz}}$ at 1 Hz and 0.8 nV/$\sqrt{\text{Hz}}$ at 10 Hz. The high frequency noise is limited by the quantization errors in ADCs, while the low frequency noise is limited by the electronic noise in the readout circuits.

The actuation efficiency of the coil-magnet actuator changes as the permanent magnet is displaced with respect to the coil. Figure 6.34 shows measured actuation efficiency of the coil-magnet actuator in an IM-OSEM, with different axial position of the permanent magnet. The actuator provides the maximum efficiency at the point 6.2 mm from the coil center. The OSEM flag is designed so that the nominal position of the flag providing the maximum sensitivity of the shadow sensor coincides with the position giving the maximum actuation efficiency.

6.3.3 Control diagram

The control diagram of the payload prototype is shown in figure 6.35, which is similar to the control diagram of the IP. The main difference from the IP control is that there is

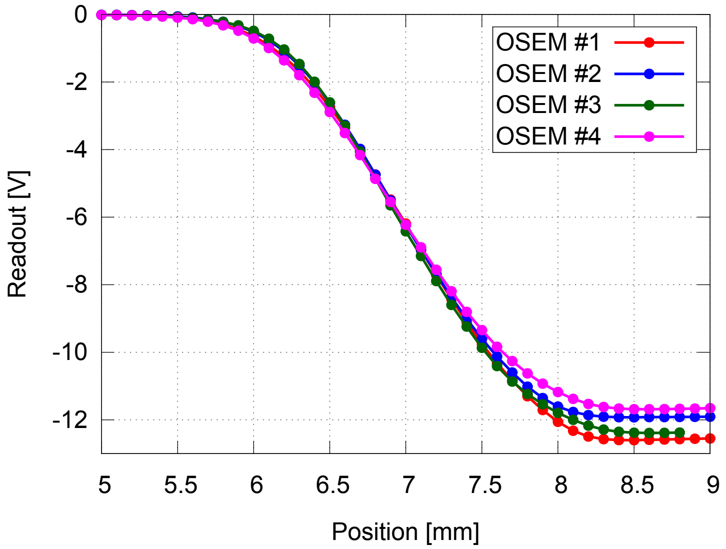

Figure 6.32: Calibration results of the OSEM shadow sensors.

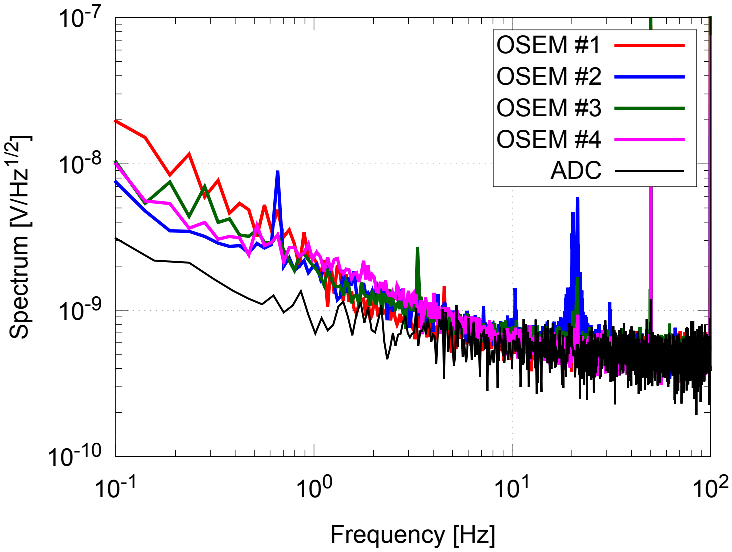

Figure 6.33: Measured noise level of the OSEM shadow sensors.

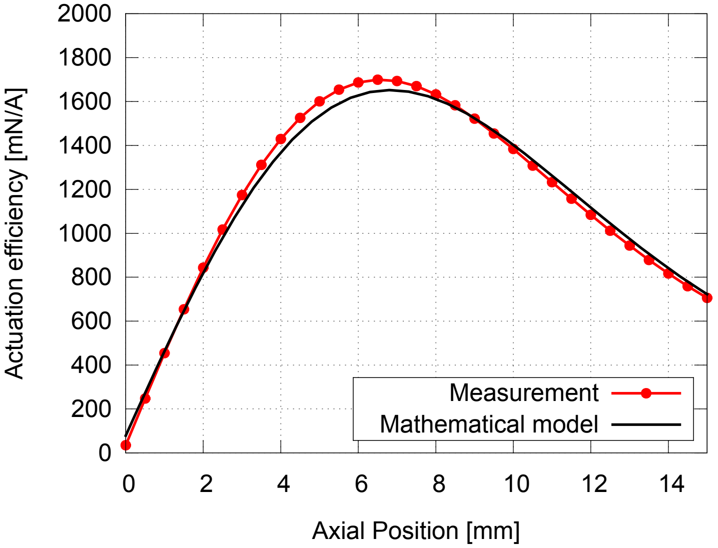

Figure 6.34: Efficiency of the coil-magnet actuator for an IM-OSEM, as a function of the magnet position.

no sensor blending in the payload control. The signals from ten OSEM shadow sensors are calibrated to displacement signals and then converted to the virtual sensor signals in 6 DoFs of IM and 3 Dofs of TM with 6 × 6 and 4 × 3 sensing matrices. The virtual actuator signals in respective DoFs are distributed to the real actuators with the coil matrices and excite the motions.

The sensing matrices converting the real sensor signals to the virtual sensor signals are shown in equations (6.9) and (6.10). The names of the coordinate variables (L, T, V, R, P, Y) are taken from the first letters of the terminology: longitudinal, transverse, vertical, roll, pitch and yaw. The elements of the coil matrices are determined by the actuator diagonalization as described in subsection 6.1.6. The actuators were diagonalized at 100 mHz for the TM level and 30 mHz for the IM level.

$$\begin{bmatrix} L_{\rm TM} \\ P_{\rm TM} \\ Y_{\rm TM} \end{bmatrix} = \underbrace{\begin{bmatrix} 0.25 & 0.25 & 0.25 & 0.25 \\ 0.5 & 0 & -0.5 & 0 \\ 0 & 0.5 & 0 & -0.5 \end{bmatrix}}_{\boldsymbol{S}_{\rm TM}} \begin{bmatrix} S_{\rm TM-OSEM,H1} \\ S_{\rm TM-OSEM,H2} \\ S_{\rm TM-OSEM,H3} \\ S_{\rm TM-OSEM,H4} \end{bmatrix}, \tag{6.9}$$

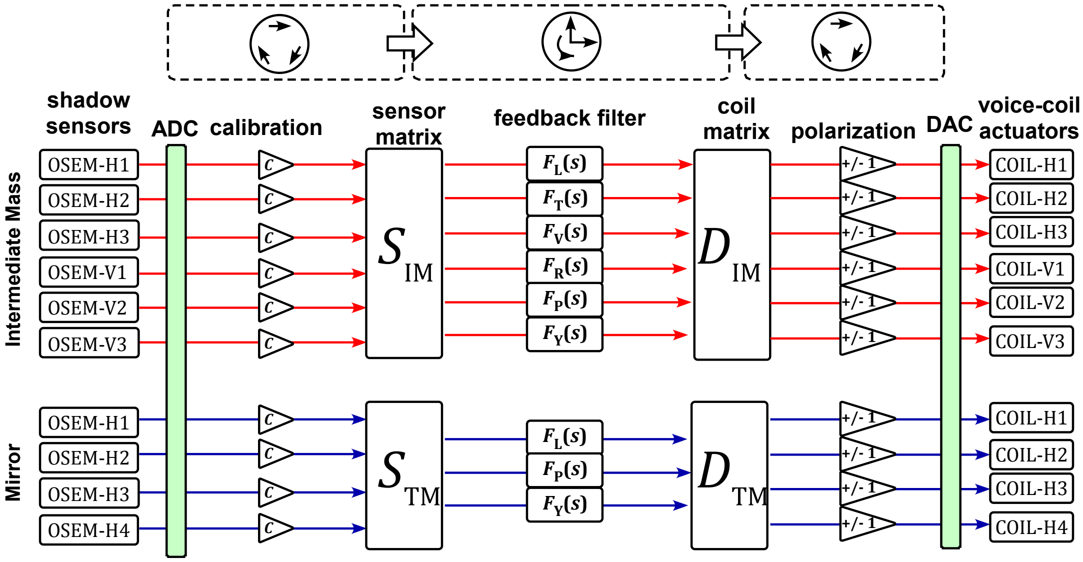

Figure 6.35: Control diagram of the payload prototype.

$$\begin{bmatrix} L_{\mathrm{IM}} \\ T_{\mathrm{IM}} \\ V_{\mathrm{IM}} \\ R_{\mathrm{IM}} \\ P_{\mathrm{IM}} \\ Y_{\mathrm{IM}} \end{bmatrix} = \underbrace{\begin{bmatrix} -1 & 0 & 0 & 0 & 0 & 0 \\ 0 & 0.5 & -0.5 & 0 & 0 & 0 \\ 0 & 0 & 0 & -0.333 & -0.333 & -0.333 \\ 0 & 0 & 0 & 0 & 0.577 & -0.577 \\ 0 & 0 & 0 & 0.667 & -0.333 & -0.333 \\ 0 & -0.5 & -0.5 & 0 & 0 & 0 \end{bmatrix}}_{\boldsymbol{S}_{\mathrm{IM}}} \begin{bmatrix} S_{\mathrm{IM-OSEM,H1}} \\ S_{\mathrm{IM-OSEM,H2}} \\ S_{\mathrm{IM-OSEM,H3}} \\ S_{\mathrm{IM-OSEM,V1}} \\ S_{\mathrm{IM-OSEM,V2}} \\ S_{\mathrm{IM-OSEM,V3}} \end{bmatrix}. \quad (6.10)$$

6.3.4 Actuator response check

In order to confirm that the payload behaved properly without any mechanical contact or friction, the mechanical responses to the actuators were investigated. Figures 6.36 and 6.37 show the measured diagonal transfer functions from the virtual actuators to the virtual sensors, in comparison with the predictions from rigid-body model simulations. The measurements fit very well with the prediction. The deviation at high frequencies is caused by the electromagnetic couplings between the sensors and actuators.

6.3.5 Damping test

The mechanical resonances appearing in the transfer functions are suppressed by closing 9 damping control loops for respective DoFs of the TM and IM motions. Figure 6.38 shows the implemented servo filter. As a preliminary test, the identically servo filters were used for all the control loops. Figure 6.38 shows the vibration spectra measured by OSEMs for

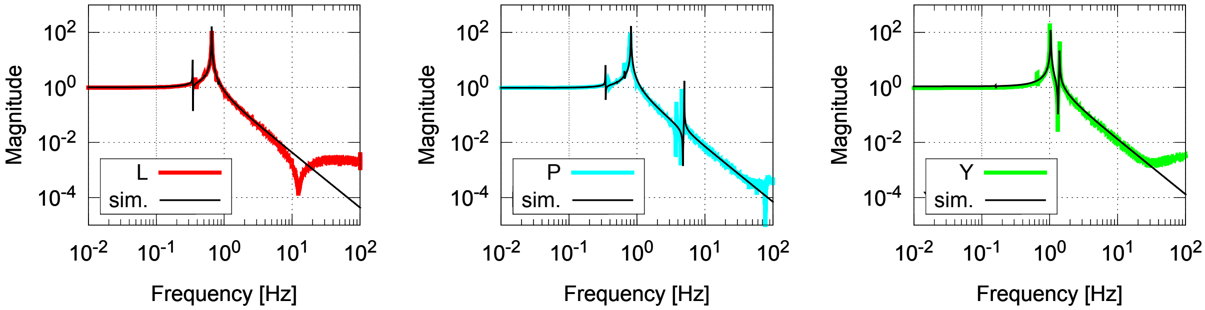

Figure 6.36: Comparison of diagonal transfer functions measured by TM-OSEMs (shown in colored lines) and prediction from the rigid-body model simulation (shown in black lines).

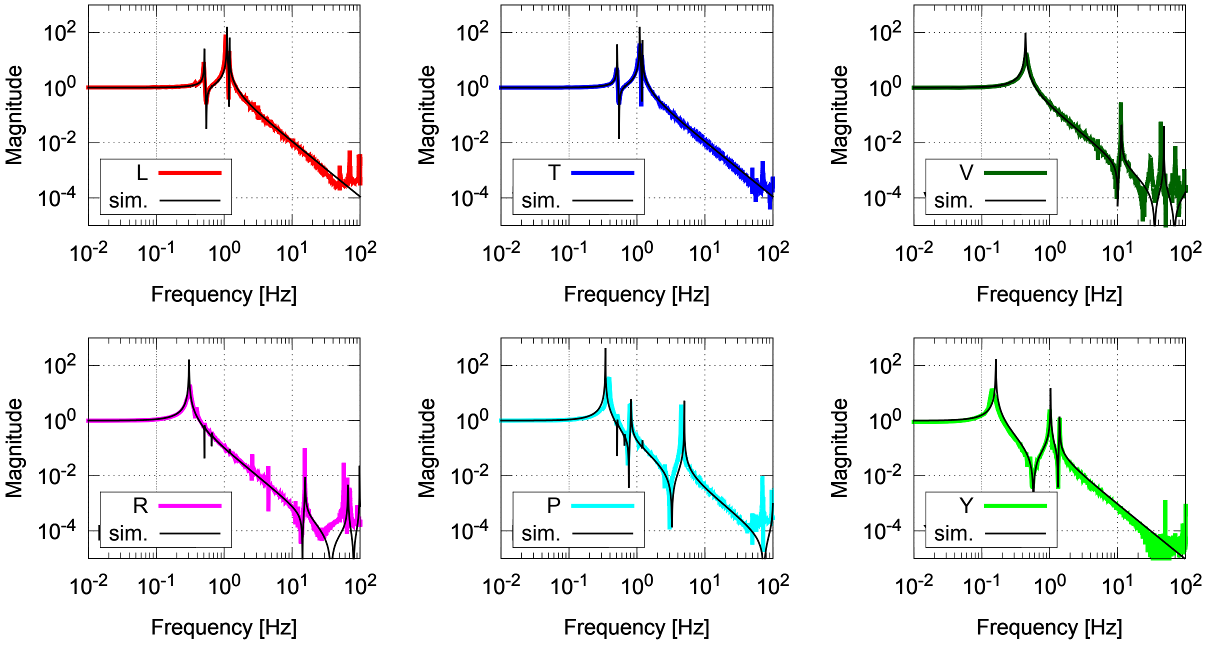

Figure 6.37: Comparison of diagonal transfer functions measured by IM-OSEMs (shown in colored lines) and prediction from the rigid-body model simulation (shown in black lines).

the IM longitudinal and IM pitch motions. The resonant peaks in the 0.1-1 Hz region are successfully suppressed and that results in the reduction of the RMS displacement/angles by roughly one order of magnitude. Note that the vibration in the 0.1-1 Hz regions is further suppressed by the IP preisolation stage in the full suspension system.

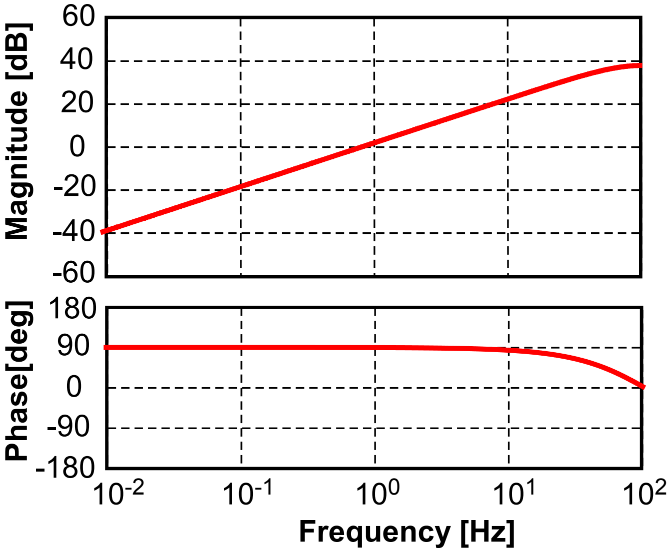

Figure 6.38: The designed servo filter for the payload control

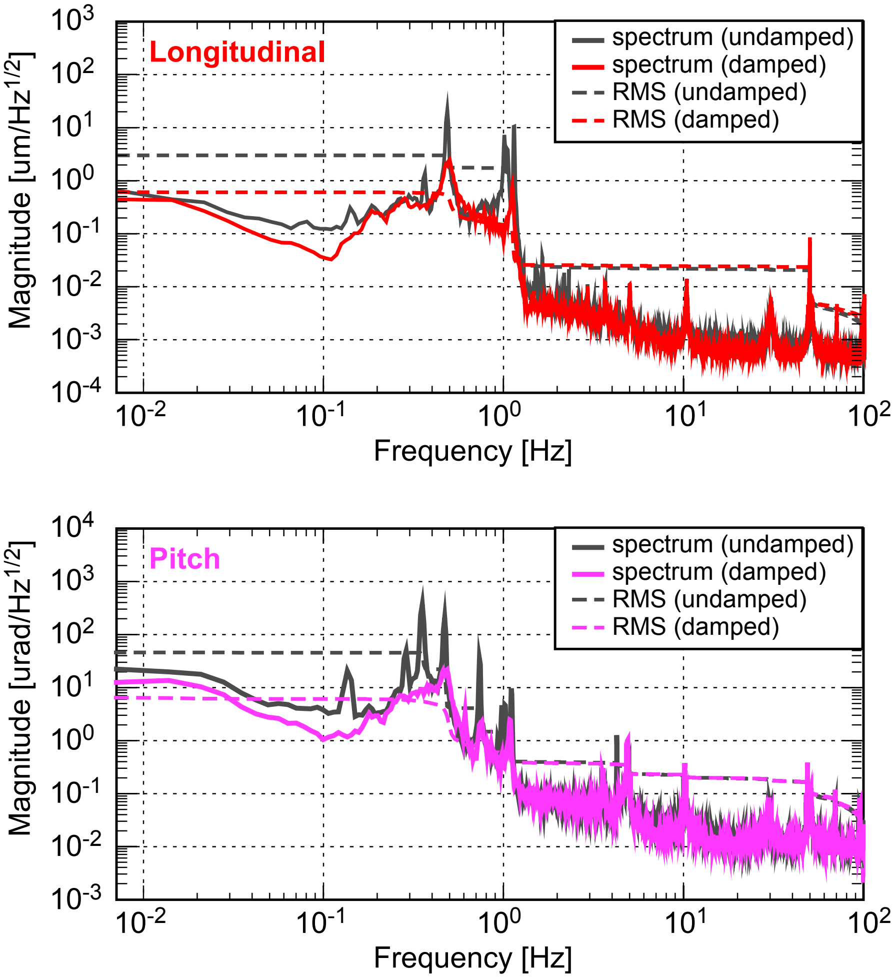

Figure 6.39: Measured vibration spectra with IM OSEM shadow sensors about longitudinal and pitch DoFs, with and without damping controls.

Type-B SAS prototype

Chapter 7

A prototype of the type-B SAS for KAGRA was assembled and tested in the facility of TAMA300, located in the Mitaka Campus of the National Astronomical Observatory of Japan. The prototype was made for the purpose of checking the ease of assembly, vibration isolation performance and controllabilty with digital system, and providing feedback on the actual design of vibration isolation systems for KAGRA.

In this chapter, the experimental setup of the type-B SAS prototype is explained in detail. Section 7.1 gives an overview of the experimental setup and associated facilities. Section 7.2 describes mechanics of the type-B SAS prototype. Section 7.3 describes sensors and actuators for active controls and some auxiliary sensors as observatories. Section 7.4 describes digital system and the design of the control servos.

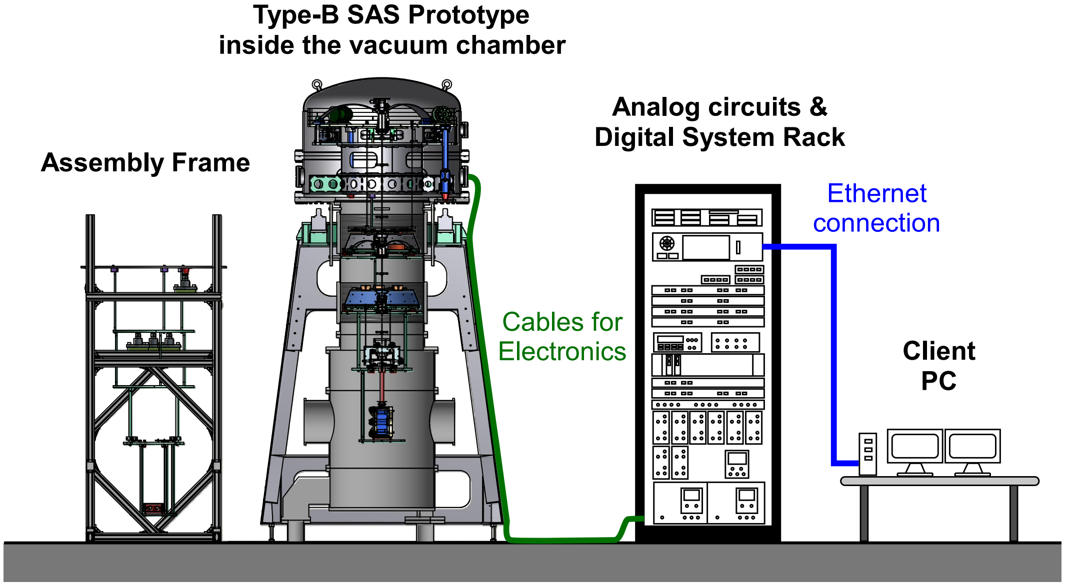

Figure 7.1: A schematic view of the experimental setup for the type-B SAS prototype test.

Figure 7.2: (*Left*) The type-B SAS prototype on an assembly frame waiting for installation into the vacuum chamber on the left. (*Right*) A rack containing digital system and analog circuits for sensors and actuators. Electrical cables from the suspension system have not been connected yet.

7.1 Overview

A schematic view and pictures of the experimental setup are shown in figures 7.1 and 7.2, respectively. The type-B SAS prototype constructed in TAMA300 was an integration of the vibration isolation components described in chapter 6. It suspended a dummy mirror made of aluminum instead of an actual mirror made of silica glass. The suspension system contained sensors and actuators for active controls, and auxiliary sensors for the performance check. The signals from the sensors and toward the actuators were integrated into digital system placed next to the type-B SAS prototype. The digital system applied active controls, actuated the suspension for the performance check and stored data of

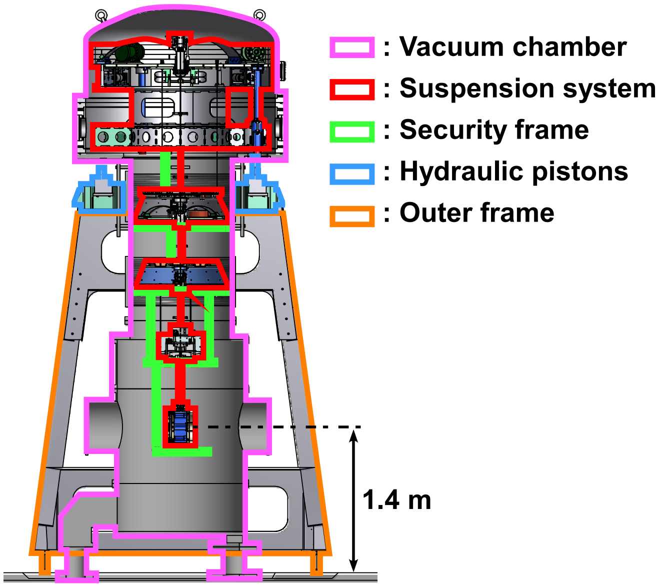

Figure 7.3: A schematic view of the suspension system and surrounding mechanical structures. Respective mechanical components are marked with colored boxes.

input/output signals. The suspension system was assembled on an aluminum assembly frame and then installed into the vacuum chamber. The chamber was evacuated using an oil-free vacuum pump, for reduction of acoustic and air-current noise.

7.2 Mechanics

This section explains the mechanics of the suspension system and related structures. The type-B SAS prototype and surrounding mechanical components are illustrated in figure 7.3. The suspension system is located inside the vacuum chamber and held the dummy mirror at a height of 1.4 m from the ground. A metal frame structure, called the security frame, is constructed around the suspension system in order to secure the suspension components in case mechanical failure occurs in suspension wires.

The base of the suspension system, which is located in the middle of the vacuum chamber, is supported by hydraulic pistons from outside the vacuum chamber. The hydraulic pistons are used for adjustment of the tilt of the suspension system base structure. The hydraulic pistons are supported from the ground by a steel frame called the outer frame, which surrounds the vacuum chamber and stands on the ground on four legs.

7.2.1 Suspension system

A picture of the assembled type-B SAS prototype is shown in figure 7.4. The bottom three stages of the suspension system, including the dummy mirror or the test mass (TM),

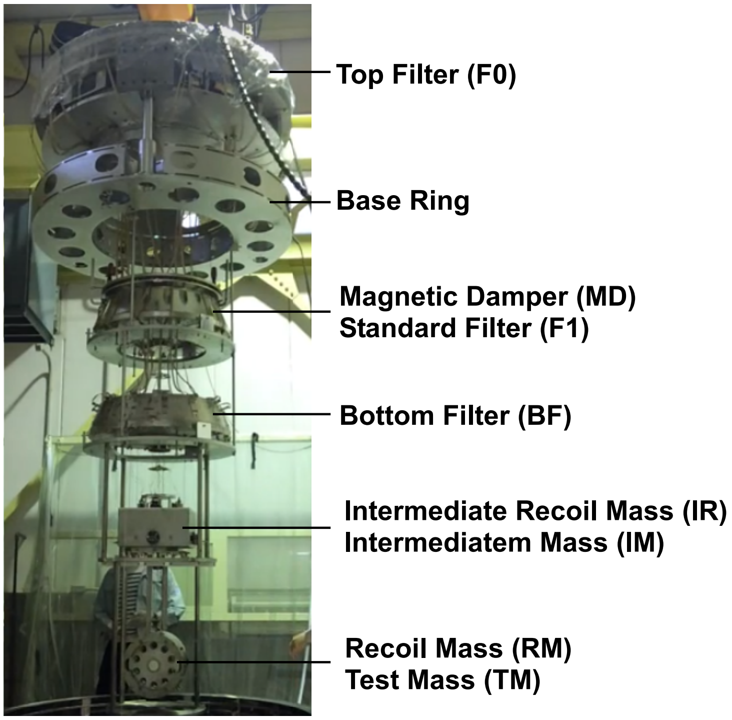

Figure 7.4: A picture of the type-B SAS prototype withdrawn from the vacuum chamber by a crane. The suspension components are fixed to the security frame during the crane operation.

the recoil mass (RM), the intermediate mass (IM), the intermediate recoil mass (IR) and the bottom filter (BF), are the same as the payload prototype described in section 6.3. They are suspended from the standard filter (F1) and the from the top filter (F0) by single-wire suspensions. The magnetic damper (MD) is placed above F1 to damp the torsion modes of the single-wire suspensions. F0 is supported from the base structure by inverted pendulum (IP) as described in section 6.1.

Suspension wires connecting the suspension components above IM are made of maraging steel. They have nail-head ends and are hooked into the masses. The wires are manufactured from rods and turned down on a lathe to the nail-head shape. The wires are heat treated after machining to increase the tensile strength.

GAS filters

The three GAS filters implemented in the type-B SAS prototype (F0, F1 and BF) have different numbers of cantilever blades with different dimensions. They are designed so that their optimal loads fit with the weight of their payloads. Table 7.1 shows parameters of the cantilever blades and measured properties of the GAS filters.

The resonant frequencies of GAS filters are tuned beforehand by changing the radial compression of the cantilever blades. They are set between 0.3 and 0.5 Hz, so that the filters provide enough isolation performance but do not suffer from hysteretic behavior. In the prototype system, the magic wands were not attached to them.

		BF	SF	TF
Thickness	[mm]	2.4	2.4	5.0
Base width	[mm]	35.3	80.0	125
Length	[mm]	274	274	606
Number of blades		3	4	3
Optimal load	[kg]	50.1	165.2	276.2
Resonant frequency	[Hz]	0.44	0.38	0.33

Table 7.1: Parameters on the GAS filters used in the type-B SAS prototype. Upper four rows describe the parameters of the cantilever blades and lower two rows describe measured properties of assembled GAS filters.

Mass distribution

Since GAS filters only work when appropriate loads are applied, the mass of each stage in the suspension system must be adjusted to ∼0.1 kg precision. Fine tuning of the weight distribution is achieved by attaching small metal discs (same as used in the payload prototype illustrated in figure 6.29) on the suspended components. The discs are also used to balance the tilt of each stage with their horizontal positions. The mass distribution of the type-B SAS prototype is shown in table 7.2.

	Mass [kg]	Sum [kg]	Note
TM	11.1		
RM	12.5		
IM	26.5	50.1	Load of BF
IR	8.1		
BF	107.0	165.2	Load of F1
F1	111.0	276.2	Load of F0
MD	17.8		
F0	545	839	Load of IP

Table 7.2: Mass distribution of the type-B SAS prototype. Mass of each stage is tuned so that the loads on GAS filters and IP are optimized.

Tuning of inverted pendulum

The diameters of the bottom flexure joints of IP were originally 10.50 mm and the corresponding critical load was 1096 kg as described in section 6.1. The weight of F0 was 300 kg without ballast masses, while the required weight of F0 to operate IP with low resonant frequencies was ∼500 kg in addition. This is huge and there is not enough space on F0 to place such a large amount of ballast masses. Therefore the flexure joints of IP were trimmed to the diameters of 9.70 mm by a lathe, which reduced the critical load of IP into ∼845 kg. The weight of F0 was adjusted ∼545 kg so that resonant frequencies of the translation modes were ∼80-100 mHz.

Tuning of magnetic damper

Simulation showed that damping coefficients between MD and F1 about yaw motions should be set to ∼2 [Nm/(rad/sec)] for efficient damping of torsion modes of single-wire suspensions. From the results of damping strength measurement (subsection 6.2.4), the number of cubic magnets attached to MD is set to 72 and the distance between MD and the copper plate on F1 was set to 5 mm.

7.2.2 Security frame

Figure 7.5 shows an illustration of the security frame designed for the type-B SAS prototype. Below each stage of the suspension chain, there is a metal disc to secure the suspended masses in case they drop due to mechanical failure of the suspension wires. The discs hold range limiters which restrict the displacement of the suspended masses into few millimeters during the operation. They also contain locking mechanism used when the assembled system is transported.

Discs are connected to the IP base by metal pillars with enough thickness that can hold the weight of suspension system in case of accidents. The diameters of the pillars are set to 25 mm in the design. However, in the prototype test, the diameters of the pillars connecting upper two stages were reduced to 15 mm because of limited space in the vacuum envelope. The resonant frequency of the lowest-order mode is as low as 3 Hz according to an FEM simulation (see figure 7.5). The frequency increases to 7 Hz when the pillars on the two stages are replaced by those in 25 mm diameter. Although the flexibility of the security frame does not affect the vibration isolation performance of SAS itself, its vibration may introduce scattered light noise in the interferometer and must be treated carefully in the actual system.

7.2.3 Vacuum envelope

The vacuum envelope for the type-B SAS prototype consists of two vacuum chambers and metal bellows connecting them. The bottom chamber, housing the payload part of the suspension system (below F2), is a reuse of the vacuum chamber for the end test

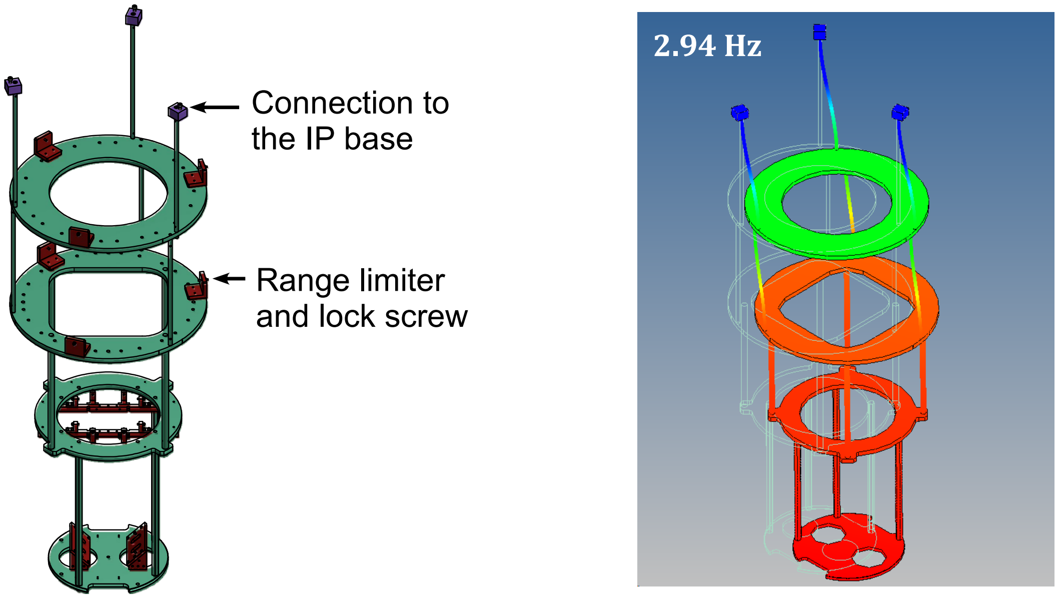

Figure 7.5: An illustration of the security frame for the prototype system (*left*) and its lowest-order resonant mode shape (*right*).

mass of TAMA300. It has several ducts with viewports, so the suspended mirror can be monitored from outside the chamber. An optical lever to monitor the TM angle was also implemented by using one of these ports.

The top chamber, of a mushroom shape, was newly manufactured for the prototype test. It has an inner diameter of 1500 mm and contains F0 and the base ring structure of the suspension system. It has several ducts with feedthroughs on the side to pass in and out the signals from sensors and actuators. The top and bottom chambers are connected by metal bellows with an inner diameter of 800 mm. The bellows contain F1 and BF inside. The structure of the bellows is strengthen by four threaded tie-rods to hold the weight of the top chamber. The length of the bellows is adjustable for positioning the top chamber at an appropriate height with respect to the base of the suspension system. On the bottom surface of the top chamber, there are three ports for mechanical connection of the suspension system inside the vacuum with the hydraulic pistons outside the vacuum. Figure 7.6 shows an extended view around the boundary between the base of the suspension system and a hydraulic piston. The suspension system base is supported by cone shape adapters placed just below IP legs, and each adapter sits on a hydraulic piston. The adapters are welded to small metal bellows which separate the vacuum and air parts.

The small bellows work as mechanical isolators separating the vibration of the suspension system from that of the vacuum chamber. Since the vacuum chamber has a huge mass and its support is not robust, vibration of the chamber tends to be enhanced by mechanical resonances at low frequencies (few Hz) and it tends to be an antenna of acoustic

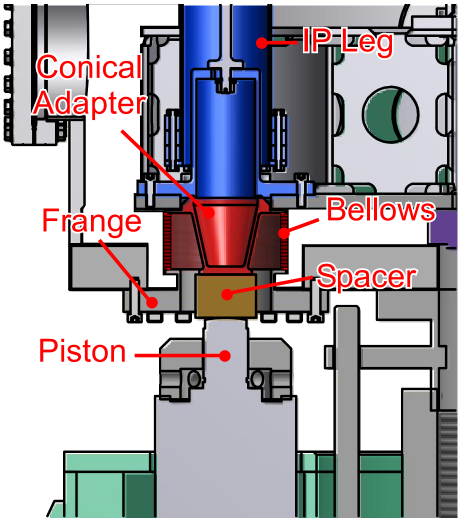

Figure 7.6: An extended view of the boundary between the suspension system base and a hydraulic piston.

noise. This may degrade performance of SAS and thus mechanical isolation between the chamber and the suspension system is indispensable.

7.2.4 Outer frame

The ground vibration is transmitted to the suspension system through the outer frame surrounding the vacuum chamber. The rigidity of the outer frame is essential since its mechanical resonances can enhance the vibration of the suspension system base and degrade the vibration isolation performance. In addition, flexibility of the outer frame causes back-action in the actuators on F0, and thus can cause instability of active controls. It is important to push the resonant frequencies as high as possible, at least higher than the bandwith of the IP active controls ($\sim$ 1 Hz). According to an FEM simulation on the currently designed outer frame, the resonant frequency of the lowest-order resonant mode (the mode shape is illustrated in figure 7.7) is $\sim$8 Hz, assuming 1400 kg load on top of the frame.

Figure 7.8 shows the measured vibration spectrum on top of the outer frame, compared with that on the floor. The amplitude ratio of the two spectra is also shown in the lower graph. The measurement shows that, in high frequency region, the amplitude of the outer frame vibration becomes 1-2 orders of magnitude larger than that of the ground vibration, due to mechanical resonances and pickup of acoustic noise. A large peak at 8.8 Hz corresponds to the lowest-order resonant mode of the outer frame.

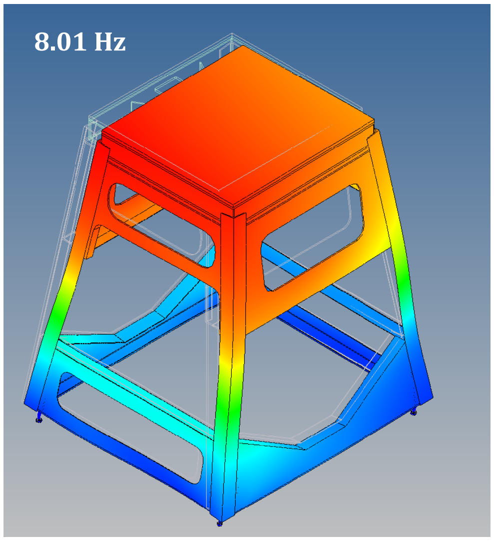

Figure 7.7: An illustration of the lowest-order resonant mode of the outer frame predicted from an FEM simulation. The simulation assumes $\sim$ 1400 kg load on top of the frame.

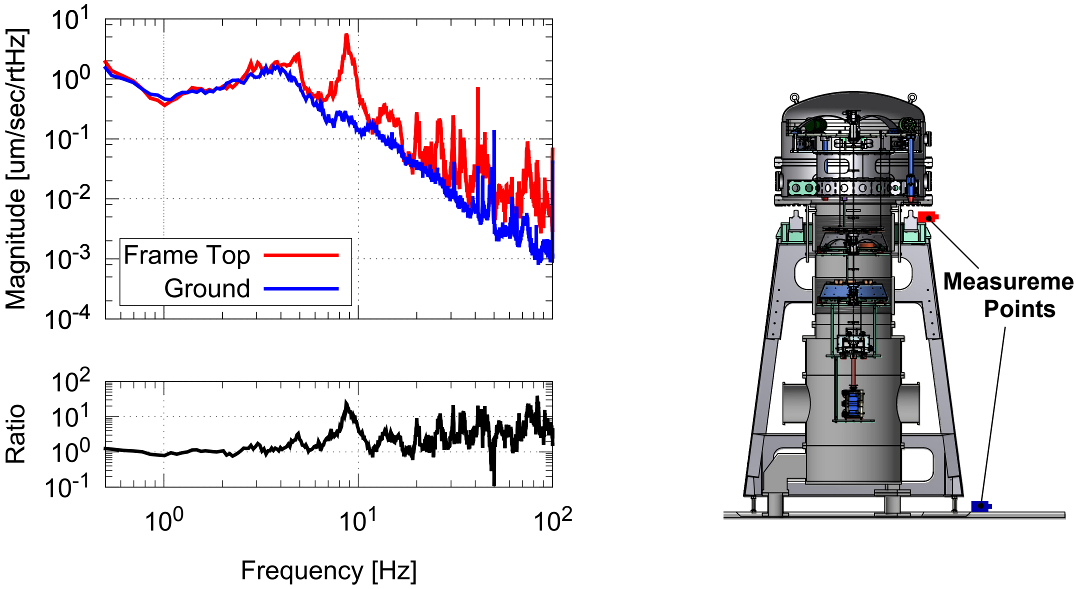

Figure 7.8: Comparison of horizontal vibration spectra on the floor and on top of the outer frame in velocities, measured by a geophone L-4C. Amplitude ratio of two spectra ($\tilde{x}_{\mathrm{frame}}/\tilde{x}_{\mathrm{floor}}$) is shown in the lower graph.

7.3 Sensors and actuators

A number of sensors and actuators are used in the prototype test for controlling and characterizing the suspension system. Sensors and actuators are categorized into three groups by purpose.

For initialization.

The sensors and actuators in this group are used for DC positioning and alignment of suspension components. They are used only in the initial setup or for the recovery after large disturbances like big earthquakes. They are not used during the observation and are often switched off to avoid noise injection.

For active controls.

The sensors and actuators in this group are used for active vibration controls of the suspension system. The noise level is important since they may introduce vibration to the suspension components through the controls.

For characterization.

The auxiliary sensors and actuators in this group are only used for the characterization of the suspension system and surrounding environment. Some of them will not be implemented or will be replaced with other ones in the actual KAGRA detector.

Details about the sensors and actuator implemented in individual suspension components are explained in chapter 6. This section describes sensors and actuators not explained in the previous chapter, some devices for vacuum operation and controllability as an integrated system.

7.3.1 Actuators for positioning and alignment

Actuators for initial positioning and alignment of the suspension components are summarized in table 7.3. They are used for relative positioing and alignment between suspension bodies, to avoid mechanical contact between them. They are used for DC positioning and alignment of TM (with respect to the interferometer beam in the actual detector),

The three hydraulic pistons implemented below the suspension system base are used for adjusting the equilibrium points of IP and the height of the whole suspension system. The horizontal DC position of F0 is adjusted by the motorized sliders (see figure 4.6) and it also determines the horizontal DC position of TM. Adjustment of the vertical DC position of TM is achieved by using a motorized spring called the fishing rod (see figure 4.8) implemented in F1. The fishing rod implemented in F0 adjusts the relative DC position between MD and F1, which determines the damping strength between the two bodies. Although the F2 fishing rod is not implemented in the prototype test due to lack of attachment mechanisms, it should be used for tuning the relative DC position of IM and IR vertically. In the prototype test, this positioning was achieved by applying DC current to the actuator coil on BF. Applying much DC current to actuator coils should

Position	Name	Actuated DoF	Main purpose
Base	Hydraulic pistons	LF0, TF0, YF0	Make IP in operation state. Rough vertical positioning of TM.
F0	Motorized springs	LF0, TF0, YF0	Horizontal positioning of TM.
	Motorized springs	VF1	Relative positioning of F1 and MD.
	Rotation mechanism	YF1	Alignment of TM in yaw.
F1	Motorized springs	VF2	Vertical positioning of TM.
F2	(Motorized springs)	(VIM)	(Relative positioning of IM and IR.)
	Moving masses	PF2, RF2	Relative alignment of IM and IR.
	Rotation mechanism	YIM	Relative alignment of IM and IR.
IM	Moving masses	PIM, PTM	Alignment of TM in pitch and roll.

Table 7.3: Actuators for initial positioning and alignment of the type-B SAS prototype. The F2 motorized springs in the vertical direction is not implemented in the prototype due to lack of attachment mechanism, but will be implemented in the actual system.

be avoided in terms of noise injection and heating problems, so the F2 fishing rod will be implemented in the actual detector.

The DC pitch and roll angles of the TM are controlled by the moving masses with picomotors on IM, as described in section 6.3. Moving masses are also implemented on the BF, while they are used for relative alignment and horizontal positioning between the IM and IR. The alignment of the TM in yaw is achieved by a rotation mechanism with a picomotor attached to the keystone of F0. The rotation mechanism is also introduced to the the keystone of the BF and is used for taking relative alignment between IM and IR.

In the prototype system, no interferometer beam exists and therefore DC position and alignment of TM were adjusted to a different standard. The motorized sliders on F0 were adjusted so that F0 was in the nominal center (where all the LVDT signals on F0 were nulled). The fishing rod on F1 was adjusted so that the keystone was at the nominal working point (where the resonant frequency is minimized). The DC pitch and yaw of the TM were adjusted to the optical lever so that the beam spot was in the center of the QPD.

7.3.2 Sensors and actuators for active controls

Sensors and actuators for active controls are summarized in table 7.4. The LVDT, geophone and coil-magnet actuators implemented on F0 in horizontal directions are used for the IP control. On the keystones of GAS filters, LVDTs and coil-magnet actuators are implemented in vertical directions and are used for damping and thermal-drift compensation of GAS filters. OSEMs, units of optical sensors and coil-magnets actuators, are implemented on the IM and TM levels for active damping of mechanical resonances of the bottom parts. An optical lever is implemented to monitor the alignment of the TM about yaw and pitch.

Position	Name	Sensed/actuated DoF
F0	LVDT+Act	LF0-LGND, TF0-TGND, YF0-YGND
	Geophone	LF0, TF0, YF0
	LVDT+Act	VF1-VGND
F1	LVDT+Act	VBF-VF1
BF	LVDT+Act	VIM-VBF
IM	OSEM	LIM-LIR, TIM-TIR, VIM-VIR RIM-RIR, PIM-PIR, YIM-YIR
TM	OSEM	LTM-LRM, PTM-PRM, YTM-YRM
	Optical lever	PTM, YTM

Table 7.4: Sensors and actuators used for active controls of the type-B SAS prototype.

Optical lever

A schematic view and a picture of the optical lever setup are shown in figures 7.9 and 7.10 respectively. The fiber-collimated light from a Super Luminescent Diode (SLD) is injected to the aluminum-coated mirror attached at the center of TM, and the reflected light is guided to a Quadrant Photo-Diode (QPD) fixed on an X-Z stage. A half mirror is inserted between the TM and QPD, which works as an attenuator to adjust the light power injected to QPD. The launcher after collimation and the QPD are placed as close as to the viewports possible for reduction of air-current noise. The optics outside the chamber are covered by a paper windshield for the same purpose.

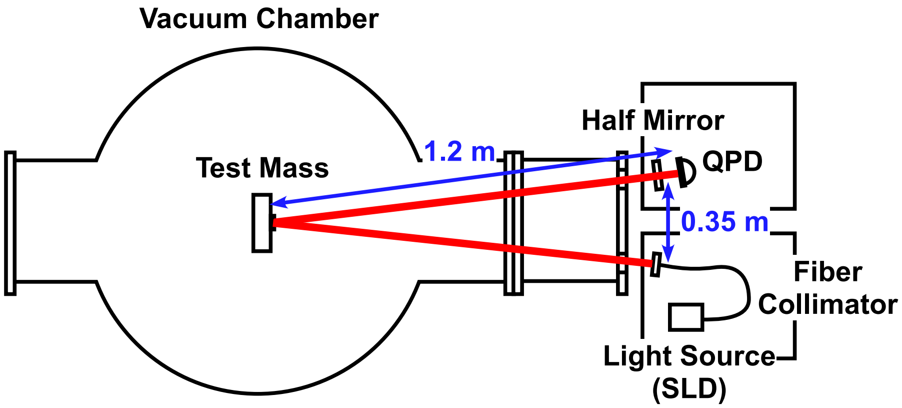

Figure 7.9: A schematic drawing of the optical lever setup.

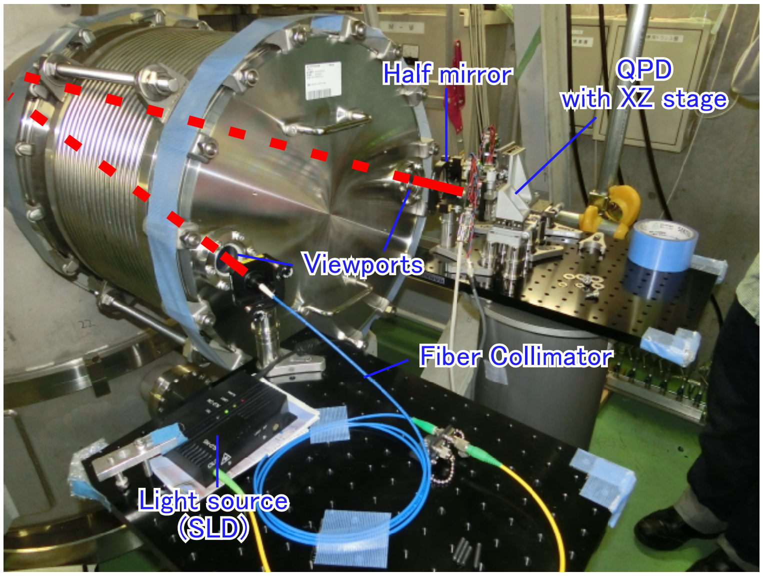

Figure 7.10: A picture of the optical lever setup. The optics shown in the picture will be covered by a windshield for air-current noise reduction.

The optics are horizontally arranged on optical tables at the level of TM. The cylindrical supports for the optical tables are made of aluminum to have good thermal conductivity and reduce the tilts of the optical tables due to thermal inhomogeneity in the supports. The lowest mechanical resonant frequency of a support is around 40 Hz, which is much higher than the bandwidth of the optical lever controls (∼1 Hz).

Vacuum pod for geophone

Since the geophone L-4C and its preamp are not vacuum compatible, they are packed in vacuum pods made of stainless steel (see figure 7.11) and their insides are kept at atmospheric pressure. Air leaks from the vacuum pods were checked beforehand in a small vacuum chamber and were proved to be small enough to be operated in vacuum at least for several months.

7.3.3 Auxiliary sensors

Several additional sensors were implemented for characterization of the prototype system. Figure 7.12 shows their disposition.

Thermometer

Two thermometers were installed to monitor the temperature of the environment and the suspension system. One of them was placed outside the vacuum chamber to measure the air temperature, and the other was attached to the base ring of the suspension system

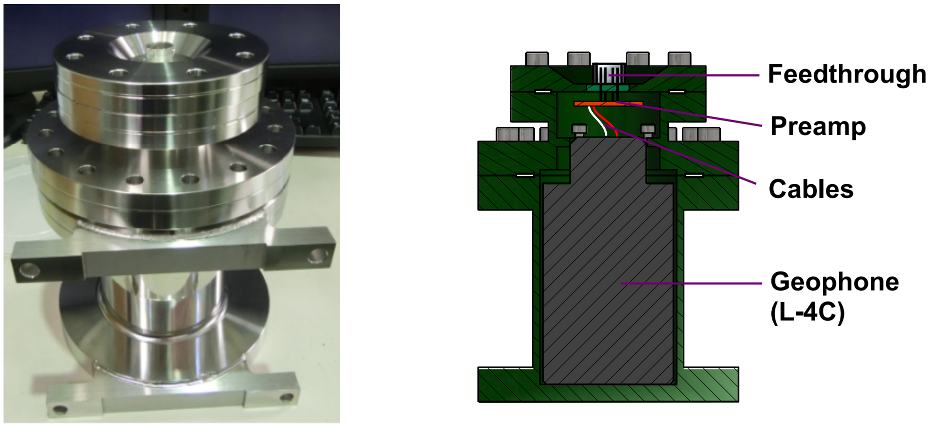

Figure 7.11: A picture of a vacuum pod for the geophone L-4C and its cut view drawing. In the picture the pod stands vertically, but is implemented on F0 horizontally in actual.

inside the vacuum chamber. The thermometers utilize temperature sensors LM45, whose output voltage is linearly proportional to the Centigrade temperature. The output voltage of LM45 is enhanced by an amplifier circuit whose DC gain is set to 10.

Seismometer

A geophone L-4C was placed on top of the outer frame to monitor the seismic vibration injected to the suspension system. The output voltage from the geophone was enhanced by a preamp as other geophones.

Photosensor

The longitudinal displacement of the TM was monitored by photosensors attached to the security frame. Figure 7.13 shows pictures of the photosensors and the detection mechanism. Note that the photosensors detect the relative displacement between the TM and the security frame, while OSEMs on the TM detect the relative displacement between TM and RM. The photosensors adopt a detection scheme used for the space gravitational wave antenna SWIM$\mu\nu$ [91]. The target object (the back surface of TM) is illuminated by an LED and the reflected light is detected by two photo detectors (PDs) placed next to the LED. The total power detected by two PDs depends on the distance between the sensor and the target. A symmetric configuration is adopted to minimize the detector's sensitivity to the the target angle.

Displacement of the TM central point cannot be measured directly due to existence of a central hole on TM. Therefore two photosensors were placed with horizontal separation and the average of two sensor readouts was used as a displacement readout of TM. Since the positioning of two photosensors was not accurate, the displacement readout could suffer from the coupling from TM yaw motion by $\sim$5 [mm/rad] at most.

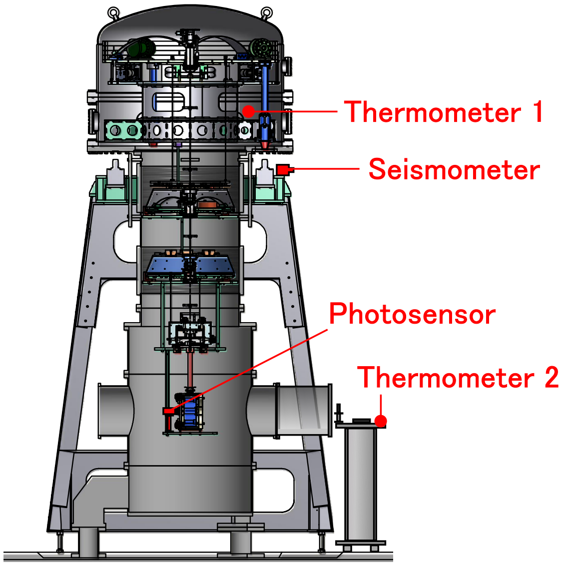

Figure 7.12: Disposition of auxiliary sensors for characterization of the prototype system.

Figure 7.14 shows the calibration result of one of the photosensors. The calibration was done by arranging the distance between an aluminum target and the photosensor with a micrometer stage. The sensor output voltage increases as the target goes away from the sensor until the distance reaches 5 mm. Then the voltage decreases if the target goes further away Although the response is non-linear overall, a linear response is obtained between 2-3 mm and the obtained sensitivity is 2.65 V/mm.

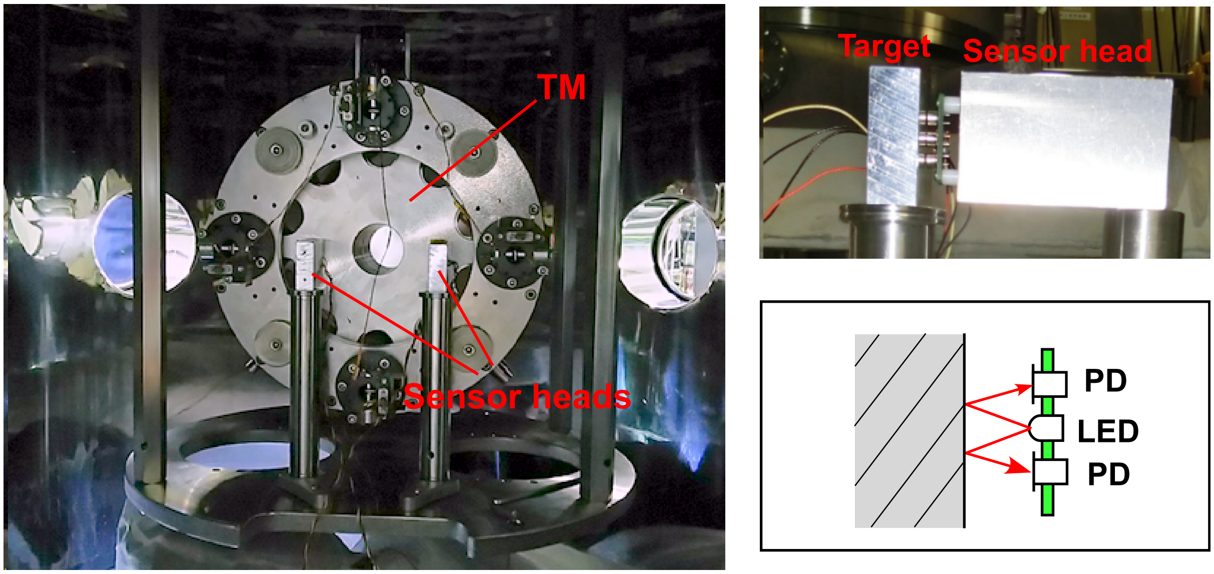

Figure 7.13: (*Left*) A picture of the photosensors installed to the suspension system. (*Right*) A closer look at a photosensor during the calibration and an illustration of the detection mechanism.

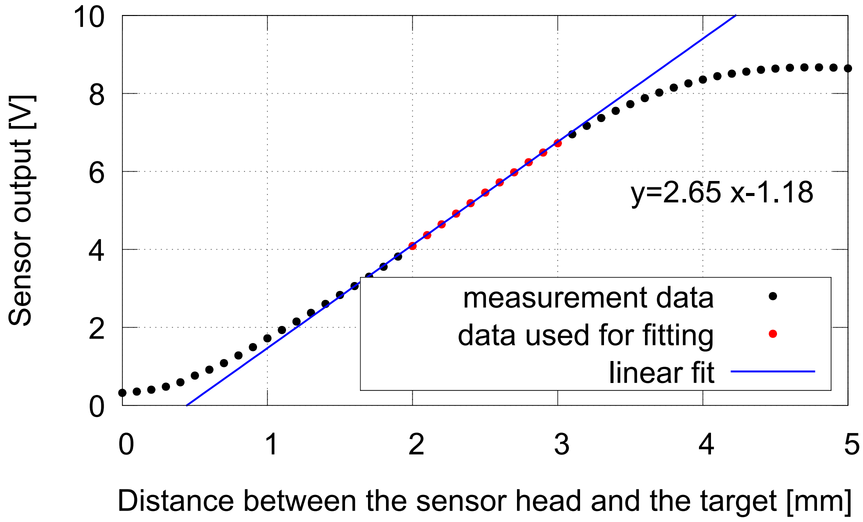

Figure 7.14: A calibration result of one of the two photosensors.

7.3.4 Cabling

Electrical cables from the sensors and actuators for the suspension system are guided upwards and collected to the feedthroughs on the top chamber. The cables are anchored to suspension stages and arranged loosely so as not to provide significant mechanical stiffness between the stages (see figure 7.15). Twisted-paired ribbon cables are used for carrying the electrical signals inside the vacuum chamber. They are plugged into 9-pin D-sub connectors on the feedthrough. Outside the chamber, the signals are carried to the rack containing digital system and electrical circuits by commercial 9-pin D-sub cables with electromagnetic interference shields.

Figure 7.15: A picture displaying electrical cables between BF and F1. Rainbow-colored ribbon cables are clamped to the suspension stages and arranged loosely between them.

7.4 Digital control

Active controls of the suspension system require complicated Multiple Input Multiple Output (MIMO) control loops and switching servo filters depending on the situation. It is unrealistic to achieve such controls only by analog circuits with manual operation and thus digital control system is required. The digital system also plays a role in storing data of signals, creating excitation signals for suspension system characterization, and automatizing control procedures which are routinely and frequently used.

7.4.1 Digital system overview

The digital system implemented in the type-B SAS prototype is basically an import from the LIGO detectors, which will be also adopted in the KAGRA detector for the interferometer control and data storage.

Real-time signal processing for the digital control is performed by a real-time OS machine customized for high-speed signal processing and data communication. The signal processor is connected to a PCIe extension board which contains a timing clock, Analog-to-Digital Convertors (ADCs) and Digital-to-Analog Convertors (DACs). The real-time data of selected signals are stored in a 1 TB data-storage hard-disc. Details of signal processing are implemented and controlled from a Scientific Linux machine connected to the real-time machine through a Local Area Network (LAN). Table 7.5 shows the specification of the digital system used in the prototype test.

Figure 7.16 shows a typical flow of signals processed by the real-time signal processor. Signals derived from numerous sensors are sent to the ADCs and digitized. The signals are passed to the processor in which a number of Infinite Impulse Response (IIR) filters, matrices, offsets and excitation signals are applied. After being processed, the signals are sent to DACs and converted to analog signals for the actuation of the suspension system.

The internal variables of the signal processor, such as feedback gains, coefficients of the IIR filters and amount of the offsets, are controlled with the system called EPICS (Experimental Physics and Industrial Control System) [92], which communicates with the real-time system at 64 Hz. The EPICS variables can be rewritten from an interface computer easily, which enables a user to program various control sequences with computer language scripts.

Digital system requires signal conditioning filters called anti-aliasing (AA) and anti-imaging (AI) filters as analog circuits. They cut off the signals at frequencies higher than the Nyquist frequency to mitigate noise caused by quantization errors. The anti-aliasing and anti-imaging filters implemented in the prototype system are identical circuits, which have third order low-pass filters with 10 kHz cutoff and notch filters at 65536 Hz.

7.4.2 Loop delay and digitization noise

Although the digital system provides significant flexibility and usability, the bandwith of the digital control is limited typically by one or two orders of magnitude less than the sampling frequency, because of time delay in the computing process. Figure 7.17 shows a transfer function from a digital system output to an input, when they are connected directly by an electrical cable. The transfer function includes the responses of analog AA

Item	Spec
Sampling rate	16384 Hz (sampled at 65536 Hz, decimated to 16384 Hz)
Number of ADC channels	64 ch. (with 2 ADC cards)
Number of DAC channels	32 ch. (with 2 DAC cards)
ADC/DAC bit resolution	16-bit = 65536 digital counts
ADC voltage range	±20 V (1 count = 0.61 mV)
DAC voltage range	±10 V (1 count = 0.31 mV)
ADC noise level	3 $\mu\mathrm{V}/\sqrt{\mathrm{Hz}}$ ($>$ 10 Hz)
DAC noise level	2 $\mu\mathrm{V}/\sqrt{\mathrm{Hz}}$ ($>$ 10 Hz)
Through delay	80 μsec

Table 7.5: Specification of the digital system for the type-B SAS prototype test.

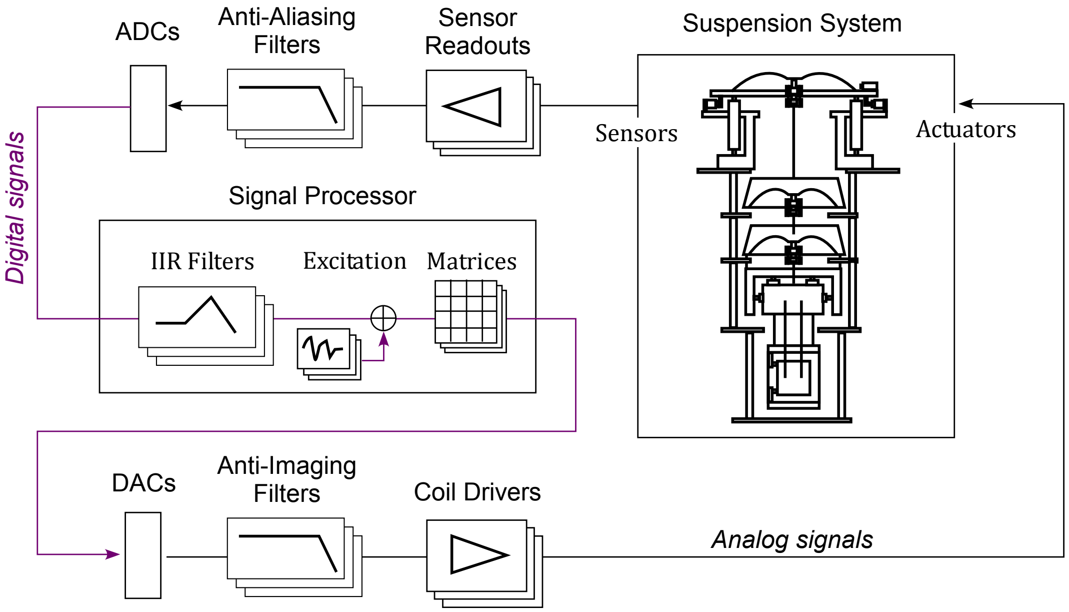

Figure 7.16: Block diagram of the real-time system for the suspension system controls.

and AI filters, while the cut-off at 5 kHz is caused by a software AA/AI filter implemented in the digital system. The measured phase delay is 15 deg. at 100 Hz and 45 deg. at 300 Hz. The measurement indicates that control signals are subjected to group delay of ∼420 μsec through the digital system. So the control bandwidth is limited by few hundred Hz using the digital system. However, this is not a problem in suspension active controls, because a typical control bandwidth is few Hz at most and is much lower than the limitation.

Another drawback of using digital control is larger sensing and actuation noises due to quantization errors in digitization processes. The power spectrum density of the quantization noise can be estimated by the following formula [17]:

$$P_{\mathrm{n}}(f) = \left(\frac{\Delta^2}{12}\right)\frac{2}{f_s}. \tag{7.1}$$

Here Δ is the step size of quantization and f_s is the sampling rate. In the prototype system, the noise level of the ADC is estimated to be 2 $\mu\mathrm{V}/\sqrt{\mathrm{Hz}}$, while the measured noise level is 3 $\mu\mathrm{V}/\sqrt{\mathrm{Hz}}$ at high frequencies and increases by $f^{-1/2}$ below 3 Hz as shown in figure 7.18. This is huge compared with the typical noise level of analog circuits (in the order of $\mathrm{nV}/\sqrt{\mathrm{Hz}}$).

Although not implemented in the prototype test, the impacts from ADC and DAC noise can be mitigated by introducing whitening and dewhitening filters in analog circuits. Whitening filters enhance the sensing signals before injected to ADCs and dewhitening

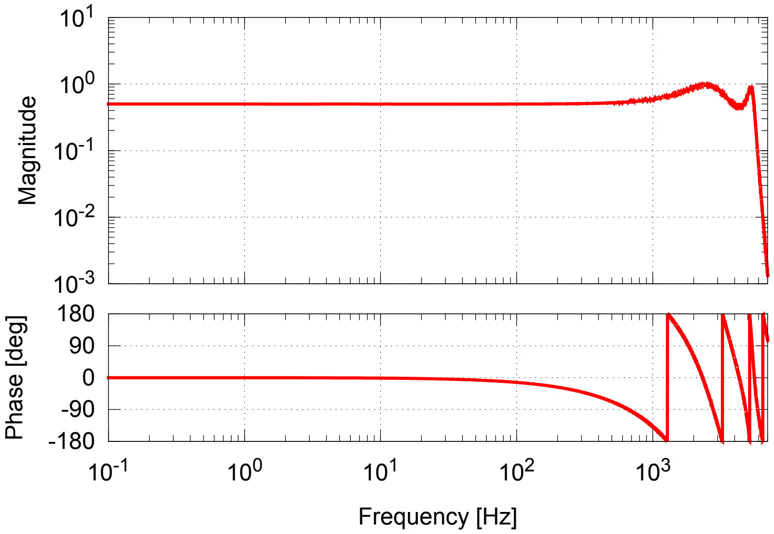

Figure 7.17: A loop-delay of the digital system measured with connecting an AA filter input and an AI filter output directly.

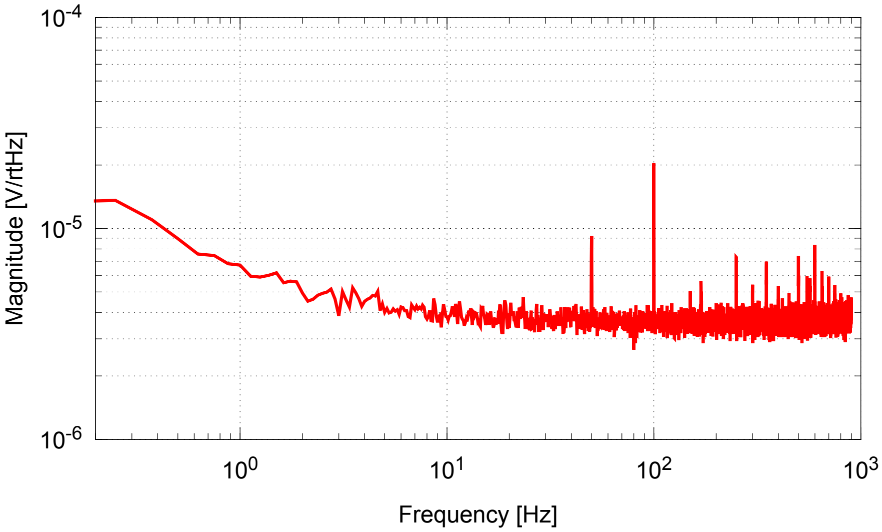

Figure 7.18: A typical noise spectrum of ADCs.

filters diminish the actuation signals after DACs, at frequencies where sensitive controls are required. The phases and loop gains are compensated by anti-whitening and anti-dewhitening filters implemented in digital system. Signal-to-noise ratio around the frequencies of interest is improved by this method, while the controllable range also decreases at those frequencies.

7.4.3 Signal processing

Figure 7.19 shows an overview of the signal processing part for the digital control of the type-B SAS prototype. The sensing signals from LVDTs and geophones on F0, OSEMs on IM and TM, and LVDTs on GAS filters are used for the main streams of the active controls. The signals after being processed are fed back to the coil-magnet actuators on corresponding stages. The signals from the optical lever and photosensors are processed in side streams, and the correction signals from these sensors are added to the actuation signals for IM and TM respectively. The signals from environmental sensors are processed by multiplying calibration factors and keep flowing in the data streams. The sensing signals including the signals from environmental monitors and feedback signals are stored in the data storage after being down-sampled to 256 Hz.

Figure 7.20 shows a typical flow in the signal processing part for the active controls of the suspension system. Raw signals from sensor readouts injected to ADCs are multiplied by calibration factors, which are measured beforehand, and converted to displacements or velocities at the sensing points. The real sensor signals are then transformed into virtual sensor signals, which describe the rigid-body motions of the suspension bodies in the Cartesian coordinate system. This transformation is done by multiplying a sensor matrix whose elements are determined from geometric layout of sensors. When several kinds of virtual sensor signals are available for the same reconstructed DoF, the measurements are blended into a super sensor signal. The virtual sensor signals are then injected to the servo systems in the signal processor. The sensor signals are firstly applied with offsets, which determines the DC operation points of the suspension bodies, and then applied with servo filters to obtain feedback signals. The control gains are switched between 0 and -1, which determines the active controls ON or OFF. The digital system can alter the control gains and offsets gradually so that the system transits to different control states smoothly.

The digital system can inject excitation signals at arbitrary points on the signal paths. When the characterization of the suspension system is performed, excitation signals are injected just after the servo filters so that the motion of a certain DoF is excited. The control signals from the optical lever and photosensors are also added at this point. Though the photosensors are treated as monitoring sensors for characterization, the signals are fed back to the actuators to simulate the lock of the interferometer.

The virtual actuator signals from the servo system are then converted to the real actuator signals using a coil matrix. Coefficients of the coil matrix are determined from the results of actuator diagonalization, as described in subsection 6.1.6. The actuator signals are then injected to output filters, in which the sign of output voltage is multiplied

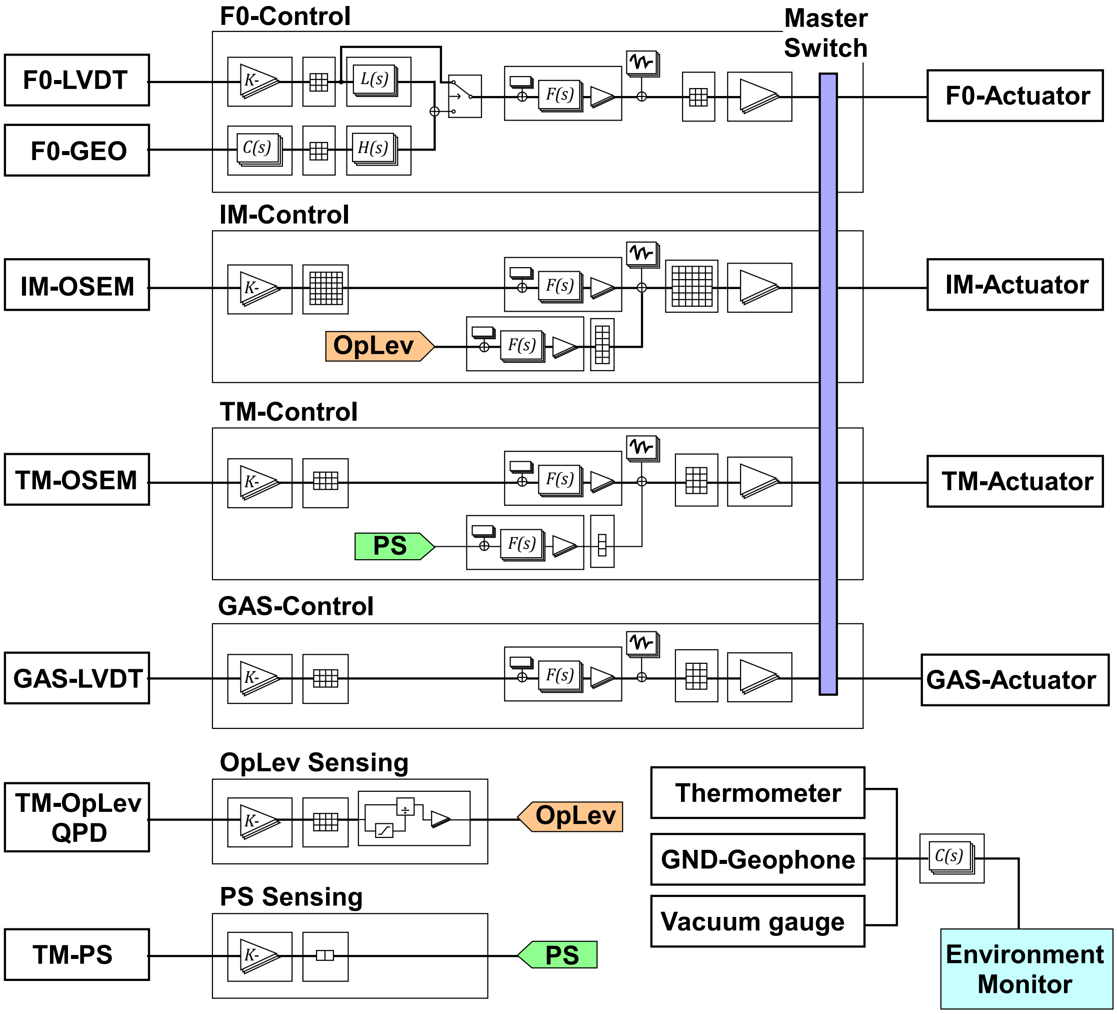

Figure 7.19: Overview of digital control and environmental monitor system.

by ±1, depending on the direction of coil windings and magnet poles. The master switch, placed after the output filters, regulates all the digital output and is switched off in case of accidents.

7.4.4 Motor controls from digital system

A number of stepper motors and picomotors implemented for DC positioning and alignment of the suspension system are controlled from the digital system through EPICS. Stepper motors are driven by using a TMCM-6110 controller/driver board, which supports up to 6 bipolar stepper motors and has various communication interfaces for digital controls. The TMCM-6110 board is connected to the digital system LAN with RS485 (2-wire) serial interface, through an Ethernet-serial convertor NPort 5110A. Picomotors are driven

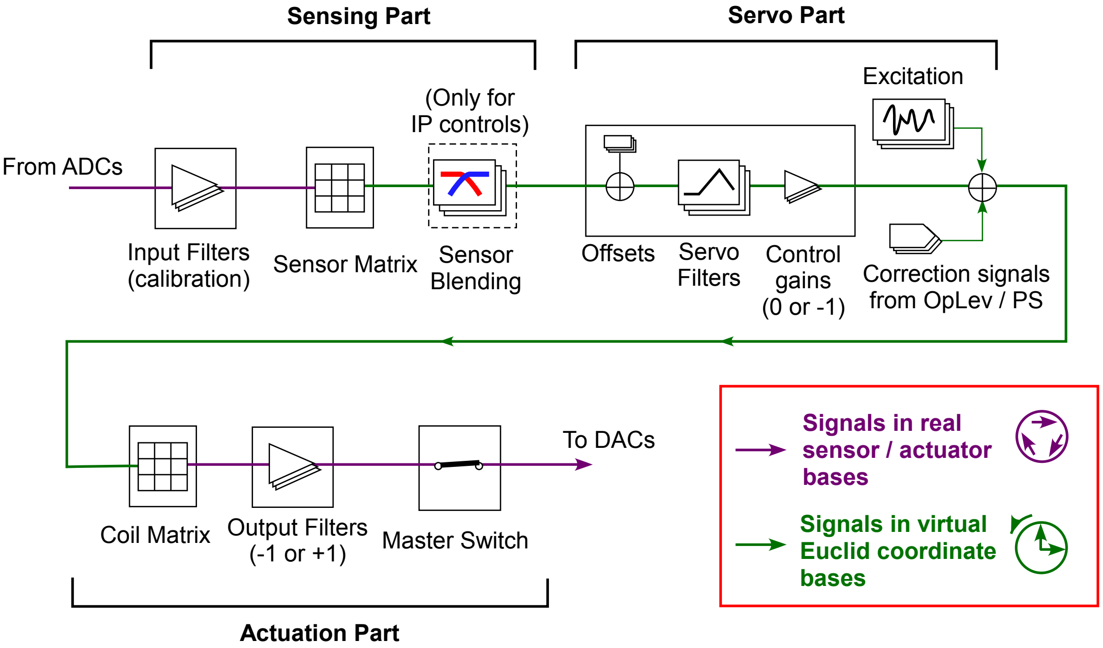

Figure 7.20: Block diagram of the signal processing in the digital system.

by using a Newport/New Focus 8752 Picomotor Controller and slaved 8753 Picomotor Drivers, and the controller is connected to the digital system LAN through an Ethernet cable.

The digital system communicates with the motor controllers using PyEpics, the EPICS Channel Access protocol interface to the Python programming language. The direction, speed and amount of rotation are controlled through a program. Motors can be activated simultaneously and thus it is possible to move the suspension stage in a certain DoF by distributing rotation angles accordingly.

Performance test of type-B SAS prototype

Chapter 8

This chapter mentions the experimental performance test of the KAGRA type-B SAS prototype, whose conofiguration was describes in the previous chapter. The primary motivation of the experiment is to demonstrate the active controls of the suspension system and confirm their stability and feasibility.

In section 8.1, the mechanical response of the suspension system is checked with built-in sensors and actuators, before enabling active controls. Measured frequency responses are compared with simulation results using a rigid-body model and the results are fed-back to the servo design of the active controls. Sections after 8.2 describe performance tests on the active control systems. As discussed in 5.2, the active control system has to adopt different control topologies for three operation phases of the interferometer: the calm-down, lock-acquisition and observation phase. Section 8.2 focuses on the control systems for the calm-down phase and describes the performance of damping controls. Section 8.3 describes the active controls for the lock-acquisition phase, in which low RMS displacement and rotation angles of TM are required. In section 8.4, the lock of the TM longitudinal displacement is demonstrated using photosensors as substitutes for a laser interferometer. The noise couplings from the control system are discussed in terms of the impact on the detector sensitivity in the observation phase. In section 8.5, a long-term control test of the suspension system is performed. An automaton is constructed in the digital system so that the control loops switches between the three control phases automatically.

8.1 Suspension mechanical responses

The mechanical responses of the type-B SAS prototype were investigated using the internal sensors and actuators. The measured frequency responses were compared with simulation results and the results were fed back to the servo filter designs.

8.1.1 Measurement setup

The frequency responses of the suspension system were described in terms of rigid-body motions of the suspension bodies in a Cartesian coordinate system. Virtual sensors and actuators, which measure and excite the rigid-body motions in certain DoFs, were constructed in the digital system with linear combination of the real sensors and actuators. The measurement was done by injecting broadband Gaussian noise from a virtual actuator in a certain DoF and taking the resulting displacements measured by virtual sensors. The virtual actuators were diagonalized beforehand with the diagonalization process described in subsection 6.1.6. They were diagonalized at the frequency of 20 mHz for the IM and TM controls, and 10 mHz for the IP control.

The amplitude and spectrum of the excitation signal were adjusted so that sufficient S/N was obtained in the whole frequency band of interest but do not excite the mechanical resonances much, so as to let the sensors stay in the linear regimes. The excitation amplitude was reduced in the 0.1-1 Hz band where many mechanical resonances exist, and notch filters are introduced for some specific resonances. The measurements at the TM and IM levels were done using OSEMs, while the measurements of the IP stage were done with coil-magnet actuators and super-sensors, which blend the low-frequency LVDT signals to the high-frequency geophone signals with blending filters described in section 5.3.1. The crossover frequency of the blending filters was set to 50 mHz. The vertical transfer functions of the GAS filters were measured by using the LVDTs and coil-magnet actuators.

8.1.2 Diagonal transfer functions

Figures 8.1-8.4 show Bode plots of the measured diagonal transfer functions (e.g. TM-longitudinal → TM-longitudinal). The measurements are compared with predictions from rigid-body model simulations, which are indicated by black curves in the graphs. Measured transfer functions basically fit well with the prediction. This indicates that the suspension system had no gross troubles like mechanical contact or friction between suspension bodies. Nevertheless, several discrepancies between the measurement and simulation were observed. The discrepancies and possible explanations are described below:

- The measured transfer functions deviate from the prediction above ∼30 Hz for the measurements with OSEMs and above ∼5 Hz for the measurement with LVDTs. The deviation is caused by electromagnetic coupling between the actuation signal and sensing signals. The measurements with LVDTs suffered from larger couplings since the sensing coils were arranged coaxially with actuation coils and the signals couple directly through the magnetic fields.

- The position of resonant peaks observed in the IM vertical, pitch and roll transfer functions deviate significantly from the prediction. The simulation predicts a resonance at 4.9 Hz in the pitch transfer function, while the measured resonant frequency is 4.3 Hz. Also the measured resonant frequencies found around 45 Hz in vertical, and 60 Hz in roll are lower than the prediction. These resonances correspond to the pitch, roll and vertical bounce modes of the RM. A possible reason for the deviation is that hanging of RM may be uneven so that one of the 4 wires suspending RM may not be loaded. The floating wire would not contribute to the stiffness in pitch, roll and vertical motions of RM and the spring constant would be reduced by 25%. Consequently the resonant frequencies of these modes would be reduced by 13%, which is consistent with the observed deviation.

- The frequency responses of the IP stage in transverse and yaw motions deviates significantly from the prediction at low frequencies. The deviation can be explained by assuming asymmetry in the IP stiffness and large couplings between the transverse and yaw motions. Actually the resonant peak corresponding to the transverse mode of IP is also found in the transfer function in yaw, and vice versa. Note that the prediction does not take into account the asymmetry.
- There are several resonant peaks observed at high frequencies but not predicted in the rigid-body model simulation. The peaks at 50 Hz and its harmonics observed in the TM longitudinal transfer function are due to hum in the electronics. Resonances found around 70-80 Hz in the IM roll and pitch transfer functions are caused by violin modes of the suspension wires for the RM. Resonant peaks above 20 Hz in F0 transfer functions are caused by the back-action of the outer frame.

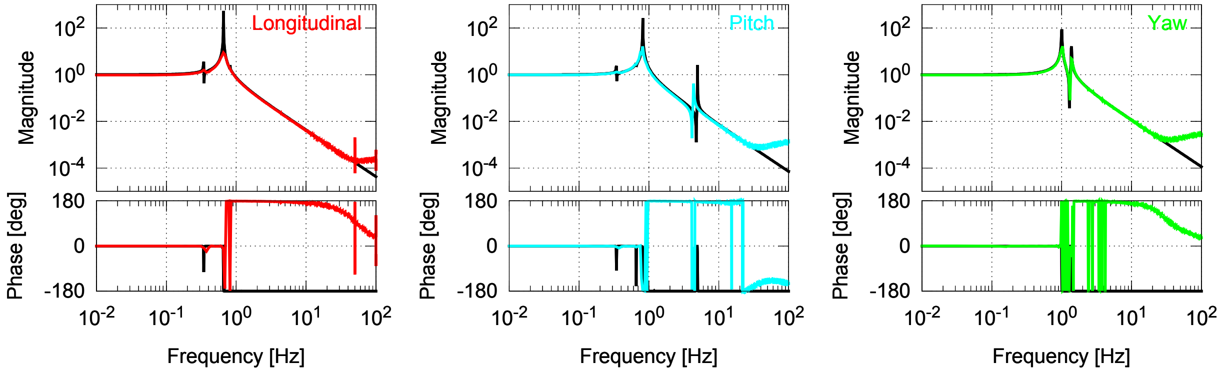

Figure 8.1: Comparison of diagonal transfer functions measured by TM-OSEMs (shown in colored lines) and prediction from the rigid-body model simulation (shown in black lines).

8.1.3 Couplings with other DoFs

The measurement results described above only showed the diagonal transfer functions, looking at the same DoFs as those of the excitation. Here the couplings between other

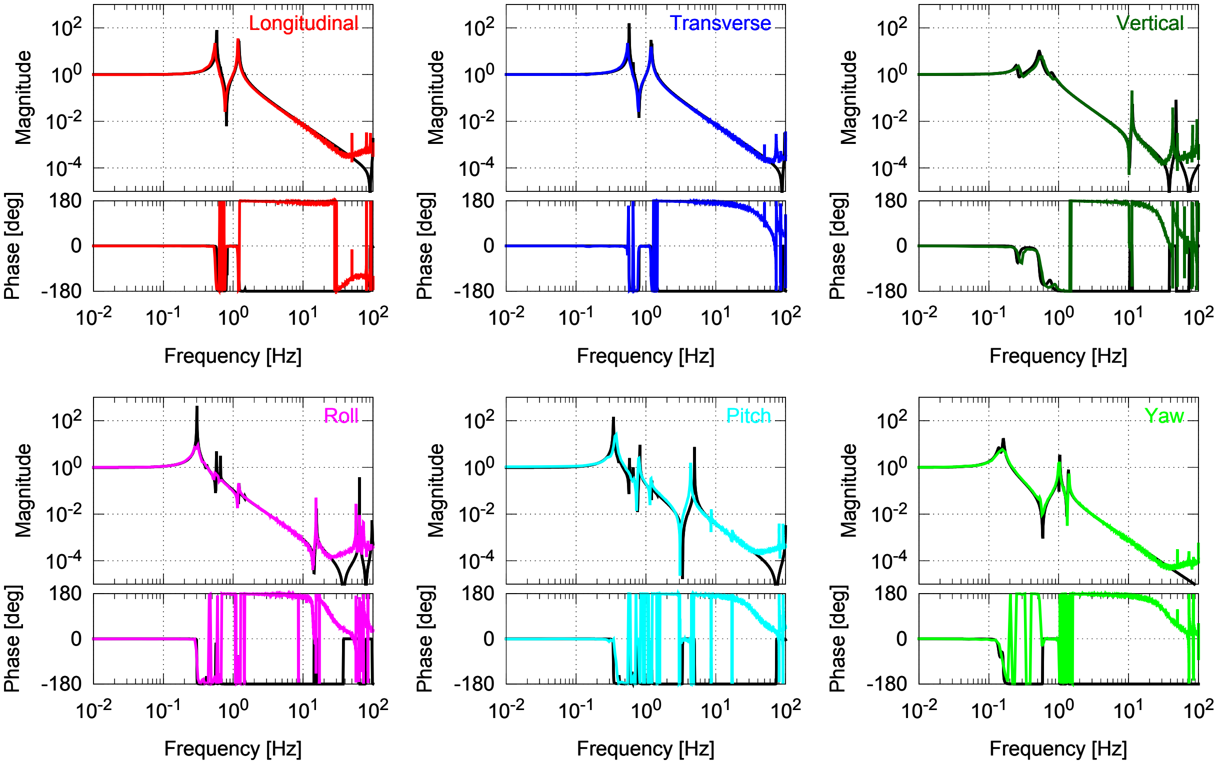

Figure 8.2: Comparison of diagonal transfer functions measured by IM-OSEMs (shown in colored lines) and prediction from the rigid-body model simulation (shown in black lines).

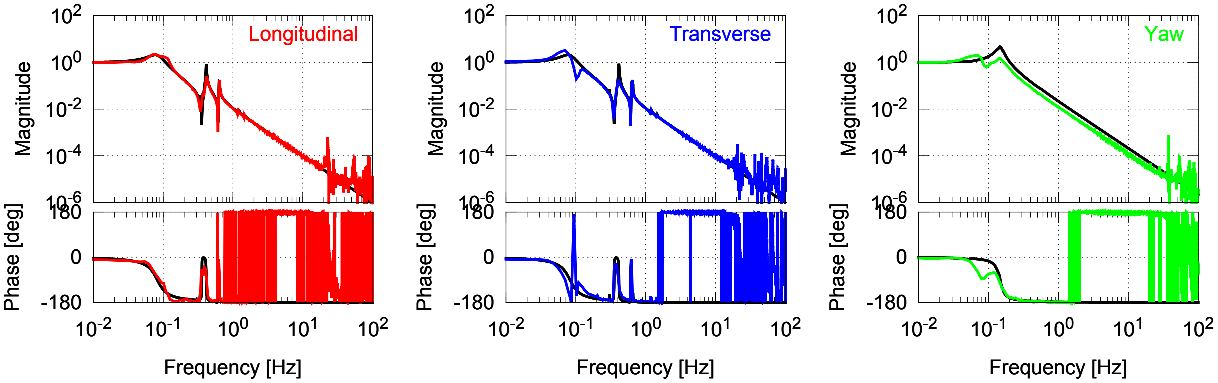

Figure 8.3: Comparison of diagonal transfer functions about F0 (shown in colored lines) and prediction from the rigid-body model simulation (shown in black lines).

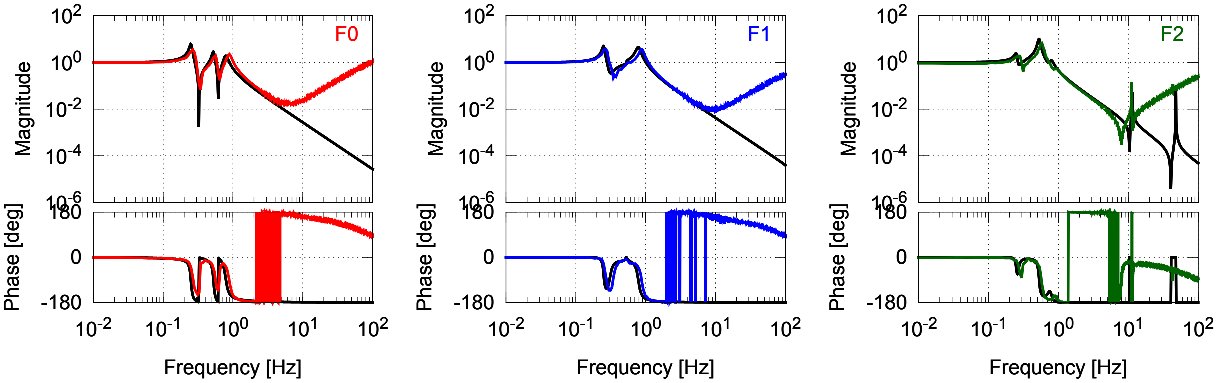

Figure 8.4: Comparison of transfer functions measured by LVDT-actuator units on GAS filters (shown in colored lines) and prediction from the rigid-body model simulation (shown in black lines).

DoFs are discussed. Figure 8.5 shows the transfer functions from the TM longitudinal actuator to the TM motions including other DoFs than longitudinal. Since the actuators were diagonalized at a low frequency, amplitudes of the off-diagonal transfer functions were much lower than that of the diagonal one (few %) at low frequencies. On the other hand, the transfer functions around and above the resonant frequencies showed larger coupling (~10% at 10 Hz).

The following tables show the magnitude of the coupling coefficients (amplitudes of transfer functions) at a low frequency (10 mHz) and a high frequency (10 Hz). The responses about the IM and TM actuators showed little couplings to other DoFs at the low frequency owing to the actuator diagonalization. The responses of the IM actuators showed large couplings at the high frequency. In particular, couplings from the rotational actuators (R, P and Y) to some DoFs are huge. The couplings to the longitudinal motions could be problematic since they can cause control noise coupling to the interferometer signals. The control noise coupling to the TM longitudinal displacement will be further discussed later. Regardless of the diagonalization, the couplings of the F0 actuators were huge at low frequencies. This is because the diagonalization condition of the F0 actuators easily changes after a large movement of the IP stage due to the hysteretic behavior of the IP, and thus one cannot diagonalize the F0 actuators precisely. In this condition, the low-frequency control signal in a certain DoF can induce a large displacement of the IP stage in other DoFs. However, the stage motions at low frequencies are robustly locked by feedback controls in all three DoFs and such movement is suppressed by control loops in other DoFs. As long as the IP stage is locked in all three DoFs, the low frequency couplings do not affect the stability or feasibility of the control.

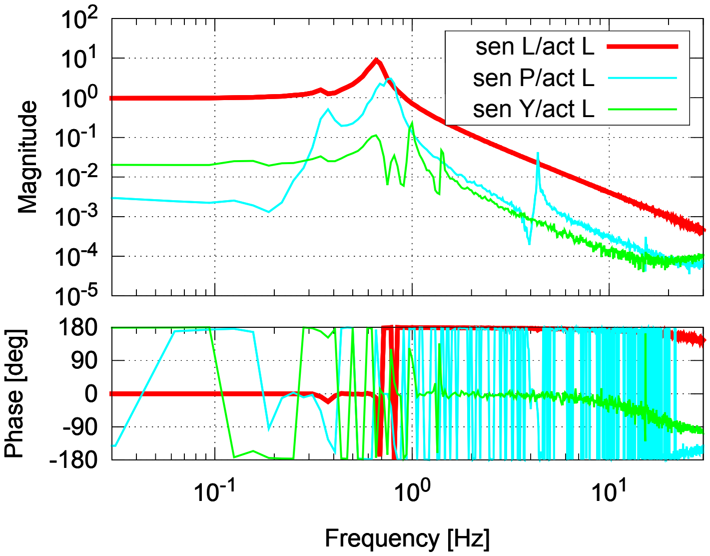

Figure 8.5: Measured transfer functions from the TM-RM longitudinal actuator to the displacements including the coupling with other DoFs.

	sensor L		sensor P		sensor Y	
	10 mHz	10 Hz	10 mHz	10 Hz	10 mHz	10 Hz
actuator L	1		0.003	0.075	0.021	0.035
actuator P	0.005	0.099	1		0.001	0.013
actuator Y	0.005	0.007	0.002	0.011	1	

Table 8.1: Coupling coefficients in the TM stage.

	sensor L	sensor T	sensor V	sensor R	sensor P	sensor Y
actuator L	1	0.001	0.002	0.002	0.011	0.001
actuator T	0.000	1	0.000	0.001	0.002	0.010
actuator V	0.003	0.001	1	0.010	0.004	0.002
actuator R	0.001	0.001	0.001	1	0.002	0.002
actuator P	0.005	0.003	0.011	0.023	1	0.010
actuator Y	0.000	0.007	0.004	0.003	0.000	1

Table 8.2: Coupling coefficients in the IM stage at 10 mHz.

	sensor L	sensor T	sensor V	sensor R	sensor P	sensor Y
actuator L	1	0.001	0.007	0.011	0.001	0.027
actuator T	0.006	1	0.006	0.009	0.013	0.015
actuator V	0.027	0.003	1	0.032	0.018	0.011
actuator R	0.165	0.627	0.019	1	0.417	0.030
actuator P	0.267	0.008	0.025	0.017	1	0.023
actuator Y	0.113	0.622	0.035	0.018	0.034	1

Table 8.3: Coupling coefficients in the IM stage at 10 Hz.

	sensor L		sensor T		sensor Y	
	10 mHz	10 Hz	10 mHz	10 Hz	10 mHz	10 Hz
actuator L	1		0.874	0.012	0.389	0.210
actuator T	0.253	0.014	1		0.466	0.116
actuator Y	0.263	0.186	0.739	0.231	1	

Table 8.4: Coupling coefficients in the F0 stage.

8.2 Controls in the calm-down phase

Here active damping servos were switched on and the decay time reduction of mechanical resonances was performed. The servo filters are designed based on the frequency responses from actuators to sensors mentioned above. Since measured frequency responses deviated from simulated responses due to non-mechanical couplings at higher frequencies, one needed to reduce the control gains at these frequencies with low-pass filters in suitable cut-off frequencies. The decay time of mechanical resonances in the actively controlled system was investigated and compared with that in the passive system.

8.2.1 Servo design

Figure 8.6 shows the schematic control diagram in the calm-down phase. Damping control loops are created at the TM, IM and F0 levels using OSEMs or LVDT+coil-magnet actuators. Resonances about vertical GAS filter modes are suppressed by the LVDT+coil-magnet actuator unit implemented in the top GAS filter (F0). DC servos are also included in the IP and GAS filter control loops to suppress the thermal drift of the IP and GAS filters. The geophones and optical lever are not used. These sensors are sensitive but have narrow linear ranges, and thus they are not suitable for the feedback controls in the calm-down phase, which require robustness rather than quietness.

Figure 8.7 shows Bode plots of the designed servo filters in the calm-down phase. To obtain viscous damping forces, displacement signals obtained by OSEM shadow sensors

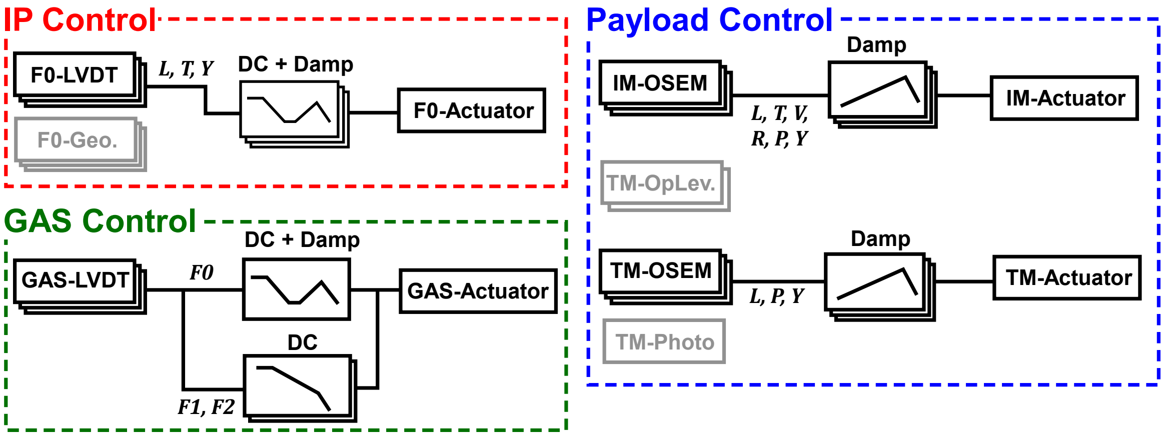

Figure 8.6: Schematic control diagram in the calm-down phase.

and LVDTs are converted to velocities with differentiation filters and sent to the actuators with appropriate gains. The feedback filters have gain proportional to f around the frequencies of mechanical resonances to be damped. The gains of damping filters are tuned to acquire optimal damping strength. A resonant gain introduced around 0.16 Hz to the IM yaw control is for damping the torsion mode of the IM suspension wire efficiently. For the F0 and GAS controls, the control gains are boosted at low frequencies for drift compensation. DC control gains are set to 1000 for the F0 control and 300 for the GAS controls with a cutoff at 10^{-4} Hz. The control gains at high frequencies are suppressed with lowpass Butterworth filters with certain cut-off frequencies. The cut-off frequencies are set lower than the frequencies where the electro-magnetic couplings of sensors and actuators get dominant. The typical frequencies are 50 Hz for OSEMs and 5 Hz for LVDT-actuator units. The cut-off frequencies are set even lower in some DoFs to avoid instability due to the resonant peaks around these frequencies.

8.2.2 Decay time measurement

In order to verify the performance of the damping controls, mechanical resonances of the suspension system were surveyed and their decay time constants were investigated using the following procedure. First, the target mechanical resonance was excited by sending a sinusoidal wave signal at the resonant frequency to an appropriate virtual actuator. After the resonance is well excited, the actuator was switched off and a decay signal was observed with implemented sensors. The observed decay signal was fitted by an exponential-decay sine wave function:

$$f(t) = A \exp\left(-\frac{t}{\tau_e}\right) \sin(2\pi f_0 t + \varphi) + x_0. \tag{8.1}$$

The time constant τ_e denotes the $1/e$ decay time of the mechanical resonance. Sometimes it was difficult to excite only one resonant mode and a superposition of two decay signals

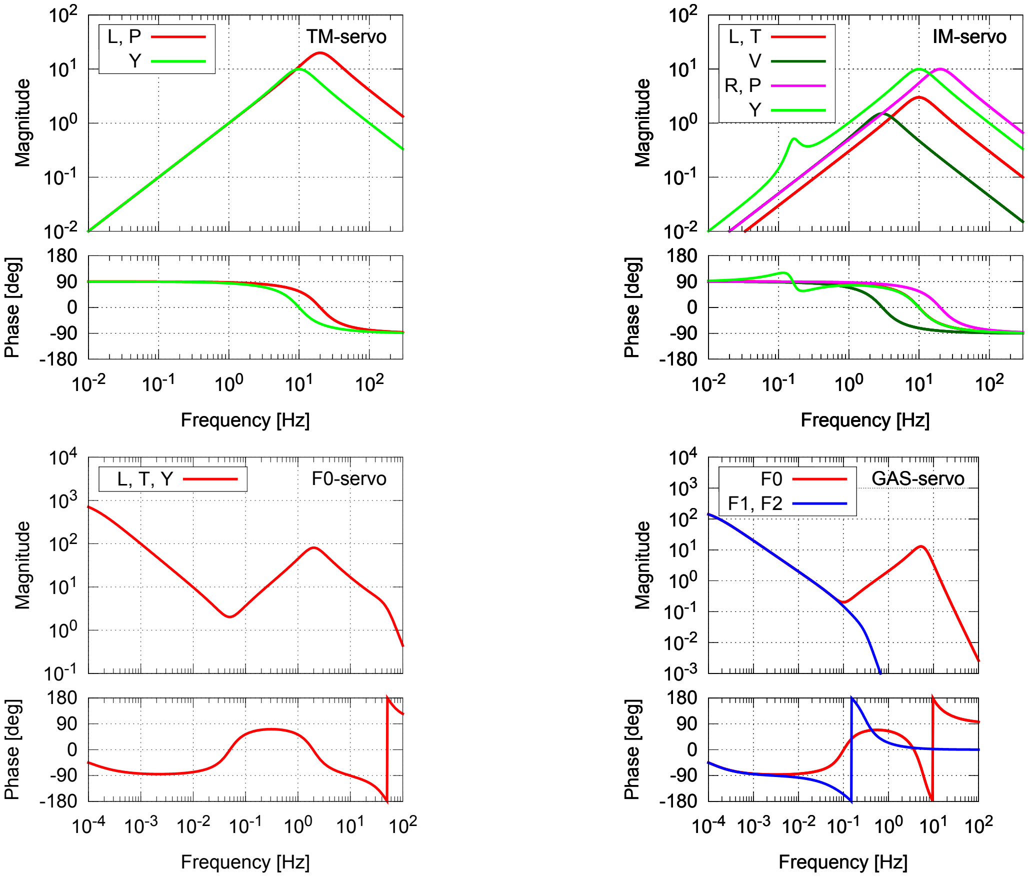

Figure 8.7: Servo filters in the calm-down phase.

was obtained. This can happen when there exist mechanical resonances with close eigen frequencies. In such a case, the decay signals were fit by a sum of two different decaying sine waves:

$$f(t) = A_1 \exp\left(-\frac{t}{\tau_{e,1}}\right)\sin(2\pi f_1 t + \varphi_1) + A_2 \exp\left(-\frac{t}{\tau_{e,2}}\right)\sin(2\pi f_2 t + \varphi_2) + x_0. \quad (8.2)$$

Figure 8.8 shows an example of decay signals, from the pendulum mode of IM (mode #17, see table 8.5). The left graph shows the measured decay signal in the passive system and the right graph shows that with active damping controls. The signals were obtained oy the readout of the longitudinal displacement with the IM OSEMs. Fittings were performed on signals over the time between 0 and 15 sec. The oscillation decays faster when the damping controls are applied, and the $1/e$ decay time is shortened by a factor more than 10 for this mode.

Note that the measured signal with damping controls deviated from the fitting curve when the oscillation amplitude became small. The decay time increased when the oscillation amplitude falled below a certain value ($\sim$ 10 μm for this mode). This indicates that damping forces were not applied well for small amplitude oscillations. Explanations on this phenomenon are given later.

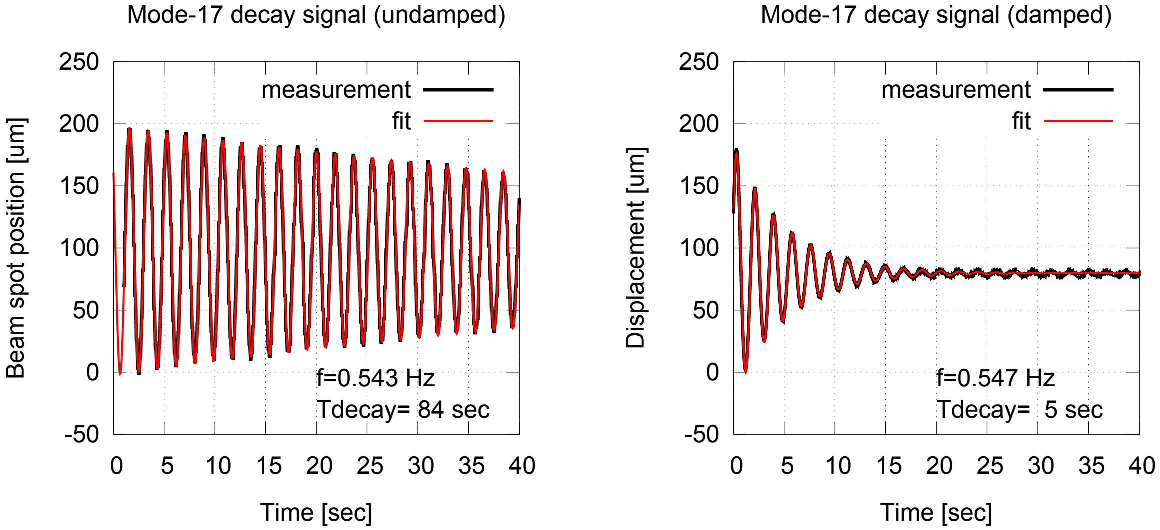

Figure 8.8: Decay signals for resonant mode #17 with and without damping control. The signals were obtained from the longitudinal displacement readout from IM OSEMs.

Table 8.5 shows a list of mechanical resonances of the suspension system predicted in a rigid-body model simulation. It shows the mechanical resonances with eigen-frequencies lower than 20 Hz. The mode shapes of the mechanical resonances are summarized and illustrated in Appendix B. The variable names used for expressing the mode shapes obey the following convention: the first letter denotes the direction of the motion (longitudinal, transverse, vertical, pitch, roll or yaw) and the last two letters denote the rigid body name.

Table 8.6 and 8.7 show measured resonant frequencies and decay times of resonant modes in the passive and actively controlled systems, respectively. There were several resonant modes which were not visible to the built-in sensors; the modes regarding the MD motions (#13-15) and the F1 tilt modes (#18,23). They were not observed since the modes do not strongly couple with the motions of F0, IM or TM, where the vibration sensors were implemented. The torsion modes of the GAS filter chain (#1,5,6) were strongly damped by the eddy-current damper and the decay time was suppressed to below 1 min. Thus the measurement results verify the effectiveness of the damping of the low-frequency torsion modes using the eddy-current damper.

In the passive system, there were several modes with long decay time, which was in the order of 10^3 sec. These resonant modes were successfully damped in the actively controlled system and most of the decay time constants were suppressed lower than the requirement (1 min.), as shown in figure 8.9. There was one resonant mode whose decay time constant exceeded 1 min., involving the transverse motions of TM and RM. The mode shape is shown in figure 8.9. Since there was no device implemented for sensing or actuating such motions, it was not able to damp this mode efficiently. However, the TM transversal motion does not interfere with the interferometer operation unless the amplitude exceeds ∼1 mm, which is the requirement of the beam spot fluctuation on the optics of the interferometer. As the amplitude of this oscillation mode never exceeds 1 mm due to mechanical constraints between TM and RM, there is no problem of having large decay time for this mode.

8.2.3 Residual vibration

Figures 8.10 and 8.11 show the residual mirror vibration in the longitudinal, vertical, pitch and yaw DoFs after the system calms down. The longitudinal vibration was measured by the photo sensor and the angular vibration was measured by the optical lever. The mirror vertical vibration was estimated by summing signals from the three LVDTs on the GAS filters. Table 8.8 summarizes the measured RMS displacement/angle and compares it to the requirement set in subsection 5.2.5. The residual mirror vibration was suppressed below the required level.

8.2.4 Feedback signals

The spectra of feedback signals sent to several OSEM actuators in the stationary state are shown in figure 8.12. The signals were measured in the digital system just before the outputs to the analog circuits. They were converted to the analog signals through DACs and then sent to the coil driver analog circuits. As the RMS amplitude of the feedback signals was less than 1 count in the stationary state, the oscillation signals dropped out in the digitization process in the DACs and were not sent to the coil-magnet actuators. This

No.	Frequency [Hz]	Mode Shape	Note
#1	0.0505	YF1, YF2, YIR, YIM, YRM, YTM	wire torsion
#2	0.0794	LF0, LMD, LF1, LF2, LIR, LIM, LRM, LTM	IP translation
#3	0.0794	TF0, TMD, TF1, TF2, TIR, TIM, TRM, TTM	IP translation
#4	0.1232	-YF0, YIM, YRM, YTM	IP rotation
#5	0.1390	-YF1, YIM, YRM, YTM	wire torsion
#6	0.1616	-YF2, -YIR, YIM, YRM, YTM	wire torsion
#7	0.2494	VF2, VIR, VIM, VRM, VTM	GAS filter
#8	0.3021	RIM, RRM, RTM	IM roll
#9	0.3418	PIM, PRM, PTM	IM pitch
#10	0.4094	TIM, TRM, TTM, RTM	main pendulum
#11	0.4196	LIM, LRM, LTM, PTM	main pendulum
#12	0.5247	-VF1, -VF2, -VIR, VIM, VRM, VTM	GAS filter
#13	0.5468	TMD	MD pendulum
#14	0.5470	LMD	MD pendulum
#15	0.5502	YMD	MD yaw
#16	0.5740	RF2, RIR	F2 roll
#17	0.5787	PF2, PIR	F2 pitch
#18	0.5889	RF1	F1 roll
#19	0.6331	-PF1, LTM, -PTM	main pendulum
#20	0.6485	RF1, TTM, RTM	main pendulum
#21	0.6571	-LRM, LTM, -PTM	TM-RM pendulum
#22	0.6580	TRM, TTM, RTM	TM-RM pendulum
#23	0.6863	PF1	F1 pitch
#24	0.7923	VF1, -VF2, -VIR	GAS filter
#25	0.8162	PTM	TM pitch
#26	1.0009	-YIM, -YRM, YTM	TM yaw
#27	1.0325	YIR	IR yaw
#28	1.1844	TIM, -TTM, -TRM	IM pendulum
#29	1.1851	LIM, -LIM, -LRM	IM pendulum
#30	1.2101	RF2, -TIR, RIR	F2 roll
#31	1.2134	PF2, LIR, PIR	F2 pitch
#32	1.3798	-YIM, YRM, YTM	RM yaw
#33	1.4738	TIR	IR pendulum
#34	1.4759	LIR	IR pendulum
#35	4.8559	-PIM, PRM	RM pitch
#36	11.320	VTM	TM vertical
#37	15.528	RTM	TM roll

Table 8.5: The eigen-mode list from a rigid-body model simulation.

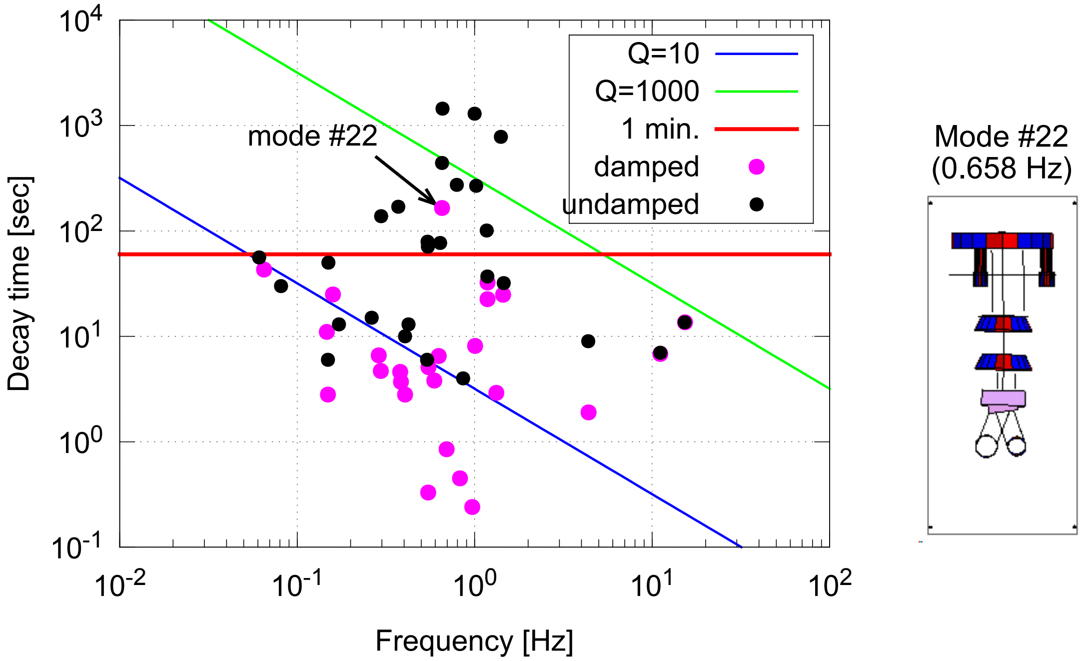

Figure 8.9: Decay time versus resonant frequency plot.

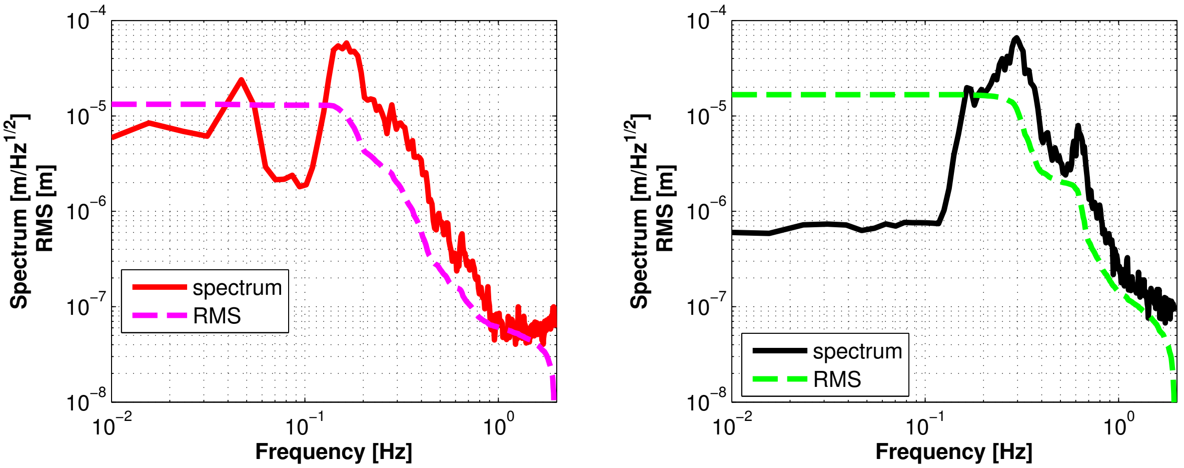

Figure 8.10: (*Left*) Residual mirror longitudinal vibration measured by the photo-sensor. (*right*) Residual mirror vertical vibration estimated from the outputs of the three LVDTs on the GAS filters.

	Frequency [Hz]					
No.	measured	simulated	difference [%]	τ [sec]	Q factor	exc. point
#1	0.061	0.0505	18	40	7.4	YF0
#2/#3	0.087	0.0794	9.6	16	4.3	LF0
#4	0.149	0.1232	20.9	6	3	YF0
#5	0.150	0.1390	7.7	50	24	YF0
#6	0.172	0.1616	6.2	13	7	YF0
#7	0.263	0.2494	5.6	15	13	VF0
#8	0.297	0.3021	1.9	138	129	RIM
#9	0.371	0.3418	8.4	170	198	PIM
#10	0.405	0.4094	1.0	10	12	TF0
#11	0.424	0.4196	1.0	13	17	LF0
#12	0.539	0.5247	2.7	6	9	VF0
#13	-	0.5468	-	-	-	-
#14	-	0.5470	-	-	-	-
#15	-	0.5502	-	-	-	-
#16	0.545	0.5740	0.6	71	122	TIM
#17	0.543	0.5787	0.6	79	135	LIM
#18	-	0.5889	-	-	-	-
#19/#20	0.639	0.6331	1.1	77	154	LF0
#21	0.659	0.6571	0.7	1448	2996	LTM
#22	0.655	0.6580	0.4	442	909	TF0
#23	-	0.6863	-	-	-	-
#24	0.861	0.7923	8.7	4	10	VF0
#25	0.793	0.8162	2.9	274	683	PTM
#26	1.000	1.0009	0.1	1295	4069	YTM
#27	1.020	1.0325	1.2	268	857	YIM
#28/#30	1.176	1.2101	2.8	39	144	TIM
#29/#31	1.178	1.2134	2.9	37	135	LIM
#32	1.406	1.3798	1.9	782	3456	YTM
#33/#34	1.456	1.4728	1.0	32	143	TF0
#35	4.361	4.8559	10.2	9	119	PTM
#36	11.11	11.320	1.9	7	237	VIM
#37	15.25	15.528	1.8	5	235	RIM

Table 8.6: Measured resonant frequencies and decay time without control.

	Frequency [Hz]					
No.	damped	undamped	difference [%]	τ [sec]	Q factor	exc. point
#1	0.065	0.061	5.6	43	8.6	YF0
#2/#3	0.156	0.081	45.6	4.2	2.1	LF0
#4	-	0.149	-	-	-	-
#5/#6	0.158	0.172	8.1	9	4.2	YF0
#7	0.288	0.263	8.5	6.6	6.6	VF0
#8	0.296	0.297	0.3	4.7	4.4	RIM
#9	0.380	0.371	0.3	4.6	5.6	PIM
#10	0.384	0.405	5.2	3.7	4.4	TF0
#11	0.405	0.424	4.5	2.8	3.5	LF0
#12	0.592	0.539	8.9	3.8	7.0	VF0
#13	-	-	-	-	-	-
#14	-	-	-	-	-	-
#15	-	-	-	-	-	-
#16	0.548	0.549	0.2	5.1	8.8	TIM
#17	0.547	0.545	0.3	5.1	8.7	LIM
#18	-	-	-	-	-	-
#19/#20	0.627	0.639	1.8	6.5	13.0	LF0
#21	0.694	0.659	5.0	0.85	1.9	LTM
#22	0.654	0.655	0.2	242	496	TF0
#23	-	-	-	-	-	-
#24	-	0.861	-	-	-	-
#25	0.826	0.793	4.0	0.45	1.2	PTM
#26	1.030	1.000	3.0	6.7	21.8	YTM
#27	1.014	1.020	1.0	5.9	18.8	YIM
#28/#30	1.180	1.176	0.3	32.5	120	TF0
#29/#31	1.180	1.176	0.3	22.5	84	LF0
#32	1.324	1.406	6.2	2.91	12	YTM
#33/#34	1.446	1.445	0.1	24.8	113	TF0
#35	4.383	4.361	0.5	1.9	26	PTM
#36	11.11	11.11	0.0	6.8	237	VIM
#37	15.30	15.25	0.3	13.6	654	RIM

Table 8.7: Measured resonant frequencies and decay time with control.

	requirement	measured RMS
longitudinal	50 μm	13 μm
transverse	1 mm	-
vertical	1 mm	16 μm
pitch	50 μrad	7 μrad
yaw	50 μrad	40 μrad

Table 8.8: Residual vibration of the mirror in the calm-down phase.

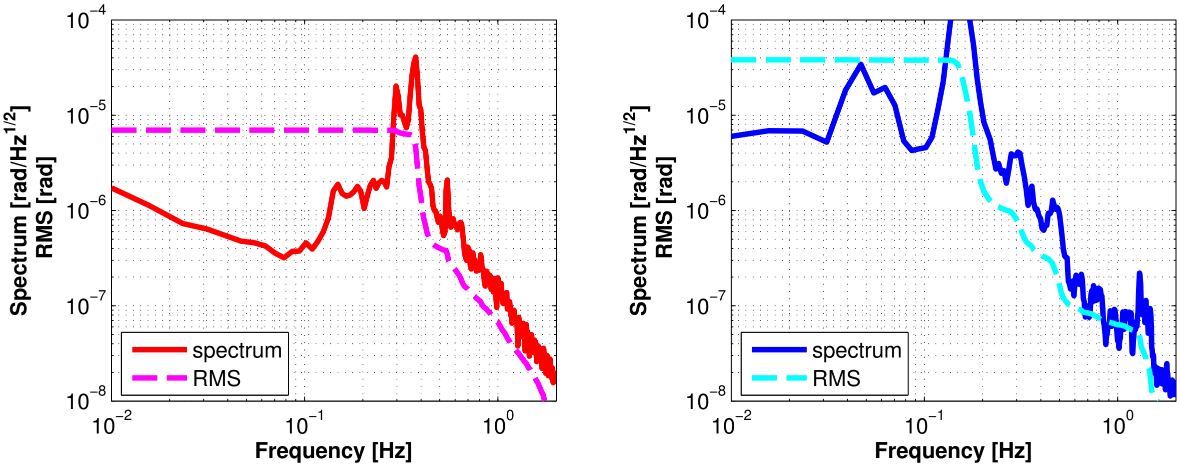

Figure 8.11: Residual mirror angular motion about pitch (*left*) and yaw (*right*) *measured by the optical level.*

means that the suspension system was not well-controlled when the oscillation amplitudes go below a certain level. The typical oscillation amplitudes to acquire the feedback signals larger than 1 count were $\sim 0.1\ \mu$m for the IP controls, and $\sim 10\ \mu$m for the IM and TM controls. This is inconvenient feature when suppressing the RMS oscillation amplitude of the suspension components.

To acquire good-quality feedback signals in the stationary states, the efficiencies of the TM and IM actuators have to be reduced by 1-2 orders of magnitude from the current prototype system. This can be achieved by reducing the size of magnets, the winding number of actuator coils, or the gains of the coil-driver circuits. Although this also reduces the maximum forces of the actuators, it is not a problem because there is a big margin between the maximum applicable voltage of DACs (10 V) and the maximum required voltage in the calm-down phase (measured to be$\sim$50 mV in the prototype system). Reduction of the actuation efficiency is also crucial in terms of actuator noise couplings in the detection band of gravitational waves.

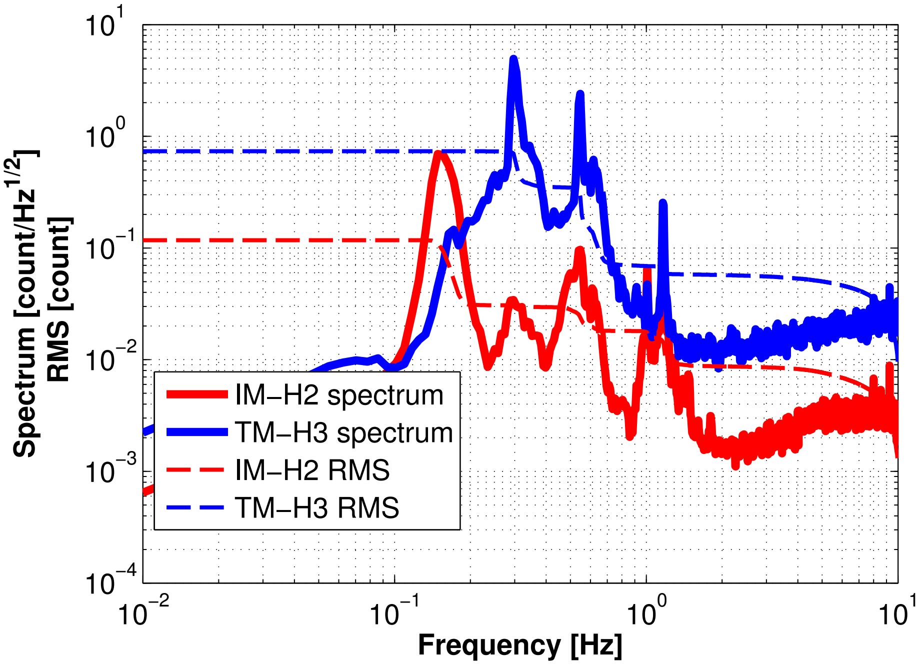

Figure 8.12: Feedback signals sent to several OSEM actuators in the stationary state.

8.3 Controls in the lock-acquisition phase

8.3.1 Control diagram

After the suspension system calms down, the active controls are switched to the low-RMS controls, aiming to suppress the RMS velocity and anglular displacements of the TM to allow the lock acquisition of the interferometer. Figure 8.13 shows the schematic control diagram in the lock-acquisition phase. Reduction of the RMS longitudinal velocity of the TM is achieved by controlling the IP stage with combined sensor signals from LVDTs and geophones. The signals of the geophones and LVDTs are blended with a crossover frequency of 50 mHz, and then sent to the servo filters, which are identical to those used in the calm-down phase. Reduction of the RMS pitch and yaw angles are performed by the alignment controls using the optical lever. The TM pitch and yaw angles monitored by the optical lever are fed back to the actuators at the IM level. When the optical lever controls are switched on, the damping control loops for pitch and yaw with the OSEMs are opened, to avoid competition between the optical lever and OSEM controls. The damping control of the top GAS filter is switched off and the GAS filter controls only employ DC servos.

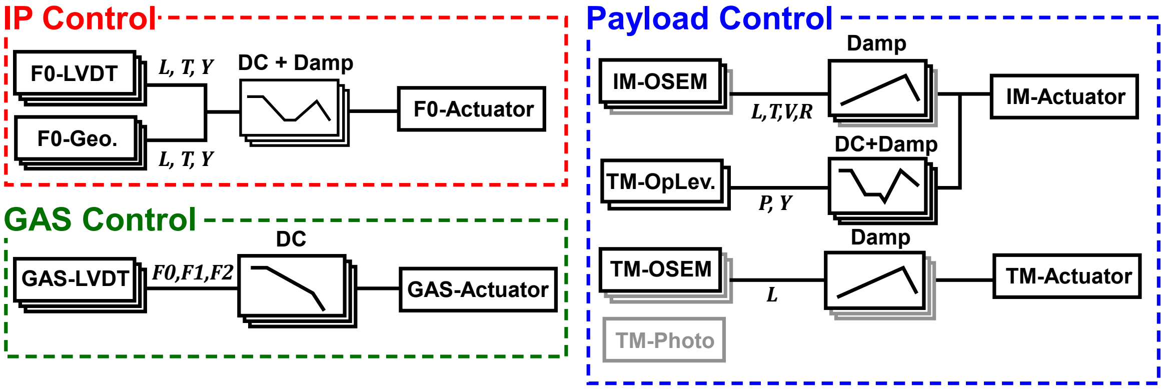

Figure 8.13: Schematic control diagram in the lock-acquisition phase.

The servo filters for the optical lever controls are shown in figure 8.14. The open-loop gains expected from the measured mechanical responses (from the IM actuators to the optical lever signals) are also plotted. The servo filters are basically the same as those used in the control simulation (see figure 5.17), but several modifications are made to the pitch servo filter:

- The frequency of the notch around 5 Hz is precisely tuned so that it cancels out the resonant peak of the RM pitch mode at 4.36 Hz.
- A shallow notch at 1.2 Hz is added, since the resonant peak of the IM pendulum mode coupled at the frequency destabilizes the control.

The bandwidths were 0.9 Hz for the pitch and 1.5 Hz for the yaw control. The DC gain was roughly 200, with a cutoff at 10^{-4} Hz.

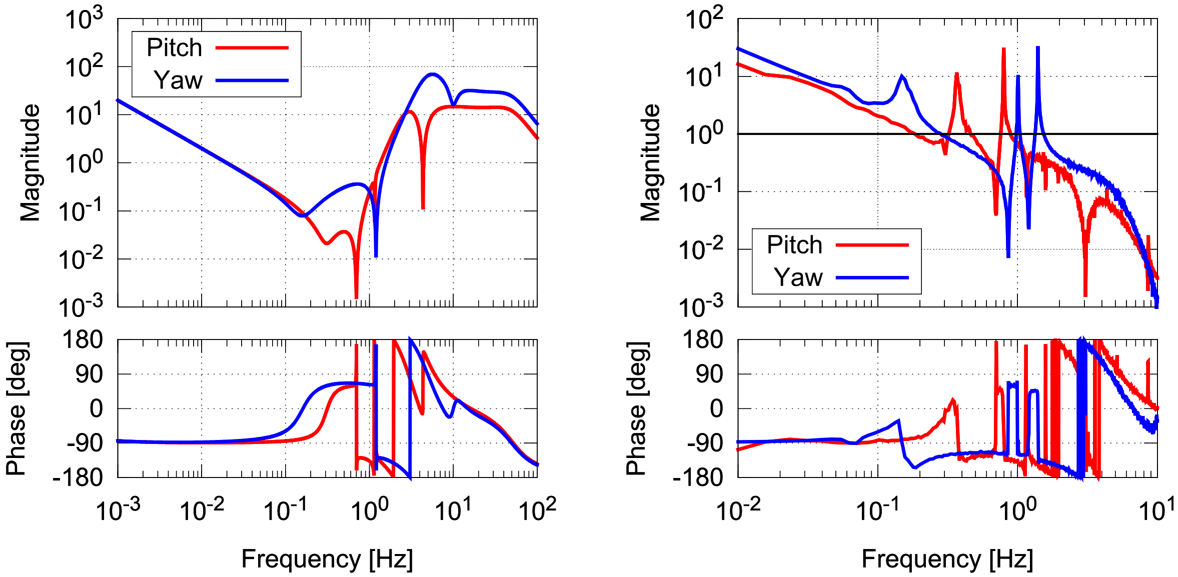

Figure 8.14: (*Left*) Servo filters for the optical lever controls. (*Right*) Expected open loop gains from the measured mechanical responses of the optical lever.

8.3.2 Performance of IP control

Figure 8.15 shows the vibration spectra of the top stage in the longitudinal direction measured by the geophones, with and without the IP control. The vibration spectrum of the IP base is also plotted as a reference (shown in the black curves). The RMS velocities are calculated by integrating the spectra below 1 Hz and are plotted with dashed curves. The active controls suppressed the top stage vibration in the 0.1-1 Hz band and reduce the RMS velocity by a factor of ∼2. The achieved RMS velocity of the top stage was 0.5 μm/sec, which is compatible with the required mirror RMS velocity of the type-B SAS.

Figure 8.16 shows a measurement of the transfer function from the ground longitudinal vibration (LGND) to the TM longitudinal vibration (LTM) in the actively controlled system, compared with the simulation. The transfer function was derived from two separate measurements; the transfer function from the ground vibration to the top stage vibration (LGND→LF0), and that from the top stage vibration to the TM vibration (LF0→LTM). The former one was taken by comparing the signals of the geophones placed on the IP base and on the top stage, induced by the natural seismic vibration (calculated from the ratio of two velocity spectra shown in figure 8.15). The latter one was taken by exciting the top stage motion with actuators and comparing the induced top stage displacement with the photosensor signals on the TM. The respective transfer functions are plotted in dashed curves in figure 8.16. The combined transfer function from LGND to LTM fits nicely with the prediction at 0.1-1 Hz. The result demonstrates the attenuation performance of the actively controlled suspension system in the frequency band where the spectrum

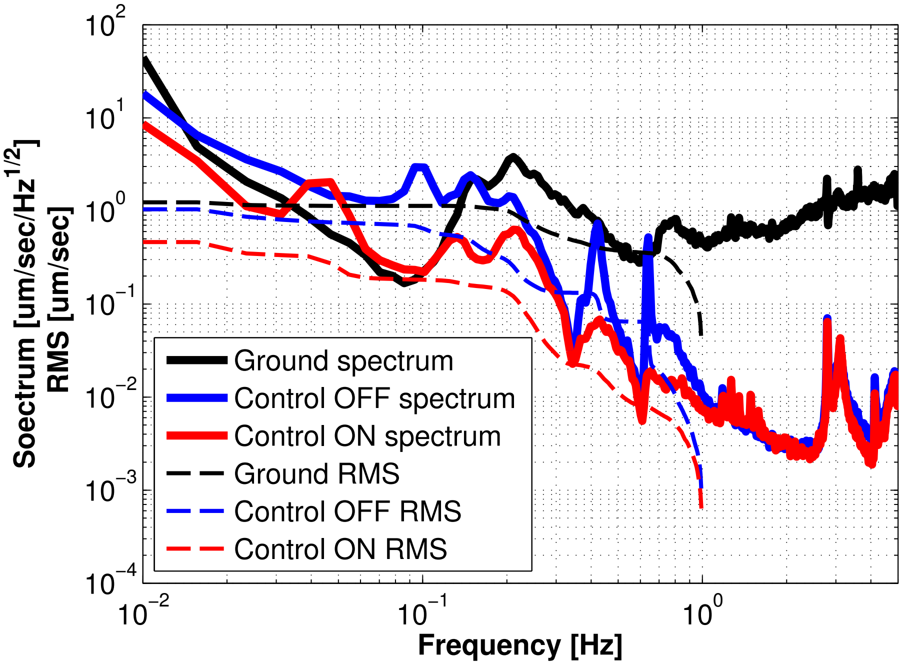

Figure 8.15: Comparison of the top stage longitudinal velocities measured by geophones, with and without the IP controls.

contributes to a large fraction of the RMS velocity. The deviation at low frequency < 0.1 Hz was due to poor sensitivities of geophones resulting in bad coherence in the transfer function measurement from LGND to LF0.

Figure 8.17 shows estimation of the mirror longitudinal velocity spectrum with the measured transfer function, assuming seismic vibration of the KAGRA site. The expected mirror RMS velocity is 0.2 μm/sec, which meets the requirement set in table 5.4 (0.5 μm/sec).

8.3.3 Performance of alignment control

The spectra of the TM pitch and yaw motions measured by the optical lever are shown in figure 8.18. The curves captioned as 'Alignment OFF' are the measurement data without the alignment control, and the curves captioned as 'Alignment ON' are those with the alignment control. Note that the measured spectra with the alignment control were taken by the 'in-loop' sensors, which were under requisition in the feedback control loops. In both cases, the active controls other than alignment control (such as the IP controls, and OSEM controls for other DoFs) were switched on. The angular motions lower than 0.5 Hz were suppressed by the alignment control, resulting in reduction of the RMS angles by a factor of 3 for the pitch and 10 for the yaw motions.

The achieved RMS angles of the TM were 1.6 μrad for pitch and 2.5 μrad for yaw respectively, while the requirement on the RMS angle is 1 μrad for the type-B system. Note

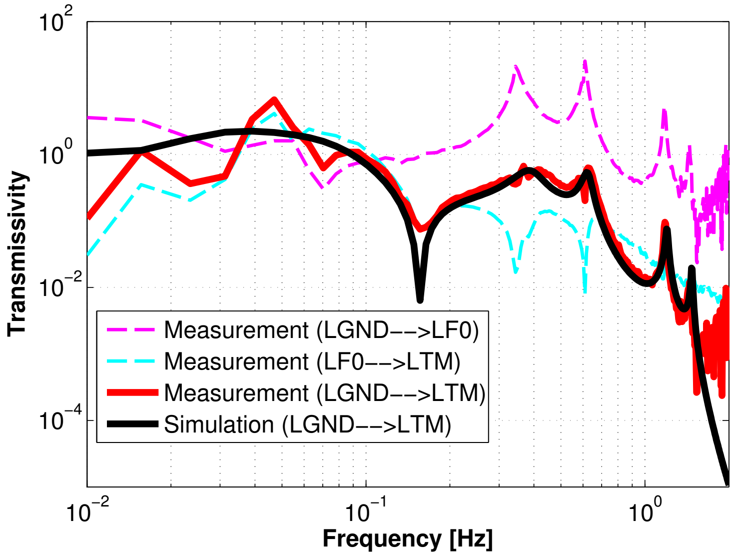

Figure 8.16: Longitudinal transfer functions of the type-B SAS prototype.

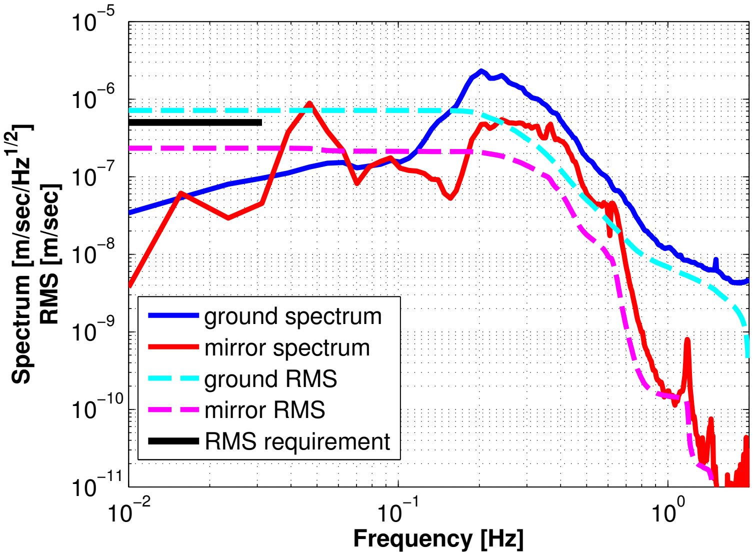

Figure 8.17: The mirror longitudinal vibration spectra estimated with the measured transfer function, assuming seismic vibration in the KAGRA site.

that the seismic vibration in the laboratory was extremely large when the alignment control tests were performed as the stormy ocean induced huge microseismic vibrations. The seismic vibration in the Kamioka site is expected to be smaller by 1-2 order of magnitudes. Figure 8.19 shows the estimated mirror angular spectra in the Kamioka site, scaled by the ratio of the seismic spectrum in the laboratory and in the Kamioka site. The estimated RMS angles are 0.1 μrad for pitch and 0.3 μrad for yaw, which meet the requirement set in table 5.4.

8.4 Controls in the observation phase

8.4.1 Demonstration of lock acquisition

The active controls of the suspension system are to be switched to those for the observation phase as the lock acquisition of the interferometer is achieved. Since there was no interferometer in the prototype system, the lock of the TM position was demonstrated by feeding the photosensor signal back to the TM longitudinal actuator. Figure 8.20 shows the servo filter designed for the TM lock and the expected open loop gain. In the actual interferometer, the control bandwidth of the lock acquisition should be set around $\sim$50 Hz to drag the mirror into the linear regime of the interferometer with fast enough response. The control bandwidth of the lock acquisition with the photosensor was however limited to 10 Hz, since the large sensing noise of the photosensor causes saturation of the feedback signals at high frequencies.

After lock of the TM position is acquired, the damping controls with the OSEMs are switched off, since the sensor noise couplings from the OSEM shadow sensors induce large TM vibration in the detection band of gravitational waves as described in subsection 5.3.3. Figure 8.21 shows the conceptual control diagram in the observation phase. The IP controls and GAS filter controls are kept the same as implemented in the lock-acquisition phase.

Figure 8.22 shows a time series of the photosensor signal and the OSEM control gain when the control status transitions from the lock-acquisition phase to the observation phase. Before the lock acquisition, the photosensor signal oscillated with about ± 10 μm amplitude, which was basically the microsesimic vibration of the frame that the photosensor was fixed to. This low frequency oscillation was suppressed after the locking servo was introduced at $t = 1.2$ [min] and the TM position was kept controlled after the OSEM controls were switched off. As the photosensor was fixed to the security frame rigidly connected to the ground, this control re-injects seismic vibration to the TM. Although the situation is different from the actual interferometer lock acquisition in this sense, the attempts demonstrate the stability of the control topology.

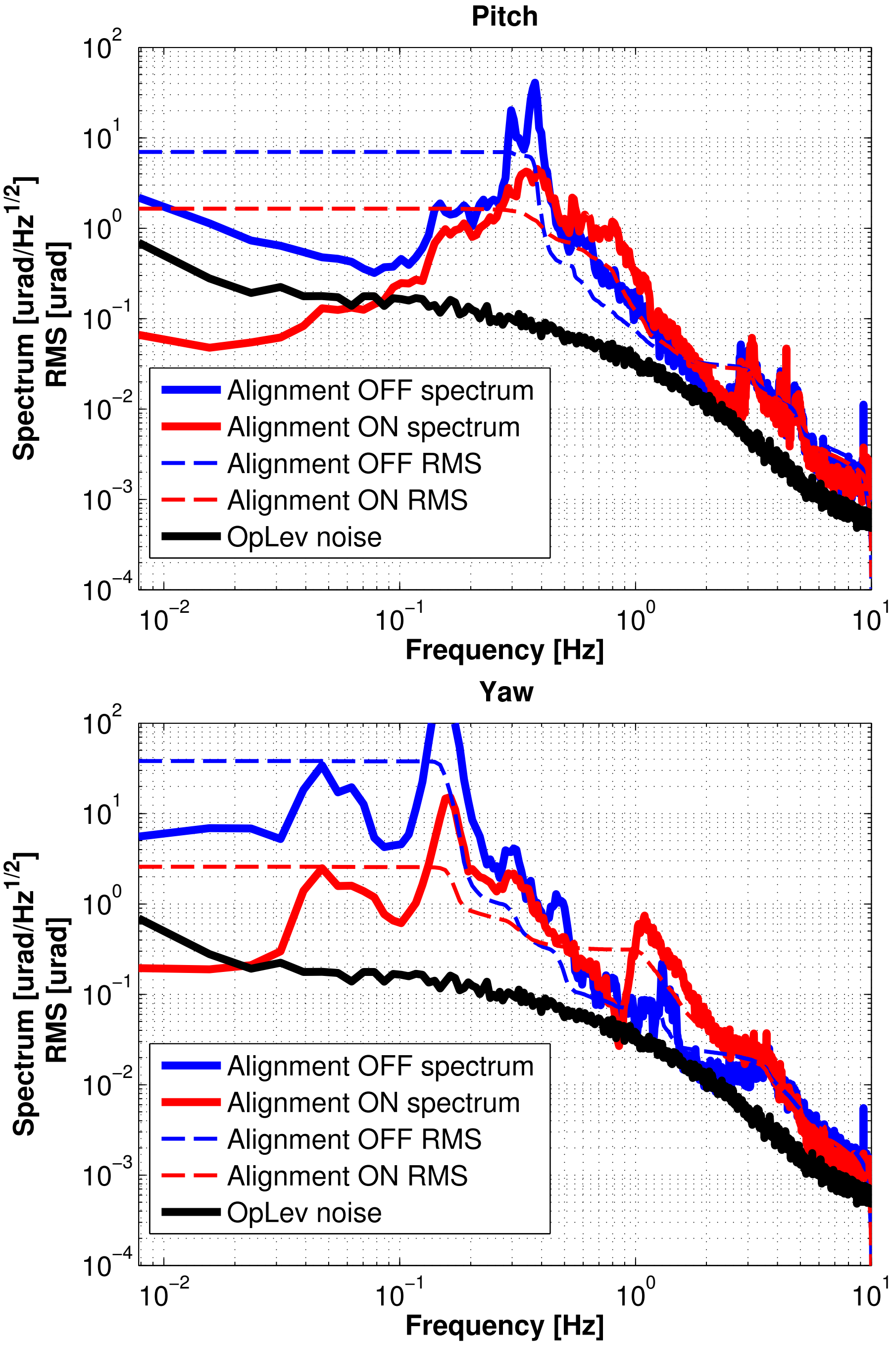

Figure 8.18: The angular spectra of the TM pitch and yaw motions measured by the optical lever, with and without the alignment control.

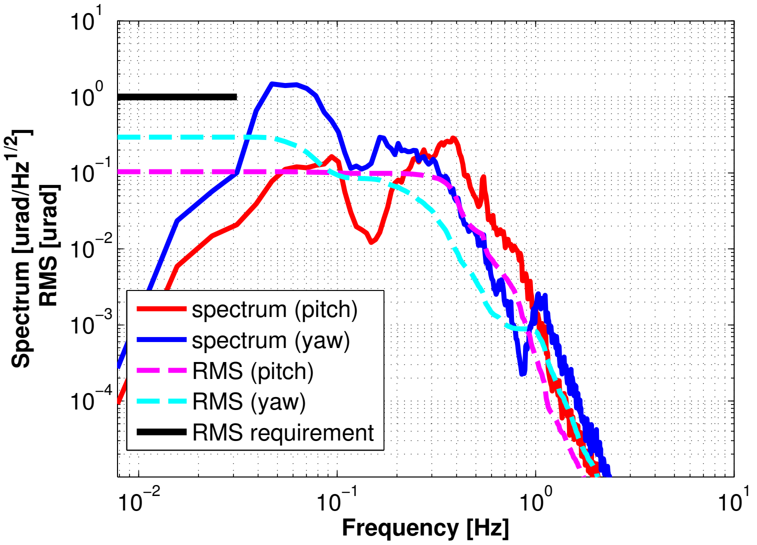

Figure 8.19: Estimation of the mirror angular spectra assuming the seismic vibration in the KAGRA site.

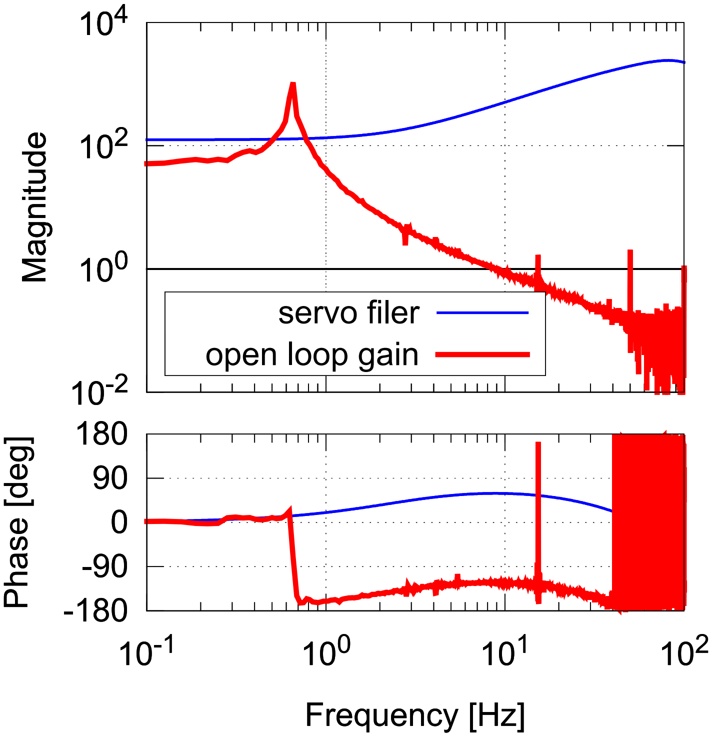

Figure 8.20: Design of the servo filter for the TM lock acquisition and the expected open loop gain.

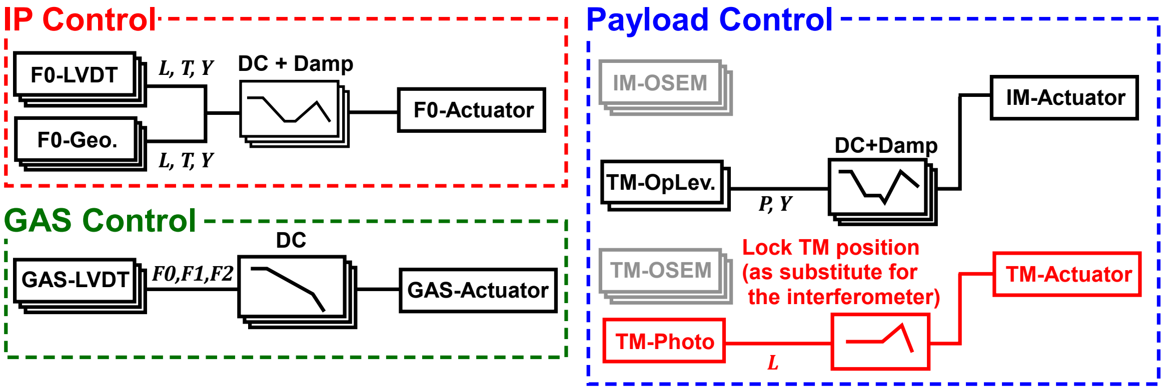

Figure 8.21: Schematic control diagram in the observation phase.

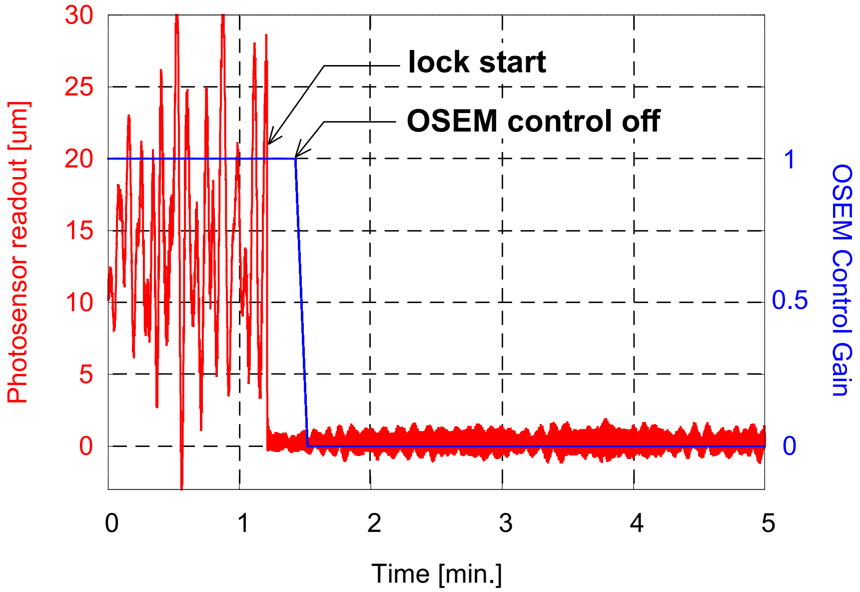

Figure 8.22: Demonstration of the TM lock acquisition with the photosensor signal.

8.4.2 Residual longitudinal displacement

In the observation phase, the RMS longitudinal displacement of the mirror should be suppressed within the controllable range with the interferometer control. Figure 8.23 shows the residual longitudinal displacement spectra of the mirror estimated by the measured vibration transfer function (figure 8.16), assuming the seismic vibration of the laboratory (TAMA site) and the Kamioka site. The estimated RMS displacement with seismic vibration of the Kamioka site is 0.35 μm, which meets the requirement for the type-B SAS (0.4 μm).

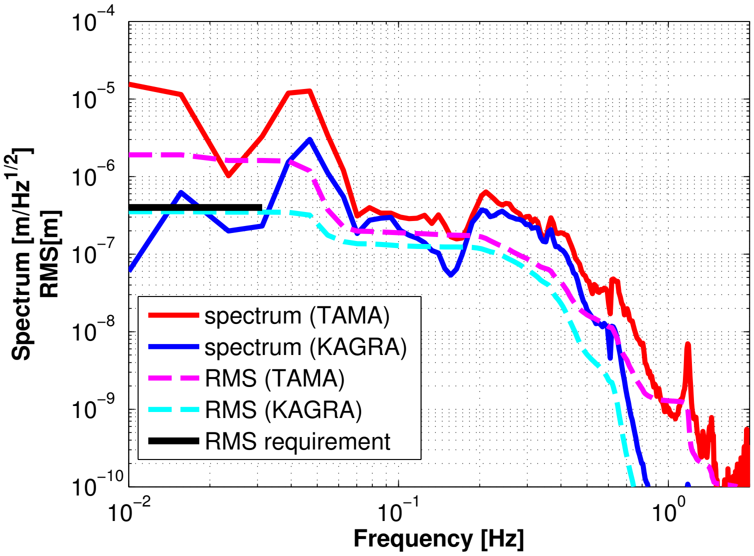

Figure 8.23: The mirror longitudinal displacement spectra estimated with the measured transfer function, assuming seismic vibration in the TAMA laboratory and the Kamioka site.

8.4.3 Sensor noise coupling

An important requirement of the active suspension control in the observation phase is suppressing the control noise coupling in the observation band for gravitational waves. The control noises are possibly introduced in the IP control, the GAS filter control, and the alignment control loops. In the prototype test, the noise couplings from the F2 GAS filter control and the alignment controls were investigated, which are expected to be the main contributors on the in-band noise.

The noise coupling was measured by injecting a sinusoidal wave signal to the sensor readout and detecting the resulting TM displacement with the photosensor. Figure 8.24 shows the measured coupling from the LVDT readout signal from the F2 GAS filter to the photosensor signal. The coupling predicted by the simulation is also plotted, which assumes 1% vertical-horizontal couplings. The measured noise coupling shows similar frequency response to the prediction, while the amplitude is about twice larger. This can be explained by assuming about 1/50 radian tilt in the working direction of the F2 GAS filter. The working direction of the GAS filter could be tilted when there is asymmetry in the stiffness or radial compressive force of the GAS blades.

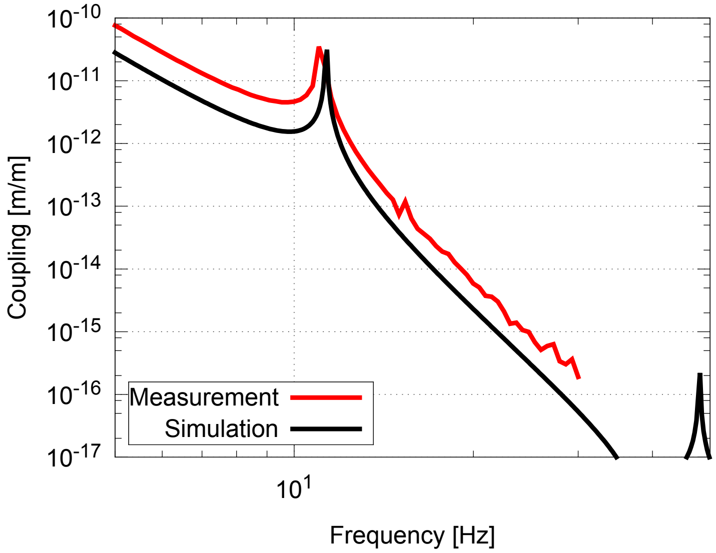

Figure 8.24: Sensor noise coupling from the vertical LVDT on the F2 GAS filter.

Figure 8.25 shows the measured noise couplings from the optical lever readout signals to the TM displacement. The simulation assumes that the measurement point of the TM longitudinal vibration is displaced from the center of mass by 1 mm (i.e. it assumes rotation-translation couplings of 10^{-3} m/rad). The measured noise couplings are 1-2 orders of magnitudes larger than the predictions. The results can be interpreted as follows:

- The measurement point of the TM longitudinal displacement with the photosensor can be off-centered by more than 1 mm. As the position of the photosensor is manually adjusted according to visual inspection, the measurement point can be displaced ∼1 cm at most from the center of mass.

- Since the actuators are not perfectly diagonalized (see section 8.1), the IM virtual actuators about pitch and yaw DoFs may excite the vibration of other DoFs. It is suspected that the couplings to the vertical motions from these actuators contributed to the measured noise couplings in the 10-20 Hz region, because the the resonance appearing in the noise coupling at 11 Hz corresponds to the TM vertical mode.

The noise couplings can be mitigated by adjusting the measurement point of the TM longitudinal vibration as close as possible to the TM center. Therefore the centering of the beam spot of the interferometer is essential in gravitational wave detectors. Another important point is the precision of the actuator diagonalization in the detection band. One can optimize signal distribution of the actuators so that noise couplings to the interferometer signal are minimized.

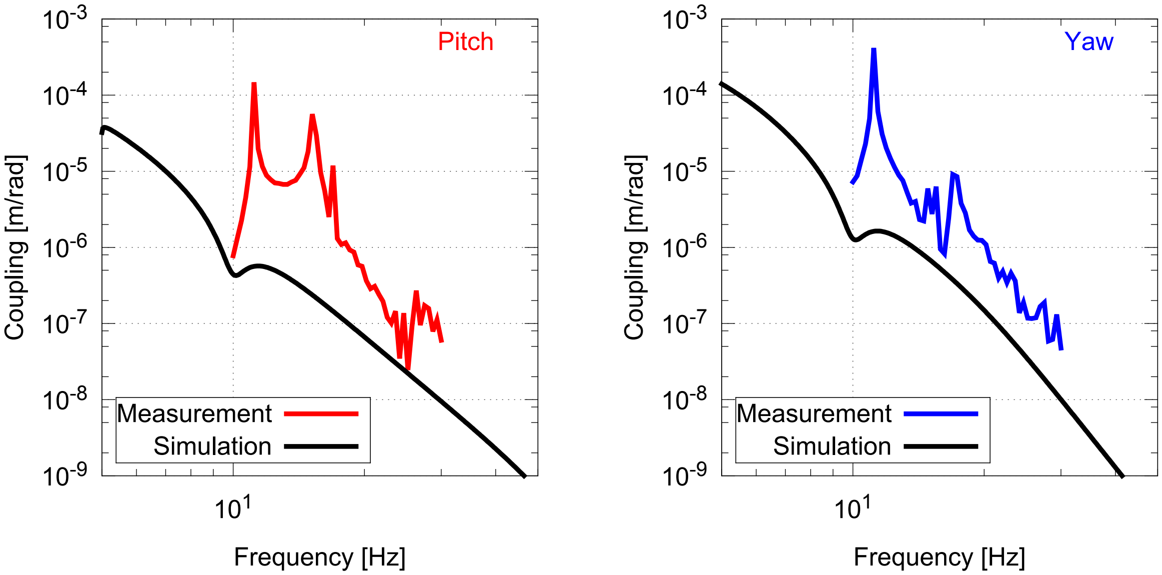

Figure 8.25: Sensor noise coupling from the optical lever.

Figure 8.26 shows the impact of the sensor noise couplings to the mirror displacement spectrum, estimated from the measured frequency responses. Here sensing noise of 10^{-12} $\mu\mathrm{rad}/\sqrt{\mathrm{Hz}}$ is assumed for the alignment sensor, as a typical noise level of the WFS. The coupling from F2 LVDT does not affect the detector sensitivity in the detection band, while the sensor noise coupling of the alignment control induces mirror displacement larger than the required level between 10-20 Hz. The result highlights the importance of control noise reduction in the frequency region.

8.5 Long-term control test

8.5.1 Automaton for suspension controls

As the gravitational wave detector is operated continuously for long time, it is convenient to automate the operation of the interferometer and the comprised suspension systems using a computer system. The automation system not only reduces the burdens of the human operators but also contributes in quick recovery from the transition states and enhances the interferometer operation time. As a demonstration of the automation system of the active controls of the KAGRA-SAS, a simple automaton (finite-state machine) was constructed in the digital control system of the type-B SAS prototype.

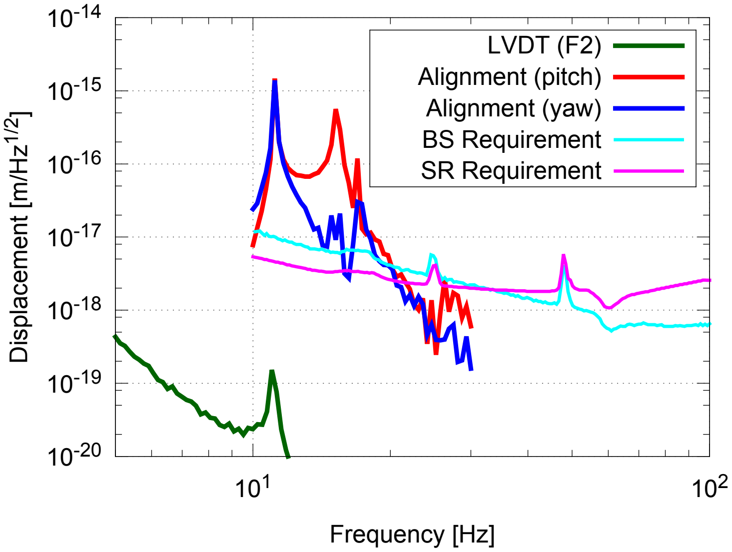

Figure 8.26: Impact of sensor noise couplings to the mirror displacement spectrum.

Figure 8.27 shows conceptual diagram of the automaton in the prototype system. The digital control system provides several process variables which are continuously updated with the states of sensors and actuators. The automaton continuously checks them and determines whether it should stay in the current state or move to another state. The automation logic is programmed in the program language Python, and the programs are operated in the background on the client PC. The states of the automaton are basically linked to the operation status of the detector (the calm-down, lock-acquisition and observation phases). The active controls in each phase are automatically switched to those in another phase when the system satisfies a pre-programmed condition. When sensor/actuator signals exceed certain thresholds due to a large excitation by an earthquake or control instability, the system is brought to the “ground” state in which the active controls for the calm-down phase are applied. If the control system finds fatal errors and the suspension is kept excited, all the active controls are shut down and the system collapses into the “emergency” state. The automaton stays in this emergency state until the problems are fixed and the system is manually brought back to the operation states.

8.5.2 Long-term operation

In order to demonstrate the stability of the active control systems, the suspension system was kept under the control of the automaton operation in the long term. Figure 8.28 shows the transition of the automaton state during the operation of the automated control system from August 26th to 31st in 2015. During the five days operation, the TM position was kept locked to the photosensor for the entire time except in the immediate aftermath of one earthquake event. It demostrates the long-term stability of the active

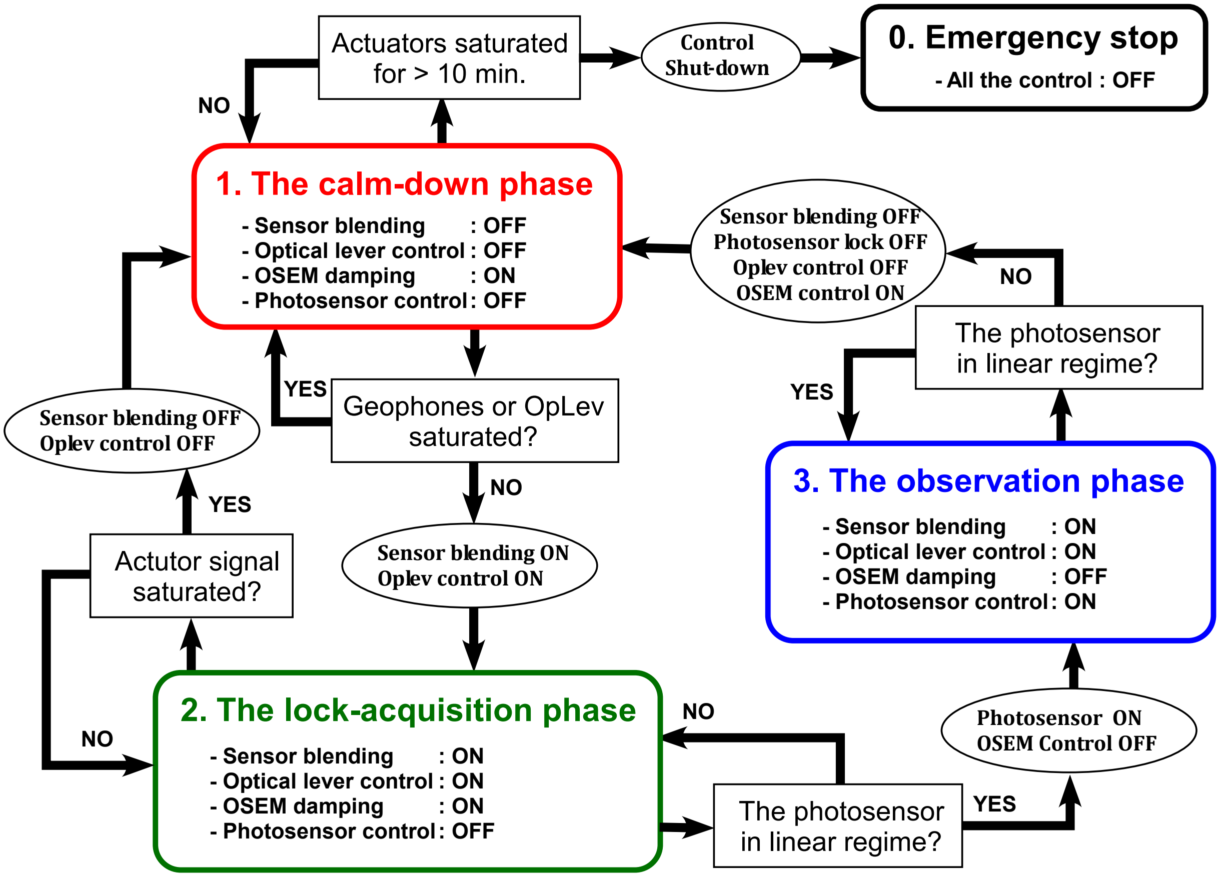

Figure 8.27: Conceptual diagram of the automaton for the prototype SAS controls.

control system in the observation phase. There was an earthquake event which caused loss of the TM lock at 23:46 on August 28th. The earthquake had a seismic intensity of 1 on the Japanese seismic scale. Although the TM position lock was lost due to the earthquake, the system quickly recovered it after an interval of ∼4 min. This demonstrates the performance of the active control systems in the calm-down phase and confirms the soundness of the state controls of the automaton.

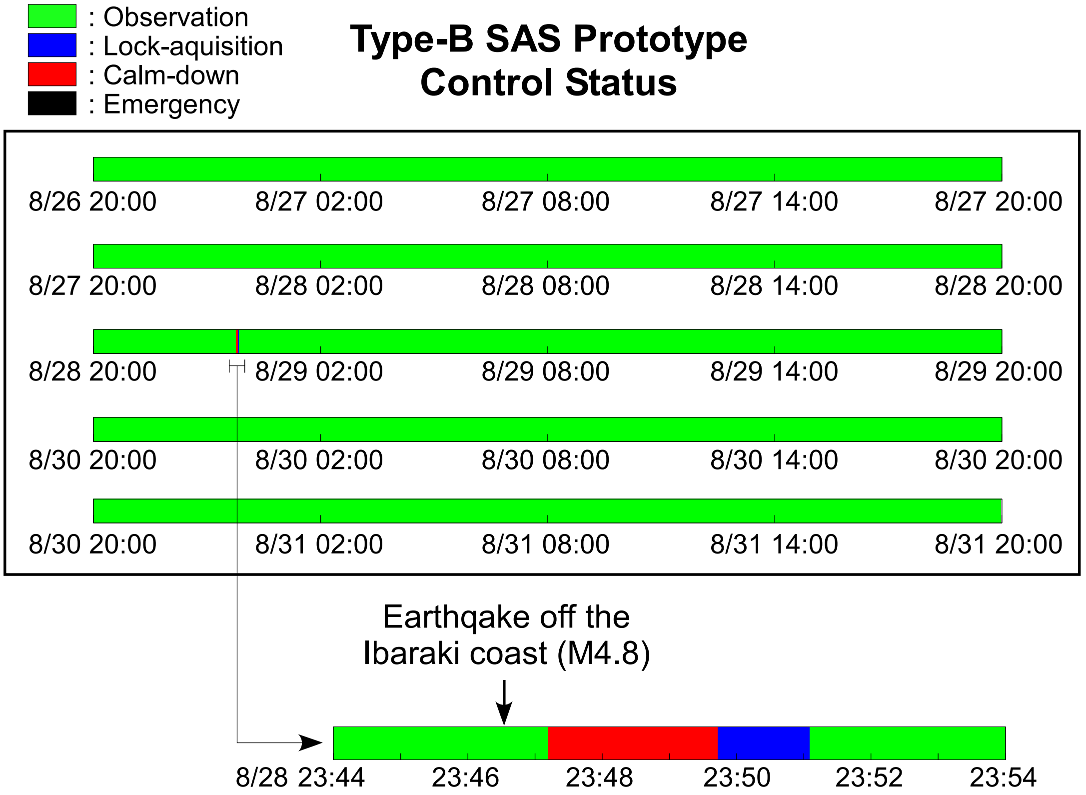

Figure 8.28: Operation states of the active control system in the long-term control test.

8.5.3 Drift measurement

For the stable operation of the interferometer in the observation phase, drift of the mirror position and angle needs to be suppressed by the active control system. The long-term drift comes mainly from the creep and thermal drift of the low frequency oscillators such as IP, GAS filters and torsion pendulums. Here the performance of the DC servos of the IP, GAS filter and alignment control was investigated in the long-term control test. Figures 8.29-8.31 show the time-domain signals of the IP stage displacements, the GAS filter displacements and the mirror angles measured by the optical lever. Each measurement data-point takes the signal averaged over 20 min and thus the frequency components higher than ∼ 1 mHz are filtered out. The measured drift amplitudes in the long-term measurement are summarized in table 8.9. The drift in the 5 DoFs is successfully suppressed by the active control system within the required amplitude.

Note that the temperature variance of the IP base structure is about 1.5 K over the measurement time. The drift of the IP stage is correlated with the IP base temperature and the dependence is 0.12 mm/K for longitudinal and 0.28 mm/K for transversal motion without DC servos.

Device	DoF	requirement	measured drift
IP	longitudinal	0.3 μm	0.15 μm
	transverse	1 mm	0.35 μm
GAS	vertical	1 mm	2.5 μm
OpLev	pitch	1 μrad	0.08 μrad
	yaw	1 μrad	0.02 μrad

Table 8.9: Drift in the 5 DoFs measured in the long-term control test.

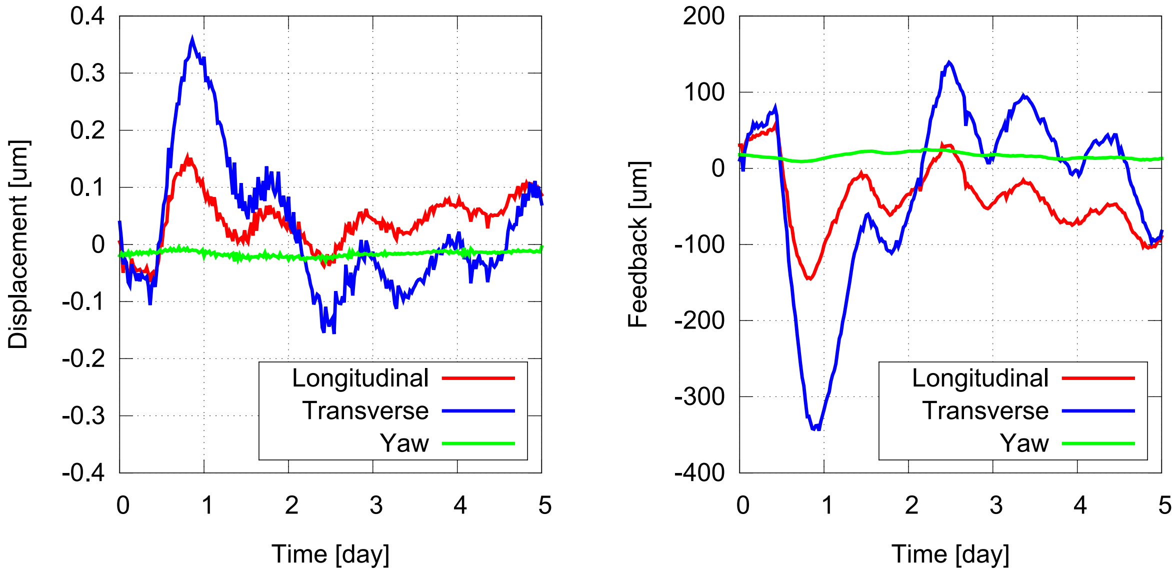

Figure 8.29: The long-term drift of the IP stage displacement; (*left*) the residual displacements and (*right*) the displacements corrected by the feedback control.

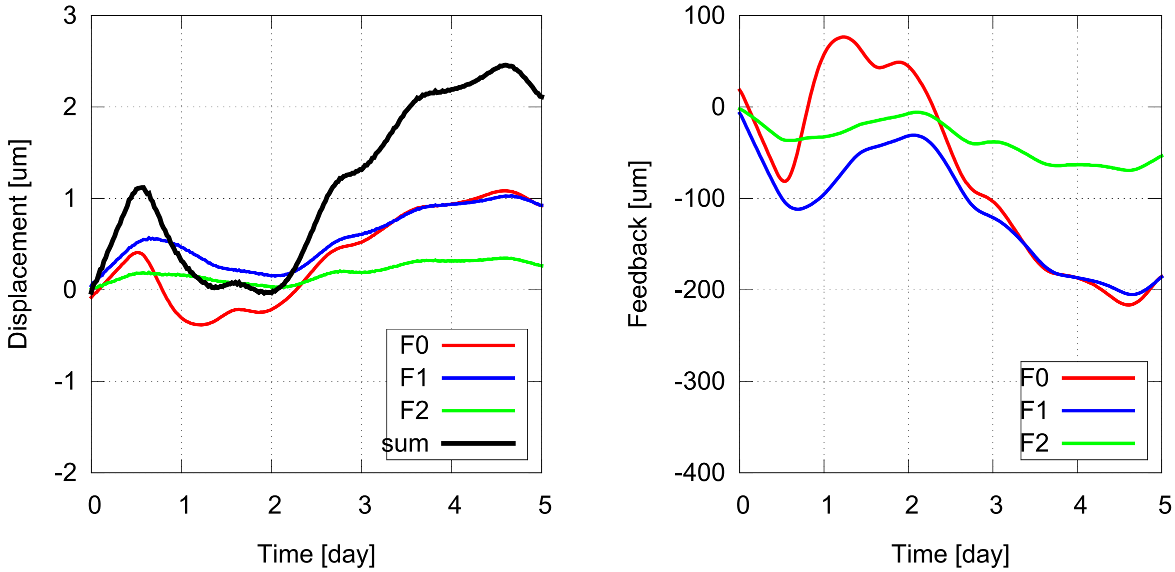

Figure 8.30: The long-term drift of the GAS filters; (*left*) the residual displacements and (*right*) the displacements corrected by the feedback control.

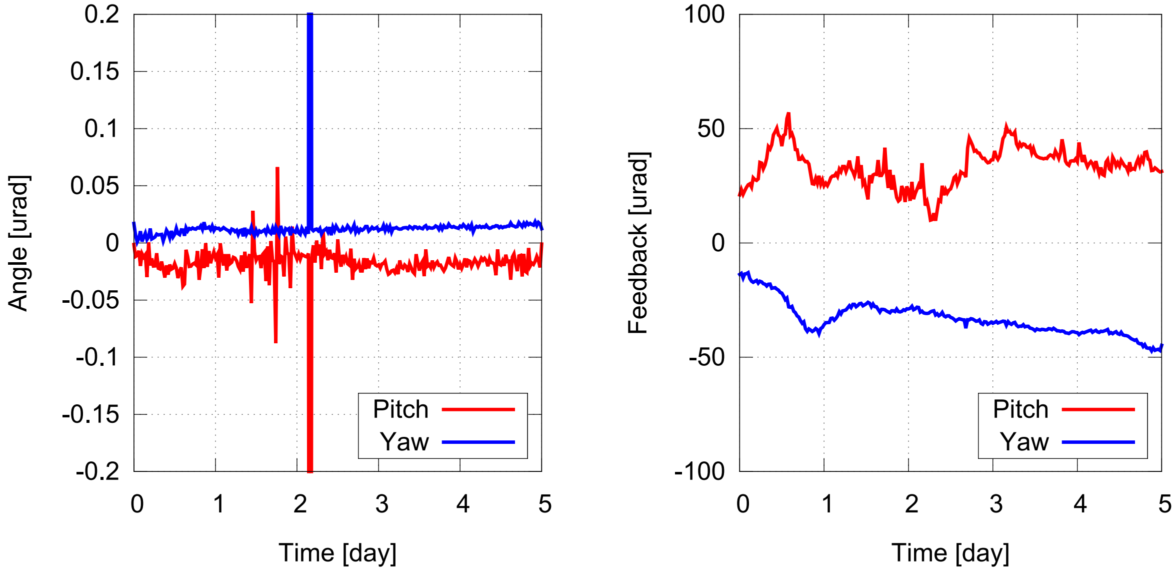

Figure 8.31: The long-term drift of the mirror angles measured by the optical lever; (*left*) the residual angles and (*right*) the angles corrected by the feedback control.

Conclusion and future work

Chapter 9

9.1 Conclusion and discussion

In the experiment with the type-B SAS prototype, practical operation and performance of the active control system were tested. Table 9.1 summarizes the requirements set for the type-B SAS active control system and the measured performance (or estimate based on the seismic vibration level of the Kamioka mine) in the prototype test. It demonstrates that the designed active controls meet the basic requirement for smooth lock acquisition and stable operation of the interferometer, which are essential for long-term observation of gravitational waves.

An important fact learned from the experiment is that the alignment control noise coupling can degrade the detector sensitivity at 10-20 Hz. The impact of the noise couplings measured in the prototype test on the detector sensitivity is shown in figure 9.1. Detection of spinning pulsars at 10-20 Hz would be hopeless with the introduced noise coupling, and the event rate of binary IMBH coalescence would be reduced by a factor of ∼2 from the design, as the low frequency limit of the detection band increases from 10 Hz to ∼20 Hz. For opening the detection band toward 10 Hz and conserving detectability of these astronomical sources, reduction of control noise coupling is desired. The control noise couplings are expected to be suppressed by improvement of the actuator diagonalization scheme, which will be discussed in the following section about future work.

Although the reduction of control noise couplings remains an issues, the type-B SAS with the designed active control system should allow long-term observation of gravitational waves with frequencies as low as 20 Hz. It should allow the detection of gravitational waves from spinning pulsars with rotation periods longer than 0.1 sec, which include the Vela pulsar, possibly emitting strong gravitational waves at 22.39 Hz. Gravitational wave signals from binary IMBH coalescences with $\lesssim 10^3 M_\odot$ are also expected to be detected with one event per several years.

1. The calm-down phase

items	requirements	experimental results	ref.
$1/e$ decay time of resonances	< 1 min.	< 33 sec.	§8.2.2
RMS displacement (longitudinal)	< 50 μm	13 μm	§8.2.3
RMS displacement (transverse)	< 1 mm	not measured	
RMS displacement (vertical)	< 1 mm	16 μm	§8.2.3
RMS angle (pitch)	< 50 μrad	7 μrad	§8.2.3
RMS angle (pitch)	< 50 μrad	40 μrad	§8.2.3

2. The lock-acquisition phase

items	requirements	experimental results	ref.
RMS velocity (longitudinal)	< 0.5 μm/sec	0.2 μm/sec	§8.3.2
RMS displacement (transverse)	< 1 mm	not measured	
RMS displacement (vertical)	< 1 mm	16 μm	§8.2.3
RMS angle (pitch)	< 1 μrad	0.1 μrad (*)	§8.3.3
RMS angle (yaw)	< 1 μrad	0.3 μrad (*)	§8.3.3

3. The observation phase

items	requirements	experimental results	ref.
control noise at 10 Hz (longitudinal)	$< 5 \times 10^{-18}$ m/$\sqrt{\text{Hz}}$	2×10^{-17} m/$\sqrt{\text{Hz}}$	§8.4.3
RMS displacement (longitudinal)	< 0.4 μm	0.35 μm (*)	§8.4.2
RMS displacement (transverse)	< 1 mm	not measured	
RMS displacement (vertical)	< 1 mm	16 μm	§8.2.3
RMS angle (pitch)	< 1 μrad	0.1 μrad (*)	§8.3.3
RMS angle (yaw)	< 1 μrad	0.3 μrad (*)	§8.3.3
displacement drift (longitudinal)	< 0.3 μm	0.15 μm	§8.5.3
displacement drift (transverse)	< 1 mm	0.35 μm	§8.5.3
displacement drift (vertical)	< 1 mm	2.5 μm	§8.5.3
angle long-term drift (pitch)	< 1 μrad	0.08 μrad	§8.5.3
angle long-term drift (yaw)	< 1 μrad	0.02 μrad	§8.5.3

Table 9.1: Requirements on the active controls for the type-B SAS and the measurement results in the prototype experiment. The results marked by (*) are converted from measured values according to the seismic vibration level in the Kamioka mine. The last column shows the subsection where the measurement results are described. The cyan highlight indicates that the requirements are not met in the experimental results.

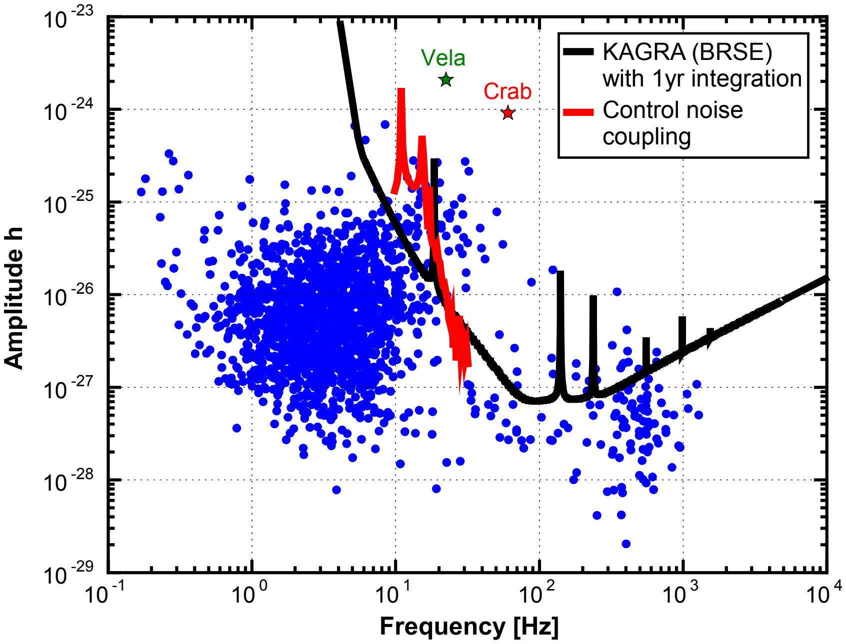

Figure 9.1: Impact of the control noise coupling in the type-B SAS to the KAGRA sensitivity.

9.2 Future works

9.2.1 Actuator issues

In the prototype test, the driving circuits of the coil-magnet actuators are ones reused from TAMA-SAS, which are not optimally designed for the control of the KAGRA-SAS. The strong actuators not only cause a loss of ability to provide delicate control (as discussed in subsection 8.2.4), but also inject large control noise from the electronics of the coil drivers in the detection band of gravitational waves [93]. The gains of the coil driver circuits should be adjusted so that the actuator noise coupling does not degrade the detector sensitivity above 10 Hz. As the maximum applicable forces of the TM and IM actuators have to be reduced due to the noise coupling issues, it is important to allocate the feedback control signal from the interferometer not only to the TM actuators but also to the IM and F0 actuators (hierarchical control [94]). The hierarchical control is required in order to remove the large DC component of the locking forces from the weak TM actuators.

The optimization of the actuator diagonalization is also an important issue in the suspension controls. The diagonalization scheme described in subsection 6.1.6 introduces large couplings in the high frequency region. The couplings can induce larger control noise as discussed in section 8.4.3. A possible solution to this problem is diagonalizing the actuators both at low and high frequencies and connecting the two diagonalization matrices with smooth frequency response. In this scheme, the elements of the coil matrix $\boldsymbol{D}$ have frequency-dependent components and thus the scheme is called the frequency-dependent diagonalization.

9.2.2 Controls of type-A and type-Bp SAS

For the operation of the full interferometer of the KAGRA detector, the control systems for other suspension systems (type-A and typeBp) should also be developed. The active control of the type-A SAS requires the development of cryogenic-compatible sensors and actuators, which will be used for damping the mechanical resonances of the cryogenic payload. There are several candidates for the cryogenic compatible vibration sensors, such as eddy-current sensors and photoreflective sensors, but the detailed design has not been fixed yet and their sensitivities and noise levels are under investigation. As the requirement on the RMS mirror angles in the type-A SAS is stricter than that in the type-B SAS, the strategy of the alignment control should be carefully investigated and the servo designs are under development.

Since the type-Bp SAS does not have the IP pre-isolation stage, it is more difficult to suppress the RMS velocity and angles of the suspended optics than other systems. Figure 9.2 shows the predicted seismic noise level in the type-Bp SAS. The resonant peak appearing at 0.42 Hz corresponds to the main pendulum mode of the attenuation chain, and is not capable of being damped due to the lack of an appropriate sensor to monitor this mode. The resulting RMS mirror velocity is 8 μm/sec and it does not meet the velocity requirement for the lock acquisition. A possible solution is introducing a longitudinal sensor and actuator on the first suspension stage (F2), to apply damping control in the lock-acquisition phase. Including the damping strategy of this mode, the mechanical and control design of the type-Bp system should be polished further to allow stable operation of the interferometer.

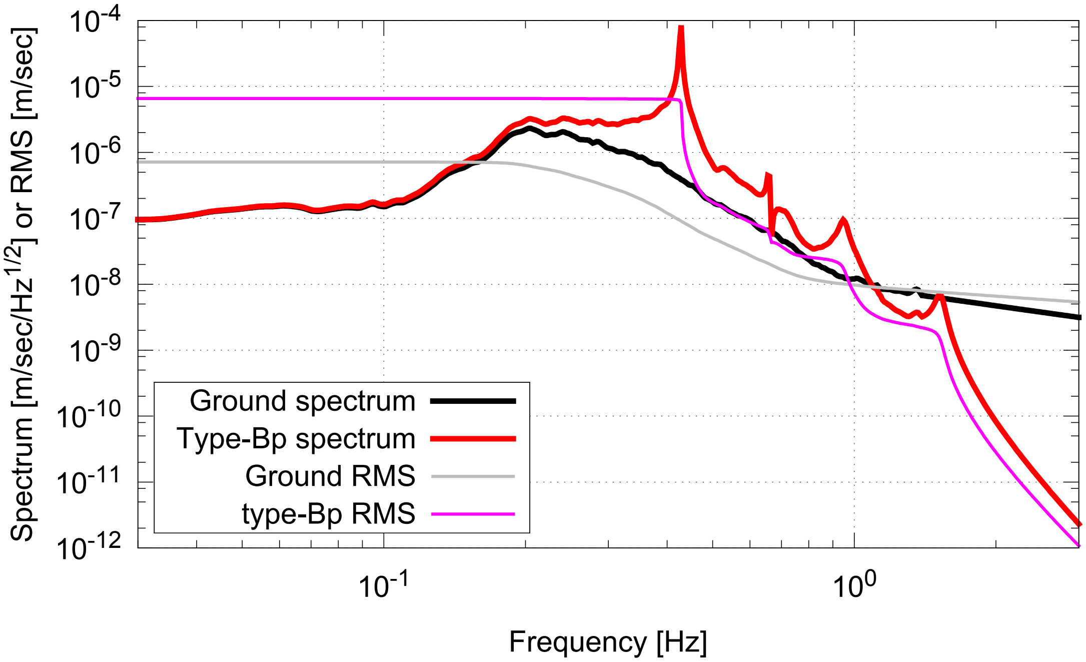

Figure 9.2: Seismic noise level of the type-Bp SAS.

Rigid-body models of KAGRA-SAS

Appendix A

A.1 Overview

In order to check the attenuation performance and controllability of KAGRA-SAS, their mathematical rigid-body models were constructed. The rigid-body modeling treats the suspension system as a combination of rigid-bodies and elastic elements connecting with them. More details on the modeling schemes and mathematical explanations are given in reference [72].

A.2 Type-A SAS

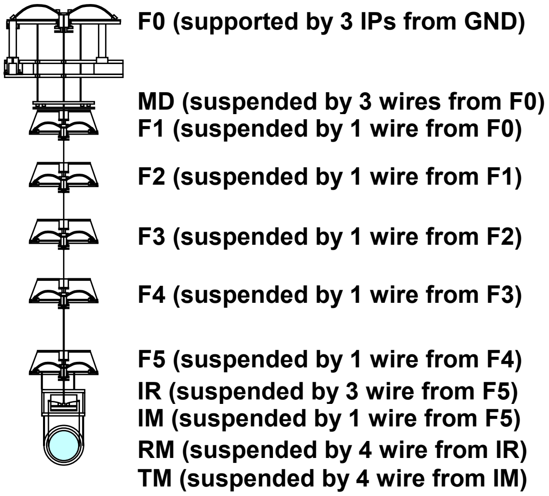

Figure A.1: Topology of type-A SAS.

description		symbol	unit	F0	MD	F1	F2	F3	F4	F5	IR	IM	RM	TM
body	mass	M	kg	474	18	104	90	87	84	61.5	44.9	53.2	33.7	22.7
	moment of inertia (R)	I_R	kg m^2	60		4.4	4.1	4.0	4.0	2.4	0.89	0.47	0.64	0.14
	moment of inertia (P)	I_P		60		4.4	4.1	4.0	4.0	2.4	0.56	0.35	0.43	0.11
	moment of inertia (Y)	I_Y		120		7.3	6.4	6.4	6.4	3.8	0.82	0.68	0.43	0.11
wire	number of wires	n	-	-	3	1	1	1	1	1	3	1	4	4
	material	-	-	-	maraging steel						BeCu			sapphire
	Young's modulus	E	GPa	-	184						136			345
	Poisson ratio	σ	-	-	0.32						0.3			0.29
	loss angle	Φ	-	-	1×10^{-3}						5×10^{-6}			2×10^{-7}
	length	L	m	-	1.94	2.27	2.27	2.27	2.37	3.39	0.3	0.4	0.3	0.3
	diameter (waist)	d	mm	-	2.0	4.5	4.5	4.5	4.5	4.5	0.6	2.0	0.7	1.6
	diameter (neck)	d_n		-	-	3.1	2.8	2.5	2.2	2.0	-	-	-	-
	y-position	D_y		-	-	-	-	-	-	-	-	-	25	15
	x-position	D_x		-	-	-	-	-	-	-	-	-	145	110
	radial distance	D_r		-	290	-	-	-		-	150	-	-	-
	upper clamp height	D_{yu}		-	-80	120	-25	-5	-5	-5	-50	-5	0	0
	lower clamp height	D_{yl}		-	17	-14	5	5	5	5	50	-4	0	0
GAS	resonant frequency	f_{GAS}	mHz	300	-	300	300	300	300	500	-	-	-	-
	quality factor	Q_{GAS}	-	10	-	10	10	10	10	100	-	-	-	-
	saturation level	B_{GAS}	dB	-60	-	-60	-60	-60	-60	-60	-	-	-	-
IP	radial distance to y-axis	R_{IP}	mm	610	-	-	-	-	-	-	-	-	-	-
	length	L_{IP}	mm	480	-	-	-	-	-	-	-	-	-	-
	horizontal mode frequen	f_{IP}	mHz	70	-	-	-	-	-	-	-	-	-	-
	quality factor	Q_{IP}	-	8	-	-	-	-	-	-	-	-	-	-
	saturation level	B_{IP}	dB	-80	-	-	-	-	-	-	-	-	-	-

Figure A.2: Parameters of type-A SAS.

A.3 Type-B/type-Bp SAS

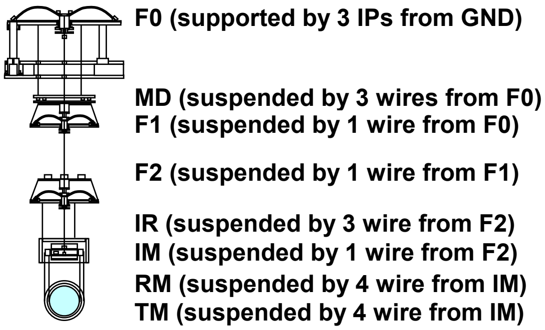

Figure A.3: Topology of type-B SAS.

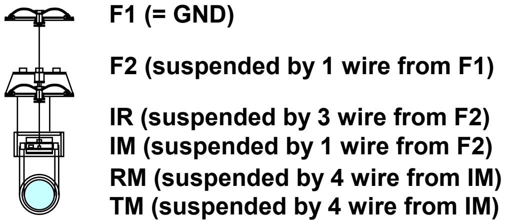

Figure A.4: Topology of type-Bp SAS.

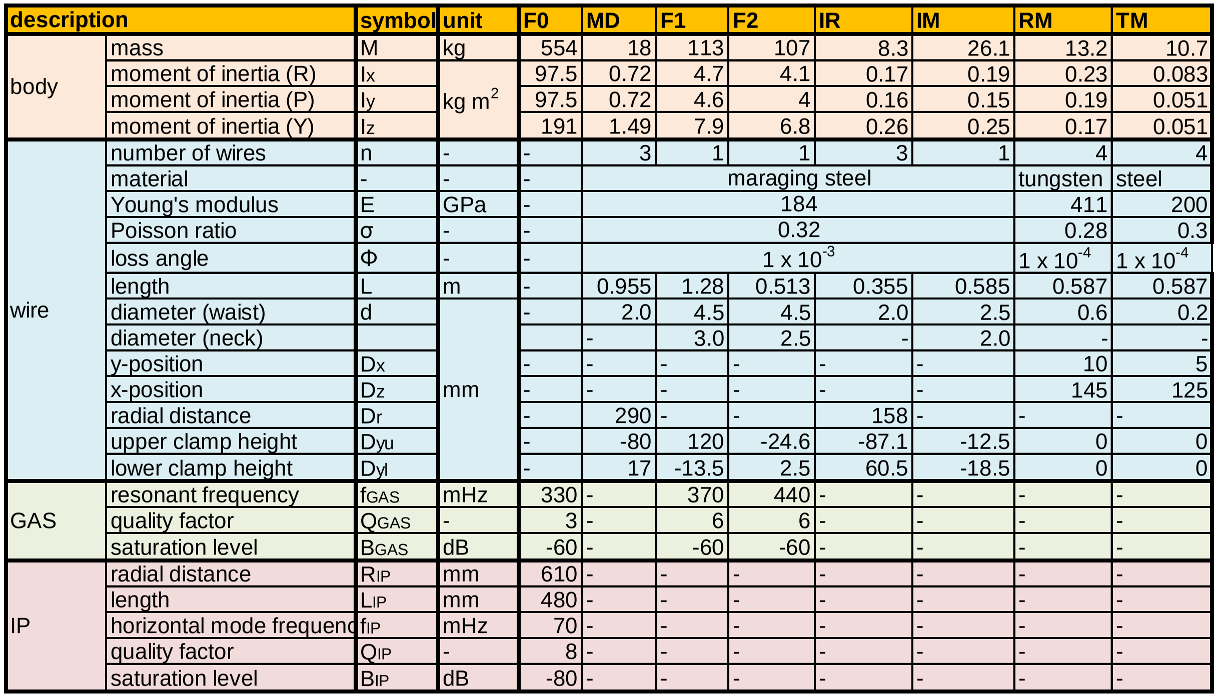

description		symbol	unit	F0	MD	F1	F2	IR	IM	RM	TM
body	mass	M	kg	554	18	113	107	8.3	26.1	13.2	10.7
	moment of inertia (R)	I_x	kg m^2	97.5	0.72	4.7	4.1	0.17	0.19	0.23	0.083
	moment of inertia (P)	I_y		97.5	0.72	4.6	4	0.16	0.15	0.19	0.051
	moment of inertia (Y)	I_z		191	1.49	7.9	6.8	0.26	0.25	0.17	0.051
wire	number of wires	n	-	-	3	1	1	3	1	4	4
	material	-	-	-	maraging steel					tungsten	steel
	Young's modulus	E	GPa	-	184					411	200
	Poisson ratio	σ	-	-	0.32					0.28	0.3
	loss angle	Φ	-	-	1×10^{-3}					1×10^{-4}	1×10^{-4}
	length	L	m	-	0.955	1.28	0.513	0.355	0.585	0.587	0.587
	diameter (waist)	d	mm	-	2.0	4.5	4.5	2.0	2.5	0.6	0.2
	diameter (neck)				-	3.0	2.5	-	2.0	-	-
	y-position	D_x		-	-	-	-	-	-	10	5
	x-position	D_z		-	-	-	-	-	-	145	125
	radial distance	D_r		-	290	-	-	158	-	-	-
	upper clamp height	D_{yu}		-	-80	120	-24.6	-87.1	-12.5	0	0
	lower clamp height	D_{yl}		-	17	-13.5	2.5	60.5	-18.5	0	0
GAS	resonant frequency	f_{GAS}	mHz	330	-	370	440	-	-	-	-
	quality factor	Q_{GAS}	-	3	-	6	6	-	-	-	-
	saturation level	B_{GAS}	dB	-60	-	-60	-60	-	-	-	-
IP	radial distance	R_{IP}	mm	610	-	-	-	-	-	-	-
	length	L_{IP}	mm	480	-	-	-	-	-	-	-
	horizontal mode frequenc	f_{IP}	mHz	70	-	-	-	-	-	-	-
	quality factor	Q_{IP}	-	8	-	-	-	-	-	-	-
	saturation level	B_{IP}	dB	-80	-	-	-	-	-	-	-

Figure A.5: Parameters of type-B / type-Bp SAS.

Eigenmodes of type-B SAS Prototype

Appendix B

♯1:0.05 Hz

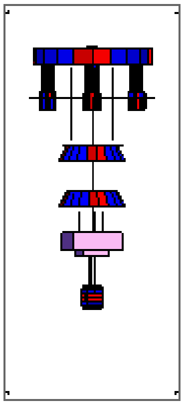

♯2:0.079 Hz

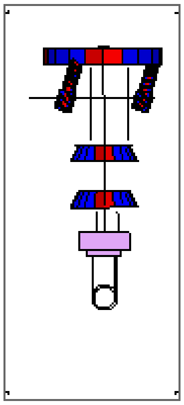

♯3:0.079 Hz

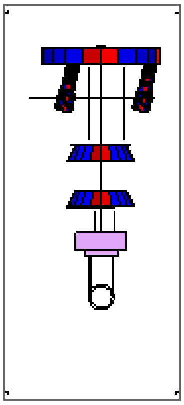

♯4:0.123 Hz

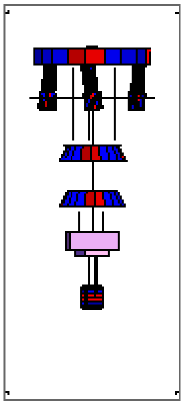

♯5:0.139 Hz

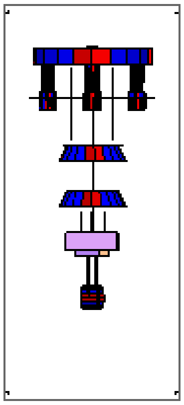

♯6:0.162 Hz

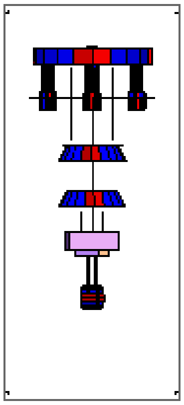

♯7:0.249 Hz

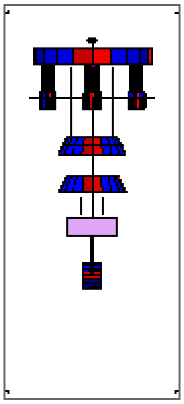

♯8:0.302 Hz

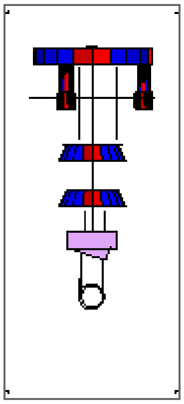

♯9:0.342 Hz

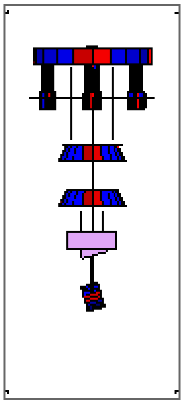

♯10:0.409 Hz

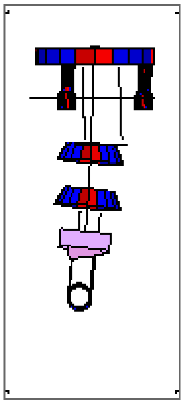

♯11:0.411 Hz

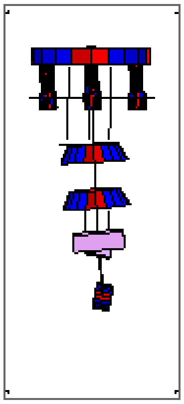

♯12:0.525 Hz

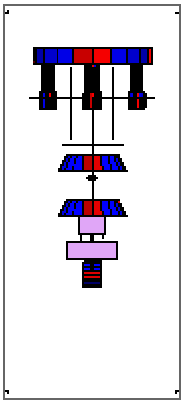

#13:0.547 Hz

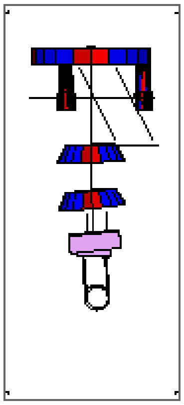

#14:0.547 Hz

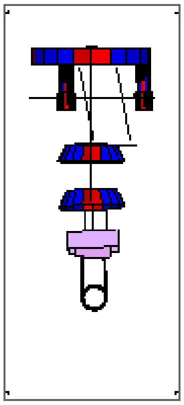

#15:0.55 Hz

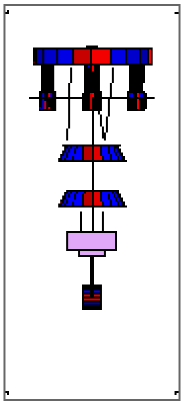

#16:0.574 Hz

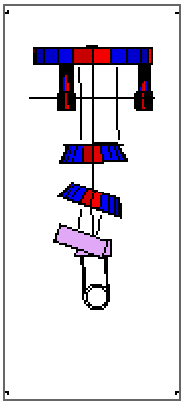

#17:0.579 Hz

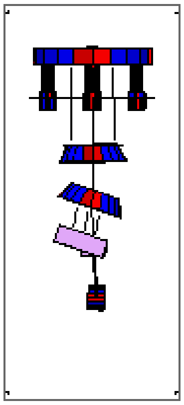

#18:0.589 Hz

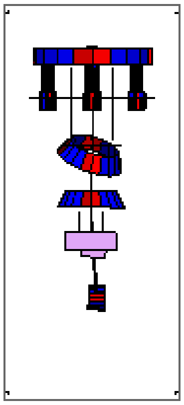

#19:0.633 Hz

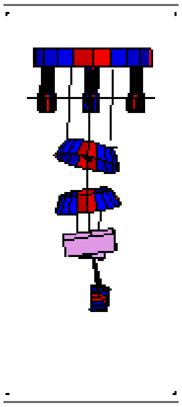

#20:0.648 Hz

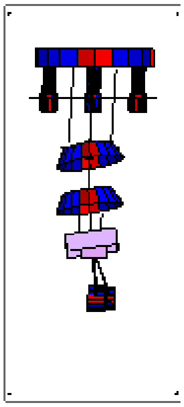

#21:0.657 Hz

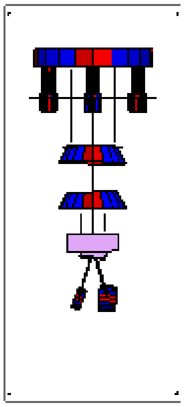

#22:0.658 Hz

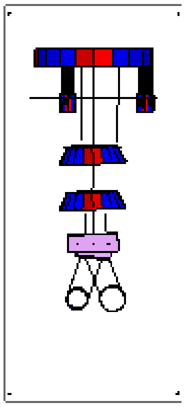

#23:0.686 Hz

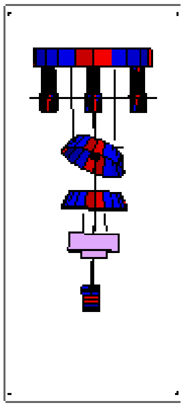

#24:0.792 Hz

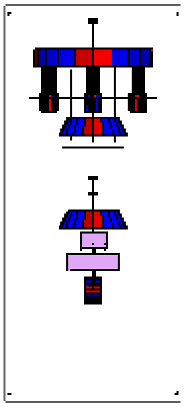

#25:0.816 Hz

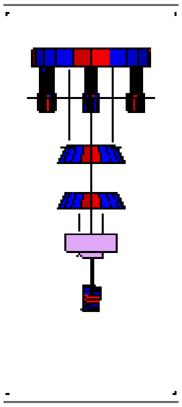

#26:1.001 Hz

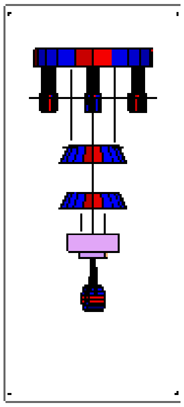

#27:1.032 Hz

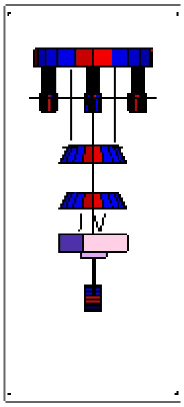

#28:1.184 Hz

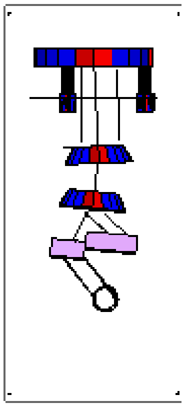

#29:1.185 Hz

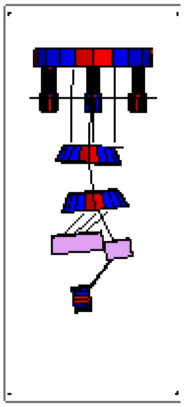

#30:1.21 Hz

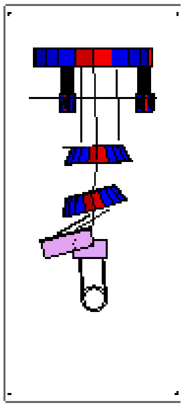

#31:1.213 Hz

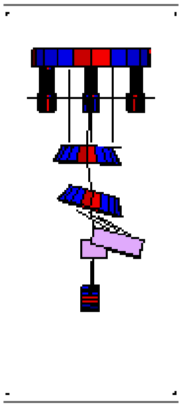

#32:1.38 Hz

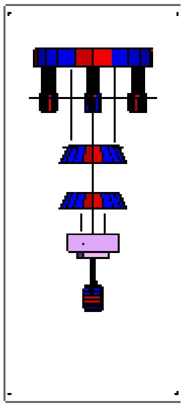

#33:1.474 Hz

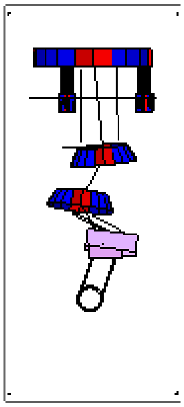

#34:1.476 Hz

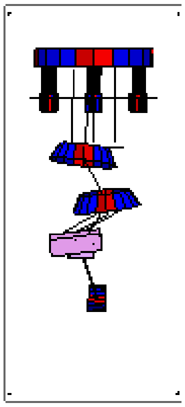

#35:4.856 Hz

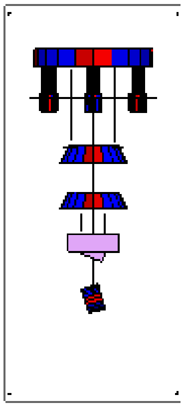

#36:11.32 Hz

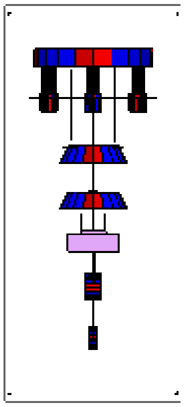

#37:15.528 Hz

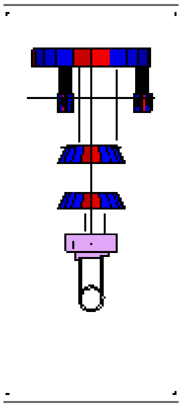

#38:46.957 Hz

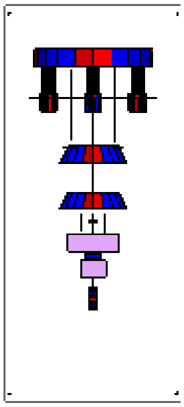

#39:50.551 Hz

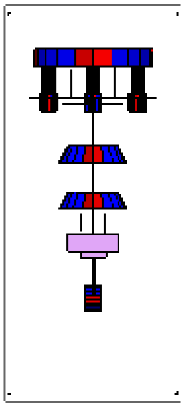

#40:51.942 Hz

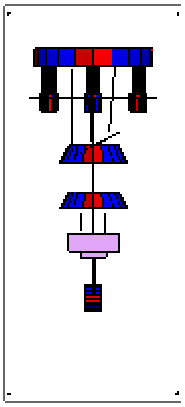

#41:51.942 Hz

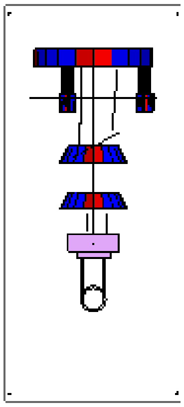

#42:62.748 Hz

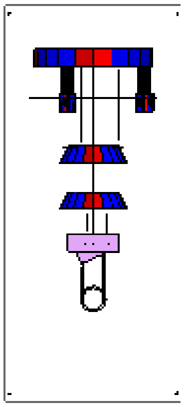

#43:97.285 Hz

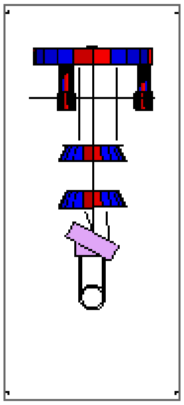

#44:100.507 Hz

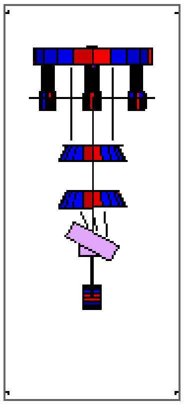

#45:126.75 Hz

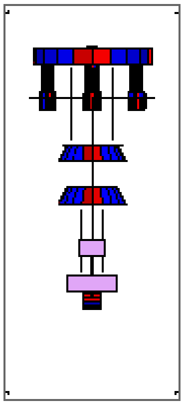

Acknowledgements

I have been supported by many people through the research activities described in this thesis. I would like to express my primary appreciation to my previous supervisor Kazuaki Kuroda, for giving me an opportunity to work on the KAGRA project. I am also indebted to Kimio Tsubono for providing me motivation to work in this interesting and exciting study field. I would like to thank my current supervisor Takaaki Kajita for promoting the KAGRA project as a principal investigator. Without his continuous efforts we would not be here to be working for the project.

Ryutaro Takahashi, the chief of the vibration isolation system (VIS) group of KAGRA, has been my first person to ask for advice in various experiments regarding the vibration isolation systems. I also relied on him a lot also for the procurement of the components of the type-B SAS. I have been helped a lot by Fabian Peña Arellano, Joris van Heijningen, Mark Barton, Yoshinori Fujii, Ayaka Shoda, Koki Okutomi and Hideharu Ishizaki in the prototype experiment of the type-B SAS. The experiments are also supported by the competent mechanical engineers in Advanced Technology Center (ATC) of NAOJ. Tomotada Akutsu served as the interface with the ATC engineers and has been a good adviser for the experiment. I am deeply grateful to Osamu Miyakawa and Masahiro Kamiizumi, for providing us the digital control system and various analog circuits, which are vital components of the active control systems. Raffaele Flaminio, my second supervisor in NAOJ, has always been a good manager and kept providing clear direction and schedule of our works.

Jo van den Brand and his research group members give me a warm welcome to their laboratory at NIKHEF and provided many valuable experiences. Alessandro Bertolini and Eric Hennese have been superb advisors with broad-based knowledge on advanced mechanical engineering techniques. I also had a great opportunity to discuss suspension controls with Jeffrey Kissel, Brian Lantz and his group members at Stanford University. The control strategy developed for KAGRA-SAS is based on the studies obtained from the fruitful discussion with them. Ettore Majorana has always been a trusted adviser and friend, providing broad knowledge on suspension controls based on his experiences in the Virgo project. It was a great fortune to have the opportunity of working with Riccardo DeSalvo, as we could not conduct the prototype experiment without his great contribution to the design of KAGRA-SAS.

I would like to give special thanks to Eiichi Hirose for having fruiteful discussions as a mentor for life. I have been happy to share my time with colleagues at ICRR and NAOJ, who have provided an enjoyable life at the Mitaka and Kashiwa campuses. I would like to thank all the KAGRA collaboration members for proceeding with the challenging project, and my family for support at home.

The research activities had financial support from ALPS for the overseas dispatch program. This work was supported by JSPS KAKENHI Grant Number 26·10236.

Bibliography

[1] A. Einstein, *Ann. der Phys.*, **354** (7), 769–822, (1916).

[2] M. Maggiore. “Gravitational Waves: Theory and Experiments”. Oxford University Press, (2008).

[3] T. Nakamura, N. Mio, and M. Ohashi. “Detecting gravitational waves”. Kyoto University Press, (1998). (in Japanese).

[4] C. Cutler and K. Thorne, *arXiv*, **0204090 [gr-qc]**, (2002).

[5] K. Oohara and T. Nakamura, *Prog. Theor. Phys.*, **82** (3), 535–554, (1989).

[6] C. D. Ott, *Class. Quant. Grav.*, **26**, 063001, (2009).

[7] T. Damour and A. Vilenkin, *Phys. Rev. D*, **71**, 063510, (2005).

[8] The LIGO Scientific Collaboration and The Virgo Collaboration, *Nature*, **460**, 990–994, (2009).

[9] J. Weber, *Phys. Rev. Lett.*, **22**, 1320–1324, (1969).

[10] P. Astone et al., *Phys. Rev. D*, **82**, 022003, (2010).

[11] K. Kawabe, *PhD thesis*, University of Tokyo, (1998).

[12] B. Bochner, *Gen. Relativ. Gravit.*, **35** (6), 1029–1055, (2003).

[13] A. Buonanno and Y. Chen, *Phys. Rev. D*, **64**, 042006, (2001).

[14] M. Ando, *PhD thesis*, University of Tokyo, (1998).

[15] B. J. Meers, *Phys. Rev. D*, **38**, 2317, (1988).

[16] J. Mizuno, *PhD thesis*, Universitat Hannover, (1995).

[17] M. G. Beker, *PhD thesis*, Vrije Universiteit, (2013).

[18] P. R. Saulson, *Phys. Rev. D*, **42** (8), 2437–2445, (1990).

[19] W. J. Startin et al., *Rev. Sci. Instrum.*, **69** (10), 3681–3689, (1998).

[20] A. V. Cumming et al., *Class. Quant. Grav.*, **29**, 035003, (2012).

[21] S. Rowan et al., *Phys. Lett. A*, **265**, 40309, (2000).

[22] T. Tomaru et al., *Phys. Lett. A*, **301**, 215–219, (2002).

[23] H. J. Kimble et al., *Phys. Rev. D*, **65**, 022002, (2001).

[24] K. Arai et al., *Class. Quant. Grav.*, **26**, 204020, (2009).

[25] H. Grote (for the LIGO Scientific Collaboration), *Class. Quant. Grav.*, **27**, 084003, (2010).

[26] D. Sigg (for the LIGO Science Collaboration), *Class. Quant. Grav.*, **25**, 114041, (2008).

[27] T. Accadia et al., *Class. Quant. Grav.*, **28**, 114002, (2011).

[28] S. Fairhurst et al., *Gen. Relativ. Gravit.*, **43**, 387–407, (2011).

[29] K. Kuroda and LCGT collaboration, *Int. J. Mod. Phys. D*, **20** (10), 1755–1770, (2011).

[30] M. Punturo, *Class. Quant. Grav.*, **27**, 194002, (2010).

[31] Y. Aso et al., *Phys. Rev. D*, **88**, 043007, (2013).

[32] K. Somiya, *Class. Quant. Grav.*, **29**, 124007, (2012).

[33] S. Hild, *Class. Quant. Grav.*, **29**, 124006, (2012).

[34] P. Amaro-Seoane and L. Santamaria, *Astrophys. J.*, **722**, 1197–1206, (2010).

[35] M. C. Miller, *Astrophys. J.*, **581**, 438–450, (2002).

[36] K. Izumi, *PhD thesis*, University of Tokyo, (2012).

[37] J. Abadie et al., *Astrophys. J.*, **722**, 1504–1513, (2010).

[38] K. Hayama, *KAGRA Internal Document*, **JGW-G1402127-v5**, (2014).

[39] P. Canizares et al., *Phys. Rev. Lett.*, **114**, 071104, (2015).

[40] T. Takiwaki and K. Kotake, *Astrophys. J.*, **743** (1), 30, (2011).

[41] K. Kotake et al., *Astrophys. J. Lett.*, **697** (2), 133–136, (2009).

[42] J. Peterson, *Open File Report*, pages 93–322, (1993).

[43] P. Shearer. "Introduction to Seismology Second Edition". Cambridge Univirsity Press, (2009).

[44] "LCGT Design Document Ver. 3.0". (in Japanese, 2009) available from `http://gwwiki.icrr.u-tokyo.ac.jp/JGWwiki/LCGT`.

[45] M. G. Beker et al., *Gen. Relativ. Gravit.*, **43**, 623–656, (2011).

[46] A. L. Kimball and D. E. Lovell, *Phys. Rev.*, **30**, 948–959, (1927).

[47] H. A. Sodano et al., *J. Vib. Acoust.*, **128**, 294–302, (2006).

[48] T. Nishi, *Master's thesis*, University of Tokyo, (2003). (in Japanese).

[49] F. Matichard et al., *arXiv*, page 1502.06300, (2015).

[50] J. Giaime et al., *Rev. Sci. Instrum.*, **67** (1), 208–214, (1996).

[51] R. Takahashi et al., *Rev. Sci. Instrum.*, **73** (6), 2428–2433, (2002).

[52] G. Ballarding et al., *Rev. Sci. Instrum.*, **72** (9), 3635–3642, (2001).

[53] M. Beccaria et al., *Nucl. Instrum. Methods A*, **394**, 397–408, (1997).

[54] F. Acernese et al., *Astrop. Phys.*, **93**, 182–189, (2010).

[55] A. Takamori, *PhD thesis*, University of Tokyo, (2002).

[56] A. Takamori et al., *Nucl. Instrum. Methods A*, **582**, 683–692, (2007).

[57] G. Losurdo et al., *Rev. Sci. Instrum.*, **70** (5), 2507–2515, (1999).

[58] A. Stochino et al., *Nucl. Instrum. Methods A*, **598**, 737–759, (2009).

[59] G. Cella et al., *Nucl. Instrum. Methods A*, **540**, 502–519, (2005).

[60] R. DeSalvo et al., *Nucl. Instrum. Methods A*, **538**, 526–537, (2005).

[61] R. DeSalvo et al., *Eur. Phys. J. Plus*, **126**, 75, (2011).

[62] A. Stochino et al., *Nucl. Instrum. Methods A*, **580**, 1559–1564, (2007).

[63] A. Wanner et al., *Class. Quant. Grav.*, **29**, 245007, (2012).

[64] The Virgo Collaboration. "Advanced Virgo technical design report". Chapter 12, VIR-0128A-12 URL: `https://tds.ego-gw.it/ql/?c=8940`, (2012).

[65] M. G. Beker et al., *Physics Procedia*, **37**, 1389–1397, (2012). Proceedings of the 2nd International Conference on Technology and Instrumentation in Particle Physics (TIPP 2011).

[66] M. Lobue et al., *J. Magn. Magn. Mater.*, **290**, 1184–1187, (2005).

[67] Y. Arase et al., *Journal of Physics: Conference Series*, **122**, 012027, (2008).

[68] Y. Aso et al., *Class. Quant. Grav.*, **29**, 124008, (2012).

[69] KAGRA Main Interferometer Working Group, *KAGRA Internal Document*, **JGW-T1200913-v6**, (2014). [1].

[70] K. Agatsuma et al., *Class. Quant. Grav.*, **27**, 084022, (2010).

[71] T. Sekiguchi, *KAGRA Internal Document*, **JGW-T1402971-v1**, (2014).

[72] T. Sekiguchi, *Master's thesis*, University of Tokyo, (2012). Archived in KAGRA Internal Document: JGW-P1200770-v2.

[73] H. Tariq et al., *Nucl. Instrum. Methods A*, **489**, 570–576, (2002).

[74] C. Wang et al., *Nucl. Instrum. Methods A*, **489**, 563–569, (2002).

[75] K. Agatsuma et al., *Journal of Physics: Conference Series*, **122**, 012013, (2008).

[76] G. Losurdo et al., *Rev. Sci. Instrum.*, **72** (9), 3653–3661, (2001).

[77] F. Cordero et al., *J. Alloys Compd.*, **310**, 400–404, (2000).

[78] M. Beccaria et al., *Nucl. Instrum. Methods A*, **404**, 455–469, (1998).

[79] G. Hammond, *LIGO Internal Document*, **T010171-00-D**, (2001). [2].

[80] A. Bernardini et al., *Rev. Sci. Instrum.*, **70** (8), 3463–3472, (1999).

[81] A. Takamori et al., *Class. Quant. Grav.*, **19**, 1615–1621, (2002).

[82] S. Aston, *LIGO Internal Document*, **T050111-04-K**, (2009).

[83] Y. Sakakibara, *PhD thesis*, University of Tokyo, (2015).

[84] E. Hirose et al., *Class. Quant. Grav.*, **31**, 224004, (2014).

[85] K. Yamamoto et al., *Journal of Physics: Conference Series*, **32**, 418–423, (2006).

---

[1] KAGRA internal documents are available from `http://gwdoc.icrr.u-tokyo.ac.jp/cgi-bin/DocDB/DocumentDatabase`

[2] LIGO internal documents are available from `https://dcc.ligo.org/cgi-bin/DocDB/DocumentDatabase`

[86] E. D. Black, *Am. J. Phys.*, **69**, 79, (2001).

[87] A. J. Mullavey et al., *Optics Express*, **20** (1), 81–89, (2011).

[88] K. Izumi, *Master's thesis*, University of Tokyo, (2009). (in Japanese).

[89] Y. Michimura, *KAGRA Internal Document*, **JGW-T1202403-v1**, (2014).

[90] *KAGRA Internal Document*, **JGW-T1201255-v1**.

[91] W. Kokuyama, *PhD thesis*, University of Tokyo, (2012).

[92] `http://www.aps.anl.gov/epics/`.

[93] Y. Michimura, *KAGRA Internal Document*, **JGW-T1203453**, (2015).

[94] F. Acernese et al., *Astrop. Phys.*, **20**, 617–628, (2004).